UNIVERSITÀ DEGLI STUDI DI MODENA E REGGIO EMILIA

SCUOLA DI DOTTORATO

Dottorato in Physics and Nanosciences

Tesi di Dottorato

Assessment of Many-body perturbation theory approximations beyond GW

Simone Vacondio

Relatrice
Prof.ssa Alice Ruini

Correlatori
Dott. Andrea Ferretti
Dott. Daniele Varsano

Coordinatore del corso di dottorato
Prof. Marco Affronte

XXXV CICLO

Summary

The GW approximation of many-body perturbation theory (MBPT) is a widespread tool for the prediction of electronic excitations in materials and chemical compounds. It has been particularly effective for the calculation of band gaps of extended systems, and has recently been shown to well describe binding energies of molecules at large, even down to core levels. However, GW does not come without its own share of limitations: self-consistency (or lack thereof), prediction of photoemission satellites and description of strong correlations are all known issues of GW.

In an attempt to address these issues, the work presented in this thesis revolves around the assessment of GW and beyond-GW theories. Spherical atoms were chosen as a test set due to not only being thoroughly characterized experimentally, but also requiring a relatively modest effort when it comes to implementing MBPT without introducing any further approximate technique (e.g. pseudopotentials, frequency representations, infinite basis set extrapolations).

Depending on their end goal, the theories being studied present different formulations within MBPT. For the computation of quasi-particle (QP) properties, the framework of vertex corrections prescribed by Hedin's equations has proven ideal. Conversely, the incoherent part of photoemission spectra, populated by the so-called satellite peaks, has seen the failure of not only GW, but also of many standard approached based on simple self-energy approximations in conjunction with the Dyson equation.

Within this broader context, one initial chunk of work presented in this thesis deals with the field of vertex corrections for the computation of QP properties (and Green's functions at large). The GW, 2nd Born and GW+second-order screened exchange (GW+SOSEX) self-energies were considered and benchmarked. These self-energies are simple enough to be written as a low-order expansion given by a vertex correction. The full time-dependent Hartree-Fock (TDHF) vertex was also studied, which entails the inclusion of ladder diagrams to infinite order in the self-energy. This required the more involved solution of a Bethe-Salpeter equation (BSE)-like problem.

These self-energies were used to solve perturbatively the Dyson equation of MBPT, yielding atomic ionization energies (and valence states) which were compared against experimental data. Furthermore, the self-energies were employed for the self-consistent solution of the linearized Sham-Schlüter (LSSE) equation, producing exchange-correlation (xc) potentials within the Kohn-Sham density functional theory (KS-DFT) framework; providing a further benchmark, these potentials were compared against exact ones available in the literature. This thesis collects the details of the implementation of these methods for spherical atoms, and the results of the calculations. The starting point dependence is

addressed for each of the self-energy approximations: the best starting points are singled out in each case, with the 2B and TDHF self-energies being fit for HF and carrying no ambiguity in this respect. It is ultimately found that an increased accuracy with respect to GW can be attained with the inclusion of higher-order terms in the self-energy, and generally with less ambiguity concerning the starting point.

Moving away from QP properties, part of the work presented in this thesis has instead been concerned with satellite prediction in photoemission spectra. This work is the product of a joint effort together with the Theoretical Spectroscopy Group of the Laboratoire des Solides Irradiés of the École Polytechnique (Palaiseau, France) led by Dr. Lucia Reining. In this case, preliminary calculations presented in the thesis support the need for accounting for hole relaxation in the photoemission process. The theory behind such calculations is only sketched in the thesis and is the subject of ongoing work.

Contents

Chapter 1

Introduction

Materials design and engineering are at the basis of new generations of (nano-)devices, such as transistors, batteries, and solar cells. A thorough characterization of (nano-)materials – that is, knowing their composition, their nanoscopic geometry, their physical properties – is necessary at many steps of their experimental realization. Among the many means of characterization of materials lies electron spectroscopy, which can provide precious information about their electronic structure. The interpretation of experimental spectra must of course go hand in hand with an understanding provided by a physical theory based on Quantum Mechanics, given the microscopic nature of the phenomena involved in the spectroscopic process. In the best case scenario, the theory should also be predictive of the experimental results in a completely *ab initio* framework.

This thesis, in particular, is about finding approximations beyond the ab initio state-of-the-art method devoted to the prediction of *photoemission spectra* in condensed matter theory, namely the so-called GW method of many-body perturbation theory (MBPT). Indeed, angle-resolved photoemission spectroscopy (ARPES) has undergone developments so notable in recent years [1–3] that highly accurate and predictive theories are to be devised in order to thoroughly interpret the experimental data. Meanwhile, the numerical implementation of these ever improving theories is being made possible by the deployment of near-exascale supercomputers through the action of high-perofrmance computing (HPC) facilities in the scientific community [4]. This ideal synergy of theory, numerics, and experiment should in the end be highly beneficial for the technological advancements mentioned earlier. The work of this thesis is situated at the very intellectually stimulating intersection between theory and numerics within the MBPT framework, whose challenges I will proceed to introduce in this Chapter, along with the advancements I pursued.

In the coming Sections I will outline the framework within which we will be moving. In Section 1.1 I will introduce the photoemission experiment and the theories which relate photoemission spectra to the electronic structure of a system, namely independent-particle and quasi-particle theory. Within the quasi-particle framework, in Section 1.2 I will specifically present the GW method of MBPT, its successes, and its limitations. In Section 1.3 I will then outline the systematic procedure that MBPT offers by means of vertex corrections in order to devise approximations beyond GW. In Section 1.4 I will focus on two of the major issues of GW, the starting point dependence and self-consistency, which vertex corrections are meant to address. In Section 1.5 I will introduce schemes to obtain

approximate self-consistency that are specifically explored in this thesis. In Section 1.6 I will introduce atoms, molecules and finite systems as testing grounds for MBPT methods. Finally, in Section 1.7 I will present the scope of the thesis and its structure.

1.1 Photoemission: experiment and theory

Photoemission spectroscopy [1, 2] is based on the photoelectric effect, which consists in electrons being emitted from a material when energy is transferred to them by photons. This takes the electrons in the material to a *positively charged excitation* state, which is only possible when the photons have enough energy to bring some electrons beyond the vacuum level and remove them from the material. Otherwise, photons may simply leave the electrons in the material in a *neutral excitation* state, without any of these being emitted; in the latter case, we may speak of *absorption spectroscopy* rather than photoemission. While in photoemission one is interested in detecting the emitted electrons and their kinetic energies, absorption is about the wavelengths at which photons get absorbed. One may also probe the charged excitations of a material by sending electrons to it and by measuring the energy gain of doing so in terms of the emitted photon's wavelength: this is called an *inverse* photoemission experiment, and is about *negatively* charged excitations. One valuable product of photoemission experiments are photoemission spectra, representing the abundance of electrons with respect to their kinetic energy upon emission (see Figure 1.1). Each spectral line is a signature of an excited state of the material being investigated. In a crude but often meaningful simplification, the electrons in the material can be thought of as independent particles (IPs) stacked into energy levels according to the Pauli principle: different lines in the spectrum can then be assigned to different levels which the electrons came from upon photoemission. In fact, supposing that the electrons of a system occupy the levels having energies ε_i, photons of energy $h\nu$ will produce spectral lines at the kinetic energies

$$\mathrm{KE}_i = h\nu - \varepsilon_i. \tag{1.1}$$

The energy ε_i of the i-th occupied IP level can then be easily found with the knowledge of the photon energy $h\nu$. The formula also holds for inverse photoemission with minor adjustments: in this case, ε_i is the energy of an empty IP level, which can be found with the knowledge of KE (set by the experiment) and $h\nu_i$ (measured by the experiment). (Notice how the index i was moved from KE to ν.) It is then natural to define ε_i as either the *removal energy*[1] or the *addition energy* of the i-th energy level, depending on occupation. In the IP picture, in particular, removing an electron from a system will leave it in a charged excitation state characterized by a *hole*, which can be called a *hole state*.

The IP picture is pervasive in the description of electronic excitations. Even the quasiparticle picture, which we will introduce later, is strongly connected to it. In fact, the IP picture led to the first successes in the electronic structure calculations of finite systems and extended systems alike. In the case of finite systems, the Hartree-Fock (HF) method [6, 7] provides a decent description of energy levels of atoms and small molecules, and is the

[1] *Binding energy* will also be used throughout equivalently to "removal energy". This term also refers to the energy scale of the photoemission spectrum once the photon energy is subtracted.

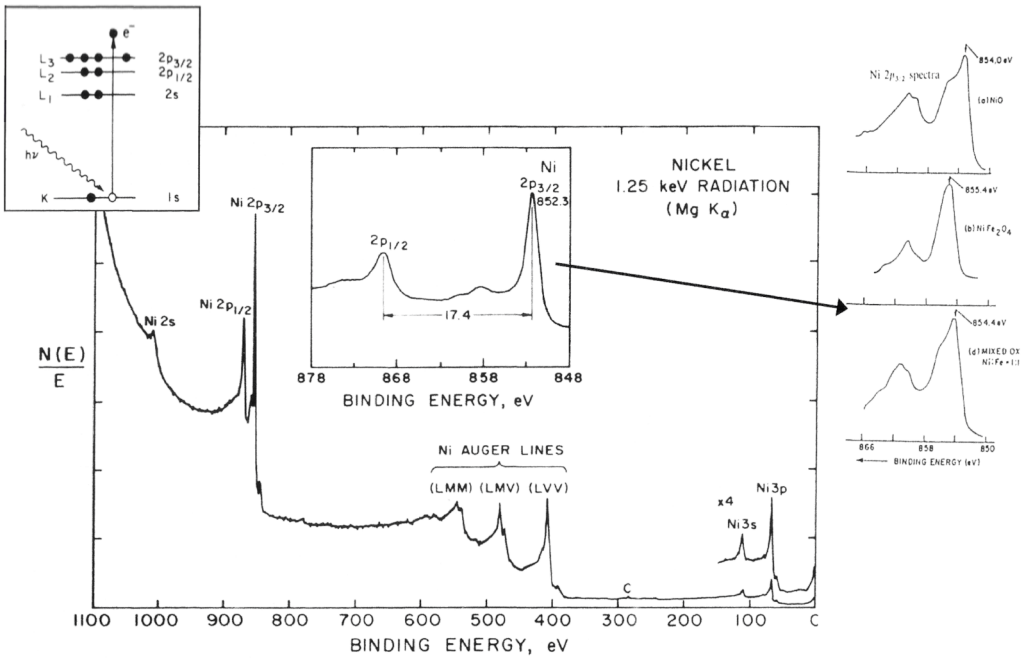

Figure 1.1. Photoemission spectrum of Ni obtained with a 1.25 keV photon. Spin-orbit splittings are well resolved in the emission from $2p$ core levels. Auger peaks are present due to the holes left by photoemitted electrons in the $n = 2$ shell (or L in spectroscopic notation), which are filled by the decay of shallower electrons (e.g. M or V electrons). The energy gain due to the decay is spent to emit the Auger electrons (e.g. M or V electrons again). The spectra on the right emphasize the little influence that the chemical environment has on the core levels of Ni. The spectrum is taken from Ref. 5.

starting point of post-HF methods belonging to the quantum chemistry domain, such as configuration interaction or coupled cluster [8]. In the case of solid state, the whole theory of band structures [9] is as well based on an IP description, which initially relied on empirical pseudopotentials to make quantitative predictions [10]. Here the discrete index i becomes a multi-index,

$$i \;\rightarrow\; n\mathbf{k},$$

where n is the band index (discrete) and $\mathbf{k}$ the crystalline wave vector (continuous); the latter gives rise to the dispersion that makes us speak of energy bands in condensed matter rather than energy levels. One of the intriguing aspects of ARPES is that it is capable of resolving bands in terms of their dispersion. Some notable quantities of interest can be identified in the IP band structure of solids: these include the *band gap* of non-conducting solids, which is the energy gap between the valence band maximum (VBM) and the conduction band minimum (CBM). This quantity is of particular interest in semiconductor physics, which was the at the core of the transistor-powered technological revolution of the XX century. In conducting systems one may be interested in occupied *bandwidths* instead. Finite systems also have their share of notable quantities: here, of all levels, one often looks at the highest-occupied molecular orbital (HOMO) and at the lowest-unoccupied molecular

orbital (LUMO). Within IP theory, their associated eigenvalues are identified with the *ionization energy* (IE) and the *electron affinity* (EA) respectively; this statement should generally be corroborated by a Koopmans' theorem, as in HF theory. Similarly to the band gap, the HOMO-LUMO gap may also be considered in finite systems, and in the following we will generically refer to *energy gaps* of finite systems and non-conducting solids alike.

Finally, the greatest success of IP theory is probably the Kohn-Sham formulation of density functional theory (KS-DFT) [11, 12], today's standard for the calculation of many properties of solids, molecules and nanosystems, such as structural properties and total energies. Despite all the achievements, IP theory is of course no silver bullet for electronic structure: it gives us a concise, and even quantitatively meaningful idea of how electrons pile up in matter, but this is a simplistic picture that may miss important many-body effects, and that is really agnostic of the means used to investigate the electronic structure itself. In our case, that of photoemission, IP theory cannot explain the broadenings of the peaks in the spectra, and some lines are not present at all; not to mention that a quantitative improvement of the energy positioning of lines that are present can still be demanded, which may be beyond possible advancements of IP theory. This is where the quasi-particle picture of MBPT enters the game.

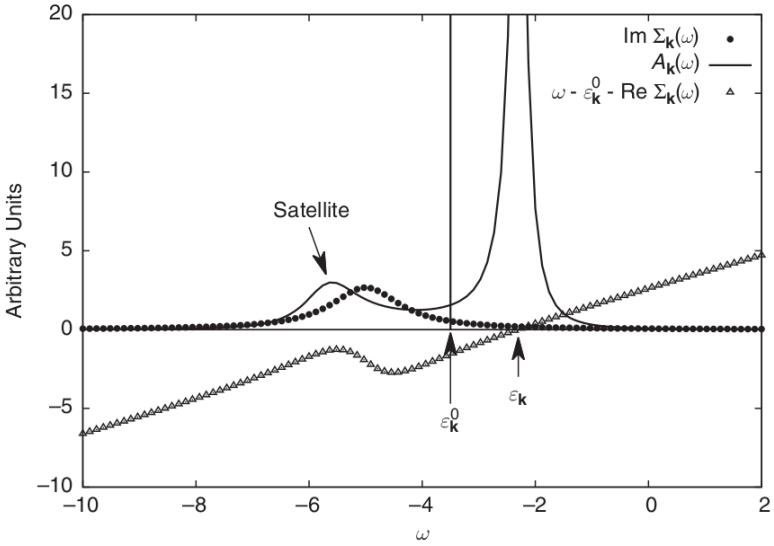

Figure 1.2. The effect of the Dyson equation on the spectral function A through the action of the self-energy Σ. Here ε^0 is the IP eigenvalue, ε the QP energy, Σ the self-energy, and A the spectral function. Picture from Ref. 13.

Within the MBPT framework, the quasi-particle (QP) picture [13, 14] constitutes a refinement of the IP picture. Here, as presented in Chapter 2, the central object is the Green's function G rather than the full many-body wavefunction Ψ afforded by the solution of the Schrödinger equation. It is a way simpler object, carrying only two spin-space-time variables,

$$G = G(1,1'),$$

where $1 \equiv (\mathbf{r}_1 t_1, \sigma_1)$, instead of having as many spin-space variables as the number of

electrons in the system. Physically, the Green's function describes the motion of a single particle in a many-particle environment, and various observables can be obtained from it: most importantly for the problem at hand, its diagonal in terms of space coordinates (while retaining time dependence) yields the spectral function A of a system, Eq. (2.32), which bears a connection with the photoemission spectrum obtained from experiment. In fact, the Green's function is a complex function which, once taken to frequency space via a Fourier transform, has its poles in correspondence to the charged excitation energies of a system, positive and negative alike. With an IP Green's function G_0, which is trivial to build once the IP hamiltonian problem is solved, these poles are the IP energies ε_i seen earlier, with i encompassing both occupied and unoccupied levels. In the spectral function obtained from G_0, these poles have the effect of producing delta-shaped peaks centered at the energies ε_i: these constitute a zero-order approximation to the spectral lines of the photoemission experiment. The real deal is, however, the possibility of building upon this level of theory by introducing the interaction among electrons through the Dyson equation,

$$G = G_0 + G_0 \Sigma G. \tag{2.128}$$

The Dyson equation relies on the self-energy operator Σ, an object accounting for the interactions of one particle with all the other particles of the system, these in turn reacting to the presence and the motion of the particle itself. Through the Dyson equation, the self-energy yields the fully interacting Green's function G starting from the IP Green's function G_0. The Dyson equation is usually solved starting from a G_0 chosen so as to minimize the self-energy correction. KS-DFT or the HF method often offer decent starting points in this sense. If the correction is small, the QP picture is valid: the self-energy then has the effect of shifting the poles found at ε_i to the QP energies $\varepsilon_i^{\mathrm{QP}}$, and the difference $\varepsilon_i^{\mathrm{QP}} - \varepsilon_i$ is called the QP shift. This shift is governed, in a diagonal approximation, by the quasi-particle equation (QPE),

$$\varepsilon_i^{\mathrm{QP}} = \varepsilon_i + \mathrm{Re}\Big\{ \langle i | \Sigma(\varepsilon_i^{\mathrm{QP}}) | i \rangle \Big\},$$

as presented in Section 2.1.6. Furthermore, the peaks of the spectral function will not only appear shifted, but also broadened, with a fractional weight smaller than 1 given by the formula

$$Z_i = \left(1 - \left. \frac{\partial \Sigma_i}{\partial \omega} \right|_{\varepsilon_i^{\mathrm{QP}}} \right)^{-1}.$$

The shifting and broadening mechanism is depicted in Figure 1.2. According to the time-energy uncertainty principle, the weight loss of the peaks results from the now finite lifetime of the QP state in which the system is found after the electron leaves it. In particular, the system is left in a state characterized by a hole, reminiscent of the hole one would have in the electron stacking of the IP picture; however, the energy of this state is now corrected for higher order exchange-correlation effects contained in the self-energy beyond IP theory, and has a finite lifetime, making it rather a quasi-hole state. This one-to-one relation between IP states and QP states, allowing one to trace the simple connection

$$\varepsilon_i \to \varepsilon_i^{\mathrm{QP}},$$

is the very foundation of the whole QP picture. Whenever it is not possible to trace such a connection, a breakdown of the QP picture takes place: this happens when e.g. the system

is characterized by strong electron correlations. It must be added that the weight loss of the QP peaks in the interacting system occurs in favour of the so-called incoherent part of the spectrum: at deeper energies than the QP ones, peaks are found which are signatures of secondary excitations of the system accompanying the photoemission process. These peaks, which are termed *satellite* peaks (again, see the one shown in Figure 1.2), have no counterpart in terms of an IP description (which QPs have): they can be related instead to e.g. the emission of an electron accompanied by the collective excitation of a plasmon, usually in extended systems; or, the emission of an electron accompanied by the neutral excitation of another electron or Auger decay (see Figure 1.1), more likely in finite systems.

1.2 The GW method

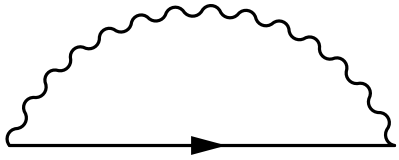

Figure 1.3. The GW self-energy diagram. G is represented by the arrowed line, while W is the wiggly line.

While the solution of the Dyson equation is often easily handled, requiring numerically no more than matrix inversions on a frequency range, computing the exact self-energy is not. In fact, it should be specified that the Green's function introduced in the Section 1.1 is the *single-particle* Green's function: it obeys an equation of motion involving the so-called *two-particle* Green's function G_2, which carries 4 spin-space-time arguments and describes the correlated propagation of two particles in the system; G_2 is in turn dependent on the three-particle Green's function G_3, and so on, until the N-particle Green's function G_N is reached, with N the number of particles in the system. Although a relatively simple object, the exact single-particle Green's function requires going through all this hierarchy of equations of motion for it to be obtained, which is just as complex as solving the full many-body problem. The self-energy is no simpler to compute: in fact, it is none other than a recasting of G_2, which also ultimately depends on G_N through the hierarchy of equations of motion. The self-energy, however, is one convenient object (although not the only one) on which approximations can be made based on physical grounds; an approximate interacting Green's function can then be obtained afterwards via the Dyson equation. Approximations to the self-energy, and its ingredients at large, can be represented making use of Feynman diagrams: these emphasize the interactions between particles that a particular approximation accounts for [15].

Hedin's scheme [16–19] (see Section 2.1.7) offers an iterative procedure to devise self-energy approximations: here Σ is written as

$$\Sigma(1,2) = iG(1,\bar{4})W(1^+,\bar{3})\tilde{\Gamma}(\bar{4},2;\bar{3}), \tag{2.132}$$

where a screened Coulomb interaction W and a vertex function $\tilde{\Gamma}$ are introduced; barred

indices are summed/integrated over. Ignoring vertex corrections both in Σ and W yields the GW approximation (Figure 1.3),

$$\Sigma^{\mathrm{GW}}(1,2) = iG(1,2)W^{\mathrm{RPA}}(1^+,2). \tag{2.137}$$

Plugging this self-energy into the Dyson equation yields an interacting Green's function that describes the propagation of a particle inside a medium whose charges polarize classically; a Dyson equation for W,

$$W^{\mathrm{RPA}}(1,2) = v(1,2) - iv(1,\bar{3})G(\bar{3},\bar{4})G(\bar{4},\bar{3})W(\bar{4},2), \tag{2.139}$$

ensures that these charges are interacting via the classical Coulomb interaction v. This is in particular the content of the random-phase approximation (RPA) to W [20], which amounts to time-dependent Hartree theory. It must be emphasized that, although the description of the polarization (and therefore of the screening in W^{RPA}) is classical, the propagation of the particle described by the Green's function retains a quantum nature: the GW self-energy is in fact a refinement of the HF self-energy, in which the Coulomb interaction appears at the bare level; namely, $\Sigma_{\mathrm{HF}} = iGv$, with v being the bare Coulomb interaction. This implies that exchange, a purely quantum effect ensuring the fermionic nature of electrons, is being taken into account (although not exactly, giving rise to a so-called self-screening error, as we shall see later). Finally, it is worth noting that the self-energy is made dependent on the final interacting G itself (which may also enter the computation of W^{RPA}), as a consequence of Hedin's scheme being iterative. As mentioned earlier, the Dyson equation is often solved rather by starting from an IP solution, possibly close to the QP one. Many choices can actually be made in this regard, as we shall see in Section 1.4.

Historically, the GW approximation was introduced in the context of Fermi liquids, particularly in the homogeneous electron gas (HEG) model for metals [20]. Here it cures unphysical behaviours affecting HF, which are due to the long-range nature of the unscreened Coulomb interaction v [16]; in fact, it avoids in general divergences due to self-energy expansions in v [21]. Furthermore, it captures properties of limiting cases, such as those of core electrons, Rydberg electrons in atoms and fast electrons in the HEG [22]. Most importantly, it reduces the (too large) HF gaps of gapped systems, and opens up the (too small) KS-DFT ones. This last property is at the basis of the success of the GW approximation in predicting band gaps over the last 40 years [17, 18, 23–30]. In particular, band gaps as computed from KS-DFT in the local density approximation (LDA) always turn out too small due to the KS-DFT band gap problem [31–33]: GW operates a rigid shift of the LDA conduction band with respect to the valence band, ultimately yielding a good estimate for the band gap in a number of semiconductors and insulators [17, 28]. The effect is, in practice, that of a so-called scissor operator. As we shall see in Section 1.6, GW has also found success in its more recent application to finite systems, including atoms and molecules, where ionization energies (IEs) and electron affinities (EAs) have been targeted instead [34–41].

However, issues are found involving the prediction of a number of properties and phenomena. For instance, the prediction of the bandwidth of sodium within GW was the subject of a longstanding debate that was never fully settled, since it was never understood whether the issue was the lack of vertex corrections, or rather a poor description of the spectroscopic process (i.e. all the effects not contained in the spectral function, like surface

effects) [42–50]. Strong correlations [51] are another known issue for GW: while the RPA is justified in the high-density limit of the HEG [20], at low density one would rather have to resort to the T-matrix formalism [52, 53] or dynamical mean-field theory (DMFT) [54]. Additionally, wrong orbital energy ordering and spacing in the starting point of one-shot GW may carry over to the GW calculation itself [55, 56], contributing to the starting point problem which is introduced in Section 1.4. Finally, plasmon satellites, although in principle accounted for at the RPA level of theory, are a known issue in GW, which required replacing the Dyson equation with a cumulant expansion [57–59].

Vertex corrections are believed to be one way to fix these issues. In the next Sections we extensively discuss how they can include features that GW misses, and address the ambiguity concerning the starting point and self-consistency. Here we shall specify what GW misses from a theoretical standpoint. First of all, GW relies on the RPA to W: this means that, while collective excitations like a plasmon may be well described, one cannot expect a good description of excitonic effects, or equivalently particle-hole interactions. The inclusion of these effects may bear little relevance (or even be detrimental if the GW form of the self-energy is retained, as seen in the Section 1.3) when one is interested in solely the QP properties, but they do become important when one is interested in the response itself [60] (this however pertaining rather to absorption spectroscopy) or in the satellite spectrum [59]. Secondly, G in GW couples to W instead of $W\tilde{\Gamma}$, meaning that a particle moving in the system experiences a screening in which the particle itself participates [29, 61–63]. This gives rise to the so-called self-screening problem of GW. Its simplest manifestation is in one-electron systems, where an electron experiences its own screening: here one obtains a non-vanishing QP shift. HF does not present this error, due to an exact cancellation of the Hartree and the Fock exchange contributions. However, both HF and GW present a so-called many-electron self-interaction error: this manifests as a piecewise-non-linearity of the total energy upon addition of fractional charges [64]; addition energies are in fact wrong even in one-electron systems if HF is used, and they generally prove more involved to correct with regard to this kind of self-interaction error [61]. A correlation is thought to be likely between the one-electron self-screening problem and the many-electron self-interaction error, but the two are ultimately inequivalent, i.e. they do not imply each other [65]. When discussing the self-screening error throughout this thesis, we will refer to the *one-body self-screening error*: self-screening freedom will then imply a vanishing QP shift.

To conclude this Section, it is interesting to analyze the failure, within the context of satellites, of the standard implementation of GW coupled with the Dyson equation. In the HEG, the spectral function obtained from GW shows a prominent peak at an energy lower than the QP one [66]: this was initially thought to be a satellite associated to the excitation of a state characterized by the coupling of a hole to a cloud of real plasmons, which was called "plasmaron". Differently from usual satellites, this state corresponds to a solution of the QP equation, yielding an unusually high "oscillator strength", or weight of the peak equivalently. It was later found, through calculations in model systems, that the plasmaron peak is actually associated to the appearance in the interacting Green's function of unphysical poles due to using an approximation to the self-energy in conjunction with the Dyson equation [67, 68]. Instead, in the electron-boson coupling model [69], only one satellite appears with GW, somewhat constituting an average of all the replicas that one would have in the exact solution [70]. A more sensible positioning of at least the first plasmon satellite is found in the self-energy itself by inspecting its pole structure

(cfr. Eq. (3.4)),

$$\Sigma^{\mathrm{GW}}(\omega) \sim \frac{1}{\omega - \varepsilon^{\mathrm{QP}} - \omega_p};$$

here one sees that the plasmon peak is found at the QP energy $\varepsilon^{\mathrm{QP}}$ plus the energy needed to excite a plasmon ω_p, which appears to be a realistic estimate. Therefore, a more realistic spectrum is obtained by truncating the Dyson equation to first order in Σ,

$$G = G_0 + G_0 \Sigma G_0,$$

rather than by solving it fully. Poles of higher-order appear in this expression due to G_0 being present twice in the second addendum; these are an undesired feature that can be removed through a shift of the initial eigenvalue spectrum contained in G_0, which amounts to the GW QP shift [68] (see also Appendix E). With the last expression for the interacting G then one roughly has a GW-corrected QP peak given by G_0 and satellites given by $G_0 \Sigma G_0$. The $G_0 \Sigma G_0$ term is a finite-order approximation yielding only one plasmon peak: corrections to infinite order can be included via a cumulant expansion based on the electron-boson coupling model [17], rather than by using the Dyson equation. Doing so leads to a modification of the GW QP shift, and especially to the physical appearance of replicas of the first plasmon peak; the last aspect determined the success of the cumulant expansion in predicting satellite spectra in condensed matter [57–59].

1.3 Vertex corrections

There is no unambiguous way to go beyond GW: iterating through Hedin's scheme with a non-trivial vertex function would in principle be an ideal and systematic way to devise beyond-GW approximations. This procedure leads to the inclusion of diagrams to infinite order in the self-energy. Nevertheless, since the vertex function includes the derivative of the self-energy Σ with respect to the Green's function G, i.e.

$$\tilde{\Gamma}(1,2;3) = \delta(1,2)\delta(1,3) + \frac{\delta \Sigma(1,2)}{\delta G(\bar{4},\bar{5})} G(\bar{4},\bar{6}) G(\bar{7},\bar{5}) \tilde{\Gamma}(\bar{6},\bar{7};3), \tag{2.129}$$

new diagrams are added at each iteration [71, 72], making a rigorous implementation of Hedin's scheme numerically unfeasible. In order to overcome this complexity, approximations and truncations in the iteration process must be made. In the GW approximation, vertex corrections are neglected altogether, making the vertex function trivial and allowing for a self-consistent solution independent of the starting point.

The simplest vertex correction is the time-dependent Hartree-Fock (TDHF) scheme, obtained by plugging the Fock self-energy into the vertex equation (see Figure 1.4, top). This vertex has been studied in a perturbative fashion, i.e. with a single or a few iterations through Hedin's scheme, starting from a HF reference [34, 73–75]; it is directly related to the TDHF method for the calculation of excited states, which found major success in atoms and molecules [76–82]. By plugging the GW self-energy into the vertex function, the time-dependent GW (TDGW) method is obtained instead (see Figure 1.4, middle). For simplicity, the dependence of the screened interaction on the Green's function is often ignored in the differentiation contained in the vertex function. By doing so, a TDGW vertex

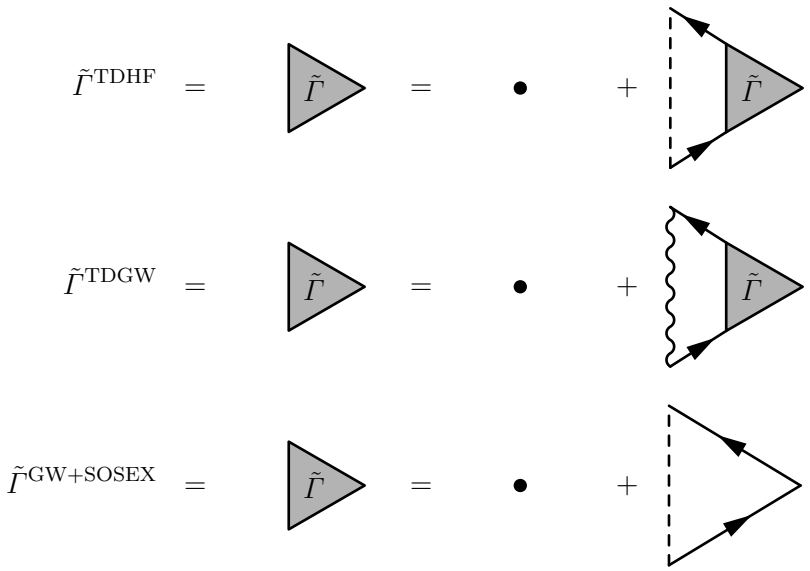

Figure 1.4. Vertex equations in the TDHF, TDGW and GW+SOSEX approximations.

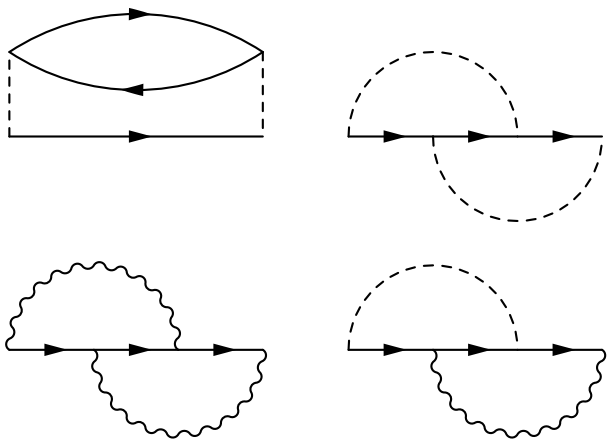

Figure 1.5. Some correlation self-energy diagrams: the 2Bd diagram (top left), the 2Bx diagram (top right), the SO-TDGW diagram (bottom left), and the SOSEX diagram (bottom right)

is obtained, leading to the same skeleton self-energy diagrams generated by the TDHF vertex, but framed in terms of the screened interaction.

A way to further simplify the scheme is to truncate the infinite summation of self-energy diagrams generated by a vertex function, retaining only lower-orders. This allows one to avoid the often cumbersome solution of the vertex equation and simply compute a number of selected self-energy diagrams. For instance, truncating to second order in the

Coulomb interaction the summation generated by the TDHF vertex yields the 2nd Born (2B) direct (2Bd) and exchange (2Bx) self-energy diagrams (Figure 1.5, top). Truncating to second order in the screened Coulomb interaction the summation generated by the TDGW vertex yields the GW self-energy plus a second-order exchange contribution, the latter corresponding to the 2Bx diagram expressed in terms of the dressed interaction W (Figure 1.5, bottom left): we shall term this the second-order time-dependent GW (SO-TDGW) diagram. When implementing this diagram, the two screened interactions have most often been considered statically [83] or with a plasmon pole approximation [84, 85]; only recently has their frequency dependence been fully taken into account [50, 86, 87]. Moreover, a treatment for this diagram enforcing positive definite spectral functions has also been proposed [88–90]. A simpler second-order approximation, devoid of double frequency integrals, can be devised by retaining only the zeroth and first-order terms in the TDHF vertex (see Figure 1.4, bottom), and then substituting them into the self-energy: this produces a second-order diagram with one screened Coulomb interaction, leaving the other at the bare level. This diagram is termed the second-order screened exchange (SOSEX, Figure 1.5, bottom right) diagram and the self-energy approximation is referred to as GW+SOSEX. This has been studied so far for molecules [87, 91, 92] and model systems [93]. Finally, for computational simplicity, local 2-point vertices have also been proposed [47, 94–98], some specifically aiming at compliance with the Ward identity [47, 98].

On a theoretical level, the schemes presented in this Section address some issues presented in Section 1.2: employing more refined polarizabilities, such as in TDHF or in TDGW, has the effect of coupling the removal or the addition of an electron with possibly a whole new set of neutral excitations; this has repercussions on the satellite spectrum, as we shall see in Section 1.6. Even retaining the RPA polarizability and simply adding the $GW\tilde{\Gamma}_1^{(1)}$ diagram has an effect on the spectral features, e.g. adding a second plasmon satellite [89]. Furthermore, vertex corrections are thought to cure, at least partially, the self-screening problem: this is the case for e.g. the SOSEX diagram [91, 93]; 2-point vertices also have potential in this regard [61]. The 2B self-energy and the TDHF vertex even solve the problem completely [73], as long as it is defined as in Section 1.2. In regard to accuracy, vertex corrections have been found to improve observable quantities such as bandwidths of metals [50], and IEs of extended systems [83, 98] and molecules [74, 75, 87, 91] alike. The ambiguity concerning self-consistency has also been addressed: by now it has been accepted that vertex corrections and self-consistency effects tend, at least partially, to cancel out [85], justifying, on the one hand, non self-consistent GW calculations: indeed, in this case early results suggested that the effect of vertex corrections on the band gap was small [84, 94]. On the other hand, full self-consistency should be pursued only in the presence of vertex corrections: if a parameter-free, self-consistent approach is sought, it can be said that vertex-corrected schemes are superior to GW even when the band gap is targeted [86, 96], since fully self-consistent GW often has poor accuracy (more on this in Section 1.4).

One last subtlety should be addressed about the topic of vertex corrections. While solvers in a 4-point formalism of the Bethe-Salpeter equation (BSE), Eq. (2.129), are by now a staple in electronic structure codes for the simulation of optical spectra [99], implementations performing the inclusion of the vertex function $\tilde{\Gamma}$ in Σ, as prescribed by Eq. (2.132), are not as widespread. Therefore, practitioners in MBPT have often been tempted to include vertex corrections only in W and not in Σ. Doing so allows one to rely on existing implementations of GW by changing only the form of W. This approximation is often referred to as $\mathrm{GW}^{\mathrm{tc-tc}}$,

with $W^{\mathrm{tc-tc}}$ being a test charge-test charge (tc-tc) response: this nomenclature emphasizes that, without inclusion of a vertex in the self-energy, the response of the system does not account for the removal or addition of actual particles, but only for the interaction of its own particles. The issue of correcting W only in GW was addressed early on [94], and recent works appear to confirm that it brings little improvement at best [41, 50, 83, 100]; others find that in some cases the improvement is more pronounced [74, 96].

1.4 Starting point and self-consistency

It is virtually impossible to make GW a method that is both highly predictive and free of a starting point ambiguity. As seen in Section 1.3, vertex corrections pave the way for a self-consistent calculation of the interacting Green's function through Hedin's scheme, in this case providing potentially accurate estimates of observables. By contrast, fully self-consistent GW (scGW) was found detrimental to the prediction of spectral properties of the HEG [101, 102]; further reports later advised against scGW in condensed matter at large [50, 103]. scGW has rather been found to be a good starting point for the polarizability in vertex-corrected approaches [50, 86].

In the absence of vertex corrections, *perturbative* or, equivalently, *one-shot* flavours of GW are often employed; these are also referred to as G_0W_0. As mentioned in Section 1.2, computing GW self-energies (and subsequently interacting Green's functions) starting from an LDA solution of the electronic problem provided the first great successes of GW. This was also a way cheaper option numerically than self-consistency. However, this implementation of the method lacks a rigorous theoretical justification: in fact, in the absence of vertex corrections, the iterative approach should start from a Hartree self-consistent solution [94], on top of which the time-dependent Hartree polarizability would be consistently built for the computation of W^{RPA}. The Hartree starting point is a very bad one, though, often yielding qualitatively wrong wavefunctions and highly inaccurate energy levels: a single-shot approach cannot then be based on just performing the fist iteration in this fashion. Therefore, the most pragmatic way to proceed at the dawn of GW was to simply adhere to a "best G, best W" philosophy: the "best G" bit translated to plugging into the self-energy the best ingredients that IP theory could give at the time, namely the eigenvalues and wavefunctions afforded by the LDA of KS-DFT; the "best W" bit was instead about using the best approximation to the polarizability that the numerics could afford, namely the RPA polarizability.

Over time, calculations were extended to a larger class of systems and properties other than the band gap, and the need to go beyond G_0W_0@LDA was soon to be faced. On the one hand, exploration of partially self-consistent schemes began: the results obtained for the HEG [101, 102] suggested that self-consistency in W is particularly detrimental for spectral properties, so that an update of G solely should be preferred [103–105]. This is the scGW_0 scheme, which is supported by at least two arguments: the first, one of theoretical rigour, states that self-consistency of W in the absence of vertex corrections renders the polarizability an improper response function, it not being obtained from the perturbation of an electron density [102]; the second one is of empirical nature, and consists in the remark that the RPA screening built on top of KS-DFT starting points is the product of a reduced energy gap that mimics excitonic effects [56, 96, 106], which is then closer to the

actual optical gap that characterizes the response function. Self-consistent schemes allowing for an easier implementation were also explored: these include eigenvalue self-consistent GW (ev-scGW) [26, 56, 103], in which only eigenvalues are made self-consistent, and quasi-particle self-consistent GW (QSGW) [107], in which an IP hamiltonian problem is devised starting from the GW self-energy. The latter method was successful at predicting and improving the band gap of an even greater number of non-conducting systems than G_0W_0@LDA did.

Meanwhile, further KS-DFT functionals became available, offering a whole new range of starting points even for simple G_0W_0 calculations: these include functionals from the optimized effective potential (OEP) method [108–110] and hybrid functionals incorporating a fraction of non-local Fock exchange (FEX) [55]. The two classes enjoy a more realistic treatment of exchange than LDA does at the IP level, a convenient feature to have in finite systems [111, 112]. Hybrid functionals, in particular, give one the possibility to tune the fraction of FEX in order to have optimal screening properties within the RPA: one can choose to be anywhere in between the overscreening limit of KS-DFT energy gaps and the underscreening limit of HF energy gaps; in fact, screening varies inversely with the energy gap (see Eq. (3.36)). Numerous schemes have recently appeared which are capable of enforcing the desired properties through a simple tuning of the FEX fraction in the starting point: one can force the GW correction to rigidly shift the whole initial eigenvalue spectrum [113], to minimize the QP shift of the highest-occupied energy level [114, 115], or to comply with the piece-wise linearity of the total energy at fractional occupations of energy levels [116]. In general, GW is found to benefit from hybrid starting points in finite systems [38, 41, 56], or when localized atomic-like wavefunctions play a relevant role in extended systems [55, 103] (see Refs. 30 and 29 for more details). The success of hybrid functionals is attributed to the fact that the fraction of FEX can alleviate the self-interaction problem typical of local and semi-local density functionals [117], especially relevant for localized orbitals, which then propagates to the overlying GW calculation. The initial G_0, in particular, is affected by the bad initial guess for eigenvalues and wavefunctions, and the error is propagated to the calculation of the GW self-energy. FEX has then the effect of reducing the error in G_0 and, at the same time, of retaining at least partially the desirable screening yielded by W^{RPA} as computed on a KS-DFT starting point (which would not be the case in the HF limit of unitary FEX fraction). scGW_0 has also been used interchangeably with G_0W_0 on top of a hybrid KS-DFT starting point [56, 118]: here the initial guess for G_0 is instead corrected iteratively by the self-consistency of eigenvalues, which takes a role analogous to that of FEX in the hybrid starting point.

Overall, the possibility of tuning the starting point, be it either by incorporating FEX or by iterating to varying levels of self-consistency, seems to allow GW to be most often up to the task. However, this is at the expense of conceptual clarity, and overall leads to a heavily system-dependent method. As discussed earlier in this Section, a clearer path is in principle given by Hedin's iterative scheme: a rigorous implementation of one-shot GW would have to rely on a self-consistent Hartree starting point, which the RPA (or alternatively time-dependent Hartree) polarizability calls for; alternatively, one could go for full self-consistency. Neither option is satisfactory from the accuracy viewpoint, and the community has had to resort to all sorts of empirical arguments to justify the numerous implementations of GW. Vertex-corrected approaches could instead provide a solution to the starting point ambiguity. A one-shot approach relying on a more sophisticated polarizability

than the time-dependent Hartree one would call for a starting point other than the Hartree one: for example, the TDHF vertex calls for a HF starting point [34, 73–75], while the TDGW vertex calls for a fully scGW starting point [50, 86]. A self-consistent approach can also be sought, keeping in mind that a rigorous one entails the generation of new diagrams at each iteration of Hedin's scheme [71, 72]; here different flavours of self-consistency are still likely to be devised for the sake of the implementation [50, 83, 85, 86]. Last but not least, checking for positivity of the spectral function generated by vertex corrections may be essential in fully self-consistent schemes [88–90]: beyond GW, one may in fact obtain negative spectral features that could severely, iteration after iteration, affect the reliability and the predictivity of the whole scheme.

1.5 Sham-Schlüter equations

After having explored the starting point dependence and self-consistency in MBPT, in this Section we introduce some schemes aimed at attaining self-consistency in a simplified way. We begin by remarking that self-consistency in IP methods is way more easily attained than in MBPT. In the latter case the emergence of the satellite spectrum substantially complicates the frequency dependence of the Green's function. On the contrary, an IP hamiltonian yields a trivial frequency dependence of the Green's function, with QPs having unitary weights and energies corresponding to eigenvalues. In this respect, the QSGW scheme [107] is not only generally more accurate than scGW for the calculation of QP properties, but also less numerically demanding. Here we will rather focus on self-consistency within KS-DFT, where a connection to MBPT can be traced in order to obtain an xc potential v_{xc} from a many-body self-energy Σ. Indeed, one can exploit the exactness of both KS-DFT and MBPT in predicting the electron density: namely, the exact density computed from the interacting G as obtained from MBPT must be equal to that computed from G^{KS} as obtained from KS-DFT. By using this density condition, one can obtain v_{xc} from Σ via a so-called Sham-Schlüter equation (SSE) [119],

$$\begin{aligned}\int \frac{d\omega}{2\pi i} \int d\mathbf{r}_1\, G^{\text{KS}}(\mathbf{r},\mathbf{r}_1,\omega) G(\mathbf{r}_1,\mathbf{r},\omega)\, v_{\text{xc}}(\mathbf{r}_1) \\ = \int \frac{d\omega}{2\pi i} \int d\mathbf{r}_1 d\mathbf{r}_2\, G^{\text{KS}}(\mathbf{r},\mathbf{r}_1,\omega)\Sigma(\mathbf{r}_1,\mathbf{r}_2,\omega;[G])G(\mathbf{r}_2,\mathbf{r},\omega). \qquad (2.162)\end{aligned}$$

Thanks to the SSE, approximate self-energies can be directly mapped to KS potentials, whose exchange-correlation part usually requires approximations based on models (such as the local density approximation, based on the HEG), rather than systematic approaches; this comes, however, at the increased computational cost that MBPT has in comparison to ordinary KS-DFT. Not only can the SSE help to unveil what accurate KS potentials look like [28], but its linearized version is also at the core of the optimized effective potential (OEP) method [119–125]. As we shall see in Section 2.3, this method originates from an optimization of the Klein energy functional, and the linearized Sham-Schlüter equation (LSSE), in which $G \to G^{\text{KS}}$ constitutes the stationarity condition. In this respect, the LSSE can be considered an alternative, if not an approximation, to the self-consistent Dyson equation of MBPT. In fact, both approaches are based on the stationarity of the Klein energy functional, the latter with an unconstrained Green's function, the former under the

restriction that the Green's function be non-interacting and subject to a local and static potential [122]. It must be noted, however, that the density condition that one has with the SSE no longer holds with the LSSE; nonetheless, one iteration of the Dyson equation is expected to largely preserve the density given by G^{KS} as obtained from the self-consistent LSSE [122, 126, 127]. This qualifies KS wavefunctions and eigenvalues given by the LSSE as starting points of interest for the Dyson equation, provided that the same self-energy approximation is used consistently at both steps.

The accuracy of the LSSE as an approximation to the self-consistent Dyson equation has not been thoroughly investigated yet. Solving the LSSE with the HF self-energy has been found to yield good approximations to the HF IEs, and the upper valence thus obtained is also in closer agreement with HF than one would get with local and semi-local KS-DFT functionals [121, 128]. In this case the static, spatially non-local FEX self-energy is approximated with a static, spatially local xc potential. In general, however, the xc potential is required to approximate dynamical, spatially non-local self-energies obtained in the self-consistent solution of the Dyson equation, which may be too demanding. As of now, an argument involving the adiabatic connection between the self-consistent Dyson equation and the self-consistent KS equations has been proposed in order to justify the LSSE solution as a starting point for many-body calculations (see Appendix B of Ref. 127): solving the Dyson quasi-particle equation on top of it (without renormalization factor) provides a first-order approximation to the self-consistent quasi-particle energies. It can be argued that this procedure is a way to add the derivative discontinuity to the KS gap [31–33, 119, 129]. Band gaps similar to those of self-consistent GW have indeed been found in condensed matter by adopting this procedure [110], and a good agreement with experiment has also been found for selected systems [130].

Theory	Fundamental quantity	Potential	Main observables
DFT	$\rho(\mathbf{r})$	$v^{\mathrm{KS}}(\mathbf{r})$	ρ, $E[\rho]$
SPT	$\rho^{\mathrm{S}}(\mathbf{r},\omega)$	$v^{\mathrm{S}}(\mathbf{r},\omega)$	ρ^{S}, ρ, $E[\rho^{\mathrm{S}}]$
MBPT	$G(\mathbf{r}\mathbf{r}',\omega)$	$\Sigma(\mathbf{r}\mathbf{r}',\omega)$	A, ρ^{S}, ρ, $E[G]$

Table 1.1. Different theories and their respective fundamental quantities, generalized potentials, and main observables of interest.

A way to more easily approach full Dyson self-consistency, possibly without inconveniences such as derivative discontinuities, may be to devise a theory in between MBPT and DFT. One could e.g. work with a spectral potential v^{S} that is spatially local like the KS one, but dynamical like a self-energy, and require it to give the correct spectral density $\rho^{\mathrm{S}}(\mathbf{r},\omega) = A(\mathbf{r}\mathbf{r},\omega)$, i.e. the diagonal of the spectral function A. This is in fact the quantity that is often of interest for comparison with experiment, rather than the full non-local spectral function $A(\mathbf{r}\mathbf{r}',\omega)$. Exploiting the exactness of the spectral density in both this theory, which we shall term spectral potential theory (SPT), and MBPT, a Sham-Schlüter

equation can again be written to obtain the spectral potential v^{S} [131–133],

$$\int \mathrm{d}\mathbf{r}_1 \, \mathrm{Im}\Big\{G^{\mathrm{S}}(\mathbf{r},\mathbf{r}_1,\omega)G(\mathbf{r}_1,\mathbf{r},\omega)\Big\}\, v^{\mathrm{S}}(\mathbf{r}_1,\omega) = \int \mathrm{d}\mathbf{r}_1 \, \mathrm{d}\mathbf{r}_2 \, \mathrm{Im}\Big\{G^{\mathrm{S}}(\mathbf{r},\mathbf{r}_1,\omega)\Sigma(\mathbf{r}_1,\mathbf{r}_2,\omega;[G])G(\mathbf{r}_2,\mathbf{r},\omega)\Big\},$$

with $G^{\mathrm{S}} = G_0 + G_0 v^{\mathrm{S}} G^{\mathrm{S}}$ and v^{S} a real potential. Provided that a potential v^{S} fulfilling the required properties exists, this equation allows one to compute it starting from a self-energy approximation; through a linearization, from this equation a self-consistent method within SPT could originate, in the fashion of the standard LSSE within the OEP method. Such method would not be as computationally expensive as MBPT, since v^{S} is spatially local, at variance with the many-body self-energy Σ; however, one may have to still resort to techniques that take care of the frequency dependence if self-consistency is sought [134–136]. Notably, a QP approximation to SPT is believed to lead to familiar orbital-dependent functionals of DFT, and a functional derivation of its LSSE counterpart is possible [137], similarly to that of the KS-DFT LSSE [122]. Although interesting, SPT is beyond the scope of this thesis and is presented for the sake of future developments. Table 1.1 summarizes the different theories presented in this Section and their respective fundamental quantities, generalized potentials, and main observables of interest.

1.6 Atoms, molecules and finite systems

The success of GW in condensed matter has pushed the community to try and apply it within domains traditionally reserved to wavefunction-based methods, such as that of finite systems. In comparison to wavefunction-based methods, GW offers a cheaper route to the prediction of electronic excitations in e.g. atoms, molecules, nanostructures. Not only this, but finite systems offer a unique possibility to test *many-body* approximations in the *few-body* limit. Therefore, not only can GW be used for the characterization of finite systems, but finite systems can be used to characterize GW itself: many of these have already been studied through experiment [138, 139] or other accurate theoretical means [112, 140, 141], so there is a whole wealth of data that GW results can be compared to. Comparison with experiment is aided by the fact that the spectroscopic process is way simpler in finite systems, in that photoelectrons do not have to travel through a material and experience a surface potential before being detected: in this case the sudden approximation is much more justified and the three-step model not needed [1]. Furthermore, the description is not complicated by the coupling to phonon modes, and in atoms one even gets rid of the coupling to roto-vibrational degrees of freedom that are present in molecules, retaining pure electronic effects.

From the standpoint of computational effort, finite systems often require a more modest one than extended systems do: for example, in atoms it is possible to reduce the numerical representation of spatial-resolved objects (e.g. wavefunctions, operators) to a radial degree of freedom, while taking care of the angular dependence through the Clebsch-Gordan algebra; and in general, in smaller systems it can be easier to get rid of further approximate techniques such as pseudopotentials, frequency representations of dynamical operators [134–136], extrapolations to the infinite basis set limit. These often hinder the accuracy assessment of a given many-body method, and make the comparison of results from different codes

difficult. Even self-consistency has been found easier to implement in atoms and molecules. The successful utilization of these small systems has led to the emergence of the GW100 [41, 87, 142–145] and other similar test sets as standardized means for large-scale benchmarks.

One of the first benchmarks of GW on finite systems was that performed by Shirley and Martin in the 90's [34] utilizing a test set consisting of atoms. The work also focused on the TDHF vertex, which was included in the self-energy in a fashion that enforced variationality while sacrificing self-screening freedom. Mostly ionic configurations of atoms were considered and much emphasis was put on correlations between the valence and the core. Later on, atoms and small molecules began to be considered in their neutral configurations, and various levels of GW self-consistency were implemented [35, 105, 146, 147]: interestingly, scGW was found to perform well with IEs of atoms and molecules, in contrast to its bad performance in condensed matter. The self-screening error was also targeted using the quintessential one-electron system: hydrogen. It was actually found to be less important than expected, provided that an accurate choice of the starting point is made [148, 149]. The helium atom, for which numerically exact results are available, was elected as another few-body system of interest [150]: in this case the TDGW vertex, in its static implementation that proved very popular in condensed matter, was found to slightly outperform the TDHF vertex at predicting neutral excitations, the latter already offering a decent estimate to begin with. Overall, the self-screening error of GW was found not to undermine calculations in few-body systems by a sizable amount; of course this may also depend on the definition that is adopted for the self-screening error, as emphasized in Section 1.2.

Atoms and molecules have also been widely used as a test bed for vertex corrections and for the starting point dependence: for example, the GW+SOSEX self-energy was introduced in the context of molecules, and Perdew-Burke-Ernzherof (PBE) and PBE0 have been found to be the starting points with which it works best, with a reduced dependence on the choice of either [87, 91, 92]; self-consistent schemes have yet to be thoroughly explored with this self-energy instead [93]. The TDHF vertex was also recently benchmarked using molecules in a perturbative fashion applied on a HF reference, which yielded promising results for their IEs [74, 75]; this is an instance in which the ambiguity resurged about the possibility of including vertex corrections in the polarizability only [74, 100]. Coming back to GW, in agreement with the discussion of Section 1.4, its application to molecules seems to work best on average with a hybrid KS-DFT starting point [38, 41, 56]; however, the HF reference and different flavours of self-consistent schemes were also considered in specific cases and proved a better option [146, 147, 151–153]. As in the case of solid state, the issue of the starting point dependence of GW is not fully settled in finite systems.

Recent applications of MBPT to atoms and molecules have been aimed at reproducing more challenging features found in the photoemission spectrum, such as core electron QP lines [118, 154] and the related satellites [155–157]. This energy domain of photoemission is pretty exciting in that it can really push many-body methods widely used in condensed matter to their limits. For instance, while the IEs of atoms are predicted with good accuracy by GW, and even improved by vertex corrections, reproducing the satellite spectra will likely require other treatments. Many new interesting phenomena can arise due to core hole relaxation, such as Auger decay and autoionization [1]. For instance, to get a feeling of what physical processes characterize a class of satellites in atoms and molecules, we can consider the simplest of these systems retaining a many-body (or few-body, for that matter)

nature: the helium atom, along with its photoemission spectrum shown in Figure 1.6. Other

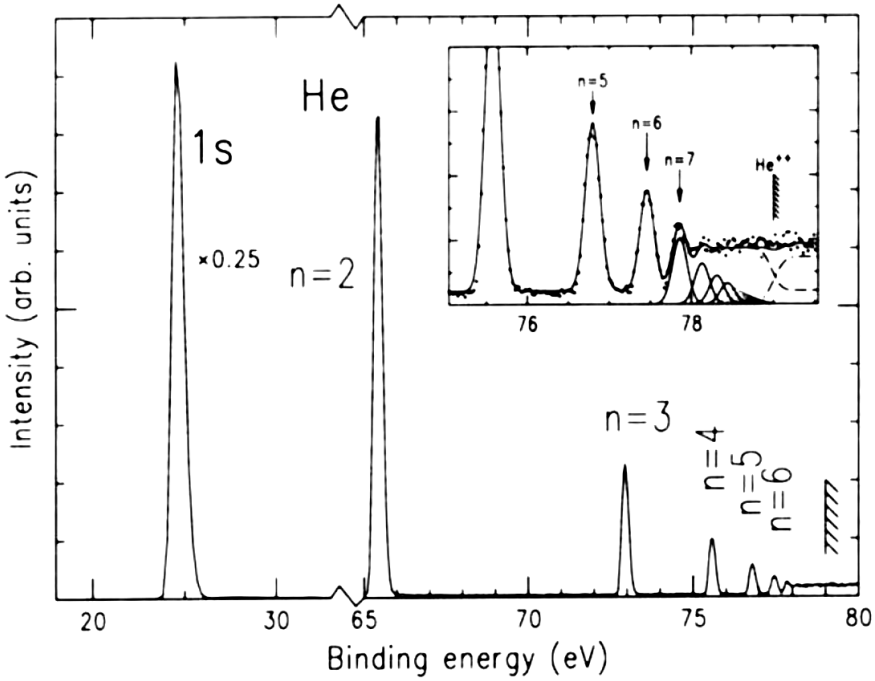

Figure 1.6. Photoemission spectrum of helium [158–161].

than the main QP peak, a series of satellite peaks is present at lower energies. These are associated to leaving the He^+ hydrogenic ion in progressively more excited states, as n in increases, whereas the main QP peak is associated to leaving it in the ground state. These satellites go under the name of "shake-up" satellites. Following Ref. 1, we can write the main transitions to charged excited states as allowed by the dipole approximation in the following way:

$$\begin{aligned}
h\nu + \mathrm{He}(1s^2) &\rightarrow \mathrm{He}^+(1s^1) + \varepsilon_{l=1}; \\
h\nu + \mathrm{He}(1s^2) &\rightarrow \mathrm{He}^+(2s^1) + \varepsilon_{l=1},\ \mathrm{He}^+(3s^1) + \varepsilon_{l=1},\ \mathrm{He}^+(4s^1) + \varepsilon_{l=1}, \\
&\quad \ldots,\ \mathrm{He}^{++} + \varepsilon_l + \varepsilon_{l'}; \\
h\nu + \mathrm{He}(1s^2) &\rightarrow \mathrm{He}^+(2p^1) + \varepsilon_{l=0},\ \mathrm{He}^+(3p^1) + \varepsilon_{l=0},\ \mathrm{He}^+(4p^1) + \varepsilon_{l=0}, \\
&\quad \ldots,\ \mathrm{He}^{++} + \varepsilon_l + \varepsilon_{l'};
\end{aligned}$$

here ε_l refers to the unbound scattering state to which the photoelectron is taken, and l indicates the angular momentum of the state. It is now evident that the satellites are given by a Rydberg series of the He^+ hydrogenic ion (whose excitation energies are degenerate with respect to the l quantum number). Eventually, as one goes to sufficiently high binding energies, the double ionization (also termed "shake-off") continuum is reached. It is also important to note that, in the dipole approximation, one unit of angular momentum is transferred either to the photoemitted electron (simple "shake-up", with the photoelectron

reaching a $l = 1$ scattering state) or to the ionized system ("conjugate shake-up", with the photoelectron reaching a $l = 0$ scattering state) [162].

Shake-up satellites are found in all sorts of small systems [1, 160], and providing an accurate description of them may prove quite challenging. In the language of MBPT, shake-up processes are neutral excitations that couple to the creation of a hole in the system. These neutral excitations are contained in W, but the RPA W of GW can at most well describe the excitation of a plasmon. A plasmon is a perturbation of the density that involves a collective participation of the electrons, whereas shake-up processes retain a much more localized, or in a way single-particle, nature as seen in the case of helium (presumably coupled with electron shell relaxations due to the hole in many-electron systems)[2]. It is then disputable whether the RPA polarizability can actually well describe shake-up processes. One may hope to have a better estimate of the neutral excitations with the TDHF method; however, even in this case the excitations contained in W are the ones of the neutral system rather than the ionized one. The appearance of the W of the neutral system is actually prescribed by Hedin's equations, so one should look elsewhere for the inclusion of relaxation effects in the ionized system. In fact, these effects should be accounted for with the inclusion of a dynamical vertex in the self-energy, which however the TDHF one is not. By comparing Eqs. (3.4) and Eq. (4.49), one can see that the pole structure of the TDHF self-energy is analogous to that of GW, and only a dynamical vertex can change it. As discussed in Section 1.2, with this pole structure satellites are found at a QP energy plus an energy for exciting the neutral system; the latter may not be a good approximation to an energy needed to excite the ionized system. Finally, one has to check whether plugging a self-energy containing a realistic description of satellites into the Dyson equation has a destructive effect, as happens in the HEG with the emergence of the plasmaron peak: namely, if one finds that the self-energy has reasonable satellite peaks, it must be ensured that these are correctly mapped to the spectral function. Self-consistency is also expected to play a role in this [163–165].

In summary, the application of MBPT methods to the description of excitations in atoms and molecules poses a whole bunch of stimulating questions: can a self-energy relying on the RPA to W provide a meaningful description for satellites in small systems? What should a dynamical $\tilde{\Gamma}$ in the $GW\tilde{\Gamma}$ form of Σ be like for it to cause the emergence of satellites due to excitations of the *ionized* system, starting from a W that rigorously contains excitations of the *neutral* system? In other words, how does one account for *hole relaxation* through vertex corrections? Finally, are there approximations to Σ that can afford a good description of satellites in conjunction with the Dyson equation without causing the emergence of spurious structures in the spectral function? Or should one resort to alternative means such as a cumulant expansion as is done in solid state?

[2]Here we are assuming a single-particle description, or at most a QP one. These are often meaningful in finite systems, especially in closed shells, but one should not forget that, in reality, in many-body systems there are only many-body excitations. The single-particle picture can in fact be conspicuously challenged with the multi-determinantal reference states needed to treat open shells.

1.7 Scope and structure of the thesis

This thesis is about the study of vertex corrections within the framework of MBPT, with the aim of overcoming the limitations of its state-of-the-art method, the GW method. The study will focus on the accuracy of different schemes in the prediction of various observables introduced in Section 1.1, in particular QPs and satellites populating the photoemission spectrum. Although GW is often successful in the calculation of band gaps and other QP properties alike, in Section 1.2 we saw that it presents issues on a theoretical level: to name a few, it is based on a very simple approximation to the polarizability, it is affected by a self-screening error, it suffers from a strong starting point dependence, and it fails at describing satellites in conjunction with the Dyson equation. These problems undermine the applicability of GW as a general method for electronic excitations, and make it necessary to devise flavours of it which are tailored for the problem at hand, including e.g. a plethora of partially or non-self-consistent schemes, and cumulant expansions.

In Section 1.3 we reviewed some vertex corrections that could cure these problems: this thesis will firstly focus on low-order truncations of vertex-corrected self-energies, namely the GW self-energy itself as the zero-order baseline, and then the 2B and the GW+SOSEX self-energies. These self-energies require no more than the solution of 2-point Dyson equations on a frequency range, which can be performed numerically with matrix inversion routines available in common linear algebra libraries. Secondly, the whole TDHF vertex is also addressed, which entails the inclusion of ladder diagrams to infinite order through the solution of the BSE; this requires the utilization of a 4-point formalism commonly adopted for BSE-like problems, and therefore a more numerically intensive effort than that needed for 2-point Dyson equations.

As emphasized in Section 1.4, the starting point dependence is a relevant issue in GW: therefore, each of these schemes is tested in a one-shot fashion starting from different solutions afforded by IP methods, such as the HF, PBE and PBE0 ones. Self-consistency is also addressed in an alternative way by utilizing the LSSE: as seen in Section 1.5, the LSSE provides a form of self-consistency within the KS-DFT formalism, and the electron density is largely preserved upon one iteration of the Dyson equation on top of an LSSE solution, provided that the same self-energy is used at each step.

Motivated by the arguments expressed in Section 1.6, all calculations presented in this thesis are performed on spherical atoms using the AGWX code suite, to whose implementation I extensively participated in: in particular, I was in charge of implementing all the self-energy methods presented in this thesis, both in the one-shot Dyson equation and in the LSSE flavours. From a practical standpoint, spherical atoms allow us to reduce the numerical problem to one spatial dimension and to treat it with a dedicated all-electron implementation based on a B-spline basis [166–170]; the angular degrees of freedom are treated analytically instead, employing spherical harmonics and the related Clebsch-Gordan algebra.

The simplicity of the problem makes it possible to avoid the use of a number of approximate techniques commonly adopted in general-purpose codes, including pseudopotentials, frequency representations and extrapolations to the complete basis set limit. Moreover, assuming a negligible contribution from relativistic effects, the numerical precision we achieve allows direct comparison with experiments; potentials as obtained by the LSSE are also compared with exact atomic references as a further benchmark. From a physical

standpoint, atoms are also a gateway to electronic excitations not commonly found in solid state, which GW is not usually required to describe: this is especially true of shake-up satellites. Therefore, atoms allow us to really push the MBPT formalism to its current limits, and possibly extend its applicability to new systems and phenomena.

The thesis is structured as follows:

- In Chapter 2, I dedicate Section 2.1 to the review of the basics of MBPT: the GW approximation is introduced, along with the iterative schemes that were used to go beyond GW. Section 2.2 is dedicated to KS-DFT, which provides the starting points for MBPT along with HF. Section 2.3 presents the Sham-Schlüter equation as a bridge between MBPT and KS-DFT.

- In Chapter 3 I present GW, 2B and GW+SOSEX as the low-order self-energies of interest for the assessment (Section 3.1). Then I will introduce the spherical problem (Section 3.2), and the treatment of MBPT within its formalism (Sections 3.3, 3.4 and 3.5). After a preliminary look at polarizabilities (Section 3.3.5), starting point dependence (Section 3.4.5), and xc potentials from the LSSE (Section 3.5.7), in Section 3.6 I will finally present the general assessment based on the accuracy of the predicted ionization energies. The assessment finds that, while GW performs decently starting from a HF reference, GW+SOSEX rather requires a (generalized) KS-DFT starting point for a good accuracy to be attained. Conversely, 2B is unambiguously fit for the HF starting point and its promising performance suggests considering the whole TDHF vertex. The LSSE is not found to be superior to the traditional one-shot schemes, but offers some further insight via the comparison of the xc potentials against exact references.

- In Chapter 4 I present the implementation of the TDHF vertex (Section 4.1) and the relative accuracy assessment (Section 4.2), now also involving the upper valence and satellites. Here it is found that the TDHF scheme proves ideal for the prediction of ionization energies of light atoms, and points to the need for screening the vertex in heavier ones. The results for satellites suggest that the account for hole relaxation within TDHF is insufficient and leads to introducing the ideas of the following Chapter.

- In Chapter 5 a $G\tilde{W}$ self-energy is presented in which $\tilde{W}$ is computed starting from the result of a self-consistent field procedure applied to the singly ionized electronic configuration of the system. G is still computed starting from the neutral configuration instead. This is an approach tailored for fitting experimental data and still lacks a complete formal justification. A sketch of the theory is given in Section 5.1, while Section 5.2 contains promising results. This part of the work was conducted in collaboration with Dr. Lucia Reining and Dr. Matteo Gatti from the Laboratoire des Solides Irradiés of the École Polytechnique (Palaiseau, France).

- In the Conclusions and perspectives chapter I finally summarize all the work that I did and the achievements of the thesis.

Chapter 2

Theoretical background

In order to interpret the photoemission spectrum of a material, an exact theory of its electronic structure and an exact theory of the photoemission process should be devised. In practice, both are impossible and approximations are required. The former would require the solution of the whole many-body hamiltonian of a material, which takes the form

$$\begin{aligned} H = &- \sum_i \frac{\nabla^2_{\mathbf{r}_i}}{2m} - \sum_I \frac{\nabla^2_{\mathbf{R}_I}}{2M_I} \\ &+ \frac{1}{2}\sum_{i\neq j} \frac{e^2}{|\mathbf{r}_i - \mathbf{r}_j|} - \sum_{i,I} \frac{Z_I e^2}{|\mathbf{r}_i - \mathbf{R}_I|} + \frac{1}{2}\sum_{I\neq J} \frac{Z_I Z_J e^2}{|\mathbf{R}_I - \mathbf{R}_J|}, \end{aligned}$$

where capital indices refer to nuclei, whereas lower case indices to electrons. The number of atoms N and the number of electrons n are of the order of the Avogadro number, $\sim 10^{23}$, making the problem solvable neither by analytical or numerical means (although a solution could mathematically exist). Assuming some kind of periodicity of the system, which makes it possible to rely on Bloch's theorem, does not make the problem much more feasible due to the intricate nature of the electronic many-body interactions. To make things worse, the photoemission process introduces a time-dependent perturbation to this hamiltonian, further complicating the picture. In this chapter I will introduce the approximate methods through which photoemission is treated theoretically.

Here I will not consider the intricacies of the spectroscopic process, by working in the sudden approximation [1]. This means assuming that photons in, say, direct photoemission are sufficiently energetic to kick away electrons from the system by leaving them in a high-kinetic energy state, resulting in a final state where the ionized system has not interacted nor will interact with the photoelectron, the latter being treated as a free particle. I will instead consider the intricacies of the electron many-body interactions. In order to do so, I will introduce many-body perturbation theory (MBPT) and its formulation based on correlation functions in Section 2.1, which ultimately yields a quantity called spectral function that can be directly compared with photoemission spectra within the sudden approximation. Since MBPT most often needs to rely on independent-particle theories, the Hartree-Fock method is also presented using the MBPT formalism in Section 2.1, while the whole of Section 2.2 is dedicated to Kohn-Sham density functional theory (KS-DFT). Finally, due to it being extensively explored in the present work, I will introduce in Section 2.3 the Sham-Schlüter

equation, which connects the frameworks of MBPT and KS-DFT.

2.1 Green's function methods

In this Section I will give a concise introduction to Green's function methods within the context of MBPT. All the formalism needed to obtain the state-of-the-art method of MBPT, the GW approximation, will be considered, along with the iterative schemes to go beyond GW. These will be applied in order to obtain higher-order self-energies in the following Chapters.

2.1.1 The one-particle Green's function

Throughout the whole manuscript, for space-spin-time variables we adopt the notation $1 \equiv (x_1, t_1) \equiv (\mathbf{r}_1, \sigma_1, t_1)$, with $\mathbf{r}$ indicating space variables, σ indicating one of the two possible spin orientations in the collinear case (always assumed), and t indicating time variables. The one-particle Green's function is defined as

$$G(1,2) = -i\langle \mathrm{T}\left[\psi(1)\psi^\dagger(2)\right]\rangle_0, \tag{2.1}$$

where T is the time-ordering operator, and $\hat{\psi}$ and $\hat{\psi}^\dagger$ are annihilation and creation field operators respectively, in the Heisenberg picture; the average is taken on the ground state, as indicated by the subscript 0. When $t_1 > t_2$, the time-ordered Green's function expresses the probability amplitude for an *electron* to propagate from point x_2 at time t_2 to point x_1 at time t_1, and is therefore called an *electron propagator*; when $t_2 > t_1$, conversely, it expresses the probability amplitude for a *hole* to propagate from point x_1 at time t_1 to point x_2 at time t_2, and is therefore called a *hole propagator*. Note that the fact that we are considering the propagation of fermions makes the Green's function antisymmetric with respect to a commutation of its arguments, due to the action of the time-ordering operator. Various quantities of interest can be obtained from the Green's function, including ground-state averages of one-particle operators and ground-state total energies. It is straightforward to see that the density and the density matrix can be obtained by

$$\rho(x) = -iG(x,t;x,t^+), \tag{2.2}$$

$$\rho(x_1,x_2) = -iG(x_1,t;x_2,t^+), \tag{2.3}$$

with $t^+ = \lim_{t' \to t^+} t'$ for time-ordering to yield $\hat{\psi}^\dagger\hat{\psi}$, and therefore the density and the density matrix operators respectively. In this section we will be particularly concerned with obtaining the charged excitation energies of a system, which we will do by tackling the spectral function.

The Green's function can be recast in terms of more fundamental building blocks, the greater Green's function and the lesser Green's function,

$$G^>(1,2) = -i\langle\hat{\psi}(1)\hat{\psi}^\dagger(2)\rangle_0 \text{ and} \tag{2.4}$$

$$G^<(1,2) = +i\langle\hat{\psi}^\dagger(2)\hat{\psi}(1)\rangle_0 \tag{2.5}$$

respectively. One can then write

$$G(1,2) = \theta(t_1 - t_2)G^>(1,2) + \theta(t_2 - t_1)G^<(1,2) \tag{2.6}$$

and see that $G^>$ describes the particle propagation, while $G^<$ describes the hole propagation. The general definition of spectral function can be given using $G^>$ and $G^<$,

$$2\pi A(1,2) = iG^>(1,2) - iG^<(1,2) \tag{2.7}$$

which is essential in approaches enforcing its positive definiteness [88–90]. $G^>$ and $G^<$ can also be used to define the retarded Green's function and the advanced Green's function,

$$\begin{aligned} G^R(1,2) = &\quad \theta(t_1 - t_2)\langle\{\hat{\psi}(1), \hat{\psi}^\dagger(2)\}\rangle_0 \\ = &\quad \theta(t_1 - t_2)\left[G^>(1,2) - G^<(1,2)\right] \quad \text{and} \end{aligned} \tag{2.8}$$

$$\begin{aligned} G^A(1,2) = &-\theta(t_2 - t_1)\langle\{\hat{\psi}(1), \hat{\psi}^\dagger(2)\}\rangle_0 \\ = &\quad \theta(t_2 - t_1)\left[G^<(1,2) - G^>(1,2)\right] \end{aligned} \tag{2.9}$$

respectively.

For the information on the charged excitations of the system to be obtained, we now need to move Green's functions and the spectral function to frequency space, which means seeking a spectral representation of them. For the sake of the derivations, it is convenient to begin by finding a spectral representation for the spectral function A; G, G^R and G^A can be easily found afterwards. Eq. (2.7) implies that one has to work on $G^>$ and $G^<$ for A to be obtained in frequency space: now we will focus on $G^>$, while $G^<$ will be found by analogy. In the hypothesis of the many-body hamiltonian $\hat{H}$ being static, we transform the field operators of Eqs. (2.4) to the Schrödinger picture,

$$\hat{\psi}_H^{(\dagger)}(t) = e^{i\hat{H}t}\hat{\psi}_S^{(\dagger)}e^{-i\hat{H}t}, \tag{2.10}$$

and then have $\hat{H}$ act on the ground state wavefunction where possible,

$$G^>(1,2) = -ie^{iE_0(t_1-t_2)}\langle\hat{\psi}(x_1)e^{-i\hat{H}(t_1-t_2)}\hat{\psi}^\dagger(x_2)\rangle_0, \tag{2.11}$$

where E_0 is the energy of the ground state. For static hamiltonians the time dependence is on the time difference $t = t_1 - t_2$. By indicating Fock space with $\{|N', \lambda'\rangle\}$, where N' is the electron number and λ the energy state at fixed N' (with $|N,0\rangle$ being the ket of the ground state), we now insert the identity using the completeness relation $\hat{I} = \sum_{N',\lambda} |N', \lambda\rangle\langle N', \lambda|$ on the left- and on the right-hand sides of $e^{-i\hat{H}(t_1-t_2)}$, in order to obtain

$$G^>(1,2) = -i\sum_\lambda e^{i(E_\lambda^{N+1}-E_0)(t_1-t_2)} f_\lambda^{N+1}(x_1) f_\lambda^{N+1*}(x_2), \tag{2.12}$$

where E_λ^{N+1} is the energy of the λ-th excited state of the system with $N+1$ particles, and the *Dyson amplitudes* have been introduced, defined as

$$f_\lambda^{N+1}(x_1) = \langle N, 0|\hat{\psi}(x_1)|N+1, \lambda\rangle. \tag{2.13}$$

The orthonormality of the Fock basis was used to obtain this result. By Fourier transforming, we finally get

$$\begin{aligned} G^>(x_1, x_2; \omega) &= -i\sum_\lambda \int \mathrm{d}t\, e^{i(E_\lambda^{N+1}-E_0)t} f_\lambda^{N+1}(x_1) f_\lambda^{N+1*}(x_2) e^{i\omega t}, \\ &= -i\sum_\lambda f_\lambda^{N+1}(x_1) f_\lambda^{N+1*}(x_2)\delta(\omega - E_\lambda^{N+1} + E_0). \end{aligned} \tag{2.14}$$

For the lesser Green's function we analogously obtain

$$G^<(1,2) = +i \sum_\lambda e^{-i(E_0 - E_\lambda^{N-1})(t_1 - t_2)} f_\lambda^{N-1*}(x_1) f_\lambda^{N-1}(x_2), \tag{2.15}$$

$$G^<(x_1, x_2; \omega) = +i \sum_\lambda f_\lambda^{N-1*}(x_1) f_\lambda^{N-1}(x_2) \delta(\omega - E_0 + E_\lambda^{N-1}), \tag{2.16}$$

where E_λ^{N-1} is the energy of the λ-th excited state of the system with $N-1$ particles, and the Dyson amplitudes are now

$$f_\lambda^{N-1}(x_1) = \langle N_0 - 1, \lambda | \hat{\psi}(x_1) | N, 0 \rangle. \tag{2.17}$$

Eqs. (2.14) and (2.16) make it clear that $G^>$ and $G^<$ contain information on particle addition and removal respectively, as mentioned earlier. The expression of the spectral function in frequency space can now be written using Eqs. (2.7), (2.14) and (2.16),

$$\begin{aligned} 2\pi A(x_1 x_2, \omega) &= [iG^>(x_1 x_2, \omega) - iG^<(x_1 x_2, \omega)] \\ &= 2\pi \sum_\lambda f_\lambda(x_1) f_\lambda^*(x_2) \delta(\omega - \varepsilon_\lambda); \end{aligned} \tag{2.18}$$

λ now runs over all the excited states with $N+1$ and $N-1$ particles: for states with $N+1$ particles we have

$$\varepsilon_\lambda = E_\lambda^{N+1} - E_0 > \mu, \tag{2.19}$$

$$f_\lambda(x_1) = f_\lambda^{N+1}(x_1); \tag{2.20}$$

whereas for states with $N-1$ particles we have

$$\varepsilon_\lambda = E_0 - E_\lambda^{N-1} < \mu, \tag{2.21}$$

$$f_\lambda(x_1) = f_\lambda^{N-1}(x_1), \tag{2.22}$$

with μ being the chemical potential. We have just obtained what we set out to seek: Eq. (2.18) shows that the spectral function is made of delta peaks centered at the charged excitation energies of the system, weighted by the Dyson amplitudes; the latter in particular determine the amplitude of peaks, which concur together to the formation of broadened structures. It can be shown that in the sudden approximation the spectral function does indeed reproduce ARPES spectra [66]. In frequency space the spectral function satisfies important conditions such as normalization,

$$\int_{-\infty}^{+\infty} \mathrm{d}\omega \, A(x_1 x_2, \omega) = \delta(x_1 - x_2), \tag{2.23}$$

and particle conservation

$$\rho(x) = \int_{-\infty}^{\mu} \mathrm{d}\omega \, A(xx, \omega). \tag{2.24}$$

The only problem now is that, in practical calculations, one obtains Green's functions first, and the spectral function afterwards. Therefore, we now proceed to obtain the Green's

function G from the spectral function A in a spectral representation, and vice versa. We begin by Fourier transforming Eq. (2.6) in order to obtain

$$G(\omega) = \frac{1}{2\pi} \lim_{\eta \to 0^+} \int d\omega' \left[\frac{iG^>(\omega')}{\omega - \omega' + i\eta} - \frac{iG^<(\omega')}{\omega - \omega' - i\eta} \right] \tag{2.25}$$

by making use of the representation of the Heaviside theta in Fourier space,

$$\theta(t) = \frac{i}{2\pi} \lim_{\eta \to 0^+} \int_{-\infty}^{+\infty} d\omega \frac{e^{-i\omega t}}{\omega + i\eta}, \qquad \theta(-t) = -\frac{i}{2\pi} \lim_{\eta \to 0^+} \int_{-\infty}^{+\infty} d\omega \frac{e^{-i\omega t}}{\omega - i\eta}. \tag{2.26}$$

We note from Eqs. (2.14), (2.16) and (2.18), that

$$2\pi A(\omega) = \begin{cases} iG^>(\omega) & \text{for } \omega > \mu \\ -iG^<(\omega) & \text{for } \omega < \mu \end{cases}, \tag{2.27}$$

so we can write

$$G(\omega) = \lim_{\eta \to 0^+} \int d\omega' \frac{A(\omega')}{\omega - \omega' + i\eta \, \mathrm{sgn}(\omega' - \mu)}. \tag{2.28}$$

The Green's function G as expressed in Eqs. (2.25) and (2.28) is said to be in a *Lehmann representation* (here in a *continuous* form). Comparing Eqs. (2.28) and (2.18) emphasizes the physical content of the spectral function: it is the spectrum of the poles of the Green's function corresponding to addition and removal energies, weighted by the Dyson amplitudes f_λ. In fact, this is further emphasized by the *discrete* Lehmann form of the Green's function, which is obtained by replacing Eq, (2.18) in (2.28), yielding

$$G(x_1, x_2, \omega) = \lim_{\eta \to 0^+} \sum_\lambda \frac{f_\lambda(x_1) f_\lambda^*(x_2)}{\omega - \varepsilon_\lambda + i\eta \, \mathrm{sgn}(\omega - \mu)}. \tag{2.29}$$

This form is very useful in practical calculations. Alternatively, one can treat Eq. (2.28) by taking the limit $\eta \to 0^+$ before integrating. This is done by applying

$$\lim_{\eta \to 0^+} \frac{1}{\omega \pm i\eta} = \mathcal{P} \frac{1}{\omega} \mp i\pi\delta(\omega), \tag{2.30}$$

and by performing the frequency integral afterwards, which gives

$$G(\omega) = \left[\mathcal{P} \int d\omega' \frac{A(\omega')}{\omega - \omega'} - i\pi \, \mathrm{sgn}(\omega - \mu) A(\omega) \right]. \tag{2.31}$$

Inverting the last formula provides the popular expression for the spectral function starting from the the time-ordered G,

$$A(\omega) = \frac{1}{\pi} \mathrm{sgn}(\mu - \omega) \, \mathrm{Im}\{G(\omega)\}. \tag{2.32}$$

Lehmann forms for G^R and G^A can be found with analogous calculations, yielding

$$G^R(\omega) = \lim_{\eta \to 0^+} \int d\omega' \frac{A(\omega')}{\omega - \omega' + i\eta}, \qquad G^A(\omega) = \lim_{\eta \to 0^+} \int d\omega' \frac{A(\omega')}{\omega - \omega' - i\eta}. \tag{2.33}$$

and the spectral function can again be found with

$$A(\omega) = -\frac{1}{\pi}\,\mathrm{Im}\Big\{G^R(\omega)\Big\}. \tag{2.34}$$

Now that Eqs. (2.33) and (2.28) provide us with a spectral representation for all the Green's functions having the different time properties, we can make remarks on their pole structure. Due to the vanishing quantity η, G^R has poles slightly below the real axis, whereas those of G^A are slightly above; G displays both configurations, with the poles above the real axis being confined to the $\omega > \mu$ semi-plane, and those below to the $\omega < \mu$ semi-plane. We also note that, from the relations we have seen, it follows that extracting the spectral function from a system allows one to switch between Green's functions with different time properties. In the context of MBPT, one usually works with Green's function and extracts the spectral function in a later moment through relations like Eq. (2.32). In particular, it is common to work with the time-ordered G, for whose calculation Wick's theorem can be used along with Feynman's diagrammatic technique [171]. Retarded correlation functions like G^R are instead often used in the context of response functions, where they ensure that the constraint of *causality* is obeyed.

We conclude this section by considering the trivial yet notable case when the Green's function is that of a system of *independent particles*. In this case, one can conveniently transform the Green's function from the coordinate basis to the single-particle orbital basis. In such basis, if we term $\hat{c}_i^\dagger$ and $\hat{c}_i$ the creation and annihilation operators of a particle in the i-th state associated with the energy eigenvalue ε_i, the independent-particle Green's function G^0 is diagonal and reads

$$\begin{aligned} G^0_{ii}(t_1,t_2) &= -i\langle \mathrm{T}\left[\hat{c}_i(t_1)_H\ \hat{c}_i^\dagger(t_2)_H\right]\rangle_0 \\ &= -ie^{-i\varepsilon_i(t_1-t_2)}[\Theta(t_1-t_2)\Theta(\varepsilon_i-\mu) - \Theta(t_2-t_1)\Theta(\mu-\varepsilon_i)], \end{aligned} \tag{2.35}$$

with the second line coming from acting with the $\hat{c}$ and $\hat{c}^\dagger$ operators on the ground state after expanding the time ordering function in terms of theta functions. By differentiating with respect to t_1, the independent-particle equation of motion can be obtained,

$$\left[i\frac{\partial}{\partial t_1} - \hat{h}^0_{ii}\right] G^0_{ii}(t_1,t_2) = \delta(t_1-t_2), \tag{2.36}$$

hence the name Green's function: Green's functions in mathematics are traditionally the inverse of objects, in this case of the operator $\left[i\hat{I}\frac{\partial}{\partial t} - \hat{h}_0\right]$.

Furthermore, Dyson amplitudes acquire a familiar meaning for independent particles: they are the single-particle orbital wave functions φ_λ,

$$f^{N+1}_\lambda(x_1) = \varphi_\lambda(x_1), \tag{2.37}$$

$$f^{N-1}_\lambda(x_1) = \varphi^*_\lambda(x_1), \tag{2.38}$$

which can be readily obtained from Eqs. (2.13) and (2.17) via the basis change formulae for the field operators,

$$\hat{\psi}(x_1) = \sum_\lambda \varphi_\lambda(x_1)\hat{c}_\lambda, \tag{2.39}$$

$$\hat{\psi}^\dagger(x_1) = \sum_\lambda \varphi^*_\lambda(x_1)\hat{c}^\dagger_\lambda. \tag{2.40}$$

Alongside this, the energy eigenvalues ε_i coincide with the charged excitation energies of the system, i.e. the poles of the Green's function. This is the foundation of independent-particle theory, as anticipated in Section 1.1. Looking at the spectral function, this means that it is made of delta peaks centered at the energy eigenvalues, whose weight is given by the energy eigenfunctions; this is a consequence of, e.g. $f_\lambda^{N+1} = \langle N,0|\hat{c}_i|N+1,i\rangle \neq 0$ only if $|N+1,i\rangle = \hat{c}_i|N,0\rangle$ (the reasoning is analogous for f_λ^{N-1}). In the general case, an overlap between different Fock excited states is possible instead, so that many different contributions lead to a spreading and a renormalization of the delta peaks (see Fig. 1.2).

2.1.2 Introduction to Dyson equations

The result of Eq. (2.35) hints at a general operatorial form of the equation of motion of the Green's function. By introducing a system described by a generic hamiltonian $\hat{h}_0$, this may be written as

$$\left[i\frac{\hat{\partial}}{\partial t} + \hat{h}_0\right]\hat{G}_0 = \hat{I}, \tag{2.41}$$

where $I_{xt,x't'} = \delta(x-x')\delta(t-t')$ is the spin-space-time identity, and $(\partial/\partial t)_{xt,x't'} = \delta(x-x')\partial/\partial t$. In a system that experiences a further contribution $\hat{v}$ to its potential, the equation of motion becomes

$$\left[i\frac{\hat{\partial}}{\partial t} + \hat{h}_0 + \hat{v}\right]\hat{G} = \hat{I}, \tag{2.42}$$

The Green's function G of the latter system can be obtained from the Green's function G_0 of the former through a Dyson equation. In fact, one need only rewrite Eq. (2.42) as

$$\left[\hat{G}_0^{-1} + \hat{v}\right]\hat{G} = \hat{I}, \tag{2.43}$$

which ultimately leads to a so-called Dyson equation,

$$\hat{G} = (\hat{G}_0^{-1} + \hat{v})^{-1} = \hat{G}_0 + \hat{G}_0\hat{v}\hat{G}. \tag{2.44}$$

By similar means one shows that if the potential $\hat{v}$ can be decomposed in two addenda as in $\hat{v} = \hat{v}_1 + \hat{v}_2$, then two coupled Dyson equations hold

$$\hat{G}_1 = \hat{G}_0 + \hat{G}_0\hat{v}_1\hat{G}_1, \tag{2.45}$$
$$\hat{G} = \hat{G}_1 + \hat{G}_1\hat{v}_2\hat{G}. \tag{2.46}$$

This is the basic machinery that will aid us in obtaining a fully-fledged Dyson equation starting from physical grounds in Section 2.1.5.

2.1.3 The two-particle Green's function

The time-ordered two-particle Green's function is defined as:

$$G_2(1,2,1',2') = (-i)^2\langle \mathrm{T}\left[\hat{\psi}(1)\hat{\psi}(2)\hat{\psi}^\dagger(2')\hat{\psi}^\dagger(1')\right]\rangle_0. \tag{2.47}$$

Note that, analogously to the one-particle Green's function, the two-particle Green's function is antisymmetric with respect to odd permutations of its arguments. The two-particle correlation function L is obtained by subtracting the uncorrelated part from the definition:

$$L(11',22') = -G_2(1,2,1',2') + G(1,1')G(2,2') \tag{2.48}$$

The one-particle Green's function contains information about the propagation of either electrons or holes, depending on the action of time ordering. The two-particle Green's function can describe a wider range of phenomena, i.e. the propagation of electron-electron pairs, hole-hole pairs or electron-hole pairs. For our purposes, we will focus on electron-hole pairs. In order to do that, we need to set

$$t_1' = t_1^+ \text{ and } t_2' = t_2^+, \tag{2.49}$$

and then define the basic building blocks

$$G_{eh}^{>}(11',22') = (-i)^2\langle\hat{\psi}^\dagger(x_1't_1^+)\hat{\psi}(x_1t_1)\,\hat{\psi}^\dagger(x_2't_2^+)\hat{\psi}(x_2t_2)\rangle_0, \tag{2.50}$$
$$G_{eh}^{<}(11',22') = (-i)^2\langle\hat{\psi}^\dagger(x_2't_2^+)\hat{\psi}(x_2t_2)\,\hat{\psi}^\dagger(x_1't_1^+)\hat{\psi}(x_1t_1)\rangle_0, \tag{2.51}$$

which in turn lead to defining

$$L_{eh}^{\lessgtr}(11',22') = -G_{eh}^{\lessgtr}(11',22') - \rho(x_1,x_1')\rho(x_2,x_2'), \tag{2.52}$$

where the density matrices are a consequence of the constraint of Eq. (2.49), and applying Eq. (2.3); here we also reverted to the $1 \equiv (\mathbf{r}_1, \sigma_1, t_1)$ notation, assuming that the time constraint is obeyed. The time-ordered electron-hole correlation function, or electron-hole propagator, can now be built,

$$L_{eh}(11',22') = \theta(t_1-t_2)L_{eh}^{>}(11',22') + \theta(t_2-t_1)L_{eh}^{<}(11',22'), \tag{2.53}$$

which is again equivalent to imposing the time constraints Eq. (2.49) to Eq. (2.48). The two couples $\hat{\psi}^\dagger\hat{\psi}$ commute like bosons in the time-ordered product, therefore the action of the time ordering operator does not cause the overall sign of L_{eh} to change.

We find a spectral representation for L_{eh} by repeating the recipe seen for the one-particle Green's function. The spectral function reads

$$A(x_1x_1', x_2x_2';\omega) = L_{eh}^{>}(x_1,x_1';x_2,x_2';\omega) - L_{eh}^{<}(x_1,x_1';x_2,x_2';\omega) \tag{2.54}$$
$$= 2\pi\sum_\lambda \left[+f_{0\lambda}^{eh}(x_1,x_1')f_{\lambda 0}^{eh}(x_2,x_2')\delta(E_\lambda^N - E_0 - \omega)\right.$$
$$\left. - f_{0\lambda}^{eh}(x_2,x_2')f_{\lambda 0}^{eh}(x_1,x_1')\delta(E_0 - E_\lambda^N - \omega)\right], \tag{2.55}$$

and the Lehmann representation of the time-ordered correlation electron-hole propagator is

$$L_{eh}(x_1x_1', x_2, x_2';\omega) = i\sum_\lambda \left[\frac{f_{0\lambda}^{eh}(x_1,x_1')f_{\lambda 0}^{eh}(x_2,x_2')}{\omega - (E_\lambda^N - E_0 - i\eta)} - \frac{f_{0\lambda}^{eh}(x_2,x_2')f_{\lambda 0}^{eh}(x_1,x_1')}{\omega - (E_0 - E_\lambda^N + i\eta)}\right], \tag{2.56}$$

with the f^{eh} amplitudes defined as

$$f_{\lambda 0}^{eh}(x_1,x_1') = \langle N,\lambda|\hat{\psi}(x_1')\hat{\psi}^\dagger(x_1)|N,0\rangle,$$
$$f_{0\lambda}^{eh}(x_1,x_1') = \langle N,0|\hat{\psi}^\dagger(x_1')\hat{\psi}(x_1)|N,\lambda\rangle. \tag{2.57}$$

Eq. (2.56) shows that, while the one-particle Green's function yielded the charged excitations as poles, the two-particle Green's function yields the *neutral excitations*, i.e. those that do not change the particle number.

If we consider the case of independent particles, the neutral excitations of the system consist in moving particles from filled orbitals to empty orbitals. Therefore, the energy differences $E^N_\lambda - E_0$ turn into eigenvalue differences $\varepsilon_c - \varepsilon_v$, and the amplitudes $f_{0\lambda}$ and $f_{\lambda 0}$ turn into products of single-particle wavefunctions,

$$f^{eh}_{\lambda 0}(x_1, x_1') = \varphi_v(x_1')\varphi^*_c(x_1), \tag{2.58}$$
$$f^{eh}_{0\lambda}(x_1, x_1') = \varphi^*_c(x_1')\varphi_v(x_1); \tag{2.59}$$

here c indicates the empty orbital to which the particle is added after being removed from the occupied orbital v.

As we shall see in Section 2.1.4, L_{eh} is connected to the density-density response function of a system: in particular, its retarded version L^R_{eh} is, which satisfies the requirement of causality. We give here its definition,

$$L^R_{eh}(11',22') = \theta(t_1 - t_2)\langle\left[\hat\psi^\dagger(1')\hat\psi(1),\, \hat\psi^\dagger(2')\hat\psi(2)\right]\rangle_0 \tag{2.60}$$
$$= \theta(t_1 - t_2)\left(L^>_{eh}(11',22') - L^<_{eh}(11',22')\right), \tag{2.61}$$

to which we shall come back later.

2.1.4 Response functions

Let us suppose we want to describe the response of the density ρ to a perturbation to the ionic potential v_{ext}. A perturbation δv_{ext} to v_{ext} couples to ρ, like v_{ext} itself does. Therefore, in second quantization, the hamiltonian $\hat H_0$ will experience a perturbation

$$\int \mathrm{d}x_2\, \hat\rho(x_2)\delta v_{\text{ext}}(x_2, t_2),$$

where $\hat\rho(x_1) = \hat\psi^\dagger(x_1)\hat\psi(x_1)$ is the density operator. Let us suppose that the perturbation is turned on at time t_0, so that at t_0 the system is in an eigenstate of $\hat H_0$. We indicate with H and S the Heisenberg picture and the Schrödinger picture respectively of the unperturbed system; and with $\tilde I$ the interaction picture of the perturbed system. By definition, states and operators are the same in the H and $\tilde I$ pictures,

$$|\alpha(t)\rangle_H = |\alpha(t)\rangle_{\tilde I} = e^{i\hat H_0(t-t_0)}|\alpha(t)\rangle_S = |\alpha(t_0)\rangle_S, \tag{2.62}$$

$$\hat O_H(t) = \hat O_{\tilde I}(t) = e^{i\hat H_0(t-t_0)}\hat O_S(t)e^{i\hat H_0(t-t_0)}. \tag{2.63}$$

Only the evolution operator changes, which in the interaction picture of the perturbed system reads

$$U_{\tilde I}(t_1, t_0) = Te^{-i\int_{t_0}^{t_1} dt_2 \int dx_2 \hat\rho_{\tilde I}(2)\delta v_{\text{ext}}(2)}. \tag{2.64}$$

The expectation value of the density operator $\hat\rho$ at space-spin-time 1 in the perturbed system is

$$\langle\hat\rho(1)\rangle_\alpha = \langle\hat\rho_{\tilde I}(1)\rangle_{\tilde I,\alpha} = \langle\alpha(t_0)|\, U^\dagger_{\tilde I}(t_1, t_0)\hat\rho_{\tilde I}(1)U_{\tilde I}(t_1, t_0)\,|\alpha(t_0)\rangle_{\tilde I}, \tag{2.65}$$

and by expanding the two evolution operators in a Taylor series we obtain

$$\langle\hat{\rho}_{\tilde{I}}(1)\rangle_{\alpha,\tilde{I}} = \langle\alpha(t_0)|\left(1+i\int_{t_0}^{t_1}\mathrm{d}t_2\int\mathrm{d}x_2\,\delta v_{\mathrm{ext}}(2)\,T\hat{\rho}_{\tilde{I}}(2)+\dots\right) \times\hat{\rho}_{\tilde{I}}(1)\left(1-i\int_{t_0}^{t_1}\mathrm{d}t_2\int\mathrm{d}x_2\,\delta v_{\mathrm{ext}}(2)\,T\hat{\rho}_{\tilde{I}}(2)+\dots\right)|\,\alpha(t_0)\rangle_{\tilde{I}}. \quad (2.66)$$

Truncating the expansion to first order, and making use of the fact that $|\alpha(t_0)\rangle_{\tilde{I}} = |\alpha(t_0)\rangle_S = |\alpha(t)\rangle_H$ [cfr. Eq. (2.62)] and that $\hat{\rho}_{\tilde{I}}(1) = \hat{\rho}_H(1)$, gives

$$\langle\hat{\rho}_{\tilde{I}}(1)\rangle_{\alpha,\tilde{I}} \simeq \langle\hat{\rho}_H(1)\rangle_{\alpha,H} + i\int_{t_0}^{t_1}\mathrm{d}t_2\int\mathrm{d}x_2\,\delta v_{\mathrm{ext}}(2)\,\langle[\hat{\rho}_H(2),\hat{\rho}_H(1)]\rangle_{\alpha,H}. \quad (2.67)$$

We now choose α to be the ground state and drop the α subscript. We define the linear variation of the density due to the perturbation as

$$\delta\rho(1) = \langle\hat{\rho}_{\tilde{I}}(1)\rangle_{\tilde{I}} - \langle\hat{\rho}_H(1)\rangle_H, \quad (2.68)$$

which from Eq. (2.67) then reads

$$\delta\rho(1) = i\int_{t_0}^{t_1}\mathrm{d}t_2\int\mathrm{d}x_2\,\delta v_{\mathrm{ext}}(2)\,\langle[\hat{\rho}_H(2),\hat{\rho}_H(1)]\rangle_H. \quad (2.69)$$

This equation can be rewritten as

$$\delta\rho(1) = \int_{-\infty}^{+\infty}dt_2\int dx_2\chi^R(1,2)\delta v_{\mathrm{ext}}(2), \quad (2.70)$$

with the linear *density-density response function* being

$$\chi^R(1,2) = -i\theta(t_1-t_2)\langle[\hat{\rho}_H(1),\hat{\rho}_H(2)]\rangle_H. \quad (2.71)$$

As the name suggests, this response function describes the variation of the density due to perturbations that couple to the density. We remark that the presence of the theta function in Eq. (2.71) keeping $\chi(1,2)$ non-vanishing only for $t_1 > t_2$ is a consequence of *causality*, i.e. perturbations to $\hat{\rho}$ at time t_1 cannot be caused by events in the perturbing field δv_{ext} that occur at times $t_2 > t_1$. By comparing with Eq. (2.60), we find that

$$\chi^R(1,2) = -iL^R(1^+,2^+). \quad (2.72)$$

In Section 2.1.5 we will give a first principles treatment for the calculation of L, and consequently of the time-ordered response function χ. Obtaining the retarded χ^R is trivial from the time-ordered one through the use of spectral functions, as seen in the previous sections.

It is interesting to obtain the dielectric function ϵ that connects the total variation of the potential δv_{tot} to the sole external perturbation δv_{ext}. Starting from

$$\delta v_{\mathrm{tot}}(1) = \delta v_{\mathrm{ext}}(1) + \int\mathrm{d}3\,v(1,3)\delta\rho(3) = \delta v_{\mathrm{ext}}(1) + \int\mathrm{d}3\int\mathrm{d}2\,v(1,3)\chi(3,2)\delta v_{\mathrm{ext}}, \quad (2.73)$$

with v being the Coulomb interaction, we introduce the inverse dielectric function

$$\epsilon^{-1}(\mathbf{r}_1\mathbf{r}_2, t_1 - t_2) = \delta(\mathbf{r}_1 - \mathbf{r}_2)\delta(t_1 - t_2) + \int \mathrm{d}\mathbf{r}_3\, v(|\mathbf{r}_1 - \mathbf{r}_3|)\chi^R(\mathbf{r}_3\mathbf{r}_2, t_1 - t_2), \tag{2.74}$$

with $\chi^R(\mathbf{r}_1\mathbf{r}_2, t_1 - t_2) = \sum_{\sigma_1\sigma_2} \chi^R(1,2)$. This allows us to rewrite Eq. (2.73) as

$$\delta v_{\mathrm{tot}}(\mathbf{r}_1, t_1) = \int \mathrm{d}\mathbf{r}_2 \int \mathrm{d}t_2\, \epsilon^{-1}(\mathbf{r}_1\mathbf{r}_2, t_1 - t_2)\delta v_{\mathrm{ext}}(\mathbf{r}_2, t_2). \tag{2.75}$$

As we shall see in Section 2.1.7, the dielectric function is also instrumental in obtaining the screened interaction W starting from the bare Coulomb interaction v.

2.1.5 Approximations via functional derivatives

We will now introduce approximate methods for the calculation of Green's functions through the use of functional derivatives. Our goal is to obtain a Dyson equation for the Green's function on the basis of Eq. (2.44); a generalized potential will emerge from first principles that will be identified with the self-energy operator Σ. We will then proceed to find schemes that aim at approximating Σ itself.

Adopting the usual notation, $1 \equiv (x_1, t_1) \equiv (\mathbf{r}_1, \sigma_1, t_1)$, from the Heisenberg equation of motion for the field operator

$$i\frac{\partial\hat{\psi}(x,t)}{\partial t} = [\hat{\psi}(x,t), \hat{H}], \tag{2.76}$$

where the hamiltonian in second quantization is given by

$$\hat{H} = \int \mathrm{d}x_1\, \hat{\psi}^\dagger(x_1,t)h(x_1)\hat{\psi}(x_1,t) + \frac{1}{2}\int\int \mathrm{d}x_1\, \mathrm{d}x_2\, \hat{\psi}^\dagger(x_1,t)\hat{\psi}^\dagger(x_2,t)v(x_1,x_2)\hat{\psi}(x_2,t)\hat{\psi}(x_1,t), \tag{2.77}$$

we obtain the equation of motion for the Green's function

$$\left[i\frac{\partial}{\partial t_1} - h(x_1)\right] G(1,1') + i\int \mathrm{d}x_2\, v(x_1,x_2)G_2(1,2,1',2^+)\Big|_{t_2=t_1^+} = \delta(1,1'); \tag{2.78}$$

here $h(x_1) = T(x_1) + v_{\mathrm{ext}}(x_2)$ contains only the kinetic and the external potential terms and $v(x_1,x_2) = \frac{1}{|\mathbf{r}_1-\mathbf{r}_2|}$ is the Coulomb interaction (which is spin-independent). Note that the two-particle Green's function G_2 appears in the equation of motion; in fact, a whole hierarchy of equations of motion can be obtained involving Green's function correlating more and more particles, giving rise to the so-called "Martin-Schwinger hierarchy" [172].

By neglecting the interactions between particles via he Coulomb potential v, Eq. (2.78) reduces to the equation of motion of an independent-particle Green's function G_0

$$\left[i\frac{\partial}{\partial t_1} - h(x_1)\right] G(1,1') = \delta(1,1'), \tag{2.79}$$

which is in agreement with Eq. (2.35). One can then apply the operator $G_0 = [i\partial/\partial t - \hat{h}]^{-1}$ to both sides of Eq. (2.78) by , in order to obtain

$$G(1,1') = G_0(1,1') - iG_0(1,\bar{2})v(\bar{2},\bar{3})G_2(\bar{2},\bar{3}^+,1',\bar{3}^{++}), \tag{2.80}$$

where barred variables like $\bar{2}$ are integrated,e.g. $f(1,\bar{2})g(\bar{2}) = \int \mathrm{d}2\, f(1,2)g(2)$. By replacing G_2 using the definition of the two-particle correlation function L, Eq. (2.48), we obtain

$$G(1,1') = G_0(1,1') + G_0(,\bar{2})v_H(\bar{2})G(\bar{2},1') + iG_0(1,\bar{2})v(\bar{2},\bar{3})L(\bar{2}1',\bar{3}^+\bar{3}^{++}), \tag{2.81}$$

which makes the contribution of the Hartree electrostatic potential

$$v_H(2) = \int \mathrm{d}\mathbf{r}_3\, \rho(\mathbf{r}_3)v(\mathbf{r}_2,\mathbf{r}_3) = -iv(2^+,\bar{3})G(\bar{3},\bar{3}^+) \tag{2.82}$$

explicit; this contribution comes from the uncorrelated GG part of L once the equal arguments $\bar{3}^+$ and $\bar{3}^+$+ of G_2 in Eq. (2.80) are taken.

We now introduce a fictitious non-local potential $\mathcal{J}(1,1')$ in the hamiltonian $\hat{H}$ which we will use to perform functional derivatives. At the end of the calculations, $\mathcal{J}$ will be set to zero. It can in fact be shown, using Schwinger's derivative technique [18, 172, 173] or a finite temperature formulation of the Green's functions [13], that

$$L_{\mathcal{J}}(11',22') = \frac{\delta G_{\mathcal{J}}(1,1')}{\delta \mathcal{J}(2',2)}. \tag{2.83}$$

Since L in Eq. (2.80) has two equal arguments, a local potential $u(3) = \mathcal{J}(3^+,3)$ can be used instead in order to obtain it,

$$L_u(21',33^+) = \frac{\delta G_u(21')}{\delta u(3)}, \tag{2.84}$$

and replacing this equation in Eq. (2.80) yields the Baym-Kadanoff equation [174],

$$G_u(1,1') = G_0(1,1') + G_0(1,\bar{2})\left\{[u(\bar{2}) + v_H(\bar{2})]G_u(\bar{2},1') + iv(\bar{2},\bar{3})\frac{\delta G_u(\bar{2},1')}{\delta u(\bar{3}^+)}\right\}. \tag{2.85}$$

We note that for this equation to be obtained, all the steps must be repeated starting from Eq. (2.78) after adding the $u(x_1)$ potential between the square brackets. We drop the u and $\mathcal{J}$ subscripts in the following for ease of notation. By applying the operators G_u^{-1} to the right and G_0^{-1} to the left on both sides of Eq. (2.78), we obtain a more convenient formulation of the Baym-Kadanoff equation for our goal,

$$G^{-1}(1,1') = G_0^{-1}(1,1') - [u(1) + v_H(1)]\delta(1,1') - i(1,\bar{3})\frac{\delta G(1,\bar{2})}{\delta u(\bar{3}^+)}G^{-1}(\bar{2},1') \tag{2.86}$$

$$= G_0^{-1}(1,1') - u(1)\delta(1,1') - \Sigma(1,1'), \tag{2.87}$$

which allows us to introduce the self-energy Σ and the exchange-correlation self-energy Σ_{xc},

$$\Sigma(1,1') = v_H(1)\delta(1,1') + \Sigma_{\mathrm{xc}}(1,1'), \tag{2.88}$$

$$\Sigma_{\mathrm{xc}}(1,1') = iv(1,\bar{3})\frac{\delta G(1,\bar{2})}{\delta u(\bar{3}^+)}G^{-1}(\bar{2},1') = -iv(1,\bar{3})G(1,\bar{2})\frac{\delta G^{-1}(\bar{2},1')}{\delta u(\bar{3}^+)}; \tag{2.89}$$

the second equality of Eq. (2.89) is obtained from the identity

$$\delta\left(G^{-1}G\right) = \delta G^{-1}G + G^{-1}\delta G = 0. \tag{2.90}$$

It is now evident that Eq. (2.87) is the inverse of an equation in the form of Eq. (2.44). Therefore, by letting temporarily $u \to 0$, it can be readily recast to the popular form of the Dyson equation,

$$G(1,1') = G_0(1,1') + G_0(1,\bar{2})\Sigma(\bar{2},\bar{2}')G(\bar{2}',2). \tag{2.91}$$

By obtaining the Dyson equation we have reached one of our goals. The self-energy Σ has emerged from first principles, which represents a generalized potential connecting the independent-particle problem described by G_0 to the fully interacting one described by G. Now we need to find approximation schemes for Σ.

We begin by going back to L and by rewriting Eq. (2.84) using again the trick of Eq. (2.90), obtaining

$$L(11',22') = -G(1,\bar{3})\frac{\delta G^{-1}(\bar{3},\bar{3}')}{\delta \mathcal{J}(2',2)}G(\bar{3},1'). \tag{2.92}$$

We substitute Eq. (2.86) into this to get

$$L(11',22') = -G(1,\bar{3})\left[-\frac{\delta \mathcal{J}(\bar{3},\bar{3}')}{\delta \mathcal{J}(2',2)} - \frac{\delta \Sigma(\bar{3},\bar{3}')}{\delta \mathcal{J}(2',2)}\right] G(\bar{3}',1') \tag{2.93}$$

$$= G(1,2')G(2,1') + G(1,\bar{3})\frac{\delta \Sigma(\bar{3},\bar{3}')}{\delta G(\bar{4}',\bar{4})}G(\bar{3}',1')L(\bar{4}'\bar{4},22'), \tag{2.94}$$

where we used the chain rule and Eq. (2.83),

$$\frac{\delta \Sigma}{\delta \mathcal{J}} = \frac{\delta \Sigma}{\delta G}\frac{\delta G}{\delta \mathcal{J}} = \frac{\delta \Sigma}{\delta G}L,$$

to obtain the second row. We now define the uncorrelated electron-hole propagator

$$L_0(11',22') = G(1,2')G(2,1') \qquad \text{and} \tag{2.95}$$

$$\Xi(11',22') = \frac{\delta \Sigma(1,1')}{\delta G(2',2)} = -i\delta(1,1')\delta(2,2')v(1,2) + \frac{\delta \Sigma_{\text{xc}}(1,1')}{\delta G(2',2)}, \tag{2.96}$$

where the second equality of Eq. (2.96) is obtained from Eq. (2.88) and from the form of the Hartree potential in Eq. (2.82); we use these definitions to rewrite Eq. (2.94) in a compact form,

$$L(11',22') = L_0(11',22') + L_0(11',\bar{3}'\bar{3})\Xi(\bar{3}\bar{3}',\bar{4}'\bar{4})L(\bar{4}\bar{4}',22'). \tag{2.97}$$

It is now evident that Eq. (2.97), which goes under the name of *Bethe-Salpeter equation* (BSE), is a Dyson equation for the 2-particle correlation function L. In passing, it is convenient to define a shorthand notation to treat multiplications of 4-point operators such as L and Ξ,

$$AB(11',22') = \int d33'\, A(11',3'3)B(33',22'),$$

so that Eq. (2.97) becomes simply $L = L_0 + L_0\Xi L$. In order to plug this result into the self-energy, we now introduce the 4-point and the 3-point *reducible vertex functions*,

$${}^4\Gamma(11',22') = -\frac{\delta G^{-1}(1,1')}{\delta \mathcal{J}(2',2)} \qquad \text{and} \qquad \Gamma(11',2) = -\frac{\delta G^{-1}(1,1')}{\delta u(2)}, \tag{2.98}$$

respectively. The latter can be obtained from the former by letting $2' \to 2^+$, given the previous definitions of the potentials $\mathcal{J}$ and u. Once the first of Eqs. (2.98) is substituted into Eq. (2.92), we get

$$L = L_0\, {}^4\Gamma, \qquad {}^4\Gamma = 1 + \Xi L; \tag{2.99}$$

here the second equation is easily deduced by comparing the first equation with the Bethe-Salpeter equation for L. Then substituting the first of Eqs. (2.99) into the second and taking the limit $2' \to 2^+$ in the definition of ${}^4\Gamma$, Eq. (2.98), yields the Bethe-Salpeter equation for the 3-point reducible vertex

$$\Gamma(11',2) = \delta(12^+)\delta(1'2) + \Xi(11', \bar{3}'\bar{3})L^0(\bar{3}\bar{3}', \bar{4}'\bar{4})\Gamma(\bar{4}\bar{4}',2). \tag{2.100}$$

Having now an equation for the calculation of the reducible vertex Γ, we can easily plug it into the xc self-energy Σ_{xc}, recognizing that Eq. (2.89) contains the second definition in Eqs. (2.98),

$$\Sigma_{\text{xc}}(11') = iG(1\bar{2})v(1\bar{3})\Gamma(\bar{2}1', \bar{3}^+). \tag{2.101}$$

We have found all the ingredients to compute the self-energy and then solve the Dyson equation. We just need to solve the Bethe-Salpeter equation for Γ, which requires the computation of the kernel Ξ and of the uncorrelated propagator L_0, which require the computation of... the self-energy itself. This means that obtaining the interacting G is in general an iterative procedure. Furthermore, Eq. (2.101), along with Eq. (2.100), emphasizes that Σ_{xc} undergoes an expansion in powers of the bare Coulomb interaction v. However, in extended systems this is in general not successful [16, 21], and an expansion in a *screened* Coulomb interaction W is to be preferred. W should contain from the very beginning some effects that are accounted for by the vertex equation, Eq, (2.100), so that a new version of the vertex equation can be devised where the term beyond the delta functions is smaller. In other words, we want to reduce the reducible vertex. Some effects that we may want to remove from the vertex are the classical electrostatic ones, governed by the Hartree potential v_H. Then we can define *irreducible* correlation functions through differentiation with respect to the total classical potential, which will either be a non-local potential $v_{\text{tot,nl}} = v_H + \mathcal{J}$ for 4-point correlation functions or a local potential $v_{\text{tot}} = v_H + u$ for 3-point correlation functions. In particular, we define the 4-point irreducible 2-particle correlation function,

$$\tilde{L}(11',22') = \frac{\delta G(11')}{\delta\left[\mathcal{J}(2',2) + v_H(2)\delta(2',2)\right]} \tag{2.102}$$

and the irreducible vertex functions,

$${}^4\tilde{\Gamma}(11',22') = -\frac{\delta G^{-1}(1,1')}{[\delta\mathcal{J}(2',2) + v_H(2)\delta(2',2)]} \qquad \text{and} \qquad \tilde{\Gamma}(11',2) = -\frac{\delta G^{-1}(1,1')}{[\delta u(2) + v_H(2)]}. \tag{2.103}$$

We note that $\tilde{L}$ can also be obtained by operating a splitting of the Bethe-Salpeter equation, Eq. (2.97), into two Dyson equations, according to the separation of the kernel Ξ into its two addenda as seen in Eq. (2.96),

$$\tilde{L} = L_0 + L_0\frac{\delta\Sigma_{\text{xc}}}{\delta G}\tilde{L}, \tag{2.104}$$

$$L = \tilde{L} + \tilde{L}(-iv)\tilde{L}. \tag{2.105}$$

This trick of splitting Dyson equations was introduced in Section 2.1.2 with Eqs. (2.45) and (2.46). The equivalence of the two definitions of $\tilde{L}$ is readily obtained by applying the chain rule to Eq. (2.83),

$$L = \frac{\delta G}{\delta \mathcal{J}} = \frac{\delta G}{\delta v_{\mathrm{tot,nl}}} \frac{\delta v_{\mathrm{tot,nl}}}{\delta \mathcal{J}} = \tilde{L}\left(1 + \frac{\delta v_H}{\delta \mathcal{J}}\right) = \tilde{L}\left(1 - iv\frac{\delta G}{\delta \mathcal{J}}\right) = \tilde{L}(1 - ivL), \tag{2.106}$$

which shows that the definition of $\tilde{L}$ via Eq. (2.102) implies Eq. (2.105). In the same way that we obtained the Bethe-Salpeter equation for the reducible vertex, Eq. (2.100), we can obtain the Bethe-Salpeter equation for the irreducible one,

$$\tilde{\Gamma}(11',2) = \delta(12^+)\delta(1'2) + \frac{\delta \Sigma_{\mathrm{xc}}(1,1')}{\delta G(\bar{3},\bar{3}')} L^0(\bar{3}\bar{3}', \bar{4}'\bar{4})\tilde{\Gamma}(\bar{4}\bar{4}',2). \tag{2.107}$$

We are now ready to compute Σ_{xc} as an expansion of W. Targeting the $\delta G^{-1}/\delta u$ term of Eq. (2.89), we compute

$$-\frac{\delta G^{-1}}{\delta \mathcal{J}} = -\frac{\delta G^{-1}}{\delta v_{\mathrm{tot,nl}}} \frac{\delta v_{\mathrm{tot,nl}}}{\delta \mathcal{J}} = {}^4\tilde{\Gamma}\left(1 - iv\frac{\delta G}{\delta \mathcal{J}}\right) = {}^4\tilde{\Gamma}(1 - ivL), \tag{2.108}$$

where we used again the chain rule and definitions that by now should be familiar. By taking the usual limit $2' \to 2^+$ in the first of Eqs. (2.103) in order to close the 4-point ${}^4\tilde{\Gamma}$ into the 3-point $\tilde{\Gamma}$, we obtain for the self-energy

$$\Sigma_{\mathrm{xc}}(11') = iG(1,\bar{2})W(1,\bar{3})\tilde{\Gamma}(\bar{2}1', \bar{3}^+), \tag{2.109}$$

with

$$W(11') = v(1,1') + v(1,\bar{2})\left[-iL(\bar{2}\bar{2}^+, \bar{3}\bar{3}^+)\right] v(\bar{3},\bar{1}'). \tag{2.110}$$

This result shows that the screened interaction W is obtained by adding to the bare Coulomb interaction v a further contribution, which includes the screening due to the polarization of classical charges, i.e. the physics of the Hartree potential. This physical content is emphasized in Hedin's scheme, that amounts to a reformulation of the main equations seen up until now in terms of response functions. We shall introduce it in Section 2.1.7.

2.1.6 Quasi-particles from the Dyson equation

Before delving into the specifics of the approximation scheme introduced in Section 2.1.5, we take a moment to examine the Dyson equation and the emergence of the quasi-particle (QP) picture from the independent-particle (IP) picture. We rewrite the Dyson equation, Eq. (2.91), in the previous form obtained from the Baym-Kadanoff equation, Eq. (2.87), after taking it to frequency space,

$$G^{-1}(xx',\omega) = [\delta(x - x')(\omega - h(x')) - \Sigma(xx',\omega)]. \tag{2.111}$$

Using the Lehmann representation for the Green's function, Eq. (2.29), we obtain

$$\int \mathrm{d}x''\,[\delta(x - x'')(\omega - h(x'')) - \Sigma(xx'',\omega)] \sum_\lambda \frac{f_\lambda(x'')f_\lambda(x')}{\omega - \varepsilon_\lambda} = \delta(x - x'). \tag{2.112}$$

If λ is a discrete non-degenerate level of the energy spectrum of the system, we can take the $\omega \to \varepsilon_\lambda$ limit and get

$$\int \mathrm{d}x'' \, [h(x'') + \Sigma(xx'', \varepsilon_\lambda)] f_\lambda(x'') = \varepsilon_\lambda f_\lambda(x), \tag{2.113}$$

which in a schematic notation means solving the eigenvalue problem

$$[\hat{h} + \hat{\Sigma}(\varepsilon)] f = \varepsilon f. \tag{2.114}$$

The solutions of the problem are identified with the QP energies ε_λ and the Dyson amplitudes f_λ. The energy dependence of Σ makes the problem in general non-hermitian. Σ is also complex in energy ranges where ε forms a continuum, in which case a solution of Eq. (2.114) still exists by performing an analytical continuation of $\Sigma(\omega)$. In the general case of complex generalized eigenvalues ε, their real part give us the charged excitation energies of the system, whereas their imaginary part give us the lifetimes of the associated charged excitation states.

If we suppose that G and Σ are diagonal on the basis $\{|i\rangle\}$ that diagonalizes the IP hamiltonian $\hat{h}$, we have

$$G_i(\omega) = \frac{1}{\omega - \varepsilon_i - \Sigma_i(\omega)}, \tag{2.115}$$

where $\varepsilon_i = h_{ii}$ and $\Sigma_i = \Sigma_{ii}$. Computing the spectral function in this basis using Eq. (2.32) gives

$$A_i(\omega) = \frac{1}{\pi} |\operatorname{Im}\{G_i(\omega)\}| = \frac{1}{\pi} \frac{|\operatorname{Im}\{\Sigma_i(\omega)\}|}{(\omega - \varepsilon_i - \operatorname{Re}\{\Sigma_i(\omega)\})^2 + (\operatorname{Im}\{\Sigma_i(\omega)\})^2}. \tag{2.116}$$

This expression presents well-defined peaks in frequency regions close to the IP eigenvalues ε_i where Σ is smooth. This is typically true at energies near the chemical potential in systems without strong correlations. We identify the energies at which these peaks are found as the QP energies. Structures due to the frequency dependence of $|\operatorname{Im}\{\Sigma(\omega)|\}$ shall be identified with satellite peaks instead.

We now expand Eq. (2.115) around a QP energy $\varepsilon_i^{\mathrm{QP}}$,

$$G_i(\omega) = \frac{1}{\omega - \varepsilon_i - [\Sigma_i(\varepsilon^{\mathrm{QP}}) + (\omega - \varepsilon_i^{\mathrm{QP}})(\partial\Sigma(\omega)/\partial\omega)\,|_{\omega=\varepsilon_i^{\mathrm{QP}}} + \ldots]} \approx \frac{Z_i}{\omega - \varepsilon_i^{\mathrm{QP}}}, \tag{2.117}$$

with

$$\varepsilon_i^{\mathrm{QP}} = \varepsilon_i + \Sigma_i(\varepsilon_i^{\mathrm{QP}}), \qquad \text{and} \tag{2.118}$$

$$Z_i = \left(1 - \frac{\partial\Sigma_i(\omega)}{\partial\omega}\right)^{-1} \Bigg|_{\omega=\varepsilon_i^{\mathrm{QP}}}. \tag{2.119}$$

The first is called the QP equation, the second is the definition of the renormalization factor Z_i; the difference $\varepsilon_i^{\mathrm{QP}} = \varepsilon_i$ is called the QP shift. The spectral function close to $\varepsilon_i^{\mathrm{QP}}$ is then

$$A_i(\omega) = \frac{1}{\pi} \frac{\left|\operatorname{Im}\left\{\varepsilon_i^{\mathrm{QP}} \operatorname{Re}\{Z_i\} + \left(\omega - \operatorname{Re}\left\{\varepsilon_i^{\mathrm{QP}}\right\}\right) \operatorname{Im}\{Z_i\}\right\}\right|}{\left(\omega - \operatorname{Re}\left\{\varepsilon_i^{\mathrm{QP}}\right\}\right)^2 + \left(\operatorname{Im}\left\{\varepsilon_i^{\mathrm{QP}}\right\}\right)^2}. \tag{2.120}$$

If $\left|\mathrm{Im}\left\{\varepsilon_i^{\mathrm{QP}}\right\}\right|$ is small, $A_i(\omega)$ has a sharp peak at $\mathrm{Re}\left\{\varepsilon_i^{\mathrm{QP}}\right\}$ whose broadening and height are determined by $\left|\mathrm{Im}\left\{\varepsilon_i^{\mathrm{QP}}\right\}\right|$ and $|\mathrm{Re}\{Z_i\}|$ respectively, while $\mathrm{Im}\{Z_i\}$ introduces an asymmetry. The renormalization factor Z_i quantifies how much the weight of the IP peak in the IP spectral function is reduced in going to the QP peak of the QP spectral function. The weight is lost to the satellite peaks so that the normalization of A is maintained according to Eq. (2.23). A sketch of the whole process of QP shifting and broadening is found in Figure 1.2. We note that in practical calculations, assuming a small QP shift, the expansion of Eq. (2.117) is often performed around ε_i instead of $\varepsilon_i^{\mathrm{QP}}$. Doing so, a linearized QP equation is obtained that reads

$$\varepsilon_i^{\mathrm{QP}} = \varepsilon_i + Z_i \Sigma_i(\varepsilon_i), \qquad Z_i = \left(\frac{\Sigma(\omega)}{\partial\omega}\right)^{-1}\Bigg|_{\omega=\varepsilon_i}. \tag{2.121}$$

2.1.7 Hedin's equations and the GW approximation

In order to obtain Hedin's equations, we turn some 4-point quantities of Section 2.1.7 into 2-point ones. By letting $1' \to 1^+$ and $2' \to 2^+$ in Eq. (2.102), we obtain the irreducible polarizability

$$P = -i\tilde{L}(11^+,22^+) = \frac{\delta\rho(1)}{\delta v_{\mathrm{tot}}(2)} \tag{2.122}$$

$$= -iL_0(11',\bar{3}'\bar{3})\tilde{\Gamma}(\bar{3}\bar{3}',2), \tag{2.123}$$

with the third equality coming from considering the analogous for $\tilde{\Gamma}$ of the first of Eqs. (2.99). In the same way, we get from Eq. (2.83) the reducible polarizability

$$\chi = -L(11^+,22^+) = \frac{\delta\rho(1)}{\delta v_{\mathrm{ext}}(2)} \tag{2.124}$$

$$= P(1,2) + P(1,\bar{3})v(\bar{3},\bar{3}')\chi(\bar{3}',2), \tag{2.125}$$

with the third equality being a Dyson equation that comes from considering the 2-point version of Eq. (2.105); we have also renamed u to v_{ext} to emphasize a change in the external potential only. χ appears in the definition of W, Eq. (2.110) so that it can be rewritten in terms of response functions,

$$W(1,2) = v(1,2) + v(1,\bar{3})\chi(\bar{3},\bar{3}')v(\bar{3}',2) \tag{2.126}$$

$$= v(1,2) + v(1,\bar{3})P(\bar{3},\bar{3}')W(\bar{3}',2), \tag{2.127}$$

with the second equality coming from the Dyson equation of χ, Eq. (2.125). We are now ready to give the set of equations that compose the iterative scheme based on the irreducible vertex $\tilde{\Gamma}$, as formulated by Hedin in his 1965 article [16]. From now on we shall drop the xc subscript from Σ_{xc}: Σ will always refer to the exchange-correlation self-energy. This implies that we are transferring the Hartree potential inside the independent-particle hamiltonian from which the initial G_0 is obtained. Such operation is easily achieved through the Dyson

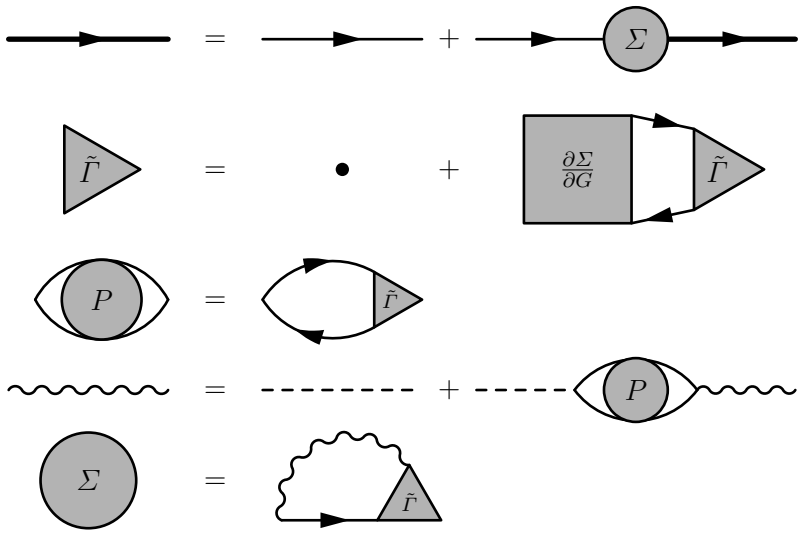

Figure 2.1. Diagrammatic depiction of Hedin's equations.

equation technology introduced in Section 2.1.2. Given this premise, Hedin's equations read

$$G(1,2) = G_0(1,2) + G_0(1,\bar{3})\Sigma(\bar{3},\bar{4})G(\bar{4},2), \tag{2.128}$$

$$\tilde{\Gamma}(1,2;3) = \delta(1,2)\delta(1,3) + \frac{\delta\Sigma(1,2)}{\delta G(\bar{4},\bar{5})}G(\bar{4},\bar{6})G(\bar{7},\bar{5})\tilde{\Gamma}(\bar{6},\bar{7};3), \tag{2.129}$$

$$P(1,2) = -iG(2,\bar{3})G(\bar{4},2)\tilde{\Gamma}(\bar{3},\bar{4};1), \tag{2.130}$$

$$W(1,2) = v(1,2) + v(1,\bar{3})P(\bar{3},\bar{4})W(\bar{4},2), \tag{2.131}$$

$$\Sigma(1,2) = iG(1,\bar{3})W(1^+,\bar{4})\tilde{\Gamma}(\bar{3},2;\bar{4}). \tag{2.132}$$

A diagrammatic depiction of Hedin's equations is given in Figure 2.1. Approximations in this scheme are cast as "vertex corrections", which means approximating the vertex function Γ (see e.g. Figure 1.4). As also seen in Section 2.1.5, the scheme is iterative: one way to proceed through it is, e.g. to make a guess for Σ and then solve the equations in order, then start again with the new Σ. This can quickly lead to very complicated expressions of Σ, or an abundance of diagrams in the Feynman diagram picture. Alternatively, one can keep the expression fixed for Σ and $\tilde{\Gamma}$ and simply seek a numerical self-consistency.

In this section we have found that the lead-up to Hedin's equations is heavily reliant on response functions. We mentioned in Section 2.1.5 that W is devised so as to already contain effects of the electrostatic screening due to the Hartree potential. In order to confirm this picture, we recall the definition of the dielectric function ϵ from Section 2.1.4: we notice that we can now identify it as

$$\epsilon(1,2) = \frac{\delta v_{\text{ext}}(1)}{\delta v_{\text{tot}}(2)} = \frac{\delta[v_{\text{tot}}(1) - v_H(1)]}{\delta v_{\text{ext}}(2)} = \delta(1,2) - v(1,\bar{3})P(\bar{3},2), \tag{2.133}$$

where we applied the definition of v_H, Eq. (2.82), and of P, Eq. (2.122). The Dyson equations of χ an d W can then be rewritten as

$$\chi(\mathbf{r},\mathbf{r}';\omega) = \int d\mathbf{r}_1 P(\mathbf{r},\mathbf{r}_1;\omega)\,\epsilon^{-1}(\mathbf{r}_1,\mathbf{r}';\omega). \tag{2.134}$$

$$W(\mathbf{r},\mathbf{r}';\omega) = \int d\mathbf{r}_1 \left[I - vP(\omega)\right]^{-1}_{|\mathbf{r}\mathbf{r}_1} v(\mathbf{r}_1,\mathbf{r}'), \tag{2.135}$$

unveiling the meaning of W: it is the screened interaction between an external charge with a charge of the system, with the screening due to the polarization of the system induced by the external charge itself. Not considering the response in terms of polarization of the system would mean to use v instead of W, or equivalently to retain only δv_{ext} in Eq. (2.73). Coherently, the charge fluctuations implied by a polarization of the density happen to be described by the electron-hole propagator L_{eh}, which happens to enter χ, and consequently W, due to the time constraints imposed on L in Eq. (2.124); in fact, these coincide to those of Eq. (2.49).

Of course, the response of a classical system may simply include density polarization under some circumstances, but a quantum one also experiences exchange-correlation effects: these are the content of P, which indeed enters the Dyson equation of χ, and are governed by the physics included in the vertex $\tilde{\Gamma}$. Furthermore, in photoemission spectroscopy we want to describe charged excitation states where an electron or a hole are found propagating *inside* the system; meanwhile, linear response accounts only for *external* perturbations of the system, or equivalently, for its interactions with with external test charges. Consequently, the vertex $\tilde{\Gamma}$ appears in the self-energy Σ in order to account for the exchange-correlation effects felt by a particle belonging to the system, in agreement with the interpretation of the self-energy as the potential experienced by a particle inside the system. We can then conclude that W describes the interaction of an external particle with *the whole* system, whereas the more involved object $\tilde{\Gamma}W$ describes the interaction between a particle belonging to the system and *the remainder* of the system.

The GW approximation consists in ignoring the exchange-correlation effects contained in the vertex. This means approximating Eq. (2.129) to

$$\Gamma^{\text{GW}}(1,2;3) = \delta(1,3)\delta(2,3), \tag{2.136}$$

with the self-energy and the irreducible polarization propagator respectively becoming:

$$\Sigma^{\text{GW}}(1,2) = iG(1,2)W(1^+,2), \tag{2.137}$$

$$P^{\text{RPA}}(1,2) = -iG(1,2)G(2,1^+), \tag{2.138}$$

$$W^{\text{RPA}}(1,2) = v(1,2) - iv(1,\bar{3})G(\bar{3},\bar{4})G(\bar{4},\bar{3})W(\bar{4},2). \tag{2.139}$$

See Figures 1.3 and 2.2 for a diagrammatic depiction. The response function in the GW approximation is said to be in the random-phase approximation (RPA) and, as implied by the preceding discussion of this section, it only describes perturbations involving density polarization. These in turn imply perturbations of the Hartree potential, so the response can equivalently be called a time-dependent Hartree response. P^{RPA} corresponds to the *independent-particle polarizability*, also denoted as χ_0. Neglecting the vertex in the self-energy implies that a particle propagating in the system interacts with the system as if it

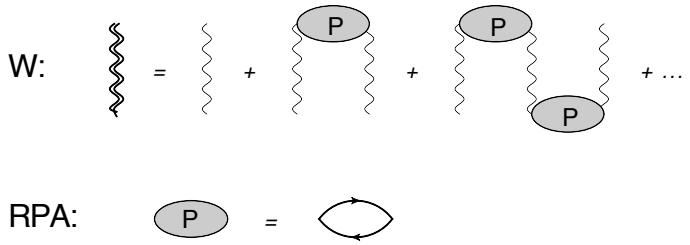

Figure 2.2. Graphical representation of the Dyson equation for W and of the RPA approximation to the irreducible polarizability P.

were an external particle; therefore, the particle also interacts with itself, giving rise to the so-called self-screening error of the GW approximation.

Although there is no non-trivial vertex, which would generate new Feynman diagrams at each cycle, iterating through Hedin's scheme in the GW approximation can still be challenging due to the handling of the spectral representations, like those seen in Sections 2.1.1 and 2.1.3, of G, Σ and W: these are complicated by the emergence of satellites beyond the independent-particle picture, and by the need to describe unbound continua. Therefore, only one iteration is often performed starting from an independent-particle solution, to which corresponds a G_0 that can be easily built using the Lehmann representation: this results in a "one-shot" scheme; alternatively, partially self-consistent schemes are devised, in which G is the only self-consistent quantity, often without even updating its Lehmann amplitudes (remaining therefore single-particle eigenfunctions) but only the eigenvalues. A possible starting point for one-shot calculations is given by the Hartree-Fock method, which we will see in Section 2.1.8; another very popular one is given by Kohn-Sham density functional theory, to which the whole of Section 2.2 is devoted.

To conclude this section we take a peek at a vertex correction to the GW self-energy. If we plug the GW self-energy into the vertex equation, Eq. (2.129), we find that we need to compute the functional derivative

$$\frac{\delta\Sigma^{\mathrm{GW}}(1,2)}{\delta G(4,5)} = iW(1,2)\delta(1,4)\delta(2,5) + G(1,2)\frac{\delta W(1,2)}{\delta G(4,5)}. \tag{2.140}$$

Inserting it into the vertex equation gives us

$$\Gamma(12,3) = \delta(1,2)\delta(1,3) + iW(1,2)G(1,3)G(3,2) + \dots, \tag{2.141}$$

which we shall term this vertex the time-dependent GW (TDGW) vertex. Retaining only the first order in W and plugging the result into the self-energy equation, Eq. (2.132), yields a beyond-GW self-energy contribution of second order in W, which we shall call the second-order TDGW (SO-TDGW) self-energy. It is given by

$$\Sigma^{\mathrm{SO-TDGW}}(1,2) = -G(1,\bar{3})W(\bar{4},1)W(\bar{3},2)G(\bar{3},\bar{4})G(\bar{4},2), \tag{2.142}$$

and its diagrammatic representation can be found in the bottom left of Figure 1.5.

2.1.8 The Hartree-Fock method

The Hartree-Fock (HF) method will provide us with starting points for one-shot calculations in the GW approximation and beyond. We introduce it here briefly as a trivial case within the MBPT formalism, while the specialized literature will have to be consulted for a more in-depth discussion [6–8].

The HF approximation corresponds to replacing W with the bare v in Eq. (2.132). Alternatively, one could have replaced L with the uncorrelated electron-hole propagator L_0 in Eq. (2.81), or could have considered the trivial case for Γ in the $Gv\Gamma$ self-energy expansion of Section 2.1.5 (as is done to obtain GW from $\tilde{\Gamma}$). Doing so causes G to become the density matrix and Σ to become static overall. Therefore, we obtain the exchange self-energy

$$\Sigma^x(1,2) = iv(1,2)G(1,2^+) = -v(\mathbf{r}_1,\mathbf{r}_2)\rho(\mathbf{r}_1,\mathbf{r}_2)_{\sigma_1}\delta_{\sigma_1\sigma_2}\delta(t_1-t_2) \tag{2.143}$$

This potential can be readily absorbed in the independent-particle hamiltonian $\hat{h}$, which becomes spatially non-local, from which G_0 is obtained. We recall that the Hartree potential v_H already resides in $\hat{h}$ from the assumptions of Section 2.1.7. The HF hamiltonian then reads

$$\hat{h} = \hat{t} + \hat{v}_{\text{ext}} + \hat{v}_H + \hat{\Sigma}^x, \tag{2.144}$$

with $\hat{t}$ being the single-particle kinetic operator. From this, the HF equations are obtained,

$$\left[-\frac{\nabla^2_{\mathbf{r}}}{2} + v_{\text{ext}}(\mathbf{r}) + v_{\text{H}}(\mathbf{r})\right]\psi_{i\sigma}(\mathbf{r}) + \int \mathrm{d}\mathbf{r}'\, \Sigma^x_\sigma(\mathbf{r},\mathbf{r}')\psi_{i\sigma}(\mathbf{r}') = \varepsilon_{i\sigma}\psi_{i\sigma}(\mathbf{r}), \tag{2.145}$$

where we made the spin degree of freedom explicit to remark that the exchange interaction is only between particles having the same spin, due the density matrix being contained in Σ^x. By expanding the density (inside v_H) and the density matrix (inside Σ^x) in the equation for the i-th orbital as sums over orbitals, one can see that the i-th addenda of the two summations cancel out. This means that HF is a self-interaction-free method. This cancellation is not by chance: it would not occur without the presence of the Fock contribution Σ^x balancing the Hartree potential v_H, as in the Hartree method. In the traditional derivation of the HF equations via the variational principle [175], the emergence of Σ^x is a consequence of antisymmetrizing the ansatz for the wavefunction, by means of packing occupied single-particle orbital products into a Slater determinant. Such antisymmetrization ensures that the fermionic nature of electrons is respected. Self-interaction (or self-screening, as in GW) errors can therefore be attributed to a lack of electron fermionicity in the underlying theories describing electron interactions.

In Hartree-Fock, quasi-particles are understood as electrons dragging a positive exchange hole, due to the fact that the exchange interaction tends to keep electrons away from each other. This implies that their Coulomb repulsion gets lowered, which translates to a lower energy of the system: the exchange potential carries, in fact, a minus sign.

2.2 Density functional theory

Density functional theory (DFT) is one of the greatest successes of condensed matter physics in predicting ground state properties of systems. It is much more computationally feasible than MBPT, but less insightful. It is a ground state theory, and even its exact formulation guarantees the exactness of only the electronic density and the total energy. In the context of this thesis, the Kohn-Sham (KS) formulation of DFT provides a good amount of the starting points used in one-shot calculations involving Green's functions. Furthermore, the Sham-Schlüter equation is explored in this thesis, which connects the MBPT and the KS-DFT frameworks. In this Section I shall therefore present the fundamentals of KS-DFT.

2.2.1 Kohn-Sham DFT

DFT rests upon the Hohenberg-Kohn (HK) theorems [11], stating that to a given ground state density there corresponds one and only one potential. As a consequence, the ground state energy E is uniquely determined by the ground state density ρ, i.e. E is a functional of ρ:

$$\begin{aligned} E[\rho(\mathbf{r})] &= \langle\psi|T + U + v_{\text{ext}}|\psi\rangle \\ &= \langle\psi|T + U|\psi\rangle + \langle\psi|v_{\text{ext}}|\psi\rangle \\ &= F[\rho(\mathbf{r})] + \int \rho(\mathbf{r}) v_{\text{ext}}(\mathbf{r}) d\mathbf{r}, \end{aligned} \tag{2.146}$$

with T the kinetic energy operator and U the electron-electron Coulomb potential operator. The problem with this formulation is that it contains a universal unknown functional F arising from the kinetic energy T and the electron-electron interaction energy U operators.

The Kohn-Sham (KS) [12] formulation of DFT partially fixes the issue by mapping the present problem to another involving non-interacting particles. This is done by using a single-particle potential, the KS potential v_{KS}, which defines a single-particle KS hamiltonian that should yield the same ground-state density as that given by the many-body hamiltonian[1]. The KS hamiltonian, applied to a single reference Slater determinant, results in Schrödinger equations for the KS single-particle orbitals and eigenvalues, φ_i and ε_i respectively,

$$\left(-\frac{\nabla^2}{2m} + v_{\text{KS}}(\mathbf{r})\right) \varphi_i(\mathbf{r}) = \varepsilon_i \varphi_i(\mathbf{r}), \tag{2.147}$$

in a similar fashion to HF, with v_{KS} however being spatially local. These equations obey a variational principle, i.e. they can be found by a minimization of the total energy with respect to the non-interacting ground state wave functions, with the constraint of being orthonormal. In practice one defines

$$E' = E - \sum_{ij} \lambda_{ij} \left(\int \mathrm{d}\mathbf{r}\, \varphi_i^*(\mathbf{r}) \varphi_j(\mathbf{r}) - \delta_{ij} \right), \tag{2.148}$$

[1] There is a problem of representability of the exact density by the single-particle potential v_{KS} that is not discussed here.

where the Lagrange multipliers λ_{ij} were introduced, and then minimizes with respect to the density,

$$\frac{\delta E'}{\delta \varphi^*(\mathbf{r})} = \frac{\delta E'}{\delta \varphi(\mathbf{r})} = 0. \tag{2.149}$$

Since the KS orbitals also must give the density of the system, i.e.

$$\rho(\mathbf{r}) = \sum_i |\varphi_i(\mathbf{r})|^2, \tag{2.150}$$

through the chain rule one can recast the functional derivatives with respect to the KS orbitals φ as derivatives with respect to the density ρ when needed. By properly identifying each contribution of the total energy E, one in the end obtains the KS equations, with the KS potential being

$$v_{\mathrm{KS}} = v_H(\mathbf{r}) + v_{\mathrm{xc}}(\mathbf{r}) + v_{\mathrm{ext}}(\mathbf{r}), \tag{2.151}$$

where v_H is the Hartree potential. The Lagrange multipliers end up being the KS eigenvalues. All the ignorance about the problem has been transferred to the so-called exchange and correlation (xc) potential v_{xc}. Along with all the other addenda that make up v_{KS}, v_{xc} comes from a functional derivative of a contribution of the total energy,

$$v_{\mathrm{xc}}(\mathbf{r}) = \frac{\delta E'[\rho]}{\delta \rho(\mathbf{r})}, \tag{2.152}$$

the so-called *xc energy functional*, which, along with the whole total energy E, must be a functional of the density by the HK theorem. This functional is where the approximations of the KS scheme are made. We will see a few of them in the next Section.

One may wonder if the KS eigenvalues bear any physical significance, in particular as addition and removal energies. This turns out to be limited: Janak's theorem [176] guarantees that the negative of the KS HOMO coincides with the ionization energy of the system. Conversely, the LUMO suffers from the lack of the so-called derivative discontinuity in the most common approximations of the xc functional, and therefore cannot be regarded as an addition energy [31–33, 119, 129]. This results in the famous band gap problem of KS-DFT, which is usually corrected by means of MBPT. As for the KS energies deeper than the HOMO, there is no rigorous interpretation of these as removal energies, although arguments have been made in order to regard them as such, at least approximately[177, 178].

2.2.2 Exchange-correlation functionals

The local density approximation (LDA) to E_{xc} relies on the xc energy density $\epsilon_{\mathrm{xc}}^{\mathrm{HEG}}$ of the homogeneous electron gas (HEG) in order to provide an estimate of the exchange-correlation energy density of the system in each point of space. In particular, $\epsilon_{\mathrm{xc}}^{\mathrm{HEG}}[\rho(\mathbf{r})]$ attains in each point $\mathbf{r}$ of space the same value it would have in the HEG. Therefore, the exchange-correlation energy E_{xc} reads:

$$E_{\mathrm{xc}}[\rho] = \int d\mathbf{r}\, \epsilon_{\mathrm{xc}}^{\mathrm{HEG}}[\rho(\mathbf{r})]\rho(\mathbf{r}). \tag{2.153}$$

The HEG exchange energy is known analytically, but the correlation one is not. Quantum Monte Carlo calculations [179] allowed for the accurate parametrization of the dependence

on the density [117]. Despite its simplistic picture and a number of known issues, the LDA is one of the most successful approximations to the exchange-correlation potential in DFT.

Having a strictly local dependence of the potential on the density is the major and most evident problem with the LDA, and leads to the overestimation of cohesive energies and bond strengths in molecules and solids. Such problems can be overcome by introducing gradient corrections: the potential is made locally dependent on both the density and its gradient, by introducing an enhancement factor F_{xc} multiplying the HEG results:

$$E_{\mathrm{xc}}[\rho] = \int d\mathbf{r}\, \rho(\mathbf{r})\, \epsilon_{\mathrm{x}}[\rho(\mathbf{r})] \cdot F_{\mathrm{xc}}(\rho(\mathbf{r}), |\nabla\rho(\mathbf{r})|). \tag{2.154}$$

The "generalized gradient approximation" (GGA) generation of functionals has provided the most viable option for overcoming the problems that the LDA encounters with bonding and structural properties. Both the LDA and the Perdew-Burke-Ernzerhof (PBE) [180] xc functional of the GGA family have been used in the work of this thesis for the calculation of starting points.

Another class of functionals that bears relevance for the present work is that of hybrid functionals [181–183]. These are obtained by incorporating a fraction of the Fock exchange energy E^{F} into the E_{xc}, and require a generalization of the KS scheme. In fact, the Fock energy functional is dependent on the density matrix, and not simply on the density. Applying this recipe to the PBE xc functional yields

$$E_{\mathrm{xc}} = \alpha E_x^{\mathrm{F}} + (1-\alpha)E_x^{\mathrm{PBE}} + E_c^{\mathrm{PBE}}, \qquad \alpha \in [0,1], \tag{2.155}$$

with E_x and E_c being exchange and correlation functionals respectively. The parameter α is often tuned to 0.25, yielding the PBE0 hybrid functional[184].

Incorporating a fraction of the Fock energy functional translates to having a fraction of non-local Fock exchange in the xc potential, making the whole KS potential non-local itself. Thanks to this addition, the KS energies reproduce more accurately the removal energies of molecules and finite systems. Solving the KS equations in the approximation given by the PBE0 hybrid functional will yield yet another starting point of the present work.

2.2.3 Time-dependent DFT

In time-dependent density functional theory (TDDFT), the uniqueness of the HK theorems is extended to systems subject to a time-dependent external potential $v_{\mathrm{ext}}(\mathbf{r},t)$. Such extension was formally put in quite general terms by Runge and Gross [185]. The Runge-Gross theorem states that densities $\rho(\mathbf{r},t)$ and $\rho'(\mathbf{r},t)$ evolving from a common initial state $\psi(t=0)$ under the influence of two potentials $v_{\mathrm{ext}}(\mathbf{r},t)$ and $v'_{\mathrm{ext}}(\mathbf{r},t)$ (both Taylor expandable about initial time 0) eventually differ if the potentials differ by more than a purely time-dependent function:

$$\delta v_{\mathrm{ext}}(\mathbf{r},t) = v_{\mathrm{ext}}(\mathbf{r},t) - v'_{\mathrm{ext}}(\mathbf{r},t) \neq c(t). \tag{2.156}$$

Once again, there is a one-to-one mapping between densities and potentials, i.e. the potential is a functional of the density, and, once again, an auxiliary system of non-interacting electrons can be defined, whose wave functions obey the equations

$$i\frac{\partial\phi_i(\mathbf{r},t)}{\partial t} = \left[-\frac{\nabla^2}{2} + v_{\mathrm{KS}}(\mathbf{r},t)\right]\varphi_i(\mathbf{r},t). \tag{2.157}$$

Like in KS-DFT, these equations could be in principle obtained by optimizing an action functional of the time-dependent density. The density obtained from the wave functions is exact and reads

$$\rho(\mathbf{r},t) = \sum_i |\varphi_i(\mathbf{r},t)|^2, \tag{2.158}$$

in analogy with the KS system.

The TDDFT framework is particularly helpful to compute excitations of the system through equations for the response function analogous to those of MBPT. By introducing the irreducible polarizability of the KS effective system, $P_{\mathrm{KS}}(1,2) = \frac{\delta\rho(1)}{\delta v_{\mathrm{KS}}(2)}$, one has

$$\begin{aligned} \chi &= P^{\mathrm{KS}} + P^{\mathrm{KS}} v\chi, \\ &= \chi_0^{\mathrm{KS}} + \chi_0^{\mathrm{KS}}[v + f_{\mathrm{xc}}]\chi, \end{aligned} \tag{2.159}$$

with the *xc kernel* being

$$f_{\mathrm{xc}}(1,2) = \frac{\delta v_{\mathrm{xc}}(1)}{\delta\rho(2)} = \frac{\delta^2 E_{\mathrm{xc}}}{\delta\rho(1)\,\delta\rho(2)}. \tag{2.160}$$

A common approximation to the f_{xc} kernel is obtained via the adiabatic local density approximation (ALDA), which amounts to using the LDA functional in the f_{xc} formula and making the time-dependence instantaneous, i.e. not dependent on previous states of the density. We also remark that all the above TDDFT equations admit a static counterpart, obtained by taking $\omega = 0$ in frequency space, which is properly framed within ordinary DFT.

2.3 The KS-DFT Sham-Schlüter equation

Both MBPT and KS-DFT are capable of yielding the exact ground-state electron density of a system, provided that the exact self-energy Σ and the exact xc potential $v_{\rm xc}$ are used for computing the interacting G and the $G^{\rm KS}$ of the KS system. By applying to both G and $G^{\rm KS}$ the linear density operator $\int \frac{d\omega}{2\pi i} e^{i\omega 0^+} \bullet\cdot$ and equating the results, one gets

$$\begin{aligned} 0 &= \rho(\mathbf{r}) - \rho^{\rm KS}(\mathbf{r}) \\ &= \sum_\sigma \frac{1}{2\pi i} \int d\omega e^{i\omega 0^+} [G_{\sigma\sigma}(\mathbf{r},\mathbf{r};\omega) - G^{\rm KS}_{\sigma\sigma}(\mathbf{r},\mathbf{r};\omega)], \end{aligned} \tag{2.161}$$

which, by usage of the Dyson equation connecting the KS system to the interacting system, can be rewritten as

$$\begin{aligned} &\int \frac{d\omega}{2\pi i} \int d\mathbf{r}_1\, G^{\rm KS}(\mathbf{r},\mathbf{r}_1,\omega) G(\mathbf{r}_1,\mathbf{r},\omega)\, v_{\rm xc}(\mathbf{r}_1) \\ &= \int \frac{d\omega}{2\pi i} \int d\mathbf{r}_1 d\mathbf{r}_2\, G^{\rm KS}(\mathbf{r},\mathbf{r}_1,\omega) \Sigma(\mathbf{r}_1,\mathbf{r}_2,\omega;[G]) G(\mathbf{r}_2,\mathbf{r},\omega), \end{aligned}$$

which is known as the Sham-Schlüter equation (SSE) [119]. The density condition employed for deriving it implies that $G^{\rm KS}$ produces the same density as G. The equation is in the form $Ax = b$, and can be solved as a linear system in the unknown x, which is the xc potential $v_{\rm xc}(\mathbf{r})$. Since the unknown itself is needed to compute $G^{\rm KS}$, which enters the kernel A and the inhomogeneous term b, the problem must, in general, be solved iteratively. Most often it is linearized by performing the substitution $G \to G^{\rm KS}$, which amounts to retaining the lowest order in $G^{\rm KS}$ in Eq. (3.83). By doing so one obtains the linearized Sham-Schlüter equation (LSSE):

$$\int d\mathbf{r}_1\, \chi_0^{\rm KS}(\mathbf{r},\mathbf{r}_1)\, v_{\rm xc}(\mathbf{r}_1) = \int \frac{d\omega}{2\pi i} \int d\mathbf{r}_1 d\mathbf{r}_2\, G^{\rm KS}(\mathbf{r},\mathbf{r}_1,\omega)\, \Sigma(\mathbf{r}_1,\mathbf{r}_2,\omega;[G^{\rm KS}])\, G^{\rm KS}(\mathbf{r}_2,\mathbf{r},\omega), \tag{2.162}$$

where $\chi_0^{\rm KS}$ is the KS independent-particle static polarizability. We refer to this approximation as the linearized Sham-Schlüter equation (LSSE). We emphasize that the dependence $\Sigma = \Sigma[G]$ in the full SSE implies that the full Dyson equation for G, Eq. (2.128), is obeyed self-consistently, while this is not the case for the LSSE, where $\Sigma = \Sigma[G^{\rm KS}]$ and there is no reference to G any longer. This implies that the density condition used to derive the SSE no longer holds exactly, and it has to be verified how close the densities produced by the fully self-consistent G and by the LSSE-self-consistent $G^{\rm KS}$ are. The KS scheme differs significantly from the MBPT scheme, in that it does not account for frequency dependence and is affected by the KS gap problem[31–33]. Nonetheless, one iteration of the Dyson equation is expected to preserve the density of $G^{\rm KS}$ as obtained from the self-consistent LSSE[122, 126, 127]. Alternatively, the LSSE can also be derived via an optimized effective potential (OEP) strategy starting from total energy functionals [122, 123, 125]. In the framework of MBPT, it is possible to build total energy functionals that depend directly on the Green's function [186, 187]. In this case, the LSSE can be obtained [122, 188] by minimizing the Klein functional with the constraint that the Geen's function be given by a static and spatially local potential. The Klein functional reads [13, 187, 189–191]

$$\begin{aligned} E^{\rm K}[G] &= E_{\rm H}[G] + \Phi_{\rm xc}[G] \\ &\quad + {\rm Tr}_\omega \left\{ I - G_0^{-1} G + \ln\left(G_0^{-1} G\right) \right\} + {\rm Tr}_\omega\{H_0 G_0\}, \end{aligned} \tag{2.163}$$

and its (unconstrained) optimization implies the Dyson equation to be obeyed self-consistently at stationarity. In this expression $\mathrm{Tr}_\omega\{\}$ stands for $\int \frac{d\omega}{2\pi i} e^{i\omega 0^+} \mathrm{Tr}\{\}$, E_H is the Hartree energy, G_0 the free-particle Green's function corresponding to $H_0 = T + v_\mathrm{ext}$. The $\Phi_\mathrm{xc}[G]$ functional, which carries electron interaction contributions beyond Hartree, is also related to the self-energy by:

$$\frac{1}{2\pi i}\Sigma(\omega) = \frac{\delta\Phi_\mathrm{xc}[G]}{\delta G(\omega)}. \tag{2.164}$$

Constraining the Klein functional to Green's functions G_s obtained from a static and spatially local potential $v_s(\mathbf{r})$ yields

$$E^\mathrm{K}[v_s] = T_s[\rho] + \int v_\mathrm{ext}\rho + E_\mathrm{H}[G_s] + \Phi_\mathrm{xc}[G_s], \tag{2.165}$$

where T_s is the kinetic energy of non-interacting particles (subject to a local potential) of density ρ. Imposing the variational condition $\frac{\delta E^\mathrm{K}[v_s]}{\delta v_s(\mathbf{r})} = 0$ yields

$$v_s(\mathbf{r}) = v_\mathrm{ext}(\mathbf{r}) + v_\mathrm{H}(\mathbf{r}) + v_\mathrm{xc}^\mathrm{oep}(\mathbf{r}), \tag{2.166}$$

where $v_\mathrm{xc}^\mathrm{oep}(\mathbf{r})$ is obtained as the solution of the LSSE, Eq. (2.162). Importantly, as in the unconstrained optimization, the self-energy in the LSSE/OEP case is obtained from the Φ functional via Eq. (2.164). Nevertheless, Σ is no longer a functional of G but rather of G^KS [see Eqs. (2.162) and (2.162)].

Chapter 3

Low-order self-energies: 2B, GW, GW+SOSEX

In this Chapter I will firstly present the specialized implementation of the GW, 2B and GW+SOSEX self-energies for spherical atoms. Secondly, I will assess the accuracy of the vertex corrections in the prediction of the ionization energies of the spherical atom test set.

3.1 Self-energies of interest

In this Section we will introduce the self-energies that will be benchmarked using spherical atoms as a test set. First we will consider GW and give some expressions for it in frequency space. Then we will introduce the time-dependent Hartree-Fock (TDHF) vertex $\tilde{\Gamma}^{\mathrm{TDHF}}$

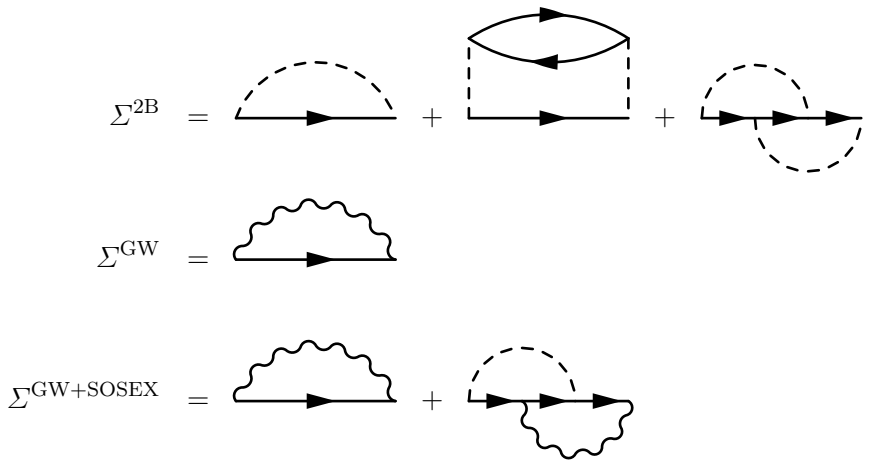

Figure 3.1. Self-energy diagrams benchmarked in this work. Solid lines represent the fermion propagators, dashed lines the bare Coulomb interaction, wiggly lines the dressed Coulomb interaction.

and will replace it in the self-energy equation, Eq. (2.132). By performing two different truncations of the expansion given by the vertex, we will obtain two self-energies: 2nd-Born (2B) and GW+second-order screened exchange (GW+SOSEX). A depiction of these self-energies is given in Figure 3.1. Expressions in frequency space for these will be given for these as well.

3.1.1 The GW self-energy

We begin by considering GW and rewrite here the equation of the self-energy,

$$\Sigma^{\mathrm{GW}}(1,2) = iG(1,2)W(1^+,2), \tag{2.137}$$

and Fourier transform it to obtain

$$\Sigma^{\mathrm{GW}}(\mathbf{r},\mathbf{r}',\omega) = -\int \frac{\mathrm{d}\omega'}{2\pi i} e^{i\eta\omega'} G(\mathbf{r},\mathbf{r}',\omega+\omega')W(\mathbf{r},\mathbf{r}',\omega'). \tag{3.1}$$

The screened interaction W is in the RPA, and is obtained from Eqs. (2.138) and Eq. (2.131). An expression in frequency space of these will be given in Section 3.3. When we turn the screening off, $W \to v$, and $\Sigma^{\mathrm{GW}} \to \Sigma^x$. It is then customary to split the Coulomb interaction as the sum of the bare interaction v plus the polarization contribution W^p, namely $W = v + W^p$. Therefore, the frequency-dependent part of Σ is the correlation self-energy Σ_c, defined as

$$\Sigma_c = \Sigma - \Sigma^x, \tag{3.2}$$

which is simply $\Sigma_c = iGW^p$ in the case of GW. We can obtain a spectral representation of Σ_c^{GW} by writing G and W in a Lehmann form, and then perform the frequency integrals by closing a contour in the complex plane with the application of Jordan's lemma. The Lehmann form of G is given by Eq. (2.29), whereas the one for W can be obtained from the Lehmann form of L_{eh}, Eq. (2.56), after plugging it into the expressions of χ and W, Eqs. (2.124) and (2.126) respectively. We obtain

$$W^p(\mathbf{r}\mathbf{r}',\omega) = \sum_s \frac{2\Omega_s V_s(\mathbf{r})V_s^*(\mathbf{r}')}{\omega^2 - (\Omega_s - i\eta)^2}, \tag{3.3}$$

with $V_s(\mathbf{r}) = \int \mathrm{d}\mathbf{r}'\, v(\mathbf{r},\mathbf{r}')f_{0s}^{eh}(\mathbf{r},\mathbf{r}')$ being the so-called *fluctuation amplitudes*, and $\Omega_s = E_s^N - E_0$ the neutral excitation energies. We recall that the f_{0s}^{eh} amplitudes are defined in Eq. (2.57). Performing now the frequency integral of Eq. (3.1) gives

$$\Sigma_c^{\mathrm{GW}}(\mathbf{r}\mathbf{r}',\omega) = \sum_{\lambda,s} \frac{f_\lambda(\mathbf{r})V_s(\mathbf{r})\, f_\lambda^*(\mathbf{r}')V_s^*(\mathbf{r}')}{\omega + (\Omega_s - i\eta)\mathrm{sgn}(\mu - \varepsilon_\lambda) - \varepsilon_\lambda}. \tag{3.4}$$

In one-shot approaches the Lehmann form of G is easily found using an independent-particle starting point, whereas the Lehmann form of W requires solving the Dyson equation (2.131): this is most easily done on a frequency grid, however doing so does not directly yield Ω_s and V_s. For them to be obtained, the problem can be recast into that of diagonalizing an excitonic hamiltonian, which we shall do when studying the full TDHF vertex in Chapter 4. For the assessment of this chapter we will rather use the less numerically demanding contour deformation technique, which we will introduce in Section 3.4.2, and for which solving the Dyson equation for W on a frequency grid is sufficient.

3.1.2 The SOSEX self-energy

We now consider the TDHF vertex, which is obtained by plugging the Fock exchange self-energy Σ^x into the vertex equation, Eq. (2.129). The functional derivative reads

$$\frac{\delta\Sigma^x(1,2)}{\delta G(4,5)} = iv(1,2)\delta(1,4)\delta(2,5) \tag{3.5}$$

and the vertex equation becomes

$$\tilde{\Gamma}^{\mathrm{TDHF}}(12,3) = \delta(1,2)\delta(1,3) + iv(1,2)G(1,3)G(3,2) + \dots \tag{3.6}$$

A diagrammatic representation of the equation is found in Figure 1.4, at the top. Retaining only the first order contribution in v and replacing it into the self-energy equation yields the SOSEX self-energy,

$$\Sigma^{\mathrm{SOSEX}}(1,2) = -\int d34\, G(1,3)G(3,4)G(4,2)W(1,4)v(3,2). \tag{3.7}$$

The truncated vertex can be regarded as a GW+SOSEX vertex, and is represented in the bottom of Figure 1.4. Note that we have basically repeated the steps that led us to obtain the SO-TDGW self-energy in Section 2.1.7, by simply replacing W with v in the vertex equation. Notably, in this case the functional derivative $\delta\Sigma/\delta G$ does not contain a term of the kind $\delta W/\delta G$ due to the bare v not having a functional dependence on G.

Moving to frequency space, we get

$$\begin{aligned}\Sigma^{\mathrm{SOSEX}}(\mathbf{r},\mathbf{r}',\omega) = -\int \frac{d\omega_1}{2\pi i}\frac{d\omega_2}{2\pi i}\int d\mathbf{r}_3 d\mathbf{r}_4\, G(\mathbf{r},\mathbf{r}_3,\omega+\omega_1) \\ \times G(\mathbf{r}_3,\mathbf{r}_4,\omega_1+\omega_2)\, G(\mathbf{r}_4,\mathbf{r}',\omega_2) \\ \times W(\mathbf{r},\mathbf{r}_4,\omega_1)\, v(\mathbf{r}_3,\mathbf{r}'),\end{aligned} \tag{3.8}$$

Coherently with the one-shot scheme, we now suppose to be building the SOSEX self-energy using an independent-particle Green's function G_0. The independent-particle hamiltonian problem has the eigenvalues ε_β and the eigenfunctions φ_β as solutions. By replacing the Lehmann form of G_0 in Eq. (3.8), we can perform the ω_2 frequency integral and end up with

$$\begin{aligned}\Sigma^{\mathrm{SOSEX}}(\mathbf{r},\mathbf{r}',\omega) = -\int \frac{d\omega_1}{2\pi i}\sum_{\mu\nu\beta}\varphi_\beta(\mathbf{r})\varphi^*_\nu(\mathbf{r}')\langle\mu|W(\mathbf{r},\omega_1)|\nu\rangle\langle\beta|v(\mathbf{r}')|\mu\rangle \\ \times\frac{1}{\omega+\omega_1-\varepsilon_\beta+i\eta\mathrm{sgn}(\varepsilon_\beta-\mu)}I_{\mu\nu}(\omega_1),\end{aligned} \tag{3.9}$$

where

$$I_{\mu\nu}(\omega_1) = \frac{\theta_\mu\bar{\theta}_\nu}{\omega_1-(\varepsilon_\mu-\varepsilon_\nu-2i\eta)} - \frac{\bar{\theta}_\mu\theta_\nu}{\omega_1-(\varepsilon_\mu-\varepsilon_\nu+2i\eta)}. \tag{3.10}$$

Here $\theta_\beta = \theta(\mu-\varepsilon_\beta)$, $\bar{\theta}_\beta = 1-\theta_\beta$, and we also introduced a notation for partially saturated Coulomb integrals, which is explained in Appendix C. The form of Eq. (3.9) is suitable for the application of the contour deformation technique, as in GW.

We may also want to study the effect that $\tilde{\Gamma}^{\mathrm{TDHF}}$ has on the polarizability. Plugging the expansion to first order of this vertex into Eq. (2.130) gives a SOSEX contribution to the irreducible polarizability beyond the independent-particle one,

$$P^{\mathrm{SOSEX}}(1,2) = \int \mathrm{d}34 G(1,3)G(4,1)v(3,4)G(2,4)G(3,2). \tag{3.11}$$

Moving to frequency space, we get

$$\begin{aligned} P^{\mathrm{SOSEX}}(\mathbf{r},\mathbf{r}',\omega) = \int \frac{d\omega_1}{2\pi i}\frac{d\omega_2}{2\pi i} \int d\mathbf{r}_3 d\mathbf{r}_4\, v(\mathbf{r}_3,\mathbf{r}_4) \\ \times G(\mathbf{r},\mathbf{r}_3,\omega_1)G(\mathbf{r}_4,\mathbf{r},\omega+\omega_1) \\ \times G(\mathbf{r}_3,\mathbf{r}',\omega_2)G(\mathbf{r}',\mathbf{r}_4,\omega+\omega_2). \end{aligned} \tag{3.12}$$

We note that, by using a Lehmann form for the G's, it can be seen that in this expression poles of higher order appear. Our spectral representation by means of lorentzian functions ends up being spoiled by these higher-order poles. This is a general issue of truncating Dyson equations to finite order. Recipes to cure this issue exist for the Dyson equation of the self-energy [68]; alternatively, one may want to proceed by including the vertex to all orders in the polarizability, while retaining a finite-order expansion for the self-energy [50, 83]. For the current assessment, as has already been done by practitioners in the field [87, 91, 92], we will simply proceed by keeping the RPA W even with the SOSEX self-energy; in Chapter 4 we will also see what the effect is of including the whole TDHF W in the GW+SOSEX self-energy.

3.1.3 The 2B self-energy

We now truncate further the self-energy expansion obtained with the TDHF vertex. In particular, we truncate it to *second order* in the bare v. This means that, if we consider the whole GW+SOSEX self-energy, in the GW contribution we have to truncate W at the first RPA bubble, by replacing W with v in the RHS of Eq. (2.139); in the SOSEX contribution, Eq. (3.8), we directly replace W with v, since one v is already present.

From these replacements in the GW and in the SOSEX contributions, a direct 2B term (2Bd) and an exchange 2B term (2Bx) arise respectively. These read

$$\begin{aligned} \Sigma^{\mathrm{2Bd}}(1,2) &= \int d34\, G(1,2)v(1,3)G(3,4)G(4,3^+)v(4,2) \\ &= i\int d34\, G(1,2)v(1,3)P^{\mathrm{RPA}}(3,4)v(4,2), \end{aligned} \tag{3.13}$$

where we replaced the expression of P^{RPA}, Eq. (2.138); and

$$\Sigma^{\mathrm{2Bx}}(1,2) = -\int d34\, G(1,3)v(1,4)G(3,4)v(3,2)G(4,2). \tag{3.14}$$

Fourier transforming these expressions gives

$$\begin{aligned}\Sigma^{\mathrm{2Bd}}(\mathbf{r},\mathbf{r}',\omega) = &-\int \frac{d\omega_1}{2\pi i}\frac{d\omega_2}{2\pi i}\int d\mathbf{r}_3 d\mathbf{r}_4\, G(\mathbf{r},\mathbf{r}',\omega+\omega_1)\\ &\times G(\mathbf{r}_3,\mathbf{r}_4,\omega_1+\omega_2)\, G(\mathbf{r}_4,\mathbf{r}_3,\omega_2)\\ &\times v(\mathbf{r},\mathbf{r}_4)\, v(\mathbf{r}_3,\mathbf{r}'), \end{aligned} \tag{3.15}$$

$$\begin{aligned}= &-\int \frac{d\omega_1}{2\pi i}\int d\mathbf{r}_3 d\mathbf{r}_4\, G(\mathbf{r},\mathbf{r}',\omega+\omega_1)\\ &\times v(\mathbf{r},\mathbf{r}_4)\, P^{\mathrm{RPA}}(\mathbf{r}_3,\mathbf{r}_4,\omega_1)\, v(\mathbf{r}_3,\mathbf{r}'), \end{aligned} \tag{3.16}$$

$$\begin{aligned}\Sigma^{\mathrm{2Bx}}\mathbf{r},\mathbf{r}',\omega) = &\int \frac{d\omega_1}{2\pi i}\frac{d\omega_2}{2\pi i}\int d\mathbf{r}_3 d\mathbf{r}_4\, G(\mathbf{r},\mathbf{r}_3,\omega+\omega_1)\\ &\times G(\mathbf{r}_3,\mathbf{r}_4,\omega_1+\omega_2)\, G(\mathbf{r}_4,\mathbf{r}',\omega_2)\\ &\times v(\mathbf{r},\mathbf{r}_4)\, v(\mathbf{r}_3,\mathbf{r}'). \end{aligned} \tag{3.17}$$

By factoring out P^{RPA}, the similarity of Eq. (3.16) with Eq. (3.1) becomes apparent: the difference is that in 2B a single RPA bubble, instead of the whole RPA series as in GW, determines the screening. 2B is then characterized by the independent-particle screening. While this may not give an accurate description when charge polarization effects become important, the 2Bx term ensures the self-screening freedom of 2B (we will prove this in Chapter 5), a property that GW lacks. In a way, the GW+SOSEX self-energy tries to merge the best of both worlds, by incorporating both a self-screening correcting exchange diagram, and the RPA screened interaction W^{RPA}.

The calculation of the two 2B self-energy terms using, again, the solution of a non-interacting hamiltonian as a starting point can be easily performed, both analytically and numerically. This time, at variance with GW and SOSEX, all frequency integrals can be performed by closing a contour in the complex plane without the need for solving a Dyson equation for W, giving

$$\Sigma^{\mathrm{2Bd}}(\mathbf{r},\mathbf{r}',\omega) = \sum_{\mu\nu\beta}\langle\mu|v(\mathbf{r})|\nu\rangle\langle\nu|v(\mathbf{r}')|\mu\rangle\,\varphi_\beta(\mathbf{r})\varphi^*_\beta(\mathbf{r}')\, I_{\mu\nu\beta}(\omega), \tag{3.18}$$

$$\Sigma^{\mathrm{2Bx}}(\mathbf{r},\mathbf{r}',\omega) = -\sum_{\mu\nu\beta}\langle\mu|v(\mathbf{r})|\nu\rangle\langle\beta|v(\mathbf{r}')|\mu\rangle\,\varphi_\beta(\mathbf{r})\varphi^*_\nu(\mathbf{r}')\, I_{\mu\nu\beta}(\omega), \tag{3.19}$$

with

$$I_{\mu\nu\beta}(\omega) = \frac{\theta_\mu\bar{\theta}_\nu\bar{\theta}_\beta}{\omega+\varepsilon_\mu-\varepsilon_\nu-\varepsilon_\beta-3i\eta} + \frac{\bar{\theta}_\mu\theta_\nu\theta_\beta}{\omega+\varepsilon_\mu-\varepsilon_\nu-\varepsilon_\beta+3i\eta}.$$

Admittedly, the vertex corrections that we introduced in these Sections are not properly framed within Hedin's scheme. In fact, following Hedin's scheme rigorously entails an expansion in W, as seen in Section 2.1.7. The SOSEX self-energy may be more rigorously framed within a scheme based on a simultaneous expansion in orders of v and W. Such a scheme has not been devised by anyone yet [91], neither is it known whether it is possible or meaningful to do so. The 2B self-energy is instead perfectly framed within the $iGv\Gamma$ scheme seen in Section 2.1.5: as such, it should be regarded as a vertex correction to HF (corresponding to the trivial case of the reducible vertex Γ) rather than to GW (corresponding to the trivial case of the irreducible vertex $\tilde{\Gamma}$).

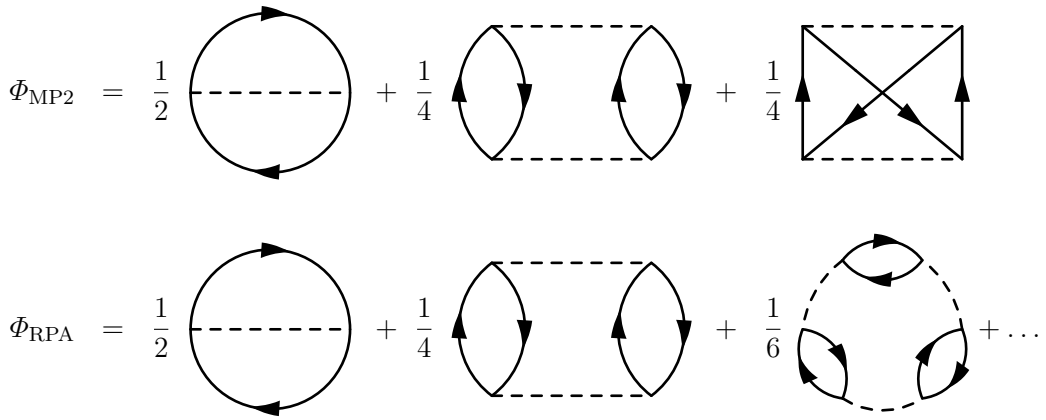

Figure 3.2. MP2 and RPA Φ functionals, from which the 2B and GW self-energies are obtained respectively upon differentiation with respect to the Green's function.

3.1.4 Φ-derivability

We conclude this introduction of the self-energies of interest by linking them to their respective total energy functionals, when available. Approximate KS-DFT total energies can be obtained via the constrained Klein functional by making approximations on the Φ functional [see Eq. (2.165)]. We remark that even with the exact Φ functional, the exact energy cannot be obtained as long as KS Green's functions are fed to the Klein functional (therefore making it the constrained Klein functional). An approximation on the Φ functional in turn entails an approximation on the self-energy [see Eq. (2.164)]. In particular, the Φ functional yielding the HF self-energy upon differentiation (first diagram of either line in Figure 3.2) leads to the exact-exchange (EXX) energy upon insertion in Eq. (2.165). Following this reasoning, the 2B self-energy corresponds to the MP2 energy (first line in Figure 3.2), and the GW self-energy corresponds to the RPA energy (second line in Figure 3.2). On the other hand, the GW+SOSEX self-energy (at least in the current formulation with W treated at the RPA level) is not Φ-derivable and is therefore not rigorously suitable for the variational argument presented in Sec. 2.3. The total energy expressions termed RPA+SOSEX introduced in the frameworks of coupled cluster theory [192] and of the adiabatic connection formula [193] are not formally linked to the GW+SOSEX self-energy. The LSSE treatment was applied to the GW+SOSEX self-energy anyway for benchmarking purposes.

For coherence with this picture and the literature, we adopt the following nomenclature: we will refer to the potential obtained from the HF self-energy through the solution of the LSSE as the EXX potential; the potential obtained from the 2B self-energy will be the MP2 potential, and the one obtained from the GW self-energy will be the RPA potential. On the other hand, the GW+SOSEX self-energy will simply correspond to the GW+SOSEX potential.

3.2 The spherical problem

We now proceed to present the technology based on spherical harmonics (SHs) that we will adopt to treat wavefunctions and operators in spherically symmetric potentials. Here we will give the basic definitions and representations for independent-particle (IP) hamiltonians that enter the self-consistent field (scf) procedure. In the following sections we will proceed to specialize response functions and self-energies to the spherical problem. The treatment of the former is necessary before turning to the latter, since the response function enters the self-energy formulation. We will not present into detail the spherical formulation of the scf procedure: this can be found in my Master's thesis [194].

In spherical polar coordinates, $\mathbf{r} = (r, \theta, \phi)$, an IP hamiltonian subject to a central potential v_0 reads

$$\hat{h}^0(\mathbf{r}) = \hat{t}(r, \theta, \phi) + v_0(r), \tag{3.20}$$

with $\hat{t}$ being the single-particle kinetic term. Hartree atomic units are assumed, i.e. $\hbar = e^2 = m = 1$. By letting $v_0(r) = -\frac{Ze^2}{r}$, with Z the atomic number, we recover the familiar case of the hydrogenic atom. It is well known [175] that in spherical polar coordinates the IP hamiltonian problem given by a central potential is separable into the sum of two addenda,

$$\hat{h}^0 = A(r) + \frac{\hat{L}^2(\theta, \phi)}{2}, \tag{3.21}$$

which depend on the radial and on the angular degrees of freedom respectively. In particular, from the kinetic term $\hat{T}$ comes $\hat{L}$, the angular momentum operator: its presence suggests that an ansatz should be made that incorporates its eigenfunctions, the SHs Y_{lm} (see Appendix A). In more abstract terms, we should say that the hamiltonian commutes with the angular momentum operator, and is therefore block diagonal in angular momentum space. Given this premise, the ansatz we seek looks like

$$\varphi_\alpha(\mathbf{r}) = \frac{1}{r} P_{nl,\sigma}(r) Y_{lm}(\theta, \phi), \qquad \alpha \equiv nlm, \sigma, \tag{3.22}$$

where α is a multi-index comprising the principal quantum number n, the orbital quantum number l, the magnetic quantum number m, and the spin quantum number σ. In the case of the hydrogenic atom, $P_{nl,\sigma}$ is a function containing Laguerre polynomials that has no actual dependence on the spin σ. Plugging this ansatz into $\hat{h}^0$ yields the equations

$$h^0(\mathbf{r}, \mathbf{r}') = \sum_{lm} Y_{lm}(\hat{\mathbf{r}}) \frac{1}{rr'} h_l^0(r, r') Y_{lm}^*(\hat{\mathbf{r}}'), \tag{3.23}$$

$$h_l^0(r, r') = r^2 h_l^0(r) \delta(r, r'), \tag{3.24}$$

$$h_l^0(r) = -\frac{1}{2r^2} \frac{\partial}{\partial r} \left(r^2 \frac{\partial}{\partial r} \bullet \right) + v_0(r) + \frac{l(l+1)}{2r^2}, \tag{3.25}$$

the latter becoming simply

$$\bar{h}_l^0(r) = -\frac{1}{2} \frac{\partial^2}{\partial r^2} + v_0(r) + \frac{l(l+1)}{2r^2} \tag{3.26}$$

when acting on the radial components $P_{nl,\sigma}$ of the radial wavefunctions. Eqs. (3.23—3.26) require the usage of the completeness of SHs,

$$\sum_{lm} Y_{lm}(\hat{\mathbf{r}}) Y_{lm}^*(\hat{\mathbf{r}}') = \delta(\hat{\mathbf{r}}, \hat{\mathbf{r}}'), \tag{A.18}$$

for them to be obtained. We note that the hamiltonian operators h_l^0 and $\bar{h}_l^0$ correctly end up being independent of the magnetic quantum number m, justifying a posteriori the ansatz R_{nl} not having a dependence on m.

As framed here, the IP particle problem per se in a given central potential v_0 is trivial to solve. However, implementing a scf procedure where v_0 is dependent on the electron density at each step (as in, say, KS-DFT) introduces complications. One way to keep the problem simple is to consider atoms whose subshells are at full or half filling (with each spin aligned following Hund's rule in the latter case). Equivalently, we may say these atoms have filled *orbital* subshells. In this hypothesis, if one computes the electron density of a given subshell (nl, σ), the result is

$$\begin{aligned}\rho_{nl,\sigma}(\mathbf{r}) = \sum_{m=-l}^{l} |\varphi_{nlm,\sigma}(\mathbf{r})|^2 &= \left|\frac{1}{r}P_{nl,\sigma}(r)\right|^2 \sum_{m=-l}^{l} |Y_{lm}(\theta,\phi)|^2 \\ &= \left|\frac{1}{r}P_{nl,\sigma}(r)\right|^2 \frac{2l+1}{4\pi},\end{aligned} \tag{3.27}$$

where we applied

$$\sum_{m=-l}^{l} Y_{lm}^*(\hat{\mathbf{r}}) Y_{lm}(\hat{\mathbf{r}}) = \frac{2l+1}{4\pi}. \tag{A.20}$$

Having complete occupation of the orbital subshell made it necessary to sum over the whole range from $-l$ to $+l$. If that had not been not the case, we would have obtained a subshell density dependent on the magnetic quantum numbers m of the occupied orbitals. This would have led us to take into account all the energetically equivalent electronic configurations having different sets of "occupied m's", leading to a degenerate reference state that ultimately would have made the treatment more complicated. With filled orbital subshells, we instead easily stick to a single reference state, characterized by a Slater determinant made up of the IP wavefunctions of Eq. (3.22). Eq. (3.27) shows that sphericity comes naturally from each subshell without a multireference treatment: therefore we shall informally call atoms with filled orbital subshells "spherical" (although spherically symmetric electron density is a property of all systems having an external central potential, including all atoms).

Up until this point, we have been considering an IP hamiltonian with a central *local* potential, which the KS hamiltonian of KS-DFT is. In the case of HF, however, the hamiltonian contains the *non-local* Fock exchange term Σ^x. Luckily, in spherical atoms the exchange term remains block-diagonal in angular momentum space, as a consequence of the density matrix also being so. Therefore, it admits a representation of the kind

$$\Sigma^x(\mathbf{r}, \mathbf{r}') = \sum_{lm} Y_{lm}(\hat{\mathbf{r}}) \frac{1}{rr'} \Sigma_l^x(r, r') Y_{lm}^*(\hat{\mathbf{r}}'). \tag{3.28}$$

which implies that Eq. (3.23) is still a good representation for the hamiltonian $\hat{h}^0$; one need only lift the locality constraint of Eq. (3.24). We can conclude that, even in the HF case, the single reference given by the wavefunctions of Eq. (3.22) is preserved at each iteration of the scf procedure. This is also proven in the Bransden and Joachain book [175], and an explicit expression of Σ_l^x is given in my Master's thesis [194].

The same procedure leading to a block-diagonal form of $\hat{h}_0$ and Σ^x indexed with l can be applied to other operators commuting with the rotations, including e.g. all local and central potentials, the one-body Green's function $G(\mathbf{r}, \mathbf{r}', \omega)$ and the corresponding self-energy $\Sigma(\mathbf{r}, \mathbf{r}', \omega)$. In fact, the Dyson equation assumes a rather intuitive block-diagonal form,

$$G_l(rr', \omega) = G_l^0(rr', \omega) + \int \mathrm{d}r_1 \, \mathrm{d}r_2 \, G_l^0(rr_1, \omega) \Sigma_l(r_1 r_2, \omega) G_l(r_2 r', \omega). \tag{3.29}$$

In general, any operator A that is block diagonal on angular momentum will be represented as

$$A(\mathbf{r}, \mathbf{r}') = \sum_{lm} Y_{lm}(\hat{\mathbf{r}}) \frac{1}{rr'} A_{lm}(r, r') \, Y_{lm}^*(\hat{\mathbf{r}}'). \tag{3.30}$$

Please note that, in the following, the radial matrix elements of most of the operators considered will not depend explicitly on m thanks to sphericity. A notable case is when the operator A is local and spherically symmetric, i.e.:

$$A(\mathbf{r}, \mathbf{r}') = A(r) \delta(\mathbf{r} - \mathbf{r}'). \tag{3.31}$$

In this case A_l is independent of l, as v_0 in Eqs. (3.23—3.26) already hinted at. In fact, by using the the representation of the δ function in spherical coordinates, $\delta(\mathbf{r} - \mathbf{r}') = \frac{1}{rr'} \delta(r - r') \delta(\hat{\mathbf{r}}, \hat{\mathbf{r}'})$, and Eq. (A.18), one can simplify the representation of the operator as follows:

$$A(\mathbf{r}, \mathbf{r}') = \frac{1}{r^2} A(r) \delta(r - r') \sum_{lm} Y_{lm}(\hat{\mathbf{r}}) Y_{lm}^*(\hat{\mathbf{r}}'). \tag{3.32}$$

The AGWX code, with which the results of this thesis were obtained, makes use of the SH technology presented in this section. The radial components of wavefunctions and operators are treated by it using a B-spline basis set, along with a Gauss-Legendre (GL) grid for radial space integrals. All the details can be found in Appendix B. Thus, when using the B-spline basis set $\{b_i\}$, the radial part of the wavefunctions is represented as

$$P_{nl,\sigma}(r) = \sum_i P_{nl,\sigma}^i b_i(r), \tag{3.33}$$

whereas the l-th component of an operator A will be

$$A_l(r, r') = \sum_{ij} [A_l]_{ij} \, b^i(r) b^j(r'). \tag{3.34}$$

Note that upper indices in the projection in B-spline space of an object go with lower indices in the basis functions, and vice versa. This is due to the B-spline basis having an overlap between its basis functions, so that an overlap matrix S_{ij} is to be used to properly perform operations such as matrix multiplications and basis changes.

3.3 Spherical response functions

In this section we outline the calculation of the RPA macroscopic polarizability α as implemented in AGWX. In doing so, we present the procedure for solving the Dyson equation for χ on a frequency grid in the RPA. This is a required step for the calculation

of W in the GW and GW+SOSEX self-energies. In Section 3.3.5 we also analyze and compare numerical results for α as computed in different approximations and with different starting points. These will help us understand how in turn self-energies behave with different starting points in Section 3.4.5.

3.3.1 Response in the RPA and in TDDFT

When taken to the frequency domain and starting from the usual independent-particle solution, the expression of the RPA irreducible polarizability, Eq. (2.138), reads

$$P^{\mathrm{RPA}}(\mathbf{r},\mathbf{r}';\omega) = \int \frac{d\omega'}{2\pi i} G(\mathbf{r},\mathbf{r}';\omega+\omega')G(\mathbf{r}',\mathbf{r},\omega') \tag{3.35}$$

Expressing the G's in a Lehmann form and performing the frequency integral by closing the contour in the complex plain gives

$$P^{\mathrm{RPA}}(\mathbf{r},\mathbf{r}';\omega) = \chi^0(\mathbf{r},\mathbf{r}';\omega) = \sum_{cv}\left[\frac{\varphi_v^*(\mathbf{r})\varphi_c(\mathbf{r})\varphi_c^*(\mathbf{r}')\varphi_v(\mathbf{r}')}{\omega-\omega_{cv}+i\eta} - \frac{\varphi_v^*(\mathbf{r}')\varphi_c(\mathbf{r}')\varphi_c^*(\mathbf{r})\varphi_v(\mathbf{r})}{\omega+\omega_{cv}-i\eta}\right], \tag{3.36}$$

with v and c running on occupied and unoccupied states respectively, and $\omega_{cv} = \varepsilon_c - \varepsilon_v$. Then one may compute ε using Eq. (2.134) and obtain χ using Eq. (2.133), which amounts to solving the Dyson equation for χ,

$$\chi = P + Pv\chi, \tag{2.125}$$

as seen in Section 2.1.7.

We note that P^{RPA} corresponds to the independent-particle response, which we may also term χ_0 and that is obtained by to closing the 4-point uncorrelated electron-hole propagator $-iL_0$ into a 2-point correlation function. Thus, in a TDDFT framework one has for χ_0^{KS} the same expression of P^{RPA}, and Eq. (2.125) can be easily adapted to also include the exchange-correlation kernel f_{xc}, as seen in Section 2.2.3,

$$\chi = \chi_0^{\mathrm{KS}} + \chi_0^{\mathrm{KS}}[v + f_{\mathrm{xc}}]\chi. \tag{2.159}$$

3.3.2 Spin-polarized response

It is worth writing down how the equations change whenever spin is taken into account. Matrix equations like Eqs. (2.125) and (2.159) acquire a broader sense since the spin degree of freedom is also implied.

Spin is made explicit in the definitions of P and χ, Eqs. (2.122) and (2.124), in the following way:

$$P(1,2) = \frac{\delta\rho_{\sigma_1}(\mathbf{r}_1 t_1)}{\delta v_{\mathrm{tot}}(\mathbf{r}_2 t_2)}\delta_{\sigma_1\sigma_2}, \qquad \chi(1,2) = \frac{\delta\rho_{\sigma_1}(\mathbf{r}_1 t_1)}{\delta v_{\mathrm{ext}}(\mathbf{r}_2 t_2)}\delta_{\sigma_1\sigma_2}. \tag{3.37}$$

We remark that the spin dependence comes from the two possible spin polarizations of the density, while the external potential v_{ext} and the total classical potential v_{tot} have no such

dependence. By defining $P_\sigma = P_{\sigma\sigma}$ and $\chi_\sigma = \chi_{\sigma\sigma}$, the Dyson equations (2.125) and (2.159) become

$$\chi = \sum_\sigma [P_\sigma + P_\sigma \sum_{\sigma'} v\chi_{\sigma'}], \tag{3.38}$$

$$\chi = \sum_\sigma [\chi^{\mathrm{KS}}_{0\sigma} + \chi^{\mathrm{KS}}_{0\sigma} \sum_{\sigma'} (v + f^{\mathrm{xc}}_{\sigma\sigma'})\chi_{\sigma'}], \tag{3.39}$$

with $\chi = \sum_\sigma \chi_\sigma$, the total response. The inverse dielectric function is now also spin-polarized and reads

$$\epsilon^{-1}_\sigma = I - \sum_{\sigma'} vP_{\sigma'}, \tag{3.40}$$

or

$$\epsilon^{-1}_\sigma = I - \sum_{\sigma'} [v + f^{\mathrm{xc}}_{\sigma\sigma'}]\chi^{\mathrm{KS}}_{0\sigma} \tag{3.41}$$

depending on whether the f_{xc} term is included or not when doing TDDFT. Note that only inserting the xc kernel f_{xc} makes ϵ_σ actually dependent on the spin σ, since it takes at least an exchange contribution to introduce spin-dependence. Eq. (2.134) becomes

$$\chi = \sum_\sigma P_\sigma \epsilon^{-1}_\sigma. \tag{3.42}$$

For spin-unpolarized calculations, we have

$$P_1 = P_2 \tag{3.43}$$

$$f^{\mathrm{xc}}_{11} = f^{\mathrm{xc}}_{12} = f^{\mathrm{xc}}_{21} = f^{\mathrm{xc}}_{22}, \tag{3.44}$$

and consequently Eq. (3.42) simplifies into

$$\chi = 2P_1\epsilon^{-1}_1, \tag{3.45}$$

with either

$$\epsilon^{-1}_1 = I - v2P_1 \tag{3.46}$$

or

$$\epsilon^{-1}_1 = I - [v + f^{\mathrm{xc}}_{11}]2\chi^{\mathrm{KS}}_{01}, \tag{3.47}$$

For the sake of simplicity, in the following we will go back to neglecting the spin degree of freedom. It can be reinserted in the treatment at any moment by using the equations presented in this section.

3.3.3 The macroscopic polarizability

The macroscopic polarizability tensor α relates the polarization vector $\mathbf{P}$ to the external electric field $\mathbf{E}_{\mathrm{ext}}$ to linear order. In cartesian coordinates we have

$$P_i = \sum_j \alpha_{ij} E_{\mathrm{ext},j}. \tag{3.48}$$

Here "macroscopic" means that the perturbing field is taken to the long-range limit, $\mathbf{E}_{\text{ext}}(\mathbf{r}) = \mathbf{E}_0 e^{i\mathbf{q}\cdot\mathbf{r}}$ for $\mathbf{q} \to 0$, i.e. $\mathbf{E}_{\text{ext}}$ constant in space. This equation can be obtained by rewriting the definition of χ, of Eq. (2.124), as

$$\delta\rho(\mathbf{r}_1, \omega) = \int d\mathbf{r}_2\, \chi(\mathbf{r}_1, \mathbf{r}_2; \omega)\delta v_{\text{ext}}(\mathbf{r}_2, \omega), \tag{3.49}$$

where we have also moved to frequency space. We apply $\int \mathrm{d}\mathbf{r}_1\, \mathbf{r}_1$ to both sides of this equation, and recognize on the LHS

$$\delta\mathbf{P}(\omega) = \int d\mathbf{r}_1 \mathbf{r}_1 \delta\rho(\mathbf{r}_1, \omega), \tag{3.50}$$

while on the RHS we have

$$\delta v_{\text{ext}}(\mathbf{r}_2, \omega) = -\mathbf{E}_{\text{ext}}(\omega) \cdot \mathbf{r}_2. \tag{3.51}$$

Finally, α_{ij} is found by comparison with Eq. (3.48), yielding

$$\alpha_{ij}(\omega) = \int d\mathbf{r} d\mathbf{r}'\, r_i\, \chi(\mathbf{r}, \mathbf{r}'; \omega)\, r'_j. \tag{3.52}$$

With the same procedure, by just replacing χ with P, the tensor α_0 that relates $\mathbf{P}$ to $\mathbf{E}_H + \mathbf{E}_{\text{ext}}$ can be obtained, with $\mathbf{E}_H(\mathbf{r}) = -\mathbf{E}_{\text{ext}}(\mathbf{r})\mathbf{r}$.

We shall consider the diagonal element of $\alpha(\mathbf{r}, \mathbf{r}'; \omega)$ by aligning $\mathbf{r}$ and $\mathbf{r}'$ along the same direction. This tensor component is what we refer to when generically speaking of "macroscopic polarizability", and it describes the response of the system in the same direction of the perturbation. Thanks to the spherical symmetry of the problem, we can align $\mathbf{r}$ and $\mathbf{r}'$ in any direction, so we shall choose the z direction and obtain

$$\begin{aligned} \alpha(\omega) &= \alpha(\hat{\mathbf{z}}, \hat{\mathbf{z}}; \omega) \\ &= \int d\mathbf{r}_1 \int d\mathbf{r}_2\; r_1 \cos(\theta_1) \chi(\mathbf{r}_1, \mathbf{r}_2; \omega) r_2 \cos(\theta_2) \\ &= \frac{4\pi}{3} \int d\mathbf{r}_1 \int d\mathbf{r}_2\; r_1 Y_{10}(\hat{\mathbf{r}}_1) \chi(\mathbf{r}_1, \mathbf{r}_2; \omega) r_2 Y_{10}(\hat{\mathbf{r}}_2), \end{aligned} \tag{3.53}$$

where we have made the dependence on SHs explicit in the third row. Then, by expanding χ on SHs,

$$\chi(\mathbf{r}, \mathbf{r}'; \omega) = \frac{1}{rr'} \sum_{LM} Y^*_{LM}(\hat{\mathbf{r}}) \chi_L(r, r', \omega) Y_{LM}(\hat{\mathbf{r}}'), \tag{3.54}$$

and by carrying out the angular integrations, one is left with only the $L = 1$ component of χ due to orthonormality. The resulting equation is

$$\alpha(\omega) = \frac{4\pi}{3} \int dr_1 dr_2 r_1^2 \chi_1(r_1, r_2; \omega) r_2^2. \tag{3.55}$$

Having only the $L = 1$ angular momentum component means being in the dipole approximation, which is indeed a consequence of working in linear response. Higher-order response functions would imply higher-order multipoles, and therefore more angular momentum components.

3.3.4 Response on spherical harmonics and B-splines

We now seek to get an expansion for the response functions like the one in Eq. (3.30); afterwards, we shall find the matrix elements of their radial components in B-spline space. We start from Eq. (3.36): by exploiting the factorization in Eq. (3.22), one can apply the rules of the SHs basis set, Eqs. (A.15) and (A.34), and the orthogonality of the Clebsch-Gordan coefficients, Eq. (A.28), to obtain

$$P(\mathbf{r},\mathbf{r}';\omega) = \frac{1}{rr'}\sum_{LM} Y^*_{LM}(\hat{\mathbf{r}})P_L(r,r',\omega)Y_{LM}(\hat{\mathbf{r}}') \tag{3.56}$$

$$\begin{aligned} P_L(r,r';\omega) = &\sum_{n_c l_c}\sum_{n_v l_v}\sqrt{\frac{(2l_c+1)(2l_v+1)}{4\pi(2L+1)}}C^{L0}_{l_c0,l_v0} \\ &\times \frac{1}{rr'}P_{n_v l_v}(r)P_{n_c l_c}(r)P_{n_v l_v}(r')P_{n_c l_c}(r') \\ &\times \left[\frac{1}{\omega-\omega_{cv}+i0^+} - \frac{1}{\omega+\omega_{cv}-i0^+}\right]. \end{aligned} \tag{3.57}$$

The matrix elements of $P_L(\omega)$ on the B-spline basis read

$$\begin{aligned} P_{L,ij}(\omega) &= \langle b_i|P_L(\omega)|b_j\rangle \\ &= \sum_{n_c l_c}\sum_{n_v l_v}\sqrt{\frac{(2l_c+1)(2l_v+1)}{4\pi(2L+1)}}C^{L0}_{l_c0,l_v0} \\ &\times (F_{n_c l_c n_v l_v})_i (F_{n_c l_c n_v l_v})_j \\ &\times \left[\frac{1}{\omega-\omega_{cv}+i0^+} - \frac{1}{\omega+\omega_{cv}-i0^+}\right], \end{aligned} \tag{3.58}$$

with

$$\begin{aligned} (F_{n_c l_c n_v l_v})_i &= \int dr\,\frac{1}{r}\,b_i(r)P_{n_v l_v}(r)P_{n_c l_c}(r) \\ &= \sum_{mn} P^m_{n_v l_v}P^n_{n_c l_c}B^3_{imn}, \end{aligned} \tag{3.59}$$

$$B^3_{imn} = \int dr\frac{1}{r}b_i(r)b_m(r)b_n(r), \tag{3.60}$$

where the radial wavefunctions have been expanded on the B-spline basis set in the second line of Eq. (3.59).

The dielectric function ϵ is obtained from Eq. (2.133) by substituting the expansions of P and v on the SHs basis set, Eqs. (3.56) and Eq. (A.41). Then one can proceed with the angular integration and exploit the orthonormality of the SHs, i.e. $\int d\Omega\, Y^*_{LM}(\Omega)Y_{lm}(\Omega) = \delta_{Ll}\delta_{Mm}$, to get

$$\epsilon(\mathbf{r},\mathbf{r}';\omega) = \frac{1}{rr'}\sum_{LM} Y_{LM}(\hat{\mathbf{r}})Y^*_{LM}(\hat{\mathbf{r}}')\epsilon_L(r,r';\omega), \tag{3.61}$$

$$\epsilon_L(r,r';\omega) = \delta(r-r') - \int dr_2 v_L(r,r_2)P_L(r_2,r';\omega). \tag{3.62}$$

The integral in the last equation becomes a matrix multiplication in B-spline space, provided that one properly manages covariant and contravariant indices (see Appendix B). We choose to work with the following representations of the operators in B-spline space :

$$(\epsilon_L)_i{}^j = \langle b_i|\epsilon_L|b^j\rangle, \tag{3.63}$$
$$(P_L)^{ij} = \langle b^i|P_L|b^j\rangle, \tag{3.64}$$
$$(v_L)_{ij} = \langle b_i|v_L|b_j\rangle; \tag{3.65}$$

we temporarily drop ω for clarity, since all the equations that follow will be diagonal in frequency space. so that we can obtain $(\epsilon_L)_i{}^j$ with the following expression:

$$(\epsilon_L)_i{}^j = I_i{}^j - \sum_k (v_L)_{ik}(P_L)^{kj}. \tag{3.66}$$

After moving to SHs space with the same procedure we have just followed for ϵ, we can also rewrite Eq. (2.134) using a matrix multiplication in B-spline space[1]:

$$(\chi_L)^{ij} = \sum_k (P_L)^{ik}(\epsilon_L^{-1})_k{}^j. \tag{3.67}$$

The final step is to obtain the macroscopic polarizabilities. In the following we will focus on α; the procedure for obtaining α_0 is the same, provided that one replaces χ by P. By expanding χ_L on the b-spline basis, one gets the final expression used by AGWX to compute the macroscopic polarizability:

$$\alpha(\omega) = \frac{4\pi}{3}\sum_{ij}\chi_1^{ij}(\omega)\int dr_1 dr_2 r_1^2 b_i(r_1)b_j(r_2)r_2^2. \tag{3.68}$$

We conclude by noting that by doing the replacements $P \to \chi_0$ and $v \to v + f_{xc}$ in Eq. (3.66), we obtain the TDDFT response function.

3.3.5 Numerical results for the response function

I will now present some results for the dipole polarizability as obtained with the methods introduced in the previous Sections. It is interesting to analyze the polarizabilities because they are mapped to the self-energy through Eq. (3.4) (analogous relations hold for 2B and SOSEX, the former containing on the IP polarizability). In Section 3.4.5 we will refer to the results of this Section to justify the features of the self-energy. Of course the self-energy contains more contributions than those coming from just the dipole polarizability: depending on the angular momentum selection rules, monopole, quadrupole, etc. transitions may also contribute to the self-energy. However, the dipole polarizability can still offer insight into the general trends.

Figure 3.3 shows the computed dynamical dipole polarizabilities solutions for the spherical atoms of the second period in the periodic table. Each atom shares similar properties with the others belonging to the same group, these being mainly determined by the occupied

[1]We are implicitly defining χ_L here.

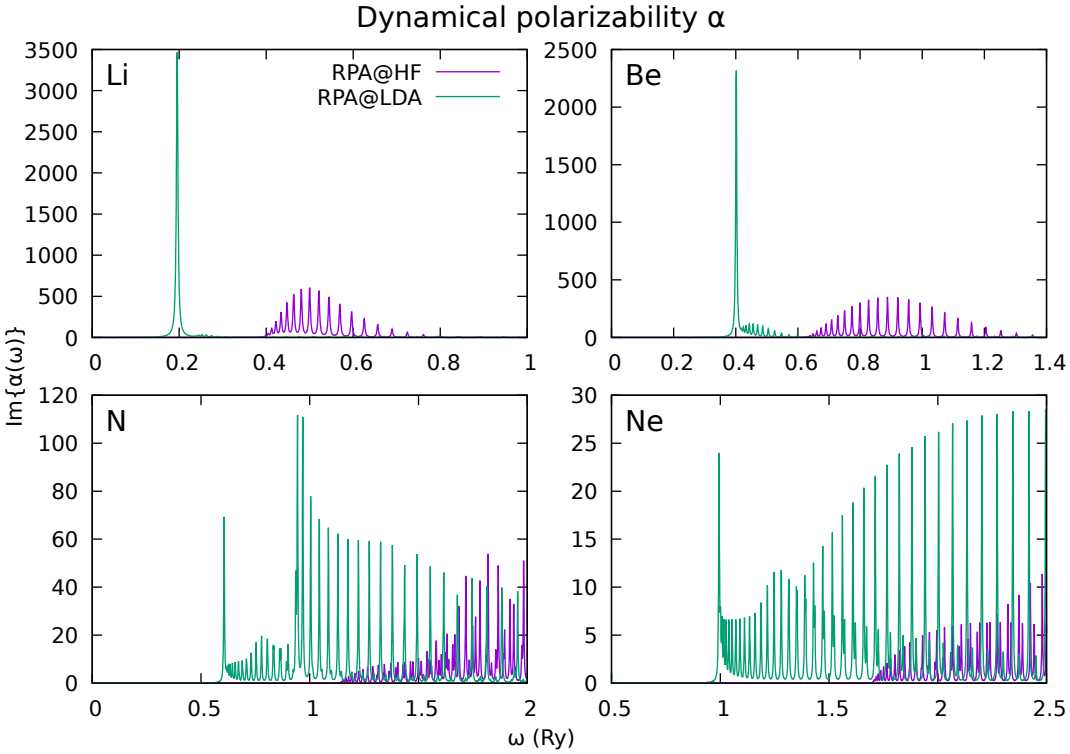

Figure 3.3. RPA dipole polarizability α of the spherical atoms in the 2nd period, computed with the HF and the LDA starting points.

valence shells, so the analysis will be quite general. In particular, atoms in the first groups are characterized by high polarizabilities, which then tend to decrease as the group of noble gases is approached. The observable targeted in Figure 3.3 is $\mathrm{Im}\{\alpha\}$ in the RPA, on top of HF (RPA@HF) and LDA (RPA@LDA) solutions. The peaks of $\mathrm{Im}\{\alpha\}$ correspond to neutral excitations of the atom, and should therefore reproduce those of a photoabsorption experiment.

It can be seen that the starting point can determine very different results for $\mathrm{Im}\{\alpha\}$: RPA@LDA in Li and Be is characterized by a strong peak corresponding to an initial bound neutral excitation, and then by the onset of a faint unbound continuum. Specifically, the initial excitation is from the occupied valence s shell to a bound unoccupied p state; the continuum is also made of excitations from the s valence shell, until an onset of even fainter core excitations appears beyond the considered energy range. The distinction between bound and unbound excitations was made by comparing excitation energies with eigenvalue differences, which are quite similar if the excitation energies are computed in the RPA [i.e. $\chi_0 = P^{\mathrm{RPA}}$, cfr. Eq. (3.36), bears a qualitative similarity to χ^{RPA}]. Comparison with higher-level theoretical calculations and experimental data shows that this spectrum dominated by a single strong peak is realistic in group-1 and -2 atoms [79–82]. As one progresses through the period, the initial peak loses weight to the continuum. If calculations for non-spherical atoms were possible in AGWX and included in the analysis, the transitions

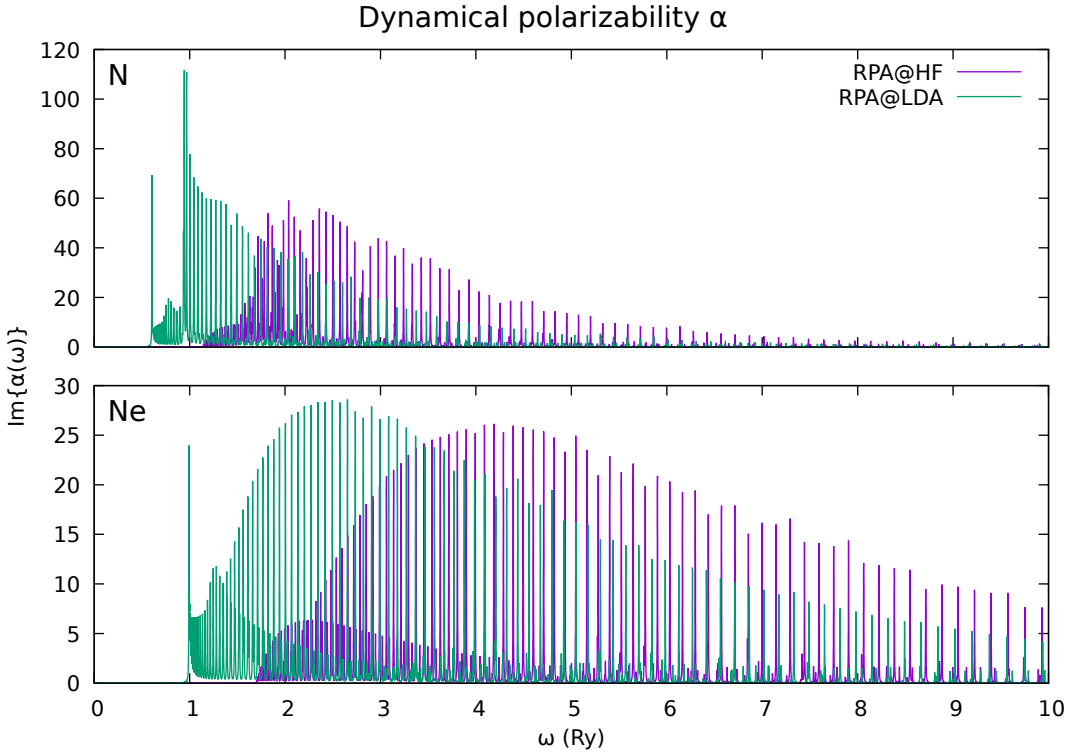

Figure 3.4. RPA dipole polarizabilites of Figure 3.3 on a wider range. The continua of N and Ne die out over a way wider frequency range than Li and Be.

from Be to N, and then from N to Ne would probably appear smoother.

Turning our attention to RPA@HF results, we can see that here only an unbound continuum is found. Its positioning is at higher energies than the energy onset of the RPA@LDA excitations. This is coherent with the fact that HF energy gaps are larger than LDA ones; and, while KS-DFT in the LDA yields at least one empty bound state in neutral atoms, HF does not. Similarly to what happens to the RPA@LDA bound excitation, the weight of the RPA@HF continuum is concentrated in a relatively narrow range in Li and Be; whereas, going up to N and Ne, the weight is spread over a way larger range instead. Figure 3.4, in particular, shows that it takes very large energies for this continuum to die out in Ne. It is interesting to note that for N and Ne the difference between RPA@HF and RPA@LDA becomes more quantitative than qualitative: with the continuum acquiring so much weight also in RPA@LDA, the two spectra almost differ by just an energy shift. It is also interesting to note that these very broad continua may prove quite challenging for simplified frequency representations to handle [134–136], especially for the plasmon pole approximation [26, 195] (which, on the other hand, will probably well approximate the RPA@LDA polarizability of Li).

In Table 3.1 I report static polarizabilities compared against accurate theoretical results from coupled cluster and configuration interaction. Here the IP and the LDA polarizabilities are also considered, on top of LDA. The latter polarizability is obtained in the static limit

Table 3.1. Static dipole polarizabilities Re$\{\alpha(0)\}$ [in Bohr^3] computed using different theoretical methods and approaches. MBPT methods: IP = Independent Particle[LDA], RPA = RPA[LDA], LDA = RPA[LDA] + f_{xc}[LDA]. Theoretical reference methods: CCSDT = coupled cluster with single, double and triple excitations, CICP = configuration interaction with semi-empirical core potential.

Atom	IP	RPA	LDA	Theory[a]	Method
He	1.810	1.465	1.660	1.384	CCSDT
Li	164.8	79.35	142.5	163.7	RCCSDT
Be	80.39	32.47	43.75	37.69	CICP
Ne	3.487	2.767	3.055	2.69	CCSDT
Na	156.7	84.99	141.0	162.9	RCCSDT
Mg	121.9	52.95	71.28	71.35	CICP
Ar	17.98	10.63	12.01	11.08	CCSDT
K	300.6	149.3	252.7	291.1	RCCSDT
Ca	276.2	106.4	148.3	159.4	CICP
Zn	68.392	30.602	38.523	38.12	CICP
Kr	27.79	15.83	18.05	16.80	CCSDT

[a]Mitroy et al. [196]

Table 3.2. HOMO-LUMO transition energies (in Ry) of group-1 atoms as obtained from LDA eigenvalue differences (IP approximation). Core shells are omitted in the shell notation used to indicate the transitions.

Atom	Transition	IP@LDA	Exp.[a]
Li	$2s[^1S] \to 2p[^1P]$	0.136	0.1358
Na	$3s[^1S] \to 3p[^1P]$	0.158	0.1545
K	$4s[^1S] \to 4p[^1P]$	0.120	0.1183

[a]NIST [197]

of the TD-DFT equation, Eq. (2.159), with the adiabatic LDA xc kernel. A more in-depth assessment of accuracy is postponed to Section 4.2.1, where time-dependent Hartree-Fock results are also considered. Here we limit ourselves to noticing that the RPA seems to work best in noble gases, whereas the LDA does better in group-1 and -2 atoms. Due to their few-electron nature, it is indeed reasonable that s shells may experience a significant self-screening effect in the RPA, which is cured by adding the f_{xc} kernel in the LDA (acting as the counterpart of the MBPT three-point vertex). In this sense, the RPA is particularly bad in group-1 atoms, where s shells are populated by a single electron whose transitions dominate contributions to the polarizability; conversely, the IP polarizability is quite accurate for group-1 atoms. This is another reasonable result, since one expects the lone s electron to hardly interact with the core electrons, but rather experience a single-particle effective potential due to the nuclear potential screened by the core electrons. The results for the IP polarizability suggest that $v^{\rm KS}$ in the LDA yields a good approximation of this

effective potential, but only limitedly to the HOMO-LUMO gap eigenvalue difference, whose associated transition contributes the most to the polarizability in group-1 and -2 atoms. This is confirmed by the LDA HOMO-LUMO excitation energies reported in Table 3.2. As for the HOMO energy, the LDA, as well as local and semi-local functionals of KS-DFT, is known to yield levels too shallow in energy due to missing the $1/r$ asymptotic decay that the xc potential should have [111, 112]. Therefore the LDA v^{KS} cannot be regarded as a generally good approximation to an effective single-particle potential for the s electron of group-1 atoms.

3.4 Spherical self-energies

In the same spirit of Section 3.3, in which we brought response functions to the SH/B-spline representation, we now turn our attention to the self-energies presented in Section 3.1 and find a formulation of them in the spherical problem. We also detail the contour deformation technique that was adopted for GW and GW+SOSEX. We will conclude this section by studying the effect of the starting point on the self-energies, as a preliminary step of the general assessment of accuracy.

3.4.1 GW on spherical harmonics and B-splines

As already seen, we aim at a representation where the self-energy is written in terms of SHs as follows:

$$\Sigma^{\mathrm{GW}}(\mathbf{r},\mathbf{r}',\omega) = \frac{1}{rr'}\sum_{LM} Y^*_{LM}(\hat{\mathbf{r}})\,\Sigma^{\mathrm{GW}}_L(r,r',\omega)\,Y_{LM}(\hat{\mathbf{r}}'). \tag{3.69}$$

By taking into account the similar representations holding for G and W, and exploiting the contraction rules for SH, one obtains

$$\Sigma^{\mathrm{GW}}_L(r,r',\omega) = \sum_{l_g l_w}\sqrt{\frac{(2l_g+1)(2l_w+1)}{4\pi(2L+1)}}C^{L0}_{l_g0,l_w0}\,GW_{l_g l_w}(r,r',\omega), \tag{3.70}$$

with

$$GW_{l_g l_w}(r,r',\omega) = -\int \frac{d\omega'}{2\pi i}e^{i\eta\omega'}\,\frac{1}{rr'}G_{l_g}(r,r',\omega+\omega')W_{l_w}(r,r',\omega'). \tag{3.71}$$

The coefficients hold a similarity to those of P seen in Eq. (3.58), since in both cases we are representing the product of two correlation functions evaluated at $(\mathbf{r},\mathbf{r}')$. The projection of $I_{l_g l_w}(r,r',\omega)$ on the B-spline basis is in turn analogous to that of P:

$$[GW_{l_g l_w}(\omega)]_{ii'} = \sum_{jj'kk'} B^3_{ijk}B^3_{i'j'k'}[GW_{l_g l_w}(\omega)]^{jj'kk'}, \tag{3.72}$$

with

$$[GW_{l_g l_w}(\omega)]^{jj'kk'} = \frac{i}{2\pi}\int d\omega' e^{i\eta\omega'}\,[G_{l_g}(\omega+\omega')]^{jj'}[W_{l_w}(\omega')]^{kk'}, \tag{3.73}$$

and B^3_{ijk} as defined in Eq. (3.60). The convolution in the GW term is treated using the contour deformation technique.

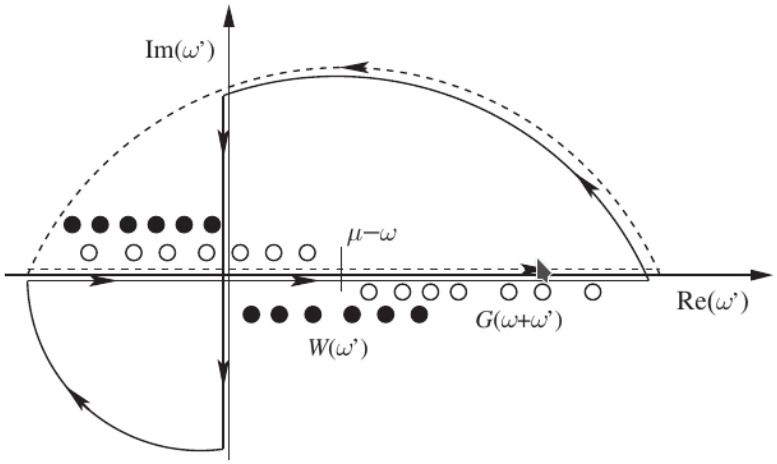

Figure 3.5. The GW convolution integral in the contour deformation technique. The integral along the solid contour is computed and the contribution from the imaginary axis removed. Thanks to this technique, only the known poles of the IP Green's function enter the contour and consequently the sum-over-poles of the residue theorem. Figure from Ref. 13.

3.4.2 The contour deformation technique for GW

In order to evaluate the convolution in Eq. (3.73), the integral is extended to a contour in the complex plane, as depicted in Figure 3.5. Thanks to Jordan's lemma, the contributions from the arcs vanish, and only those from the real and the imaginary axes survive. If the residue theorem is applied to compute the integral over the chosen contour, yielding a sum over poles, one can obtain the integral over the real axis by removing the contribution coming from the imaginary one:

$$[GW_{l_g l_w}(\omega)]^{jj'kk'} = -\left\{ \sum_{z_p \in \{\text{poles of } G\}} \lim_{z \to z_p} [G_{l_g}(z)]^{jj'} [W_{l_w}(z)]^{kk'} (z - z_p) \right. \\ \left. - \frac{1}{2\pi i} \int_{+\infty}^{-\infty} d i\omega' [G_{l_g}(\omega + i\omega')]^{jj'} [W_{l_w}(i\omega')]^{kk'} \right\}. \quad (3.74)$$

From this equation, the a semi-analytical formula used in AGWX is derived,

$$[GW_{l_g l_w}(\omega)]^{jj'kk'} \sim \sum_n P^j_{nl_g} P^{j'}_{nl_g} \left\{ -[W_{l_w}(\varepsilon_{nl_g} - \omega + i\eta)]^{kk'} \theta(\varepsilon_{nl_g} - \omega)\theta(\mu - \varepsilon_{nl_g}) \right. \\ + [W_{l_w}(\varepsilon_{nl_g} - \omega - i\eta)]^{kk'} \theta(\omega - \varepsilon_{nl_g})\theta(\varepsilon_{nl_g} - \mu) \\ \left. - \frac{1}{\pi} \sum_{i=1}^{N} \mathrm{Re}\left\{ [W_{l_w}(i\Omega_i)]^{kk'} \right\} [\mathrm{atan}(x)]^{\frac{\omega_i}{\omega - \varepsilon_{nl_g}}}_{\frac{\omega_{i-1}}{\omega - \varepsilon_{nl_g}}} \right\}, \quad (3.75)$$

where we left out the B^3_{ijk} contributions for ease of notation. The radial wavefunctions in the first line come from expressing the G in our representation of choice, Eq. (3.30), which

is readily obtained from the Lehmann representation. Then, the first two addenda between the curly brackets are a consequence of the pole cancellation (see first line of Eq. (3.74)). The expression in terms of θ functions of the sum over poles can be deduced from Figure 3.5 and is a consequence of poles entering and exiting the contour depending on ω. The last line of Eq. (3.75) is obtained by splitting the integral into two integrals over the $(-\infty,0]$ and $[0,+\infty)$ frequency domains by making the following replacement in one of the former:

$$W(i\omega') = W(-i\omega') = W^*(i\omega'). \tag{3.76}$$

This is possible because the vanishing $i\eta$ parameter, if sufficiently small numerically, can be neglected for $i\omega'$ on the imaginary axis. Moreover, a semi-analytical procedure has been employed, keeping W_c constant over the intervals of a mesh defined by the sequence $\omega_0 = 0 < \omega_1 < \ldots < \omega_N$, and by carrying out the analytical integrals of the remaining factor (denominators of the Green's function) on such intervals. The values at which W_c is kept fixed are those it attains in $\Omega_n = \frac{\omega_n+\omega_{n-1}}{2}$, $n = 1,\ldots,N$. The result of this procedure is given in Eq. (D.1). Given that W_c is expected to be a sum of lorentzian functions (centered around the zero frequency), a mesh given by

$$\omega_n = \Omega \tan\left(\frac{\pi/2}{N} n\right), \qquad n = 0,\ldots,N \tag{3.77}$$

is employed in AGWX, making the sampling points denser around the center of the peak. N and Ω are parameters to be adjusted for convergence of the calculations. Although the contour deformation technique can in principle be applied to the whole W, it makes sense to apply it only to the frequency-dependent polarization contribution W^p for the computation of the correlation self-energy Σ_c; this is what AGWX does, while the Fock self-energy Σ^x is simply obtained with the same procedure use in the scf method [194]. The two contributions are then summed together to obtain the whole Σ.

3.4.3 Contour deformation and representation for SOSEX

The contour deformation technique can be applied to the SOSEX self-energy without substantial differences as compared with what we have seen for GW in Section 3.4.2. One just needs to perform a preliminary analytical integration with respect to ω_2 in Eq. (3.8), in order to obtain the result of Eq. (3.9). $I_{\mu\nu}$ is the frequency integral of the RPA irreducible polarizability, and has the same pole structure and frequency dependence that W has; therefore, analogously to GW, the only poles that will enter the sum over poles obtained by integrating along the contour of Figure 3.5 are those explicitly written in the second row of Eq. (3.9), coming $G(\mathbf{r},\mathbf{r}_3,\omega+\omega_1)$ in Eq. (3.8). The result is:

$$\begin{aligned}\Sigma^{\mathrm{SOSEX}}(\mathbf{r},\mathbf{r}';\omega) = &-\sum_{\mu\nu\beta}\varphi_\beta(\mathbf{r})\varphi^*_\nu(\mathbf{r}')\langle\beta|v(\mathbf{r}')|\mu\rangle \\ &\times\Bigg\{ i\int_{-\infty}^{+\infty}\frac{d\omega_1}{2\pi i}\frac{I_{\mu\nu}(i\omega_1)\langle\mu|W(\mathbf{r};i\omega_1)|\nu\rangle}{\omega+i\omega_1-\varepsilon_\beta\pm i\eta} \\ &\quad +\theta(\varepsilon_\beta-\omega)\theta(\mu-\varepsilon_\beta)\, I_{\mu\nu}(\varepsilon_\beta-\omega+i\eta)\,\langle\mu|W(\mathbf{r};\varepsilon_\beta-\omega+i\eta)|\nu\rangle \\ &\quad -\theta(\omega-\varepsilon_\beta)\theta(\varepsilon_\beta-\mu)\, I_{\mu\nu}(\varepsilon_\beta-\omega-i\eta)\,\langle\mu|W(\mathbf{r};\varepsilon_\beta-\omega-i\eta)|\nu\rangle \Bigg\}\end{aligned} \tag{3.78}$$

The integral over the imaginary axis in the last row can be evaluated using the usual semi-analytical procedure (see Eq. (D.3)). The final result in the SH/B-spline representation reads

$$\begin{aligned}\Sigma_L^{\mathrm{SOSEX}}(r,r';\omega) = &-\sum_{qsr}\sum_{\substack{l_q l_s l_r\\ l_c l_w}} C_{l_w l_r l_q}^{l_c l_s L}\frac{P_{rl_r}(r)P_{sl_s}(r')}{rr'}\\ &\times\langle q,l_q|W(r;\omega_1)|s,l_s\rangle\langle r,l_r|v(r')_{l_c}|q,l_q\rangle\\ &\times\Big\{\theta(\varepsilon_{rl_r}-\omega)\bar{\theta}_{rl_r}I_{qs}^{l_q l_s}(\omega_1)|_{\omega_1=\varepsilon_{rl_r}-\omega+i\eta}\\ &-\theta(\omega-\varepsilon_{rl_r})\theta_{rl_r}I_{qs}^{l_q l_s}(\omega_1)|_{\omega_1=\varepsilon_{rl_r}-\omega-i\eta}\\ &+\frac{1}{\pi}\sum_{m=1}^{M}\frac{\theta_{ql_q}\bar{\theta}_{sl_s}-\bar{\theta}_{ql_q}\theta_{sl_s}}{\varepsilon_{rl_r}+\varepsilon_{sl_s}-\varepsilon_{ql_q}-\omega}|_{\omega_1=\Omega_m}\\ &\times\left[\arctan\left(\frac{\omega'}{\varepsilon_{ql_q}-\varepsilon_{sl_s}}\right)-\arctan\left(\frac{\omega'}{\varepsilon_{rl_r}-\omega}\right)\right]_{\omega'_m}^{\omega'_{m+1}}\Big\},\end{aligned}\tag{3.79}$$

with

$$I_{qs}^{l_q l_s}(\omega_1)=\frac{\theta_{ql_q}\bar{\theta}_{sl_s}}{\omega_1-(\varepsilon_{ql_q}-\varepsilon_{sl_s}-2i\eta)}-\frac{\bar{\theta}_{ql_q}\theta_{sl_s}}{\omega_1-(\varepsilon_{ql_q}-\varepsilon_{sl_s}+2i\eta)}.$$

The contraction of four $C_{l_1m_1,l_2m_2}^{LM}$ coefficients has yielded a $C_{L_1L_2L_3}^{l_1l_2l_3}$ coefficient containing a Wigner 6j symbol. The definition of these coefficients and symbols can be found in Appendix A.

3.4.4 2B on spherical harmonics and B-splines

From Eqs. (3.18) and (3.19), the 2B self-energy in the B-spline/SH representation reads :

$$\begin{aligned}\left[\Sigma^{\mathrm{2Bd}}(\omega)_L\right]^{ii'} = &\,2\sum_{l_c}\sum_{\substack{qsr\\ l_q l_s l_r}}\sqrt{\frac{(2l_r+1)(2l_s+1)}{(4\pi)^2(2L+1)}}C_{l_q0,l_s0}^{l_c0}C_{l_c0,l_r0}^{L0}\\ &\times\sum_{ijk}\sum_{i'j'k'}B_{ijk}^3B_{i'j'k'}^3\,P_{rl_r}^{j}P_{rl_r}^{j'}\\ &\times\langle ql_q|v_{l_c}|sl_s\rangle^k\langle sl_s|v_{l_c}|ql_q\rangle^{k'}\\ &\times I_{qsr}^{l_q l_s l_r}(\omega),\end{aligned}\tag{3.80}$$

$$\begin{aligned}\left[\Sigma^{\mathrm{2Bx}}(\omega)_L\right]^{ii'} = &-\sum_{l_c l_w}\sum_{\substack{qsr\\ l_q l_s l_r}}C_{l_w l_r l_q}^{l_c l_s L}\\ &\times\sum_{ijk}\sum_{i'j'k'}B_{ijk}^3B_{i'j'k'}^3\,P_{rl_r}^{j}P_{sl_s}^{j'}\\ &\times\langle ql_q|v_{l_w}|sl_s\rangle^k\langle rl_r|v_{l_c}|ql_q\rangle^{k'}\\ &\times I_{qsr}^{l_q l_s l_r}(\omega).\end{aligned}\tag{3.81}$$

The factor 2 in the direct term stems from considering the spin-unpolarized case; in the spin-polarized one the self-energy becomes spin-dependent through the single-particle oribtals φ and eigenvalues ε and the factor must be removed.

3.4.5 Study of the starting point

In this Section I will show a preliminary study of the starting point dependence of one-shot calculations in atoms. I will present an attempt to correct the overbinding and underbinding issues that GW@HF and GW@LDA encounter respectively. The correction involves a trick aimed at mimicking self-consistent calculations.

We begin by noting that, in one-shot schemes, the Dyson equation must be adapted in order to remove the exchange-correlation contributions already present in the starting point. This is not really necessary when starting from HF, since exchange in the final self-energy is given by Σ^x from HF itself. Therefore, when starting from HF the Dyson equation reads

$$G = G^{\mathrm{HF}} + G^{\mathrm{HF}}\Sigma_c[G^{\mathrm{HF}}]G. \tag{3.82}$$

In this case one just needs to add the correlation contribution Σ_c to the previously calculated Σ_x. When instead starting from a KS-DFT solution, the exchange-correlation contribution already present in the starting point, given by the local potential v_{xc}, must be removed, while the non-local Σ must be added:

$$G = G^{\mathrm{KS}} + G^{\mathrm{KS}}(\Sigma_x[G^{\mathrm{KS}}] + \Sigma_c[G^{\mathrm{KS}}] - v_{\mathrm{xc}})G, \tag{3.83}$$

The diagonal QPEs consequently become

$$\varepsilon_i^{\mathrm{QP}} = \varepsilon_i^{\mathrm{HF}} + \mathrm{Re}\left\{\langle i|\Sigma_c(\varepsilon_i^{\mathrm{QP}})|i\rangle\right\} \text{ and} \tag{3.84}$$

$$\varepsilon_i^{\mathrm{QP}} = \varepsilon_i^{\mathrm{KS}} + \mathrm{Re}\left\{\langle i|\Sigma_x + \Sigma_c(\varepsilon_i^{\mathrm{QP}}) - v_{\mathrm{xc}}|i\rangle\right\}. \tag{3.85}$$

Through similar manipulations of the QPE, it is possible to incorporate into the energy spectrum of the starting point an initial shift aimed at attaining self-consistency on the HOMO energy [17]. Imposing the self-consistency condition implies that the shift has to be

$$\Delta E = \langle\varphi_{\mathrm{HOMO}}|\Sigma^0(\varepsilon_{\mathrm{HOMO}})|\varphi_{\mathrm{HOMO}}\rangle, \tag{3.86}$$

with Σ^0 being evaluated using single-particle eigenvalues and eigenfunctions as the one-shot procedure prescribes. Eq. (3.4) implies that a ΔE shift in the eigenvalue spectrum is equivalent to considering $\Sigma^0(\omega - \Delta E)$ instead of $\Sigma^0(\omega)$.

In Table 3.3 I report the results of computing the ionization energies (IEs) as negatives of HOMO energies, using HF, GW@HF, the LDA of KS-DFT, GW@LDA, and GW@LDA with the initial shift ΔE; Z-factors are also present in parentheses. In Table 3.4 I report the mean absolute error (MAE) and the mean mean error (ME) of each method, along with mean Z-factors. The results of applying the ΔE shift to GW@HF were not reported because they were found to be very similar to one-shot GW@HF: this is a hint that GW@HF is already quite close to GW self-consistency in atoms, as found in other works [35, 146]. Looking at the ME in Table 3.4, trends that are already known for finite systems are apparent, like GW@HF overbinding HOMOs and GW@LDA underbinding them [38]. It is

Table 3.3. HOMO energy negatives (in Ry)and Z-factors (in parenthesis) from one-shot GW, with and without an initial shift of the G_0 energies of $\Delta E = \langle \varphi_{\text{HOMO}} | \Sigma(\varepsilon_{\text{HOMO}}) | \varphi_{\text{HOMO}} \rangle$.

Atoms	**HF**	**GW@HF**	**LDA**	**GW@LDA**		**Exp.**[a]
				no shift	shift	
H	1.000	1.003 (0.963)	0.538	0.914 (0.721)	0.989 (0.903)	0.99947
He	1.835	1.819 (0.957)	1.140	1.735 (0.830)	1.817 (0.912)	1.80714
Li	0.393	0.422 (0.956)	0.233	0.406 (0.686)	0.454 (0.836)	0.39628
Be	0.618	0.675 (0.939)	0.412	0.661 (0.757)	0.719 (0.834)	0.68521
N	1.143	1.104 (0.943)	0.614	1.004 (0.767)	1.084 (0.878)	1.06824
Ne	1.702	1.613 (0.943)	0.997	1.529 (0.818)	1.619 (0.891)	1.58496
Na	0.364	0.396 (0.958)	0.226	0.388 (0.724)	0.424 (0.871)	0.37772
Mg	0.506	0.565 (0.940)	0.351	0.554 (0.782)	0.595 (0.859)	0.56199
P	0.785	0.802 (0.943)	0.461	0.744 (0.790)	0.798 (0.882)	0.77076
Ar	1.183	1.198 (0.942)	0.766	1.138 (0.841)	1.195 (0.893)	1.15831
K	0.295	0.332 (0.955)	0.192	0.332 (0.743)	0.362 (0.863)	0.31904
Ca	0.390	0.452 (0.936)	0.283	0.450 (0.771)	0.490 (0.823)	0.44931
Zn	0.583	0.665 (0.943)	0.444	0.679 (0.834)	0.715 (0.886)	0.69046
As	0.742	0.765 (0.947)	0.440	0.712 (0.802)	0.758 (0.894)	0.71945
Kr	1.050	1.080 (0.945)	0.694	1.028 (0.850)	1.076 (0.901)	1.02895

[a]Ref. 139

Table 3.4. Mean absolute error (MAE) on the IEs, mean error (ME) on the IEs (in Ry) and mean Z for each self-energy and starting point, with and without initial shift of $\Delta E = \langle \varphi_{\text{HOMO}} | \Sigma(\varepsilon_{\text{HOMO}}) | \varphi_{\text{HOMO}} \rangle$.

Method	IE MAE	IE ME	Mean Z
HF	0.041	-0.002	
GW@HF	0.023	0.018	0.947
GW@LDA	0.027	-0.023	0.781
GW@LDA w. shift	0.033	0.032	0.875

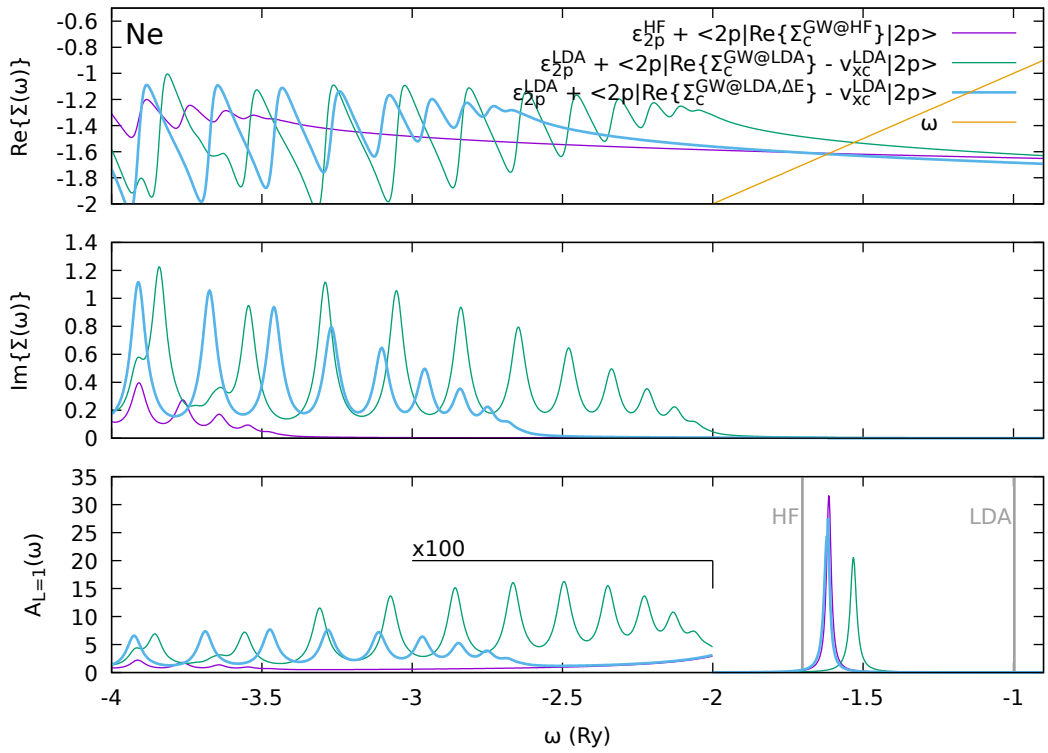

Figure 3.6. $2p$ orbital self-energy and spectral function of Ne as obtained with GW upon various starting points: HF, LDA and LDA with initial shift ΔE.

rather interesting to note that applying the initial shift to GW@LDA makes it overbind the HOMOs, even more than GW@HF, in total opposition to what happens without shift.

To have better insight into the issue, two different limiting cases can be distinguished looking at Table 3.3: the case of noble gases, in which GW@LDA with the ΔE shift brings the HOMO energies remarkably close to the GW@HF ones; and the case of group-1 atoms, in which the same does not happen, and the initial shift is rather responsible for increasing the slight overbinding that is found in this group (an exception for GW@LDA). In Figures 3.6 and 3.7 the correlation self-energies Σ_c and the spectral functions A of Li and Ne are plotted. In particular, for $\mathrm{Re}\{\Sigma_c\}$ a rearrangement of the QPE is plotted, in order to make it possible to compare self-energies obtained with different starting points. One can see that in the case of Ne, which has a large HOMO-LUMO gap, the shift by ΔE acts in such a way that the QPE solution is found in a rather flat region of $\mathrm{Re}\{\Sigma_c\}$. In the region around the QPE solution, the shifted GW@LDA and the GW@HF descriptions of $\mathrm{Re}\{\Sigma_c\}$ are quite close, explaining why the QP HOMO energies end up being similar. The satellite onsets, corresponding to the onset of the excitations in the RPA W [cfr. Eq. (3.4)], are still different (see also $\mathrm{Im}\{\Sigma_c\}$), since the initial shift has no effect on the HOMO-LUMO gap; however, the QPE in the shifted GW@LDA case has now a solution far from the satellites, and less weight is lost to them in the spectral function as compared with plain GW@LDA. This is coherent with the Z-factors reported in Table 3.3, and with their definition, Eq. (2.119),

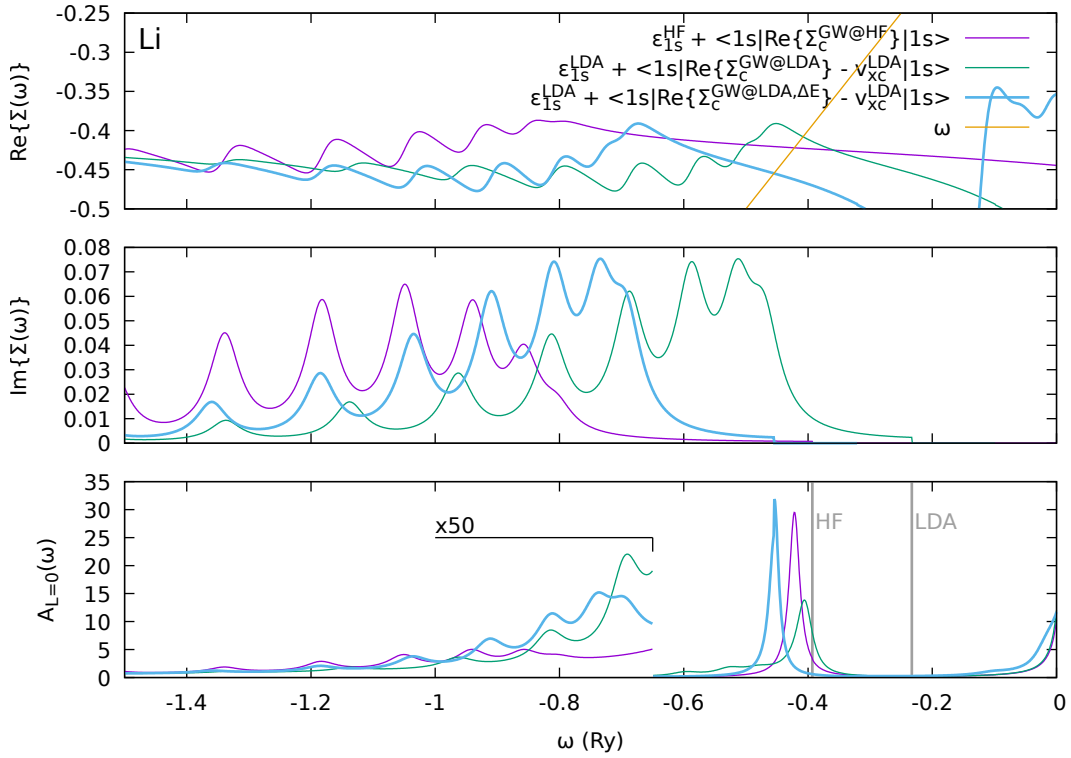

Figure 3.7. $1s$ orbital self-energy and spectral function of Li as obtained with GW upon various starting points: HF, LDA and LDA with initial shift ΔE.

which implies that a flatter Σ_c gives less QP renormalization.

Things are different for Li, as one can see in Figure 3.7. With GW@HF the QPE solution is found again in a rather flat region of $\mathrm{Re}\{\Sigma_c\}$, whereas the opposite is true with GW@LDA. Using the ΔE shift does not change the situation, since $\mathrm{Re}\{\Sigma\}$ shows a significant slope over the whole region of the QPE solution: this is due to the excitations at $\varepsilon_{\mathrm{HOMO}} - \Omega_s$ and $\varepsilon_{\mathrm{LUMO}} + \Omega_s$ [cfr. Eq. (3.4)] being close to each other, as a consequence of the small HOMO-LUMO gap. Furthermore, there is also a qualitative difference between GW@HF and GW@LDA that makes it difficult for the respective $\mathrm{Re}\{\Sigma_c\}$ to be made similar through a simple shift: the satellites with GW@LDA have a steep onset, where much of the weight is concentrated; whereas with GW@HF the onset is more gentle and the weight is concentrated at lower ω. This is consistent with the results for the dynamical polarizabilities seen in Section 3.3.5 (although the differences are in general not as stark in the self-energy, and in the current Section larger broadenings are being used).

Overall, correcting the general issues of overbinding and underbinding, found in GW@HF and GW@LDA respectively, appears to be beyond the capability of the ΔE shift. The shift has basically no effect on GW@HF, so one has to turn their attention to GW@LDA. In the limiting case of noble gases, a description similar to that of GW@HF is recovered with the ΔE shift, so that overbinding is obtained. In the limiting case of group-1 atoms, the ΔE shift worsens the overbinding already present in GW@LDA. In these atoms an error

cancellation between the overscreening and the eigenvalue inaccuracy, both features of the LDA starting point, seems to make GW@LDA somewhat accurate. Therefore using the ΔE shift treatment may end up breaking the balance.

In order to find the right compromise between the overbinding of GW@HF and the underbinding of GW@LDA, it was found successful to incorporate a fraction of non-local Fock exchange in the KS-DFT starting point [38, 56], for example by using the PBE0 functional. This means resorting to a generalized KS scheme. In the general assessment of Section 3.6, the PBE and PBE0 starting point will be indeed considered.

3.5 Spherical Sham-Schlüter equation

In this Section we specialize the SSE, Eq. (2.162), for the spherical problem in the usual B-spline/SH representation.

3.5.1 Linear system on spherical harmonics and B-splines

We begin by noting that the SSE linear system is a rank-deficient one [125, 126], due to the degree of freedom given by the possibility of incorporating inside the xc potential an arbitrary shift of the zero energy. In the spherical problem, this degree of freedom can be saturated by imposing the known theoretical asymptotic behaviour dominated by the exchange contribution [111, 112, 126],

$$v_{\mathrm{xc}}(r) = \bar{v}_{\mathrm{xc}}(r) - e^2/r, \tag{3.87}$$

with $\bar{v}_{\mathrm{xc}} \to 0$ for $r \to \infty$.

We now consider the unknown of the SSE, the xc potential v_{xc}, and choose to treat it as a wave-function-like object (or a vector) adopting the representation of Eq. (3.22), i.e.:

$$v_{xc}(\mathbf{r}) = \frac{1}{r}\sum_{lm}[v^0_{\mathrm{xc}}(r)]_l Y_{lm}(r). \tag{3.88}$$

The spherical symmetry of the charge density implies a spherically symmetric xc potential, meaning all the angular components of v_{xc} with $l \neq 0$ vanish. Therefore, we can define

$$v_{\mathrm{xc}}(r) = v_{\mathrm{xc}}(\mathbf{r}) \qquad \text{and} \qquad v^0_{\mathrm{xc}}(r) = [v^0_{\mathrm{xc}}(r)]_0, \tag{3.89}$$

and write

$$v_{\mathrm{xc}}(r) = \frac{1}{r}v^0_{\mathrm{xc}}(r)Y_{00}(r) = \frac{1}{\sqrt{4\pi}r}v^0_{\mathrm{xc}}(r). \tag{3.90}$$

By expressing all the operators in Eq. (2.162) in the SH representation, Eq. (3.30), and by plugging in Eq. (3.90), the linear system can be expressed as

$$\sum_j A_{ij}x_j = b_i, \tag{3.91}$$

with x being v^0_{xc}. We shall term A and b the *kernel* and the *inhomogeneity* of the SSE respectively. In real space, they read

$$A(r,r') = \sum_l^{l_{\max}} (2l+1) C^{00}_{l0,l0} \frac{1}{rr'} \int \frac{d\omega}{2\pi i} G^{\text{KS}}_l(r,r',\omega) G_l(r',r,\omega), \tag{3.92}$$

$$b(r) = \sum_l^{l_{\max}} (2l+1) \frac{1}{r} \int dr' \int dr'' \int \frac{d\omega}{2\pi i} G^{\text{KS}}_l(r,r',\omega) \Sigma_l(r',r'',\omega) G_l(r'',r,\omega); \tag{3.93}$$

whereas in B-spline space they become

$$A_{ii'} = \sum_l^{l_{\max}} (2l+1) C^{00}_{l0,l0} \int \frac{d\omega}{2\pi i} \sum_{jkj'k'} [G^{\text{KS}}_l(\omega)]^{jj'} [G_l(\omega)]^{kk'} B^3_{ijk} B^3_{i'j'k'}, \tag{3.94}$$

$$b_i = \sum_l^{l_{\max}} (2l+1) \int \frac{d\omega}{2\pi i} \sum_{jk} [G^{\text{KS}}_l(\omega) \Sigma_l(\omega) G_l(\omega)]^{jk} B^3_{ijk}. \tag{3.95}$$

Imposing the constraint in Eq. (3.87) amounts to replacing its analogous form for v^0_{xc} (which tends to $-\sqrt{4\pi}e^2$ in the long range) in the linear system and then solving for $\bar{v}^0_{\text{xc}}$ (which tends to zero instead). Then a solution with minimum norm can be found for $\bar{v}^0_{\text{xc}}$ using a singular value decomposition (SVD)-based solver [198]. Further details on the numerical inversion of the SSE are found in Section 3.6.2.

Note that in the iterative procedure it is necessary to use the solution from one step as an input for the next one. However, the solution given at each step is v^0_{xc} in B-spline space, and it is represented as a vector. In order to obtain G^{KS}, one needs v_{xc} in the form of a rank-2 vector needed to compute the KS Hamiltonian to be diagonalized. This is achieved by AGWX by converting the solution v^0_{xc} to real space, computing v_{xc} according to Eq. (3.90), and re-converting v_{xc} to B-spline space as a rank-2 operator.

3.5.2 Frequency integrations

Different methods can be employed to carry out the frequency integrals involved in the SSE. We shall focus on two of them, the choice of which depends on the knowledge of the poles of the Green's functions and the self-energy entering the SSE. Indeed, if the poles are known, the Lehmann representation can be used for all the Green's functions and the self-energy entering the frequency integrals. The integrations can then be simply performed analytically by closing a contour in the complex plane. Doing this to the kernel of the SSE yields

$$\begin{aligned} A_{ii'} =& \sum_l^{l_{\max}} \sum_{mn} (2l+1) C^{00}_{l0,l0} \\ & \times \sum_{jk} B^3_{ijk} (P^{\text{KS}}_{ml})^j (P_{nl})^k \sum_{j'k'} B^3_{i'j'k'} (P^{\text{KS}}_{ml})^{j'} (P_{nl})^{k'} \\ & \times \frac{1}{\varepsilon^{\text{KS}}_{ml} - \varepsilon_{nl}} \left[\bar{\theta}_{ml} \theta_{nl} - \theta_{ml} \bar{\theta}_{nl} \right]. \end{aligned} \tag{3.96}$$

Here single-particle orbitals and eigenvalues were used also for the interacting G. It should be noted that if the LSSE is used, this integration method is always trivial to apply to the calculation of the kernel, for it only contains non-interacting G^{KS}'s.

In the general case, the poles of the interacting G and those of Σ are unknown. In AGWX we have the means to compute these operators on a grid in a one-shot fashion, as seen in Section 3.4.2, but then their poles would have to be found, by employing e.g. costly fitting procedures. An integration over the real frequency axis is also prohibitive if the accuracy required by the inversion of the SSE kernel is to be attained.

A smarter way to perform the frequency integrals may be to take advantage of the time-ordered structure of the poles of the operators inside the integrands, much like is done in the contour deformation technique. A contour can be closed comprising the real axis, and a vertical path in the complex plane passing through the KS system's Fermi energy, which is found somewhere in the KS gap region of real frequencies. If the contour is closed by leaving the poles of the operators outside (in a similar fashion of the contour in Figure 3.5 leaving the poles of W outside), Cauchy's theorem then guarantees the vanishing of the integral over the contour, and the integral over the real axis equates the negative of the integral over the vertical path. This would then allow one to integrate over the vertical path instead of the real axis, amounting to an analytical continuation technique. The advantage of this method over a real axis integration would seemingly be the same that the contour deformation has: integrating a sum of lorentzian function products over an imaginary grid given by the vertical path, with the lorentzian functions all being centered around the same frequency.

I tried applying this method to the kernel of the non-linearized SSE, but the results were found to be very poor. Some matrix elements of the kernel's integrand, albeit small, were found to decay at very high frequencies, requiring far reaching grids to converge the integral. This is a consequence of the hard-to-integrate "fat tails" of lorentzian functions associated to poles higher in energy. Rational interpolation techniques [199–202] were employed to try and approximate these tails, but they also failed to give satisfactory results, although showing an improvement with small basis sets.

A similar and more suitable technique was found to be the semi-analytical procedure used in the contour deformation, which relies on the analytical integration of all the G's, followed by an integration over an imaginary grid for the remaining W (if any) inside Σ. Obviously, the analytical integration of all the G's is in practice possible only in the LSSE, when these become G^{KS}'s and the poles are known. This technique is described in Section 3.5.5.

3.5.3 Integration in the EXX inhomogeneity

The exact-exchange (EXX) inhomogeneity is obtained by plugging the Fock exchange Σ^x in the SSE. In the general case of no linearization, one has to rely on an initial HF calculation, which produces a HF G and the Fock self-energy Σ^x obtained with the HF density matrix. Both then have to be plugged into the SSE. The poles of the HF G are known, whereas the exchange potential trivially does not have any. Therefore, analytical integration by closing

a contour gives

$$
\begin{aligned}
b_i^{\mathrm{EXX}} =& \sum_{mn} \sum_{l}^{l_{\max}} (2l+1) \\
& \times \sum_{j'k'} (P_{ml}^{\mathrm{KS}})^{j'} (\Sigma_l^x)_{j'k'} (P_{nl})^{k'} \sum_{jk} B_{ijk}^3 (P_{ml}^{\mathrm{KS}})^j (P_{nl})^k \\
& \times \frac{1}{\varepsilon_{ml}^{\mathrm{KS}} - \varepsilon_{nl}} \left[\bar{\theta}_{ml} \theta_{nl} - \theta_{ml} \bar{\theta}_{nl} \right],
\end{aligned} \tag{3.97}
$$

whereas the kernel is the same seen in the previous section, Eq. (3.96). The LSSE in EXX approximation is obtained by replacing all the wavefunctions and energies with the KS ones, both in the kernel and in the inhomogeneity.

3.5.4 Integration in the MP2 inhomogeneity

In order to avoid most of the difficulties encountered with the frequency integrals discussed in Section 3.5.2, we shall make the problem simpler from now on by focusing on the LSSE. We then retain the results of Eqs. (3.96) and (3.97) for the kernel and the EXX inhomogeneity, with all the eigenvalues and eigenfunctions changed to the KS ones.Here we present the calculation of the 2B inhomogeneity.

Computing the KS xc potential from the 2B self-energy using the LSSE is almost equivalent to computing it by applying the optimized effective potential (OEP) method to the MP2 energy functional. Following the notation of Ref. 124, one can see that the former method lacks the contribution coming from the term $E_c^{\Delta\mathrm{HF}}$ in the energy functional, accounting for MP2 theory being applied on top of KS eigenvalues and orbitals instead of HF ones. However, this term is negligible and therefore dropped in many calculations, such as those reported in Refs. 198 and 203. The self-energy-based method presented and the OEP method are then, in practice, equivalent. For continuity with the literature, from now on we shall refer to the xc potentials obtained from the 2B self-energy as MP2 potentials.

By plugging the 2B self-energy, from Eqs. (3.16) and (3.17), into the linearized inhomogeneity, obtained from Eq. (3.95) and the replacement $G \to G^{\mathrm{KS}}$, we get the correlation part of the inhomogeneity,

$$
\begin{aligned}
b_{c,i}^{\mathrm{MP2,d}} =& \sum_{pqrst} \sum_{Ll_q l_r l_s l_c} \frac{2e^2}{4\pi} C^{L0}_{l_r 0, l_c 0} C^{l_c 0}_{l_q 0, l_s 0} \\
& \times \sqrt{(2L+1)(2l_q+1)(2l_r+1)(2l_s+1)} \\
& \times \langle pL, ql_q | \, v_{l_c} \, | rl_r, sl_s \rangle \langle rl_r, sl_s | \, v_{l_c} \, | tL, ql_q \rangle \\
& \times I^{pqrst}_{Ll_q l_r l_s} \sum_{jk} B^3_{ijk} P^j_{pL} P^k_{tL},
\end{aligned} \tag{3.98}
$$

$$
\begin{aligned}
b_{c,i}^{\mathrm{MP2,x}} =& - \sum_{pqrst} \sum_{Ll_q l_r l_s l_c l_w} e^2 (2L+1) C^{l_c l_s L}_{l_w l_r l_q} \\
& \times \langle pL, ql_q | \, v_{l_w} \, | rl_r, sl_s \rangle \langle rl_r, sl_s | \, v_{l_c} \, | ql_q tL \rangle \\
& \times I^{pqrst}_{Ll_q l_r l_s} \sum_{jk} B^3_{ijk} P^j_{pL} P^k_{tL}.
\end{aligned} \tag{3.99}
$$

where

$$I^{pqrst}_{Ll_ql_rl_s} = \left[\theta_{pL}\theta_{ql_q}\bar{\theta}_{rl_r}\bar{\theta}_{sl_s} - \bar{\theta}_{pL}\bar{\theta}_{ql_q}\theta_{rl_r}\theta_{sl_s}\right] \times \left[\frac{\delta_{pt}}{(\varepsilon_{pL}+\varepsilon_{ql_q}-\varepsilon_{rl_r}-\varepsilon_{sl_s})^2} + \frac{2(1-\delta_{pt})}{(\varepsilon_{tL}-\varepsilon_{pL})(\varepsilon_{pL}+\varepsilon_{ql_q}-\varepsilon_{rl_r}-\varepsilon_{sl_s})}\right]. \tag{3.100}$$

b_c will then have to be summed to b^{EXX} in the LSSE. The factor 2 in the direct term stems from considering the spin-unpolarized case; in the spin-polarized one the inhomogeneity becomes spin-dependent and the factor must be removed. More insight on how the frequency integrals are performed, resulting in the $I^{pqrst}_{Ll_ql_rl_s}$ term, can be found in the next section.

3.5.5 Integration in the RPA inhomogeneity

In integrating the GW self-energy inside the so-called RPA inhomogeneity of the LSSE, we face the same problem that led us to using the contour deformation in GW: not knowing where the poles of W are. By changing the order of the frequency integrals in the RPA correlation inhomogeneity we get

$$b_{\mathrm{c}}^{\mathrm{RPA}}(\mathbf{r}) = -\int\frac{d\omega'}{2\pi i}\int\frac{d\omega}{2\pi i}\int d\mathbf{r}_1\int d\mathbf{r}_2 \times G^{\mathrm{KS}}(\mathbf{r},\mathbf{r}_1;\omega)G^{\mathrm{KS}}(\mathbf{r}_1,\mathbf{r}_2,\omega+\omega')G^{\mathrm{KS}}(\mathbf{r}_2,\mathbf{r};\omega) \times W(\mathbf{r}_1,\mathbf{r}_2,\omega'). \tag{3.101}$$

The ω integral involving the G^{KS} can be performed analytically by using the Lehmann form of G^{KS}, obtaining

$$\int\frac{d\omega}{2\pi i}\sum_{\alpha\beta\gamma}\varphi^{\mathrm{KS}}_\alpha(\mathbf{r})\varphi^{\mathrm{KS}*}_\alpha(\mathbf{r}_1)\varphi^{\mathrm{KS}}_\beta(\mathbf{r}_1)\varphi^{\mathrm{KS}*}_\beta(\mathbf{r}_2)\varphi^{\mathrm{KS}}_\gamma(\mathbf{r}_2)\varphi^{\mathrm{KS}*}_\gamma(\mathbf{r}) \times\left[\frac{1}{\omega-\varepsilon^{\mathrm{KS}}_\alpha\pm i\eta_\alpha}\times\frac{1}{\omega+\omega'-\varepsilon^{\mathrm{KS}}_\beta\pm i\eta_\beta}\times\frac{1}{\omega-\varepsilon^{\mathrm{KS}}_\gamma\pm i\eta_\gamma}\right],$$

and then applying the residue theorem (closing above here). This yields two contributions: one summation having the indices $\alpha\neq\gamma$,

$$\sum_{\alpha\neq\gamma,\beta}\varphi^{\mathrm{KS}}_\alpha(\mathbf{r})\varphi^{\mathrm{KS}*}_\alpha(\mathbf{r}_1)\varphi^{\mathrm{KS}}_\beta(\mathbf{r}_1)\varphi^{\mathrm{KS}*}_\beta(\mathbf{r}_2)\varphi^{\mathrm{KS}}_\gamma(\mathbf{r}_2)\varphi^{\mathrm{KS}*}_\gamma(\mathbf{r}) \times\left\{\frac{\theta(\mu-\varepsilon^{\mathrm{KS}}_\alpha)}{[\varepsilon^{\mathrm{KS}}_\alpha+\omega'-\varepsilon^{\mathrm{KS}}_\beta\pm i(\eta_\alpha\pm\eta_\beta)][\varepsilon^{\mathrm{KS}}_\alpha-\varepsilon^{\mathrm{KS}}_\gamma\pm i(\eta_\alpha\pm\eta_\gamma)]}\right. +\frac{\theta(\mu-\varepsilon^{\mathrm{KS}}_\beta)}{[\varepsilon^{\mathrm{KS}}_\beta-\omega'-\varepsilon^{\mathrm{KS}}_\alpha\pm i(\eta_\beta\pm\eta_\alpha)][\varepsilon^{\mathrm{KS}}_\beta-\omega'-\varepsilon^{\mathrm{KS}}_\gamma\pm i(\eta_\beta\pm\eta_\gamma)]} +\left.\frac{\theta(\mu-\varepsilon^{\mathrm{KS}}_\gamma)}{[\varepsilon^{\mathrm{KS}}_\gamma-\varepsilon^{\mathrm{KS}}_\alpha\pm i(\eta_\gamma\pm\eta_\alpha)][\varepsilon^{\mathrm{KS}}_\gamma+\omega'-\varepsilon^{\mathrm{KS}}_\beta\pm i(\eta_\gamma\pm\eta_\beta)]}\right\}, \tag{3.102}$$

and one summation having $\alpha = \gamma$,

$$\sum_{\alpha\beta} \varphi_\alpha^{\mathrm{KS}}(\mathbf{r})\varphi_\alpha^{\mathrm{KS}*}(\mathbf{r}_1)\varphi_\beta^{\mathrm{KS}}(\mathbf{r}_1)\varphi_\beta^{\mathrm{KS}*}(\mathbf{r}_2)\varphi_\alpha^{\mathrm{KS}}(\mathbf{r}_2)\varphi_\alpha^{\mathrm{KS}*}(\mathbf{r}) \times \left\{ \frac{\theta(\mu-\varepsilon_\beta^{\mathrm{KS}})}{[\varepsilon_\beta^{\mathrm{KS}}-\omega'-\varepsilon_\alpha^{\mathrm{KS}}\pm i(\eta_\beta\pm\eta_\alpha)]^2} - \frac{\theta(\mu-\varepsilon_\alpha^{\mathrm{KS}})}{[\varepsilon_\alpha^{\mathrm{KS}}+\omega'-\varepsilon_\beta^{\mathrm{KS}}\pm i(\eta_\alpha\pm\eta_\beta)]^2} \right\}. \tag{3.103}$$

Let us now consider the last expression: if we multiply the first addendum and the second addendum by the identity written as

$$[\theta(\mu-\varepsilon_\alpha^{\mathrm{KS}})+\theta(\varepsilon_\alpha^{\mathrm{KS}}-\mu)] \qquad \text{and} \qquad [\theta(\mu-\varepsilon_\beta^{\mathrm{KS}})+\theta(\varepsilon_\beta^{\mathrm{KS}}-\mu)]$$

respectively, only the two terms containing

$$\theta(\mu-\varepsilon_\alpha^{\mathrm{KS}})\theta(\varepsilon_\beta^{\mathrm{KS}}-\mu) \qquad \text{and} \qquad \theta(\varepsilon_\alpha^{\mathrm{KS}}-\mu)\theta(\mu-\varepsilon_\beta^{\mathrm{KS}})$$

will survive. The same trick can be applied twice to the leftover contribution, after expressing the middle addendum as

$$\frac{\theta(\mu-\varepsilon_\beta^{\mathrm{KS}})}{\varepsilon_\alpha^{\mathrm{KS}}-\varepsilon_\gamma^{\mathrm{KS}}\pm i(\eta_\alpha\pm\eta_\gamma)} \times \left[\frac{1}{\varepsilon_\beta^{\mathrm{KS}}-\omega'-\varepsilon_\alpha^{\mathrm{KS}}\pm i(\eta_\beta\pm\eta_\alpha)} - \frac{1}{\varepsilon_\beta^{\mathrm{KS}}-\omega'-\varepsilon_\gamma^{\mathrm{KS}}\pm i(\eta_\beta\pm\eta_\gamma)} \right].$$

We are left with a function of ω' having the time-ordered pole structure:

$$\begin{aligned}
&\sum_{\alpha\beta\gamma} \varphi_\alpha^{\mathrm{KS}}(\mathbf{r})\varphi_\alpha^{\mathrm{KS}*}(\mathbf{r}_1)\varphi_\beta^{\mathrm{KS}}(\mathbf{r}_1)\varphi_\beta^{\mathrm{KS}*}(\mathbf{r}_2)\varphi_\gamma^{\mathrm{KS}}(\mathbf{r}_2)\varphi_\gamma^{\mathrm{KS}*}(\mathbf{r}) \\
&\times \left\{ \delta_{\alpha\gamma} \left[\frac{\theta(\varepsilon_\alpha^{\mathrm{KS}}-\mu)\theta(\mu-\varepsilon_\beta^{\mathrm{KS}})}{(\varepsilon_\alpha^{\mathrm{KS}}-\varepsilon_\beta^{\mathrm{KS}}+\omega'-i\eta)^2} - \frac{\theta(\mu-\varepsilon_\alpha^{\mathrm{KS}})\theta(\varepsilon_\beta^{\mathrm{KS}}-\mu)}{(\varepsilon_\alpha^{\mathrm{KS}}-\varepsilon_\beta^{\mathrm{KS}}+\omega'+i\eta)^2} \right] \right. \\
&+(1-\delta_{\alpha\gamma}) \frac{1}{\varepsilon_\gamma^{\mathrm{KS}}-\varepsilon_\alpha^{\mathrm{KS}}} \\
&\times \left[\frac{\theta(\varepsilon_\alpha^{\mathrm{KS}}-\mu)\theta(\mu-\varepsilon_\beta^{\mathrm{KS}})}{\varepsilon_\alpha^{\mathrm{KS}}-\varepsilon_\beta^{\mathrm{KS}}+\omega'-i\eta} - \frac{\theta(\mu-\varepsilon_\alpha^{\mathrm{KS}})\theta(\varepsilon_\beta^{\mathrm{KS}}-\mu)}{\varepsilon_\alpha^{\mathrm{KS}}-\varepsilon_\beta^{\mathrm{KS}}+\omega'+i\eta} \right. \\
&\left. \left. - \frac{\theta(\varepsilon_\gamma^{\mathrm{KS}}-\mu)\theta(\mu-\varepsilon_\beta^{\mathrm{KS}})}{\varepsilon_\gamma^{\mathrm{KS}}-\varepsilon_\beta^{\mathrm{KS}}+\omega'-i\eta} + \frac{\theta(\mu-\varepsilon_\gamma^{\mathrm{KS}})\theta(\varepsilon_\beta^{\mathrm{KS}}-\mu)}{\varepsilon_\gamma^{\mathrm{KS}}-\varepsilon_\beta^{\mathrm{KS}}+\omega'+i\eta} \right] \right\}.
\end{aligned} \tag{3.104}$$

Thanks to the time-ordered pole structure of both this expression and W, it is possible to perform the ω' integration in Eq. (3.101) via analytic continuation to the imaginary axis.

Given the similarity with the contour deformation technique, a semi-analytical procedure on a tangent-like grid can be employed to perform the numerical integration. After moving to the imaginary axis and taking $\eta \to 0$, two kinds of integrals will need to be computed using such procedure, corresponding to those in Eqs. (D.1) and (D.2).

All is left to do is give an expression of b_c in B-spline space for the spherical problem. The smartest way to do that is by replacing the GW self-energy expression in the B-spline/SH representation, Eq. (3.70), (3.72) and (3.73), inside Eq. (3.95), and repeat the steps of this section. We obtain

$$\begin{aligned} b_{c,i} =& \sum_{L=0} \frac{2L+1}{\pi} \sum_{l_g l_w} \sqrt{\frac{(2l_g+1)(2l_w+1)}{4\pi(2L+1)}} C^{L0}_{l_g 0 l_w 0} \\ & \times \sum_{m=1}^{M} \sum_{ptn} I(i\omega_m, i\omega_{m+1})^{ptn}_{Ll_g} \langle pL, nl_g | W(i\Omega'_m)_{l_w} | nl_g, tL \rangle \sum_{jk} B^3_{ijk} P^j_{pL} P^k_{tL}, \end{aligned} \tag{3.105}$$

with

$$\begin{aligned} & I(i\omega_m, i\omega_{m+1})^{ptn}_{Ll_g} \\ & = \delta_{pt} \left[\frac{\omega'}{(\omega')^2 + (\varepsilon^{\mathrm{KS}}_{nl_g} - \varepsilon^{\mathrm{KS}}_{pL})^2} \right]_{\omega_m}^{\omega^{m+1}} \\ & \times \left[\theta(\mu - \varepsilon^{\mathrm{KS}}_{pL}) \theta(\varepsilon^{\mathrm{KS}}_{nl_g} - \mu) - \theta(\mu - \varepsilon^{\mathrm{KS}}_{nl_g}) \theta(\varepsilon^{\mathrm{KS}}_{pL} - \mu) \right] \\ & + (1 - \delta_{pt}) \frac{1}{\varepsilon^{\mathrm{KS}}_{pL} - \varepsilon^{\mathrm{KS}}_{tL}} \left[\arctan\left(\frac{\omega'}{\varepsilon^{\mathrm{KS}}_{nl_g} - \varepsilon^{\mathrm{KS}}_{pL}} \right) \right]_{\omega'_m}^{\omega'_{m+1}} \\ & \times \left[\theta(\mu - \varepsilon^{\mathrm{KS}}_{pL}) \theta(\varepsilon^{\mathrm{KS}}_{nl_g} - \mu) - \theta(\varepsilon^{\mathrm{KS}}_{pL} - \mu) \theta(\mu - \varepsilon^{\mathrm{KS}}_{nl_g}) \right] \\ & - (1 - \delta_{pt}) \frac{1}{\varepsilon^{\mathrm{KS}}_{pL} - \varepsilon^{\mathrm{KS}}_{tL}} \left[\arctan\left(\frac{\omega'}{\varepsilon^{\mathrm{KS}}_{nl_g} - \varepsilon^{\mathrm{KS}}_{tL}} \right) \right]_{\omega'_m}^{\omega'_{m+1}} \\ & \times \left[\theta(\mu - \varepsilon^{\mathrm{KS}}_{tL}) \theta(\varepsilon^{\mathrm{KS}}_{nl_g} - \mu) - \theta(\varepsilon^{\mathrm{KS}}_{tL} - \mu) \theta(\mu - \varepsilon^{\mathrm{KS}}_{nl_g}) \right]. \end{aligned} \tag{3.106}$$

Since W is real on the imaginary axis after $\eta \to 0$ is taken, the two contributions multiplied by $(1 - \delta_{pq})$ give the same contribution after the summations are performed.

3.5.6 Integration in the SOSEX inhomogeneity

For the integration of the SOSEX self-energy, the same technique introduced in the previous section can be used. The ω integral of the inhomogeneity can still be performed by using the ω-dependent G in Eq. (3.8) together with the other two outside Σ, obtaining a result similar to Eq. (3.104). The ω_2 integral of Eq. (3.8) is also easily evaluated as done in Section 3.1.2. Putting the two results together and applying the analytic continuation to

the imaginary axis gives

$$\begin{aligned}
&\int \frac{d\omega_1}{2\pi} \sum_{\substack{\alpha\beta\gamma \\ \mu\nu}} \langle \alpha\mu | \, W(i\omega_1) \, | \nu\beta \rangle \, \langle \nu\beta | \, v \, | \mu\gamma \rangle \, \varphi_\alpha(\mathbf{r}) \varphi^*_\gamma(\mathbf{r}) \\
&\times \Bigg\{ \delta_{\alpha\gamma} \frac{(\theta_\alpha \bar{\theta}_\beta - \bar{\theta}_\alpha \theta_\beta)(\theta_\mu \bar{\theta}_\nu - \bar{\theta}_\mu \theta_\nu)}{[i\omega_1 - (\varepsilon_\beta - \varepsilon_\alpha)]^2 [i\omega_1 - (\varepsilon_\mu - \varepsilon_\nu)]} \\
&- \frac{1 - \delta_{\alpha\gamma}}{\varepsilon_\alpha - \varepsilon_\gamma} \Bigg[\frac{(\theta_\alpha \bar{\theta}_\beta - \bar{\theta}_\alpha \theta_\beta)(\theta_\mu \bar{\theta}_\nu - \bar{\theta}_\mu \theta_\nu)}{[i\omega_1 - (\varepsilon_\beta - \varepsilon_\alpha)][i\omega_1 - (\varepsilon_\mu - \varepsilon_\nu)]} \\
&- \frac{(\theta_\gamma \bar{\theta}_\beta - \bar{\theta}_\gamma \theta_\beta)(\theta_\mu \bar{\theta}_\nu - \bar{\theta}_\mu \theta_\nu)}{[i\omega_1 - (\varepsilon_\beta - \varepsilon_\gamma)][i\omega_1 - (\varepsilon_\mu - \varepsilon_\nu)]} \Bigg] \Bigg\}
\end{aligned} \tag{3.107}$$

Employing the semi-analytical procedure to compute the ω_1 integral requires the approximate evaluations of Eqs. (D.3) and Eq. (D.4) when poles are first order; when $(\beta, \alpha) = (\mu, \nu)$ (i.e. $a = b$) in the summation, Eqs. (D.2) and (D.5) are needed instead. Using these results and moving to the B-spline/SH representation yields an equation resembling the one for the MP2 exchange inhomogeneity, Eq. (3.99):

$$\begin{aligned}
b_{c,i}^{\mathrm{SOSEX}} = &- \sum_{pqrst} \sum_{Ll_q l_r l_s l_c l_w} \sum_{m=1}^{M-1} e^2 \frac{(2L+1)}{\pi} C^{l_c l_s L}_{l_w l_r l_q} \\
&\times \langle pL, ql_q | \, W(i\Omega_m)_{l_w} \, | rl_r, sl_s \rangle \\
&\times \langle rl_r, sl_s | \, v_{l_c} \, | ql_q tL \rangle \, I(\omega_m, \omega_{m+1})^{pqrst}_{Ll_q l_r l_s} \\
&\times \sum_{jk} B^3_{ijk} P^j_{pL} P^k_{tL},
\end{aligned} \tag{3.108}$$

where

$$\begin{aligned}
&I(\omega_m, \omega_{m+1})^{pqrst}_{Ll_q l_r l_s} \\
&= \delta_{pt} \Big[\Big(1 - \delta_{(p,q,L,l_q),(s,r,l_s,l_r)} \Big) \, R(\omega_m, \omega_{m+1})^{pqrs}_{Ll_q l_r l_s} \\
&+ \delta_{(p,q,L,l_q),(s,r,l_s,l_r)} R(\omega_m, \omega_{m+1})^{pr}_{Ll_r} \Big] \\
&+ \frac{1 - \delta_{pt}}{\varepsilon_{tL} - \varepsilon_{pL}} \Big[\Big(1 - \delta_{(p,q,L,l_q),(s,r,l_s,l_r)} \Big) \\
&\times \Big(S(\omega_m, \omega_{m+1})^{pqrs}_{Ll_q l_r l_s} - S(\omega_m, \omega_{m+1})^{tqrs}_{Ll_q l_r l_s} \Big) \\
&+ \delta_{(p,q,L,l_q),(s,r,l_s,l_r)} \\
&\times \Big(S(\omega_m, \omega_{m+1})^{pr}_{Ll_r} - S(\omega_m, \omega_{m+1})^{tr}_{Ll_r} \Big) \Big] ;
\end{aligned} \tag{3.109}$$

The terms in the analytical integral I read:

$$\begin{aligned}
&R(\omega_m,\omega_{m+1})^{pqrs}_{Ll_ql_rl_s} \\
&= \frac{1}{\varepsilon_{rl_r}-\varepsilon_{pL}-(\varepsilon_{ql_q}-\varepsilon_{sl_s})}\left[\frac{\omega}{\omega^2+(\varepsilon_{rl_r}-\varepsilon_{pL})^2}\right. \\
&\left.+\frac{\arctan\left(\frac{\omega}{\varepsilon_{rl_r}-\varepsilon_{pL}}\right)-\arctan\left(\frac{\omega}{\varepsilon_{ql_q}-\varepsilon_{sl_s}}\right)}{\varepsilon_{rl_r}-\varepsilon_{pL}-(\varepsilon_{ql_q}-\varepsilon_{sl_s})}\right]^{\omega_{m+1}}_{\omega_m} \\
&\times\left[\theta_{pL}\bar{\theta}_{rl_r}-\bar{\theta}_{pL}\theta_{rl_r}\right]\left[\theta_{ql_q}\bar{\theta}_{sl_s}-\bar{\theta}_{ql_q}\theta_{sl_s}\right],
\end{aligned} \tag{3.110}$$

$$\begin{aligned}
&S(\omega_m,\omega_{m+1})^{pqrs}_{Ll_ql_rl_s} \\
&= -\left[\frac{\arctan\left(\frac{\omega}{\varepsilon_{rl_r}-\varepsilon_{pL}}\right)-\arctan\left(\frac{\omega}{\varepsilon_{ql_q}-\varepsilon_{sl_s}}\right)}{\varepsilon_{rl_r}-\varepsilon_{pL}-(\varepsilon_{ql_q}-\varepsilon_{sl_s})}\right]^{\omega_{m+1}}_{\omega_m} \\
&\times\left[\theta_{pL}\bar{\theta}_{rl_r}-\bar{\theta}_{pL}\theta_{rl_r}\right]\left[\theta_{ql_q}\bar{\theta}_{sl_s}-\bar{\theta}_{ql_q}\theta_{sl_s}\right],
\end{aligned} \tag{3.111}$$

$$\begin{aligned}
R(\omega_m,\omega_{m+1})^{pr}_{Ll_r} &= \left[-\frac{(\varepsilon_{rl_r}-\varepsilon_{pL})\omega}{[\omega^2+(\varepsilon_{rl_r}-\varepsilon_{pL})^2]^2}\right]^{\omega_{m+1}}_{\omega_m} \\
&\times\left[-\theta_{pL}\bar{\theta}_{rl_r}-\bar{\theta}_{pL}\theta_{rl_r}\right],
\end{aligned} \tag{3.112}$$

$$\begin{aligned}
S(\omega_m,\omega_{m+1})^{pr}_{Ll_r} &= \left[\frac{\omega}{\omega^2+(\varepsilon_{rl_r}-\varepsilon_{pL})^2}\right]^{\omega_{m+1}}_{\omega_m} \\
&\times\left[-\theta_{pL}\bar{\theta}_{rl_r}-\bar{\theta}_{pL}\theta_{rl_r}\right].
\end{aligned} \tag{3.113}$$

3.5.7 Numerical results for xc potentials

The xc potentials for atoms as obtained from the self-consistent solution of Eq. (2.162) using the EXX, MP2 and RPA functionals have already been documented and characterized in the literature for a number of atoms, mostly up to Ar [121, 128, 169, 198, 204–208]. Here we also consider the solution of Eq. (2.162) with the GW+SOSEX self-energy and calculations are presented for an extended set of spherical atoms, including those from the 4th period (i.e. K, Ca, Mn, Zn, As and Kr), in which the $3d$ shell comes into play starting from Mn. Moreover, RPA calculations previously performed on closed-shell spherical atoms [169] were extended to spin-polarized spherical atoms having half-filled shells.

In Figure 3.8 I show the potentials for two of the heavier atoms presented in this work, Ca and Zn. The shell structure of the electronic charge in atoms is reflected on the potential

through the presence of bumps. These bumps are found between two regions in space where the charge density originates from different orbitals [33, 137, 209]. Local functionals used in KS-DFT such as LDA cannot describe the charge localization due to the atomic shell structure, displaying a smoother behaviour in the xc potential. PBE does better in this regard, but still yields xc potentials far away from the LSSE solutions, which properly account for exchange. Moreover, neither LDA nor PBE capture the correct $1/r$ decay of the xc potential (insets of Fig. 3.8), which is due to the predominance of exchange in the long-range [111, 112]. Finally, it can also be noticed how filling the shells progressively shortens the range of the potentials, in analogy with the density.

The inclusion of correlation of any kind generally has the effect of damping the bumps of the xc potential. In order to study correlation with a suitable scale, it is customary to resort to the correlation potential, which is obtained by removing the exchange contribution from the xc potential. Here we adopt the definition of Ref. 169, relying on the difference between two potentials evaluated at the respective self-consistent densities,

$$v_{\mathrm{c}}(\mathbf{r}) = v_{\mathrm{xc}}(\mathbf{r}; [\rho_{\mathrm{xc}}]) - v_{\mathrm{x}}(\mathbf{r}; [\rho_{\mathrm{x}}]), \tag{3.114}$$

i.e. the potential to be subtracted is the EXX one, v_{x} evaluated at its self-consistent density ρ_{x}. Some correlation potentials calculated that I computed are plotted in Figs. 3.9, 3.10, and 3.11. For He, Be and Ne a comparison is made with the exact results obtained by Umrigar and Gonze [112]. We note that we are comparing potentials obtained at self-consistency using the respective functionals: this is not the approach adopted by all authors, some preferring to evaluate the potentials with one iteration of the LSSE starting from accurate densities [198]. In any case, I verified that either choice does not change the final remarks that we will make.

Table 3.6 in Section 3.6.1 collects the ionization energies (IEs) as obtained from the KS HOMOs, which can be rationalized observing the behaviour of the respective xc potential as displayed in Fig. 3.9. The MP2 functional is known to yield the main features of the exact correlation potential, although often missing the correct scale [198, 207]. For instance, in He the MP2 potential is close to the exact one in the region near the nucleus, but poorly matches it in the medium and long range, consistently attaining higher values. As a result,

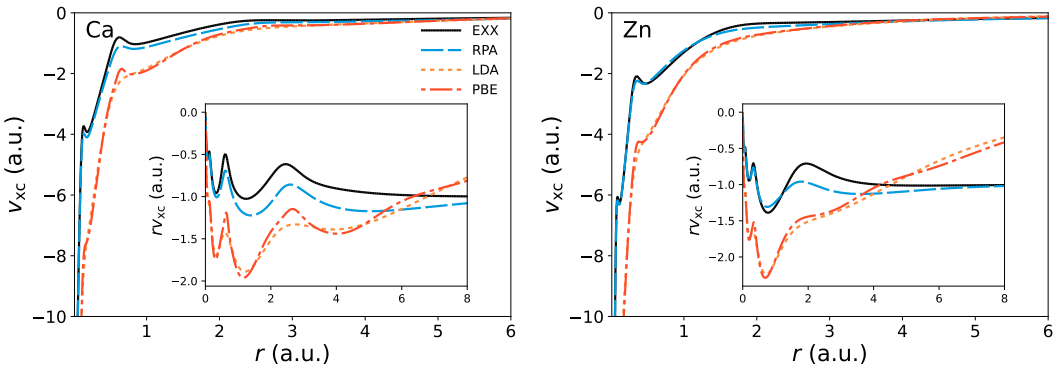

Figure 3.8. EXX, RPA, LDA and PBE xc potentials for Ca (left) and Zn (right). In the inset, the xc potentials multiplied by the radial coordinate.

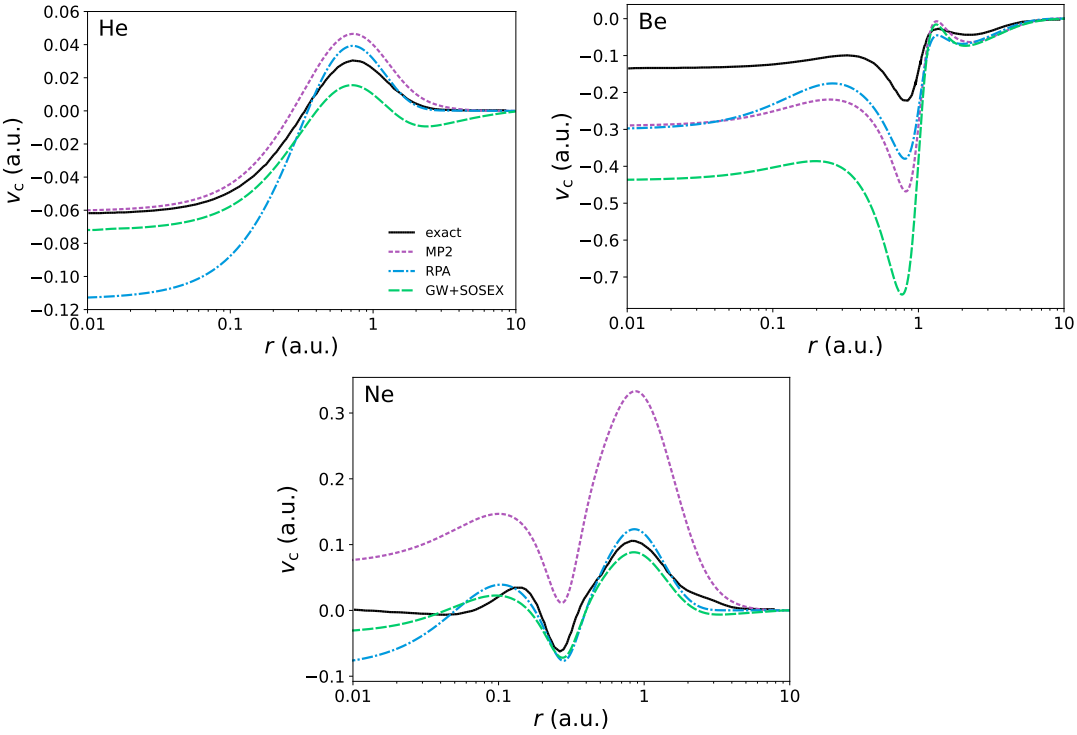

Figure 3.9. Correlation potentials for Helium, Beryllium and Neon. The MP2 correlation potential for Beryllium is computed on top of EXX orbitals and eigenvalues. Exact correlation potentials are from Ref. 112.

the MP2 HOMO level of He is too shallow and shows little improvement as compared with the EXX one. On the contrary, the RPA potential offers a poorer description in the short-range radial region, but more closely resembles the exact potential in the middle and long range. This leads to a markedly improved KS eigenvalue, almost exactly matching the one from experiments. In evaluating these results, one should not be fooled by the logarithmic scale commonly adopted for plotting the potentials, which has the effect of extending over a considerable length very small radial regions.

Moving on to Be, we recall that for this atom no self-consistent xc potential can be obtained from the MP2 functional [198]. The MP2 energy functional is divergent in the presence of a vanishing gap, and the self-consistent procedure leads indeed to the closure of the KS gap. This instability is likely to occur in systems with small KS gaps, as is the case for Be. Ca also presents a small KS gap and our calculations confirm the presence of the instability also for this atom. As a consequence, the MP2 correlation potentials for Be and Ca are computed by iterating the LSSE solver only once starting from EXX orbitals and eigenvalues. Switching to the RPA functional restores the possibility of having a self-consistent xc potential. It must be noted, however, that the improvement towards the exact potential in Be is modest, as is the improvement of the KS HOMO. Finally, for Ne the MP2 functional produces an especially bad result, whereas the RPA functional performs much better. As we shall see in the Section 3.6.1, the 2B self-energy also performs poorly

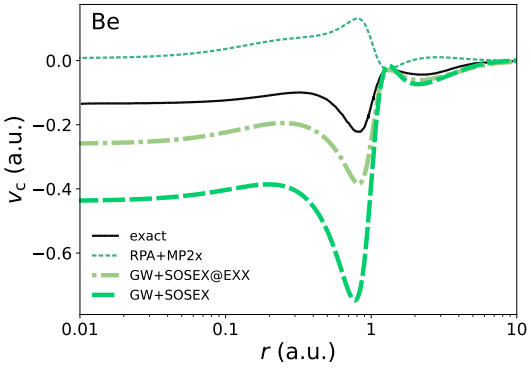

Figure 3.10. Alternative beyond-RPA correlation potentials for Beryllium. Self-consistency has little impact on the GW+SOSEX HOMO: we have $\varepsilon_{\mathrm{HOMO}}^{\mathrm{scGW+SOSEX}} = -0.733$ Ry and $\varepsilon_{\mathrm{HOMO}}^{\mathrm{GW+SOSEX@EXX}} = -0.735$ Ry. Exact correlation potential is from Ref. 112.

with Ne. There we discuss why it is likely that it is necessary to fully include screening at least at the RPA level in atoms such as Ne.

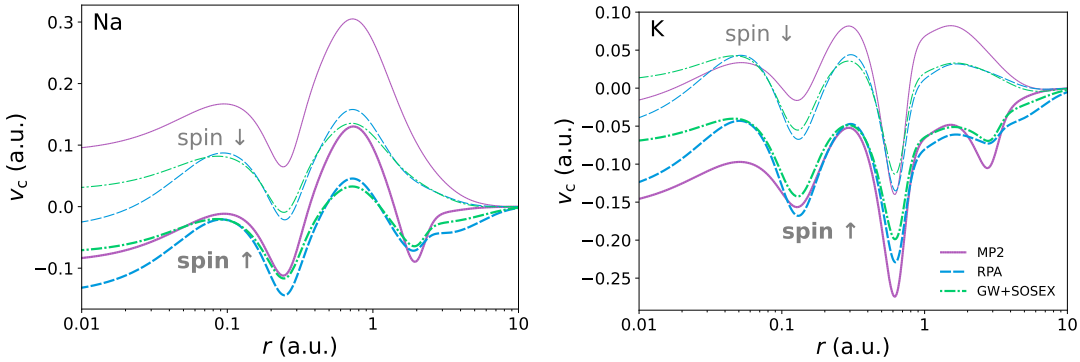

Figure 3.11. Correlation potentials for Sodium and Potassium. Thick lines are for the spin majority channel, thin lines are for the spin minority channel.

We now consider the GW+SOSEX potentials. As a first remark, we observe that the tail of the correlation potential is strikingly off in He, with the zero being approached from below. The issue becomes less relevant in heavier atoms, but is still present as one can see in Ne. As a consequence, the GW+SOSEX HOMO levels are generally deeper (with the exception of the group 1 atoms) than the RPA ones, which are already too low as compared with experiment. Even in the short-range region the GW+SOSEX potential is not always satisfactory: while there is an improvement with respect to RPA in He and Ne, in Be there is a visible worsening. It should be noted, however, that the inclusion of a screened exchange diagram allows for a self-consistent solution in Be, whereas the bare second-order diagram in MP2 did not. If one computes the GW+SOSEX potential for Be with a single iteration of the LSSE on an EXX self-consistent solution, as was done in the MP2 case, a short-range description in line with the ones of MP2 and RPA is recovered

(see Fig. 3.10). In this case self-consistency appears to exacerbate the bad features of the GW+SOSEX potential, as already found with the MP2 functional [198]. The KS HOMO is subject to little influence by self-consistency anyway, since it mainly affects the potential in the short range.

In Figure 3.10 we can also briefly explore the "RPA plus MP2 exchange" (RPA+MP2x) functional in the case of Be, yielding a self-energy consisting of the GW plus 2Bx diagram in the LSSE. The resulting xc potential presents features in opposition with those of the exact potential, suggesting that the unscreened 2Bx diagram is not properly balanced by the GW diagram. In He I even found the peak in the correlation potential to disappear. Overall, all the calculations I performed show that the RPA+MP2x functional performs badly with atoms and should probably not be employed in general. The related GW+2Bx self-energy has also been found to perform poorly in the past [56]. This suggests that, in order to build upon the RPA/GW level of theory, some amount of screening should always be included in the higher-order diagrams. The results shown here suggest that doing it with the SOSEX diagram restores the features of the exact potential, although retaining a sub-optimal asymptotic behaviour. The GW+SOSEX diagram can then be viewed more positively and considered as a starting point for more sophisticated self-energies which could possibly yield better results. For instance, it is an ingredient of the full second-order (in the screened interaction) diagram, which would also restore variationality if employed in the LSSE, it being a Ψ-derivable self-energy [189, 210]. Additionally, a set of diagrams enforcing the positive-definiteness of the spectral function could be obtained starting from the SOSEX diagram, following the recipe provided in Ref. 88.

Another positive aspect of the GW+SOSEX potential is that it does circumstantially improve on the RPA one. As we shall discuss in Section 3.6.1, the GW+SOSEX self-energy leads to a better prediction of the IE of group 1 atoms (save for H) with either the self-consistent LSSE solution discussed in this Section, or with the one-shot QPE starting from HF (see Figure 3.13). Therefore, I present in Fig. 3.11 the correlation potentials of two atoms from group 1 (Na and K). We can only speculate on what the improvements of the GW+SOSEX potential are on the RPA one, since no exact potential is currently available for these atoms. Looking at the majority spin-channel potentials, we see that the GW+SOSEX potential is found between the MP2 and the RPA potentials in the medium and long range. From the results of the Section 3.6.1 we can see that for atoms in group 1 the best prediction of the IE is given by the MP2 functional, limitedly to the LSSE framework. Thus, including a screened exchange diagram, which tends to bring the RPA potential closer to the MP2 one, has the effect of improving the IE energy, although not making it as accurate as the MP2 one.

3.6 Assessment of the low-order self-energy approximations

3.6.1 Ionization energies

In this Section we address the performance of the different self-energies introduced in Section 3.1. We do this by evaluating the mean absolute error (MAE) with respect to the experiment of the ionization energies (IEs) computed with each self-energy approximation

(Figure 3.12). These are obtained as the negative of the HOMO energies, i.e. IE $= -\varepsilon_{\text{HOMO}}$. In Table 3.5 I also provide the maximum and minimum errors found on the test set, and in Figure 3.13 the error contributions resolved on each atom. The LSSE results are considered at the scf level without an iteration of the QPE. In fact, as I shall discuss at the end of this Section, the LSSE does provide a consistent starting point for the QPE, if the same self-energy approximation is used in both steps, so that the QPE produces a mostly negligible QP shift on the HOMO.

The first notable result is that on average the 2B self-energy performs remarkably well on the studied atoms on top of the HF starting point. However, not considering alkali metals, it falls short of this result if the PBE or PBE0 functionals are used instead, also displaying a strong starting point dependence. We note that the 2B self-energy is generated by one iteration through Hedin's scheme with the TDHF vertex, and subsequent truncation to 2nd order in the Coulomb interaction. Therefore, employing the HF starting point implies having a consistent functional derivative of the self-energy with respect to the Green's function in the vertex equation, Eq. (2.129) (i.e. a physical polarizability) [74]. This, together with other results from the literature [50, 74, 208], points to a possible relevant role of a consistent inclusion of the vertex corrections. This may also explain why, as seen in Section 3.5.7, the MP2 functional treated at the LSSE level produces underwhelming results, along with perturbative QPE schemes using starting points different from HF.

We note, however, that with some atoms such as Ne the 2B self-energy fails even with the HF starting point. This can be explained with the findings of Bruneval [146], who pointed out the sizable difference that including all the infinite GW self-energy diagrams can sometimes make as compared with including just the first single-ring one, i.e. the 2Bd diagram in this work. This difference suggests that screening plays an important role also in finite systems, as already emphasized by Shirley and Martin in Ref. 34. Here, we find it

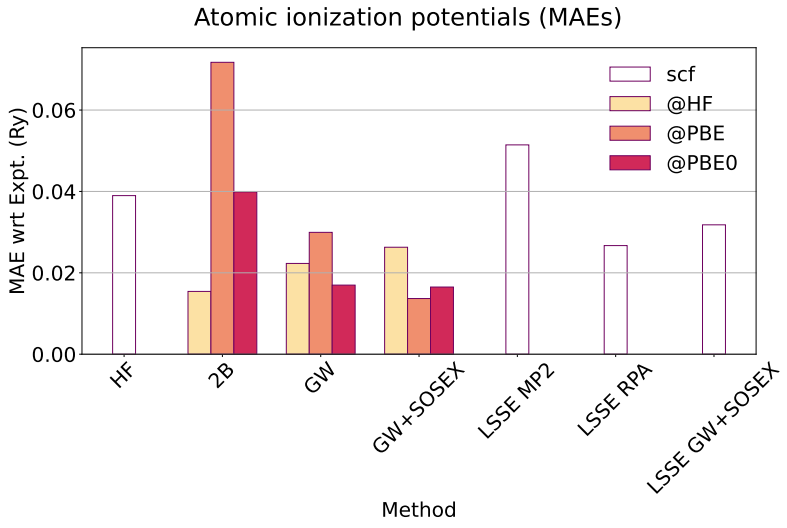

Figure 3.12. Mean absolute error (MAE) on the ionization energies for each method and starting point. In white we indicate the independent-particle self-consistent field (scf) methods.

Table 3.5. Negative of HOMO energies (Ry) as computed with different self-energies and starting points: mean absolute error (MAE), maximum absolute error (Max AE) and minimum absolute error (Min AE).

$-\varepsilon^{\mathrm{2B}}_{\mathrm{HOMO}}$

	@HF	@PBE	@PBE0	LSSE
MAE	0.015	0.072	0.040	0.051
Max AE	0.088	0.491	0.250	0.273
Min AE	0.000	0.001	0.000	0.000

$-\varepsilon^{\mathrm{GW}}_{\mathrm{HOMO}}$

	@HF	@PBE	@PBE0	LSSE
MAE	0.022	0.030	0.017	0.027
Max AE	0.048	0.086	0.042	0.060
Min AE	0.001	0.001	0.001	0.003

$-\varepsilon^{\mathrm{GW+SOSEX}}_{\mathrm{HOMO}}$

	@HF	@PBE	@PBE0	LSSE
MAE	0.026	0.014	0.017	0.032
Max AE	0.054	0.039	0.031	0.047
Min AE	0.001	0.001	0.001	0.000

to be especially important in Ne in order to obtain an accurate result.

However, this does not imply that the RPA screening on top of a HF solution (RPA@HF), which is being used in GW@HF, is necessarily the best choice in general. In fact, according to Ref. 146 the QP shift in N is also sensitive to the full inclusion of the RPA screening beyond the 2Bd diagram via GW. However, 2B performs quite well with N, whereas GW does considerably worse. Including the SOSEX diagram further worsens the result for N, suggesting that adding more diagrams with the RPA@HF screening can do little to improve the description. The results of Section 3.3.5 confirm that the RPA@HF polarizability is inaccurate due to not accounting for bound excitations in atoms. The fact that GW@HF is sometimes accurate has to be attributed to the fact that higher-order diagrams are being neglected both in the polarizability and in the self-energy; adding more self-energy diagrams while maintaining the RPA@HF polarizability destroys this balance. The same reasoning was made for GW@LDA in Section 3.4.5.

The behaviour described for N is confirmed for many of the selected atoms: in most cases, GW@HF overbinds the HOMO and GW+SOSEX@HF increases the error. A similar trend has also been recently found using the GW100 test set [87]. Therefore, the introduction of the SOSEX diagram does not seem justified with the HF starting point, owing to the sub-optimal RPA@HF screening. A few notable exceptions are alkali metals, i.e. Li, Na and K: it could be argued that the self-screening of the lone s electron is particularly relevant

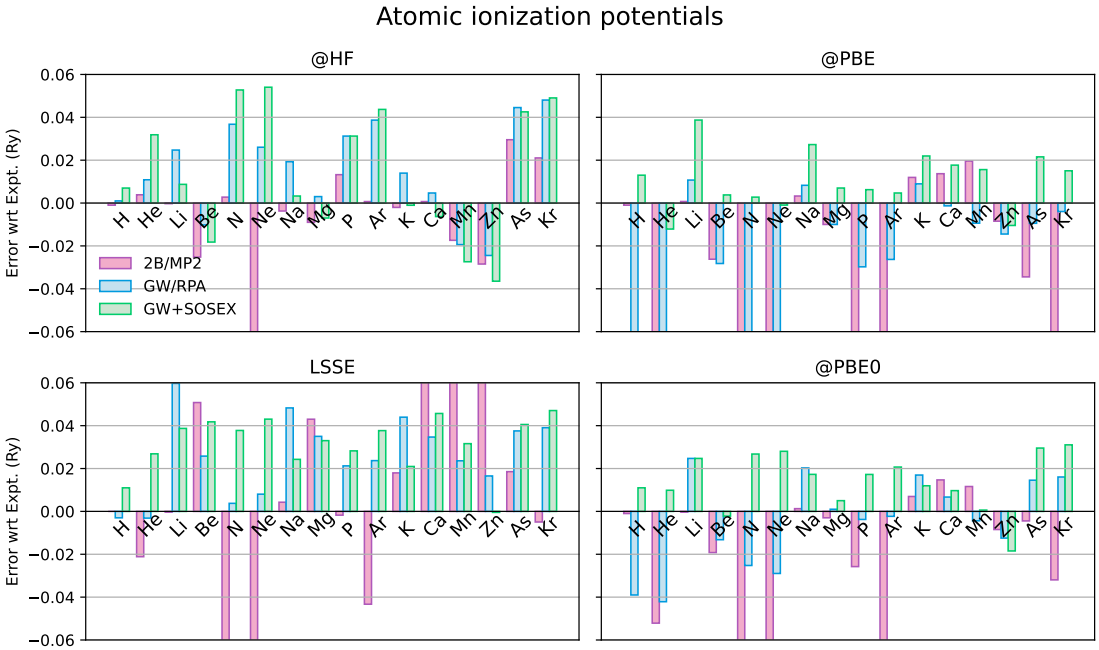

Figure 3.13. Deviation from experiment of the ionization energies of the neutral atoms as computed with the selected self-energies and starting points. The LSSE-MP2 IEs of Be and Ca and the LSSE-GW+SOSEX IE of Mn are computed starting from EXX orbitals and eigenvalues. Experimental IEs are from Ref. 139.

in these atoms and is thus the main source of error for GW, which can be ameliorated by GW+SOSEX. However, this explanation is not confirmed by the H atom, the archetypal system for self-screening detection: in this case the error of GW@HF is already small to start with, and GW+SOSEX@HF does worse. As we shall see, the picture is puzzlingly the opposite when using (generalized) KS-DFT solutions from the PBE and PBE0 functionals as starting points.

Interestingly, the results for GW@HF and GW+SOSEX@HF are generally mirrored in the LSSE framework: GW+SOSEX consistently improves on GW in atoms of group 1, and consistently does worse in almost all the others. This may be explained by the fact that the EXX contribution is dominant in determining the LSSE occupied orbitals and eigenvalues, which end up being similar to the HF ones, especially in the upper valence[128]. We therefore conclude that the KS spectrum as obtained from the LSSE is not sufficient to provide a better RPA screening than the HF one. The remaining discrepancies between the QPE@HF and the LSSE methods may be explained by the following two major facts: (*i*) the solution of the LSSE has a different unoccupied spectrum, with the LUMO being a KS bound state, whereas it is an unbound state in QPE@HF; (*ii*) the LSSE also involves a form of KS self-consistency. As compared with GW@HF and GW+SOSEX@HF, these two differences provide some advantage to the LSSE in noble gases, in atoms of the N family and in Zn (the LSSE-GW+SOSEX IE of Zn surprisingly matching the experiment), but end up worsening the results in group 1 and 2 atoms.

If solutions using density functionals in the (generalized) KS scheme are used as a starting point, the picture drastically changes. GW@PBE is seen to do worse than GW@HF, now strongly underbinding the HOMO in a lot of lighter atoms (similarly to GW@LDA, as seen in Section 3.4.5). Adding the SOSEX diagram greatly improves the HOMO energies, reducing by a half the MAE. The GW+SOSEX self-energy is now seen to perform worst with the atoms with which it performed best using the the HF starting point, i.e. the group 1 atoms; and conversely, GW performs better. Notably, the rationale for the SOSEX diagram as a cure for the self-screening problem of GW seems now justified if H is considered. This confirms early observations that the GW self-screening problem in H can be exacerbated by a starting point which suffers from a self-interaction/delocalization error, and is instead small when an accurate starting point is adopted [148, 149].

Going from the PBE to the PBE0 starting point greatly affects the performance of GW, which is now comparable with GW+SOSEX@PBE, and scarcely the one of GW+SOSEX. On the one hand this confirms a reduced starting point dependence of the GW+SOSEX self-energy [87, 91], also seen in self-consistent schemes [93]. On the other hand, a fraction of exchange in the starting point might as well be sufficient for obtaining accurate IEs with GW [41]. Of course one should consider larger test sets for a more reliable assessment: the IEs of Ref. 91 obtained with the larger G2 test set seem to confirm this picture. The more recent results of Ref. 87 obtained with the GW100 test set do show a marked improvement with the GW+SOSEX self-energy instead, even with the PBE0 reference. Moreover, other observables such as deeper binding energies may also be considered for a more comprehensive assessment, which we will not do here.

We conclude this Section by checking the validity of the LSSE starting points as approximate self-consistent solutions. In Table 3.6 we report the ionization energies of all atoms as obtained from self-consistent solutions of the LSSE, and from the solution of the QPE [Eq. (3.85)] on top of the LSSE solutions. As expected on the basis of the LSSE construction (preserving the charge density, and therefore the IE, to first order in converting the KS equations into the Dyson equation) [122, 126, 127], it can be seen that 2B@LSSE-MP2 and GW@LSSE-RPA calculations exhibit almost no QP shift in the IEs, the discrepancy between the KS HOMO and the QP HOMO being at most 1 mRy (with the exception of the 2B@LSSE-MP2 calculation for Zn). The discrepancies between the GW+SOSEX HOMOs are more sizable instead, but still within 10 mRy (with the exception of Li). The reason why this occurs may be due to the fact that the GW+SOSEX self-energy is not suitable for the variational argument presented in Section 2.3. Moreover, the sub-optimal long-range behaviour of the GW+SOSEX xc potential may also hint at some underlying numerical issue in the solution of the LSSE. In fact, these potentials are more sensitive to the r_{cut} parameter chosen for the matching with the long-range solution (see Section 3 of the Supporting Information); therefore, a larger error bar is to be expected on the IEs as obtained from the GW+SOSEX HOMO energies than one gets with the MP2 and RPA potentials, however not undermining the assessment presented in this section. One may conservatively estimate this error from the QP shift obtained from the Dyson equation, which, as already mentioned, can be up to the order of 10 mRy.

In order to check whether the LSSE could be an approximate pathway to self-consistency, it would also be useful to compare the MP2 and RPA IEs with the self-consistent 2B and GW ones respectively. In Table 3.7 we compare our IEs from the solution of the LSSE with those from the self-consistent calculations of Refs. 211 and 35 (see also Section 1 of the

Table 3.6. IEs (Ry) from the self-consistent solution of the LSSE vs IEs from the one-shot solution of the QPE upon the self-consistent LSSE. No self-consistent MP2 xc potentials can be computed for Be and Ca owing to an instability due to the closure of the KS gap in the self-consistency procedure. No self-consistent GW+SOSEX potential for Mn is present either due to numerical issues. Basis set size = 100 B-splines.

Atoms	**LSSE**			**QPE@LSSE**			**Exp.**[a]
	MP2	RPA	GW+SOSEX	2B	GW	GW+SOSEX	
H	1.000	0.997	1.011	0.999	0.997	1.017	1.00000
He	1.785	1.802	1.833	1.785	1.803	1.841	1.80714
Li	0.396	0.455	0.437	0.396	0.455	0.449	0.39628
Be		0.710	0.733		0.709	0.741	0.68521
N	1.000	1.072	1.106	1.001	1.071	1.113	1.06824
Ne	1.316	1.594	1.629	1.316	1.594	1.639	1.58496
Na	0.381	0.426	0.403	0.381	0.426	0.411	0.37772
Mg	0.604	0.596	0.595	0.603	0.596	0.601	0.56199
P	0.770	0.792	0.799	0.771	0.793	0.807	0.77076
Ar	1.117	1.183	1.196	1.117	1.183	1.206	1.15831
K	0.333	0.363	0.340	0.333	0.364	0.345	0.31904
Ca		0.483	0.495		0.483	0.503	0.44931
Mn	0.623	0.570		0.623	0.570		0.54639
Zn	0.800	0.707	0.689	0.795	0.707	0.696	0.69046
As	0.738	0.757	0.759	0.737	0.758	0.766	0.71945
Kr	1.024	1.069	1.075	1.025	1.070	1.082	1.02895

[a]Ref. [139]

Table 3.7. Self-consistent LSSE RPA and MP2 IEs (Ry) of selected atoms compared to self-consistent GW and 2B ionization energies from the literature.

Atoms	**LSSE-RPA** (B-spline)	**sc-GW**[a] (Slater orb.'s)	**LSSE-MP2** (B-spline)	**sc-2B**[b] (Slater orb.'s)	**Exp.**[c]
He	1.804	1.805	1.786	1.811	1.80714
Be	0.711	0.636		0.660	0.68521
Ne	1.593	1.600	1.312	1.497	1.58496
Mg	0.597	0.535	0.605	0.553	0.56199

[a]Ref. [35]
[b]Ref. [211]
[c]Ref. [139]

Supporting Information). We find a generally poor agreement of the 2B/MP2 IEs and a partial agreement of the GW/RPA ones, i.e. only for He and Ne we have similar GW/RPA IEs. While some aspects of our numerical treatment may differ from that of Ref. 211, this does not seem sufficient to explain a so-large discrepancy between the 2B and MP2 results. Therefore, it can be argued that the LSSE does not provide a good approximation to the self-consistent Dyson equation when the 2B self-energy is employed. The agreement between the two methods appears to be sometimes better with the GW self-energy, but still system-dependent. Further precise self-consistent calculations are needed to assess when and whether the two methods yield similar results. Other observable quantities should also be targeted in the LSSE approximate self-consistency, such as the HOMO-LUMO gap upon inclusion of the derivative discontinuity correction [110].

3.6.2 Numerical details

All results are obtained with the AGWX code. The B-spline basis set is generated over a cubic grid extending over a 30 Bohr-radius $r_{\max}$. By construction of the B-spline basis sets, all functions and operators represented with it vanish at the boundaries of the grid. Matrix diagonalizations and inversions are performed in the B-spline basis, ensuring smoothness and faithful representation of functions and operators. We checked that 300 B-splines ensure the convergence within 1 mRy of the energy values presented throughout. It was necessary to sometimes resort to a smaller basis set of 100 B-splines for more demanding computations, such as those producing the GW+SOSEX potentials. It was verified that this does not heavily impact the quality of the results, which remain converged well within a threshold of 10 mRy even with this smaller basis.

Self-energies are calculated using the techniques presented in Section 3.4 over a frequency grid around the expected QP HOMO energy, in order to thereafter solve the QPEs, Eqs. (3.84) and (3.85). The parameters introduced in Section 3.4.2 for the imaginary grids of are usually set to $\Omega = 10.0$ Ry and $N = 100$. Integrations over imaginary grids are used for grid-resolved self-energies (contour deformation for GW and SOSEX) and LSSE inhomogeneities (frequency integrations in RPA and SOSEX inhomogeneities) alike.

The numerical solution of the LSSE requires care. The LSSE linear system is rank-deficient, due to the degree of freedom given by the possibility of incorporating inside the xc potential an arbitrary energy shift [125, 126]. In the spherical problem, this degree of freedom can be saturated by imposing the theoretical asymptotic behaviour seen in Section 3.5.1,

$$v_{\mathrm{xc}}(r) = \bar{v}_{\mathrm{xc}}(r) - 1/r, \tag{3.87}$$

with $\bar{v}_{\mathrm{xc}} \to 0$ faster than $1/r$ for $r \to \infty$. In AGWX one solves for $r\bar{v}_{\mathrm{xc}}$ with a singular value decomposition (SVD) treatment for the linear system inversion. The SVD allows one to impose the vanishing of v_{xc} for $r \to \infty$. Thanks to the B-spline basis set, the unphysical oscillations in the potentials found when solving the problem on a radial grid are avoided [169, 198]. However, found numerical noise was found in the matching of v_{xc} with the long-range solution $-1/r$. Although the SVD showed some efficacy in removing such noise, it was found that it still impacted the quality of the KS HOMOs. Improving them was possible by adopting the following procedure: At each LSSE iteration, v_{xc} is discarded in the interval $[r_{\mathrm{cut}}, r_{\max}]$, with r_{cut} being the radial coordinate at which the noise onset is found, and replaced with $-1/r$; then v_{xc} is shifted in the leftover interval $[0, r_{\mathrm{cut}}]$ in order

to match $-1/r$ at r_{cut}. Unfortunately r_{cut} is system-dependent and has to be evaluated for every atom and spin polarization. Nevertheless, this procedure allows one to obtain EXX HOMOs in very good agreement with the HF ones, and MP2 and RPA HOMOs in excellent agreement with those in the literature [169, 198].

3.6.3 Comparison with the existing literature

Since the AGWX results are easily converged thanks to the B-spline basis set we employ, it is preferable to verify them against data affected by an error as small as possible coming from basis set incompleteness. This seems to be the case for the data in Refs. 211, 35 and 212, where GW and 2B calculations are presented. In Ref. 211 a basis set consisting of 30-40 Slater orbitals is used; the basis set of Ref. 35 is presumably analogous. In Ref. 212 a basis set consisting of numeric atom-centered orbitals is employed, enriched with an auxiliary basis instrumental in the resolution of the identity technique; the calculations are performed with the 'tier 4 + a5Z-d' set, except the ones for noble gases, with which the 'tier 4 + aug-cc-pV5Z' set is used instead.

Table 3.8 reports the GW@HF and the 2B@HF IEs of our work as compared with these references; Table 2 in the main text does the same with the self-consistent results. Overall, the GW@HF results compare well with both the results obtained with the 'tier 4 +a5Z' basis and those obtained with the Slater orbital basis. In the latter case the agreement is notably up to 1 mRy. The situation is different for the 2B@HF results: a good agreement is found again with those from the 'tier 4 + a5Z' basis, but it is worse than before with those from the Slater orbital basis. As the atomic number increases, the agreement worsens noticeably with the latter basis. While the GW results by the same authors compare extremely well with ours, the 2B ones do not, and we have not found an explanation to this.

In Table 3.9 the comparison is repeated with the 'tier 4 + a5Z' results, this time using GW@PBE and GW+SOSEX@PBE IEs from Ref. 91. As with the HF starting point, a good agreement is obtained once more, this time also considering the GW+SOSEX self-energy.

3.7 Conclusive remarks

In this Chapter I presented the implementation of the 2B, GW and GW+SOSEX self-energies for spherical atoms. Both their treatments within the Dyson equation (Section 3.4) and the LSSE (Section 3.5) frameworks were considered. Then an assessment of all the methods was carried out in Section 3.6.

In Section 3.5.7 the novel GW+SOSEX correlation potential was explored in the LSSE framework: we found that it brings the correlation potentials closer to the exact ones in the short range for He and Ne, but not for Be; in the long range the description is even worsened, with these potentials reaching zero from below. This is especially noticeable in lighter atoms, whose HOMO is affected worst by this bad feature. On the contrary, the GW+SOSEX potential seems to improve on GW in group 1 atoms by bringing the description closer to the MP2 one.

The bottom line of this part of the work is that, as is known in MBPT, also in the LSSE framework "more diagrams" does not necessarily mean "better results": the GW+2Bx/RPA+MP2x calculations I briefly presented are explanatory in this regard. At

Table 3.8. GW and 2B IEs (Ry) of selected atoms computed using different codes wih the HF starting point.
†'tier 2 + aug-cc-pV5Z' for noble gases.

Atoms	GW**@HF**			2B**@HF**			**Exp. [139]**
	This work (B-spline)	FHI-AIMS [212] (tier 4 + a5Z)†	Ref. 35 (Slater orb.'s)	This work (B-spline)	FHI-AIMS (tier 4 + a5Z)†	Ref. 211 (Slater orb.'s)	
H	1.001	1.000		0.999	1.000		1.000
He	1.818	1.814	1.819	1.811	1.807	1.8118	1.80714
Li	0.421	0.417		0.396	0.395		0.39628
Be	0.675	0.673	0.675	0.660	0.660	0.6550	0.68521
N	1.105	1.091		1.071	1.101		1.06824
Ne	1.611	1.599	1.610	1.497	1.486	1.4726	1.58496
Na	0.397	0.395		0.374	0.374		0.37772
Mg	0.565	0.556	0.565	0.553	0.547	0.5210	0.56199
P	0.802	0.788		0.784	0.792		0.7707575
Ar	1.197	1.182		1.159	1.147		1.15831

Table 3.9. GW and GW+SOSEX IEs (Ry) of selected atoms computed using different codes wih the PBE starting point.

Atoms	**GW@PBE**		**GW+SOSEX@PBE**		**Exp. [139]**
	This work (B-spline)	FHI-AIMS [91] (tier 4 + a5Z)	This work (B-spline)	FHI-AIMS (tier 4 + a5Z)	
H	0.917	0.920	1.015	1.014	1.000
He	1.722	1.734	1.795	1.791	1.80714
Li	0.405	0.417	0.435	0.434	0.39628
Be	0.657	0.664	0.689	0.697	0.68521
N	0.997	0.997	1.071	1.067	1.06824
Ne	1.514	1.510	1.584	1.560	1.58496
Na	0.383	0.401	0.405	0.400	0.37772
Mg	0.552	0.567	0.569	0.579	0.56199
P	0.743	0.743	0.777	0.772	0.7707575
Ar	1.132	1.118	1.163	1.145	1.15831

least we find the GW+SOSEX potentials to restore the correct main features of the exact potentials by building upon the GW+2Bx/RPA+MP2x level of theory. Therefore it is likely that improving on the GW+SOSEX level of theory with a sensibly chosen criterion could fix the issue of the long range behaviour. Among these criteria we include variationality (e.g. considering the self-energy diagram of second order in the screened interaction) or positive definiteness of the spectral function (following Ref. 88).

In Section 3.6.1 we found that the LSSE generally performs poorly as compared with the resolution of the QPE starting from independent-particle solutions given by either the HF method or semi-local/hybrid functionals in (generalized) KS-DFT. In this regard, we got the best performance from GW+SOSEX@PBE/PBE0, 2B@HF and GW@PBE0. This confirms the common knowledge that hybrid functionals provide good starting points for GW applied to finite systems [38, 56], even in the atomic limit. The justification of the SOSEX diagram as a cure for the self-screening error of GW seems to be correct only with the PBE and PBE0 starting points. On the contrary, adding the SOSEX diagram to GW with the HF starting point appears to be inaccurate, likely due to the poor description given by the RPA screening computed on top of a HF solution.

Finally, the good performance of the 2B self-energy is impressive, and the unambiguous choice of its starting point quite appealing. This provided a good motivation to build upon its level of theory in order to fix its occasional failures. In Chapter 4 we will see how this is done by considering the full time-dependent Hartree-Fock vertex for spherical atoms.

Chapter 4

The time-dependent Hartree-Fock vertex

The assessment of the 2B self-energy in Section 3.6 gave very encouraging results, and provided an unambiguous choice of the starting point for 2B, that being HF. In this Chapter I will build upon the 2B level of theory by introducing the time-dependent Hartree-Fock (TDHF) vertex. The 2B self-energy is in fact a truncation to 2nd order in the bare v of the full self-energy generated by the TDHF vertex. In Section 4.1 I will introduce TDHF theory, and in Section 4.2 I will present the assessment of the TDHF self-energy and of some intermediate diagrammatic inclusions.

4.1 TDHF theory and specialization to the spherical problem

4.1.1 Iterative scheme

In order to introduce the TDHF vertex, we go back to the reducible vertex Γ introduced in Section 2.1.5 and pick up where we left off. As we have seen, the the 4-point and 3-point reducible vertices are respectively defined as

$$ {}^4\Gamma(11',22') = -\frac{\delta G^{-1}(1,1')}{\delta \mathcal{J}(2',2)} \qquad \text{and} \qquad \Gamma(11',2) = -\frac{\delta G^{-1}(1,1')}{\delta u(2)}. \tag{2.98} $$

The 3-point Γ obeys the BSE

$$ \Gamma(11',2) = \delta(12^+)\delta(1'2) + \Xi(11',\bar{3}'\bar{3})L^0(\bar{3}\bar{3}',\bar{4}'\bar{4})\Gamma(\bar{4}\bar{4}',2), \tag{2.100} $$

in which the BSE kernel reads

$$ \Xi(11',22') = \frac{\delta\Sigma(1,1')}{\delta G(2',2)} = -i\delta(1,1')\delta(2,2')v(1,2) + \frac{\delta\Sigma_{\text{xc}}(1,1')}{\delta G(2',2)}, \tag{2.96} $$

and an analogous BSE equation holds for the 4-point ${}^4\Gamma$. The reducible vertex yields for the self-energy an expansion in the bare v,

$$ \Sigma_{\text{xc}}(11') = iG(1\bar{2})v(1\bar{3})\Gamma(\bar{2}1',\bar{3}^+). \tag{2.101} $$

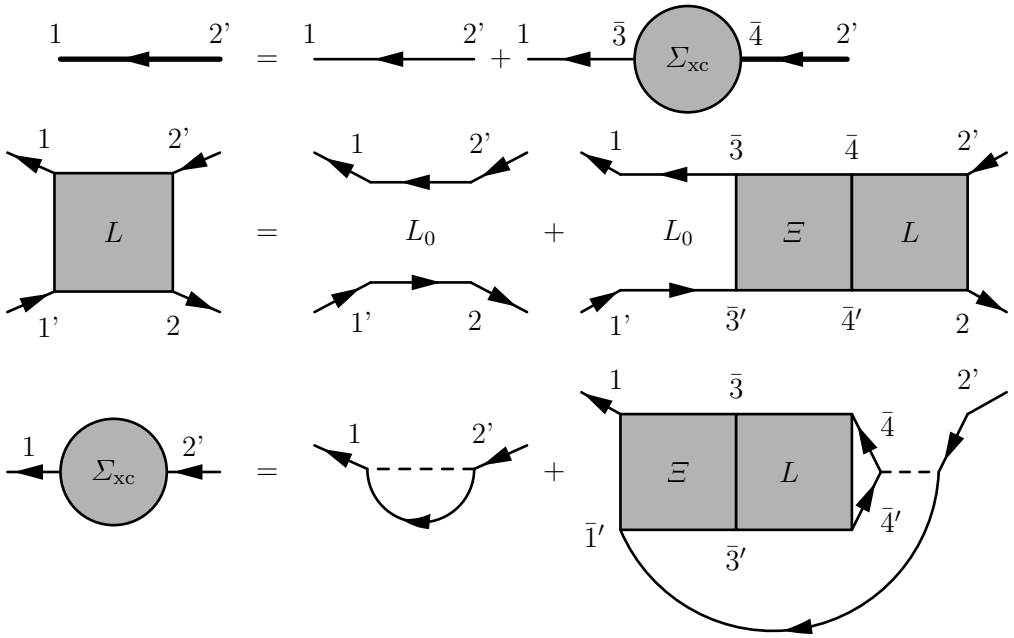

Figure 4.1. Diagrammatic representation of the iterative scheme based on an expansion in the bare v.

Through the relations

$$L = L_0\,{}^4\Gamma, \qquad {}^4\Gamma = 1 + \Xi L \tag{2.99}$$

we obtain, from the BSE for ${}^4\Gamma$, the BSE for the 2-particle propagator L (which was defined in Eq. (2.48)),

$$L = L_0 + L_0 \Xi L. \tag{2.97}$$

An iterative scheme similar to Hedin's is obtained by choosing to work with the reducible vertex Γ. With an initial guess for the self-energy, one can compute the Green's function via the Dyson equation for G and the functional derivative of the BSE kernel Ξ. Then the BSE, Eq. (2.100), can be solved, and L used to compute a new self-energy from Eq. (2.101). The new self-energy can be fed to the Dyson equation for the Green's function for a new iteration to begin. In order to summarize this scheme in a compact fashion, we introduce a 4-point formalism similar to that in Ref. 74. We define

$$V(11',22') = v(1,2)\delta(11')\delta(2^+2') \tag{4.1}$$

so that the self-energy in Eq. (2.101) can be re-written as

$$\Sigma_{\rm xc}(2,1') = i \int d1d2'\; G(2'1)\; \Gamma V(11',22'). \tag{4.2}$$

This can be adopted as a definition of contraction of a 4-point quantity to a 2-point quantity; in the following we will adopt the equivalent equation

$$\Sigma_{\rm xc}(1,2') = i \int d1'd2\; G(1'2)\; \Gamma V(11',22'). \tag{4.3}$$

The formalism thus introduced allows us to briefly summarize the iterative scheme with the following equations:

$$G = G_0 + G_0 \Sigma_{\text{xc}} G, \tag{4.4}$$
$$L = L^0 + L^0 \Xi L, \tag{4.5}$$
$$\Sigma_{\text{xc}} = iG(1 + \Xi L)V. \tag{4.6}$$

The contraction defined in Eq. (4.3) is implied in the last equation. In Figure 4.1 a diagrammatic depiction of the iterative scheme is given. By choosing to neglect the functional derivative $\delta\Sigma_{xc}/\delta G$ in the BSE kernel, Eq. (2.96), one obtains the RPA for the reducible polarizability L, and the GW approximation for the xc self-energy Σ_{xc}. The kernel takes the form

$$\Xi^{\text{RPA}} = -iV \tag{4.7}$$

and the BSE can be treated as a simple 2-point equation yielding an infinite sum of "ring diagrams".

4.1.2 The time-dependent Hartree-Fock vertex

The time-dependent Hartree-Fock (TDHF) vertex is obtained by plugging the Fock self-energy Σ_x into the functional derivative of the BSE kernel, Eq. (2.96), yielding

$$\Xi^{\text{TDHF}} = \Xi^x + \Xi^d, \tag{4.8}$$

where the exchange contribution coming from the differentiation of v_H is again $\Xi^x = \Xi^{\text{RPA}} = -iV$, and the direct contribution coming from the differentiation of Σ_x is

$$\Xi^d = iv(1,2)\delta(12')\delta(1'2). \tag{4.9}$$

This further term in the kernel yields the "ladder diagrams" and makes it no longer possible to reduce the BSE to a 2-point equation. We note that truncating to 2nd order the self-energy diagrams obtained with the TDHF vertex yields the 2B self-energy.

For clarity, we conclude this section by making explicit the degrees of freedom of the two kernel contributions, emphasizing the underlying delta structures. We have

$$\begin{aligned}\Xi^x(11',22') = -iv(\mathbf{r}_1\mathbf{r}_{2'})\ \delta_{s_1 s_{1'}}\delta_{s_2 s_{2'}}\ \delta(\mathbf{r}_1\mathbf{r}_{1'})\delta(\mathbf{r}_2\mathbf{r}_{2'}) \\ \times\delta(t_1 - t_{1'})\delta(t_2 - t_{2'})\delta(t_1 - t_{2'})\end{aligned} \tag{4.10}$$

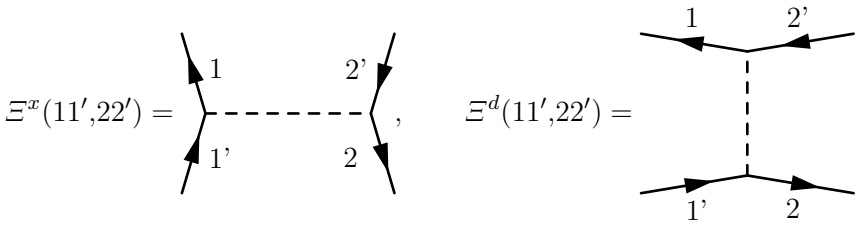

Figure 4.2. Diagrammatic representation of the TDHF kernel contributions Ξ^x and Ξ^d.

and

$$\Xi^d(11',22') = iv(\mathbf{r}_1\mathbf{r}_{1'})\ \delta_{s_1 s_2'}\delta_{s_{1'}s_2}\ \delta(\mathbf{r}_1\mathbf{r}_{2'})\delta(\mathbf{r}_{1'}\mathbf{r}_2) \times\delta(t_1 - t_{2'})\delta(t_{1'} - t_2)\delta(t_1 - t_2). \tag{4.11}$$

The delta structure in time of the two kernel contributions, coming from the bare Coulomb interaction v, implies that they are static. Furthermore, the time equalities will imply that in the BSE L will be constrained to be the electron-hole propagator L_{eh}, as defined in Eq. (2.53). In Figure 4.2 a diagrammatic depiction of the TDHF kernel contributions is given.

4.1.3 Spin structure

The free particle-hole propagator L^0 describes the independent propagation of a particle and a hole. Both carry a spin, which is conserved along a free-quasiparticle propagator line, but also by the bare Coulomb interaction which we are considering in the TDHF kernel. However, the diagonality in spin space is not the same in the two contributions to the TDHF kernel, as one can see from Eqs. (4.10) and (4.11) (we note in passing that Ξ^d has the same spin diagonality as L^0). The two contributions to the BSE kernel conserve spin along propagator lines connecting different couples of vertices: when the two contributions are summed together and plugged in the BSE, they make it impossible to conserve the spins of the single particles in building L from L^0. Nonetheless, they conserve the total spin: moving to the total spin basis leads to a significant simplification of the problem for spin-saturated systems.

In order to do so, we follow Bechstedt [213]. The Green's function is represented on the basis given by the product of two spinors $\chi_{m_s}(s)\chi^\dagger_{m'_s}(s')$:

$$G(11') = \sum_{m_s} G_{m_s}(\mathbf{r}_1\mathbf{r}'_1, t_1 - t'_1)\chi_{m_s}(s)\chi^\dagger_{m'_s}(s'). \tag{4.12}$$

With this, one can swiftly write the spinorial part of L^0 in the spin-product basis. Then the transformation to the basis of eigenvectors of the total spin $\{\zeta_\alpha\}_{\alpha=1,\dots,4}$ can be performed, following the basis transformation rules of the field operators appearing in the definitions of either L^0 or L. The basis eigenvectors $\zeta_\alpha(ss')$ of the total spin are obtained by taking symmetric and antisymmetric normalized linear combinations of $\chi_{m_s}(s)\chi^\dagger_{m'_s}(s')$: $\alpha = 1$ corresponds to the symmetric singlet state with $S = 0$, $M_S = 0$; and $\alpha = 2,3,4$ corresponds to the antisymmetric triplet states with $S = 1$, $M_S = 1,0,-1$ respectively. The transformation to this basis reads

$$L_{\alpha\beta}(11',22') = \sum_{\substack{s_1,s'_1\\ s_2,s'_2}} \zeta^\dagger_\alpha(s_1 s'_1)L_{s_1 s'_1,s_2 s'_2}(11',22')\zeta_\beta(s'_2 s_2), \tag{4.13}$$

which holds for both L and L^0. Notice that we have temporarily detached the spin degree of freedom from the numerical multi-index, i.e. $1 \equiv (\mathbf{r}_1, s_1, t_1) \to 1 \equiv (\mathbf{r}_1, t_1)$. By carrying out the basis transformation for L^0 we get

$$L^0_{\alpha\beta}(11',22') = \sum_{m_s,m'_s} G_{m_s}(12')G_{m_{s'}}(21')\ \eta^\dagger_\alpha(m_s, m'_s)\eta_\beta(m_s m'_s), \tag{4.14}$$

where we have defined the projections of the total spin basis on the product spin basis:

$$\eta_\alpha(m_s m'_s) = \sum_{s,s'} \chi^\dagger_{m_s}(s)\chi_{m'_s}(s')\zeta_\alpha(ss'). \tag{4.15}$$

In spin-saturated systems, projecting the BSE onto the total spin basis yields two decoupled equations for the spin-diagonal blocks of L, viz.:

$$\begin{aligned} L_{\alpha\alpha} &= L^0 + L^0(2\Xi^x + \Xi^d)L_{\alpha\alpha} \quad \text{for } \alpha = 1 \text{ (singlet)}, \\ L_{\alpha\alpha} &= L^0 + L^0\Xi^d L_{\alpha\alpha} \qquad\quad \text{for } \alpha = 2{,}3{,}4 \text{ (triplet)} \end{aligned} \tag{4.16}$$

with $L^0 = L^0_{\alpha\alpha}$, $\alpha = 1{,}2{,}3{,}4$. All the total spin off-diagonal elements vanish. Notably, by performing the contraction of Eq. (4.3) one easily finds that only the spin singlet component of L contributes to Σ. Unfortunately all these simplifications do not occur in the more general, spin-polarized case. We will then consider the spin-saturated case and restrict ourselves to the the singlet state of L in the following, and drop the spin degree of freedom for simplicity. It can be shown that in the spin-saturated case only the spin singlet component of L enters the self-energy.

4.1.4 Angular structure in the spherical problem

In the spherical approximation, working with saturated orbital angular momentum shells leads to a simplification analogous to the one presented in the previous section for spin-saturated systems. Such simplification is attained by moving to the representation of the total angular momentum. We have already made use of it in the 2-point formalism involving Green's functions, self-energies etc. by employing the SHs and applying their coupling rules. We must now extend the angular treatment based on SHs to the 4-point formalism needed in the solution of the BSE. In order to do so, we come to a natural angular representation in the 4-point formalism by constructing the basic 4-point quantity with a known 2-point quantity, i.e. we build L^0 with G:

$$\begin{aligned} L^0(\mathbf{r}_1\mathbf{r}'_1, \mathbf{r}_2\mathbf{r}'_2; t) = \frac{1}{r_1 r'_1 r_2 r'_2} \sum_{\substack{l_p m_p \\ l_h m_h}} & G_{l_p}(r_1 r'_2, t) G_{l_h}(r_2 r'_1, -t) \\ & \times Y_{l_p m_p}(\hat{\mathbf{r}}_1) Y^*_{l_h m_h}(\hat{\mathbf{r}}'_1)\, Y_{l_h m_h}(\hat{\mathbf{r}}_2) Y^*_{l_p m_p}(\hat{\mathbf{r}}'_2). \end{aligned} \tag{4.17}$$

We now expand the two pairs of SH on the total angular momentum basis. The Clebsch-Gordan (CG) coefficients are the coefficients of the expansion:

$$Y_{l_p m_p}(\hat{\mathbf{r}}_1) Y^*_{l_h m_h}(\hat{\mathbf{r}}'_1) = (-1)^{m_h} \sum_{LM} \langle LM | l_p l_h m_p - m_h \rangle Y^{LM}_{l_p l_h}(\hat{\mathbf{r}}_1, \hat{\mathbf{r}}'_1). \tag{4.18}$$

The object $Y^{LM}_{l_p l_h}$ is defined by the inverse of this formula, amounting to standard coupling of two angular momenta (see Appendix A.4). Applying this expansion twice in Eq. (4.17) and applying the orthogonality of the CG coefficients yields

$$\begin{aligned} L^0(\mathbf{r}_1\mathbf{r}'_1, \mathbf{r}_2\mathbf{r}'_2; t) = \frac{1}{r_1 r'_1 r_2 r'_2} \sum_{\substack{LM \\ l_p l_h}} & G_{l_p}(r_1 r'_2, t) G_{l_h}(r_2 r'_1, -t) \\ & \times Y^{LM}_{l_p l_h}(\hat{\mathbf{r}}_1, \hat{\mathbf{r}}'_1) Y^{LM*}_{l_p l_h}(\hat{\mathbf{r}}'_2, \hat{\mathbf{r}}_2). \end{aligned} \tag{4.19}$$

It is an instructive exercise to recover from Eq. (4.19) the form of the 2-point independent-particle polarizability $\chi_0 = P^{\rm RPA}$ in the 2-point angular representation, Eq. (3.56), by letting $1' \to 1$ and $2' \to 2$ and using the formula $P = -iL^0(11,22)$. Eq. (4.19) lends itself to an easy generalization to any 4-point quantity,

$$A(\mathbf{r}_1\mathbf{r}'_1,\mathbf{r}_2\mathbf{r}'_2) = \frac{1}{r_1 r'_1 r_2 r'_2} \sum_{\substack{LM \\ l_{p_1} l_{h_1} \\ l_{h_2} l_{p_2}}} A^L_{\substack{l_{p_1} l_{h_1} \\ l_{h_2} l_{p_2}}}(r_1 r'_1, r_2 r'_2)\; Y^{LM}_{l_{p_1} l_{h_1}}(\hat{\mathbf{r}}_1, \hat{\mathbf{r}}'_1) Y^{LM*}_{l_{p_2} l_{h_2}}(\hat{\mathbf{r}}'_2, \hat{\mathbf{r}}_2), \tag{4.20}$$

which is the analogous of Eq. (3.30) in the 4-point formalism. The presence of the $Y^{LM}_{l_{p_1} l_{h_1}}\, Y^{LM*}_{l_{p_2} l_{h_2}}$ product in the expansion of A implies that all components vanish for which any of the two angular deltas

$$\{l_{p_1}, l_{h_1}, L\} \qquad \text{and} \qquad \{l_{p_2}, l_{h_2}, L\}$$

also vanishes. When necessary, the angular deltas will be made explicit in the following.

With the definitions given in this section, the BSE in the spherical approximation with the TDHF kernel becomes

$$L^L_{\substack{l_1 l'_1 \\ l_2 l'_2}} = L^{0,L}_{\substack{l_1 l'_1 \\ l_2 l'_2}} + \sum_{\substack{l_3 l'_3 \\ l_4 l'_4}} L^{0,L}_{\substack{l_1 l'_1 \\ l'_3 l_3}} (\Xi^{x,L}_{\substack{l_3 l'_3 \\ l_4 l'_4}} + \Xi^{d,L}_{\substack{l_3 l'_3 \\ l_4 l'_4}}) L^L_{\substack{l'_4 l_4 \\ l_2 l'_2}},$$

where we defined

$$L^{0,L}_{\substack{l_1 l'_1 \\ l_2 l'_2}}(11',22') = G_{l_1}(1,2')G_{l'_1}(2,1')\delta_{l_1 l'_2}\delta_{l'_1 l_2}\{l_1\ l'_1\ L\}. \tag{4.21}$$

The kernel is obtained from Eqs. (4.10) and (4.11) by expanding the angular delta using SHs as in Eq. (A.18) and contracting the SH with the same angular argument. The two contributions to the TDHF kernel read

$$\begin{aligned}
\Xi^{x,L}_{\substack{l_1 l'_1 \\ l_2 l'_2}}(11',22') &= -i \frac{\sqrt{(2l_1+1)(2l'_1+1)(2l_2+1)(2l'_2+1)}}{4\pi} \\
&\quad \times \begin{pmatrix} l_1 & l'_1 & L \\ 0 & 0 & 0 \end{pmatrix} \begin{pmatrix} l_2 & l'_2 & L \\ 0 & 0 & 0 \end{pmatrix} \\
&\quad \times v_L(r_1 r'_2)\ \delta(11')\delta(22')\delta(t_1 - t'_2) \\
&= -iC^{x,L}_{l_1 l'_1, l_2 l'_2}\ v_L(r_1 r'_2)\ \delta(11')\delta(22')\delta(t_1 - t'_2),
\end{aligned} \tag{4.22}$$

and

$$\begin{aligned}
\Xi^{d,L}_{\substack{l_1 l'_1 \\ l_2 l'_2}}(11',22') &= i \sum_{l_c} (-1)^{l_c + L}(2l_c + 1) \\
&\quad \times \frac{\sqrt{(2l_1+1)(2l'_1+1)(2l_2+1)(2l'_2+1)}}{4\pi} \\
&\quad \times \begin{pmatrix} l_1 & l'_2 & l_c \\ 0 & 0 & 0 \end{pmatrix} \begin{pmatrix} l'_1 & l_2 & l_c \\ 0 & 0 & 0 \end{pmatrix} \begin{Bmatrix} l_2 & l'_2 & L \\ l_1 & l'_1 & l_c \end{Bmatrix} \\
&\quad \times v_{l_c}(r_1 r_2)\ \delta(12')\delta(1'2)\delta(t_1 - t_2). \\
&= i \sum_{l_c} C^{d,Ll_c}_{l_1 l'_1, l_2 l'_2}\ v_{l_c}(r_1 r_2)\ \delta(12')\delta(1'2)\delta(t_1 - t_2),
\end{aligned} \tag{4.23}$$

where the angular coefficients were packed into the prefactors C^x and C^d in the last lines.

In order to build the self-energy from L as obtained from the solution of the BSE, we also need to be able to perform the contraction defined by Eq. (4.3). A generic contraction of a 4-point operator A reads

$$GA(12',t) = \frac{1}{r_1 r_2'} \sum_{LM} \sum_{L' l_g} \frac{2L'+1}{2L+1} Y_{LM}(\hat{\mathbf{r}}_1) Y^*_{LM}(\hat{\mathbf{r}}_2') \times \int dr_1' dr_2 \; G_{l_g}(r_1' r_2, t) A^{L' l_g}_{l_g L}(r_1 r_1', r_2 r_2'; t). \tag{4.24}$$

It is an instructive exercise to recover the 2-point expression of the two 2B self-energy contributions of Eqs. (3.80) and (3.81) by letting $A = \Xi^{\mathrm{TDHF}} L^0 V$.

4.1.5 The electron-hole problem

The BSE can be solved as a generalized eigenvalue problem yielding a spectral representation for L. In fact, by expanding the BSE in a geometric series with a static kernel one can show that each L_0 is constrained to have $t_1' = t_1$ and $t_2' = t_2$; the constraint can also be assumed for the two external L_0 on each order without loss of generality. As already mentioned, this implies working with electron-hole propagators. We emphasize that this constraint is due to having a static kernel like the TDHF one. Fourier transforming L_0 in time yields the same frequency dependence one finds for the independent-particle polarizability χ_0:

$$L^{0,L}_{\substack{l_1 l_1' \\ l_2 l_2'}}(r_1 r_1', r_2 r_2'; z) = i \sum_{\substack{n_1 n_1' \\ n_2 n_2'}} \frac{P_{n_1 l_1}(r_1) P^*_{n_1' l_1'}(r_1') P_{n_2 l_2}(r_2) P^*_{n_2' l_2'}(r_2')}{z - (\varepsilon_{n_1 l_1} - \varepsilon_{n_1' l_1'})} \times (f_{n_1' l_1'} - f_{n_1 l_1}) \delta_{n_1 l_1, n_2' l_2'} \delta_{n_1' l_1', n_2 l_2} \{l_1, l_1', L\}. \tag{4.25}$$

Here we have continued the frequency argument z to the complex plane. As mentioned in Section 4.1.4, letting $\mathbf{r}_1 \to \mathbf{r}_1'$ and $\mathbf{r}_2 \to \mathbf{r}_2'$ yields the expression of $\chi_0 = P^{\mathrm{RPA}}$, in this case in frequency domain. Therefore, by also applying Eq. (A.27), one obtains

$$\chi_{0,L}(r_1, r_2; z) = \sum_{l_1 l_1'} \sqrt{\frac{(2l_1+1)(2l_1'+1))}{4\pi(2L+1)}} C^{L0}_{l_1 0, l_1' 0} \times \sum_{n_1 n_1'} \frac{P_{n_1 l_1} P^*_{n_1' l_1'}(r_1) P_{n_1' l_1'}(r_2) P^*_{n_1 l_1}(r_2)}{z - (\varepsilon_{n_1 l_1} - \varepsilon_{n_1' l_1'})} (f_{n_1' l_1'} - f_{n_1 l_1}), \tag{4.26}$$

which is equivalent to Eq. (3.58).

L^0 is diagonal in the *wave-function product* space:

$$L^{0,L}_{\substack{l_1 l_1' \\ l_2 l_2'}}(n_1 n_1', n_2 n_2'; z) = i \frac{f_{n_1' l_1'} - f_{n_1 l_1}}{z - (\varepsilon_{n_1 l_1} - \varepsilon_{n_1' l_1'})} \delta_{n_1 l_1, n_2' l_2'} \delta_{n_1' l_1', n_2 l_2} \{l_1, l_1', L\}. \tag{4.27}$$

The product basis in 3D space is defined as

$$\xi^{LM}_{\substack{n_1 l_1 \\ n_1' l_1'}}(\mathbf{r}_1, \mathbf{r}_1') = \frac{1}{r_1 r_1'} P_{n_1 l_1}(r_1) P^*_{n_1' l_1'}(r_1') Y^{LM}_{l_1 l_1'}(\hat{\mathbf{r}}_1, \hat{\mathbf{r}}_1'), \tag{4.28}$$

and its completeness and orthonormality relations read

$$\sum_{LM}\sum_{l_1l_1'}\sum_{n_1n_1'}\xi^{LM}_{\substack{n_1l_1\\n_1'l_1'}}(\mathbf{r}_1,\mathbf{r}_1')\xi^{LM*}_{\substack{n_1l_1\\n_1'l_1'}}(\mathbf{r}_2',\mathbf{r}_2)=\frac{\delta(r_1-r_2')\delta(\hat{\mathbf{r}}_1-\hat{\mathbf{r}}_2')}{r_1r_2'}\times\frac{\delta(r_1'-r_2)\delta(\hat{\mathbf{r}}_1'-\hat{\mathbf{r}}_2)}{r_1'r_2}$$

and

$$\int d\mathbf{r}_3d\mathbf{r}_4\;\xi^{L'M'*}_{\substack{n_2'l_2'\\n_2l_2}}(\mathbf{r}_3,\mathbf{r}_4)\xi^{LM}_{\substack{n_1l_1\\n_1'l_1'}}(\mathbf{r}_3,\mathbf{r}_4)=\delta_{LL'}\delta_{MM'}\delta_{l_1l_2'}\delta_{l_1'l_2}\delta_{n_1n_2'}\delta_{n_1'n_2}\tag{4.29}$$

respectively. A projection in product space of a 4-point operator A will read

$$\begin{aligned}A^L_{\substack{n_1l_1,n_1'l_1'\\n_2l_2,n_2'l_2'}}&=\int d\mathbf{r}_3\mathbf{r}_3'\int d\mathbf{r}_4\mathbf{r}_4'A(\mathbf{r}_3\mathbf{r}_3',\mathbf{r}_4'\mathbf{r}_4)\xi^{LM*}_{\substack{n_1l_1\\n_1'l_1'}}(\mathbf{r}_3,\mathbf{r}_3')\xi^{LM}_{\substack{n_2'l_2'\\n_2l_2}}(\mathbf{r}_4,\mathbf{r}_4')\\&=\int dr_3r_3'\int dr_4r_4'A^L_{\substack{l_1l_1'\\l_2l_2'}}(r_3r_3',r_4'r_4)P^*_{n_1l_1}(r_3)P_{n_1'l_1'}(r_3')\end{aligned}\tag{4.30}$$

and reverting back to real space is achieved through

$$A^L_{\substack{n_1l_1,n_1'l_1'\\n_2l_2,n_2'l_2'}}=\sum_{LM}\sum_{\substack{n_1l_1,n_1'l_1'\\n_2l_2,n_2'l_2'}}A^L_{\substack{n_1l_1,n_1'l_1'\\n_2l_2,n_2'l_2'}}\xi^{LM}_{\substack{n_1l_1\\n_1'l_1'}}(\mathbf{r}_1,\mathbf{r}_1')\xi^{LM*}_{\substack{n_2'l_2'\\n_2l_2}}(\mathbf{r}_2',\mathbf{r}_2).\tag{4.31}$$

Finally, a product in product space reads

$$[AB]^L_{\substack{n_1l_1,n_1'l_1'\\n_2l_2,n_2'l_2'}}=\sum_{\substack{n_3l_3\\n_3'l_3'}}A^L_{\substack{n_1l_1,n_1'l_1'\\n_3'l_3',n_3l_3}}B^L_{\substack{n_3l_3,n_3'l_3'\\n_2l_2,n_2'l_2'}}.\tag{4.32}$$

We notice that representing L^0 requires only a subspace of the whole product basis, due to the presence of the $(f_{n_1'l_1'}-f_{n_1l_1})$ factor and of the angular delta $\{l_1,l_1',L\}$. This factor implies that the energy differences in the denominator of Eq. (4.27) are the independent-particle excitation energies. Therefore, we will term said subspace the *excitation basis* for the L-th angular momentum component A^L of a generic A operator. The allowed wave-function products in the excitation basis are indexed by the set of indices given by

$$\{(i,a),(a,i)\}\;\substack{i\in\text{occ.}\\a\in\text{unocc.}\\\{l_a,l_i,L\}\neq0}.\tag{4.33}$$

From now on we will in general consider the $i\equiv(n_i,l_i),j,k\ldots$ indices to refer to occupied states and the $a\equiv(n_a,l_a),b,c\ldots$ indices to refer to unoccupied states. The indices are also subject to the constraint of obeying the angular momentum selection rules imposed by the angular delta $\{l_a,l_i,L\}$. We notice that expansions of the BSE to finite orders show that each order is representable on the excitation basis, as will also be the excitonic hamiltonian.

In the wave-function product basis, without restricting ourselves to the excitation basis yet, the BSE can be rewritten as

$$\begin{aligned}\mathcal{L}^L_{\substack{l_1l_1'\\l_2l_2'}}(n_1n_1',n_2n_2';z)=i&\frac{f_{n_1l_1}-f_{n_1'l_1'}}{\varepsilon_{n_1l_1}-\varepsilon_{n_1'l_1'}-z}\\&\times\left\{\delta_{n_1l_1,n_2'l_2'}\delta_{n_1'l_1',n_2l_2}\{l_1,l_1',L\}+\sum_{\substack{l_3l_3'\\n_3n_3'}}\Xi^{\text{TDHF},L}_{\substack{l_1l_1'\\l_3'l_3}}(n_1n_1',n_3'n_3)\mathcal{L}^L_{\substack{l_3l_3'\\l_2l_2'}}(n_3n_3',n_2n_2';z),\right\}\end{aligned}\tag{4.34}$$

where $\mathcal{L}$ is the continuation of L to the plane of complex frequencies z. By following Bechstedt [213], the problem can be recast to

$$\mathcal{L}(z) = i(z\mathcal{I} - \mathcal{F}\mathcal{H})^{-1}\mathcal{F} \tag{4.35}$$

with

$$\begin{aligned}\mathcal{F}_{\substack{l_1 l_1' \\ l_2 l_2'}}(n_1 n_1', n_2 n_2') &= \delta_{n_1 l_1, n_2' l_2'}\delta_{n_1' l_1', n_2 l_2}(f_{n_1 l_1} - f_{n_1' l_1'}), \\ &= \delta_{n_1 l_1, n_2' l_2'}\delta_{n_1' l_1', n_2 l_2}\mathrm{sgn}(\varepsilon_{n_1' l_1'} - \varepsilon_{n_1 l_1})\end{aligned} \tag{4.36}$$

$$\begin{aligned}\mathcal{H}^L_{\substack{l_1 l_1' \\ l_2 l_2'}}(n_1 n_1', n_2 n_2') &= i\Xi^{\mathrm{TDHF},L}_{\substack{l_1 l_1' \\ l_2 l_2'}}(n_1 n_1', n_2 n_2') \\ &\quad + \delta_{n_1 l_1, n_2' l_2'}\delta_{n_1' l_1', n_2 l_2}\,\{l_1, l_1', L\}\,\left|\varepsilon_{n_1' l_1'} - \varepsilon_{n_1 l_1}\right|.\end{aligned} \tag{4.37}$$

The matrix $\mathcal{H}$ is hermitian and can be regarded as the *unsigned excitonic hamiltonian*, whereas the product $\mathcal{F}\mathcal{H}$ as the *signed* excitonic hamiltonian. $\mathcal{F}\mathcal{H}$ is a product of two hermitian matrices and belongs to a class of operators having real eigenvalues (pseudo-hermitian operators). Indeed, the problem of Eq. (4.35) is equivalent to a generalized (non-hermitian) eigenvalue problem for $\mathcal{F}\mathcal{H}$,

$$\mathcal{F}\mathcal{H}|\Phi_\Lambda\rangle = \Omega_\Lambda|\Phi_\Lambda\rangle, \tag{4.38}$$

whose solution allows one to rewrite Eq. (4.35) as

$$\mathcal{L}(z) = i\sum_\Lambda |\Phi_\Lambda\rangle(z - \Omega_\Lambda)^{-1}\langle\Phi_\Lambda|\mathcal{F} \tag{4.39}$$

The problem of Eq. (4.38) can be turned into an ordinary eigenvalue problem with overlap by applying $\mathcal{H}$ to both sides,

$$\mathcal{H}\mathcal{F}\mathcal{H}|\Phi_\Lambda\rangle = \Omega_\Lambda\mathcal{H}|\Phi_\Lambda\rangle, \tag{4.40}$$

since the $\mathcal{H}\mathcal{F}\mathcal{H}$ matrix is hermitian. The problem has a solution only if $\mathcal{H}$ is positive-definite, in which case the neutral excitations of the system turn out positive (in particular the eigenvalues of $\mathcal{H}$ do). Otherwise, for a general BSE kernel one may have to check for an instability against the formation of charge density waves or excitonic insulator states; or, when the TDHF kernel is used, one may have to consider the inclusion of screening to avoid a spurious closure of the HOMO-LUMO gap.

Taking Eq. (4.39) back to the real frequency axis and representing it in the product basis gives

$$\begin{aligned}L^L_{\substack{l_1 l_1' \\ l_2 l_2'}}(n_1 n_1', n_2 n_2'; \omega) &= i\left(f_{n_1 l_1} - f_{n_1' l_1'}\right)\left(f_{n_2' l_2'} - f_{n_2 l_2}\right) \\ &\quad \times \sum_\Lambda \mathrm{sgn}\left(\Omega^L_\Lambda\right)\frac{\left[\Phi^L_\Lambda\right]_{n_1 l_1, n_1' l_1'}\left[\Phi^L_\Lambda\right]^*_{n_2' l_2', n_2 l_2}}{\omega - \Omega^L_\Lambda + i\eta\mathrm{sgn}(\Omega_\Lambda)}.\end{aligned} \tag{4.41}$$

It is clear that the eigenvalues Ω_Λ assume the role of the neutral excitation energies, and the associated eigenfunctions Φ_Λ that of the excitation amplitudes. Eigenvalues occur pairwise

with opposite signs, i.e. for each index Λ there exists an index Λ' such that $\Omega_\Lambda = -\Omega'_\Lambda$. The eigenvectors associated to such pairs satisfy the condition $[\phi^L_\Lambda]_{n_1 l_1, n'_1 l'_1} = [\phi^L_{\Lambda'}]^*_{n'_1 l'_1, n_1 l_1}$. In the following we will use positive indices for positive eigenvalues and negative indices for negative eigenvalues.

These properties of eigenvalues and eigenvectors are a consequence of the structure of the excitonic hamiltonian, which we will examine now. As mentioned earlier, the excitation basis is sufficient to represent the BSE. Then, for the diagonalization of the signed excitonic hamiltonian $\mathcal{FH}$ one just needs to represent it schematically as

$$[\mathcal{FH}]^L = \{l_a, l_i, L\} \begin{pmatrix} \varepsilon_a - \varepsilon_i & 0 \\ 0 & \varepsilon_i - \varepsilon_a \end{pmatrix} + i \begin{pmatrix} \Xi^L_{ai,jb} & \Xi^L_{ai,bj} \\ -\Xi^L_{ia,jb} & -\Xi^L_{ia,bj} \end{pmatrix}, \tag{4.42}$$

where $i \equiv (n_i, l_i)$ is for occupied states and $a \equiv (n_a, l_a)$ is for unoccupied states, as mentioned earlier. The upper and the lower blocks of the diagonal are called the *resonant* and the *antiresonant* blocks respectively. The two off-diagonal blocks are the *coupling* blocks. These are neglected in the so-called Tamm-Dancoff approximation, which is not however fit for small systems and therefore for the present case. Now, to give an example, we consider a matrix element belonging to the resonant block. Here, the mapping

$$\begin{aligned} (n_1, l_1) &\to (n_a, l_a), \quad (n'_1, l'_1) \to (n_i, l_i), \\ (n_2, l_2) &\to (n_j, l_j), \quad (n'_2, l'_2) \to (n_b, l_b) \end{aligned}$$

holds, and the exchange and direct kernel matrix elements, obtained from Eqs. (4.22) and (4.23) by applying the projection of Eq. (4.30), respectively read

$$\Xi^{x,L}_{ai,jb} = -iC^{x,L}_{l_i l_a, l_j l_b} \langle aj|v_L|ib\rangle, \tag{4.43}$$

$$\Xi^{d,L}_{ai,jb} = i \sum_{l_c} C^{d,L}_{l_i l_a, l_j l_b} \langle aj|v_L|bi\rangle, \tag{4.44}$$

where completely saturated Coulomb integrals, as defined in Appendix C, appear. The matrix elements of the remaining blocks are obtained by swapping the indices as happens in Eq. (4.42).

4.1.6 The TDHF self-energy

For the computation of the *correlation* self-energy Σ^{TDHF}_c, therefore not including the iGV term amounting to the Fock contribution, we must use Eq. (4.6) of the iterative scheme, which requires a contraction of the 4-point quantity $\Xi^{\mathrm{TDHF}} LV$ to a 2-point quantity, by means of connecting two points of it with a G. This is done by applying, in the spherical representation, Eq. (4.24).

For the computation of $\Xi^{\mathrm{TDHF}} LV$ we need the representation in radial space of L, which in turn requires finding the representation of the Φ_Λ amplitudes according to Eq. (4.41). Therefore, by applying the basis transformation of Eq. (4.31) to Eq. (4.41), we obtain

$$\begin{aligned} \left[\Phi^L_\Lambda\right]_{\mathbf{r}_1 \mathbf{r}'_1} &= \frac{1}{r_1 r'_1} \sum_{l_1 l'_1} \left[\Phi^L_\Lambda\right]^{l_1 l'_1}_{r_1 r'_1} \; Y^{LM}_{l_1 l'_1}(\hat{\mathbf{r}}_1, \hat{\mathbf{r}}'_1) \\ &= \frac{1}{r_1 r'_1} \sum_{l_1 l'_1} \sum_{n_1 n'_1} \left[\Phi^L_\Lambda\right]_{n_1 l_1, n'_1 l'_1} \; P_{n_1 l_1}(r_1) P_{n'_1 l'_1}(r'_1) \; Y^{LM}_{l_1 l'_1}(\hat{\mathbf{r}}_1, \hat{\mathbf{r}}'_1) \end{aligned} \tag{4.45}$$

We will restrict the summations over n_1 and n_1' to the indices of the excitation basis at a later time. The L-th component of the product $\Xi^{\mathrm{TDHF}}LV$ can now be written as

$$\left[\Xi^{\mathrm{TDHF}}LV(z)\right]^{L}_{r_1r_1',r_2r_2'} = \sum_{\Lambda}\sum_{l_1l_1'l_2l_2'} \frac{[\mathcal{A}^L_\Lambda]^{l_1l_1'}_{r_1r_1'}\,[\mathcal{B}^L_\Lambda]^{l_2l_2'}_{r_2r_2'}}{z-\Omega^L_\Lambda}, \tag{4.46}$$

where

$$\begin{aligned}\left[\mathcal{A}^L_\Lambda\right]^{l_1l_1'}_{r_1r_1'} &= \sum_{l_3l_3'}\int \mathrm{d}r_3\,\mathrm{d}r_3'\left[2i\Xi^x + i\Xi^d\right]^{L}_{\substack{r_1l_1,r_1'l_1'\\ r_3'l_3',r_3l_3}} \\ &\quad\times\sum_{n_3n_3'}\left[\Phi^L_\Lambda\right]_{n_3l_3,n_3'l_3'} P_{n_3l_3}(r_3)P_{n_3'l_3'}(r_3'),\end{aligned} \tag{4.47}$$

$$\begin{aligned}\left[\mathcal{B}^L_\Lambda\right]^{l_2l_2'}_{r_2r_2'} &= \sum_{l_3l_3'}\int \mathrm{d}r_3\,\mathrm{d}r_3'\,V^L_{\substack{l_2l_2'\\ l_3l_3'}}(r_2r_2',r_3r_3') \\ &\quad\times\sum_{n_3n_3'}\left[\Phi^L_\Lambda\right]_{n_3l_3,n_3'l_3'} P_{n_3l_3}(r_3)P_{n_3'l_3'}(r_3').\end{aligned} \tag{4.48}$$

Finally using the contraction of Eq. (4.24) and moving to frequency space, we obtain the TDHF self-energy,

$$\begin{aligned}\Sigma^{\mathrm{TDHF}}_{c,L}(r_1r_2',\omega) = \sum_{l_w}\frac{2l_w+1}{2L+1}\sum_{\substack{n_g,l_g\\ \Lambda>0}}\int \mathrm{d}r_1'\left[\mathcal{A}^{l_w}_{-\mathrm{sgn}(\mu-\varepsilon_{n_gl_g})\Lambda}\right]^{Ll_g}_{r_1r_1'} P_{n_gl_g}(r_1') \\ \times\int \mathrm{d}r_2\left[\mathcal{B}^{l_w}_{-\mathrm{sgn}(\mu-\varepsilon_{n_gl_g})\Lambda}\right]^{l_gL}_{r_2r_2'} P_{n_gl_g}(r_2) \\ \times\frac{1}{\omega+\mathrm{sgn}(\mu-\varepsilon_{n_gl_g})(\Omega^{l_w}_\Lambda - i\eta)-\varepsilon_{n_gl_g}}.\end{aligned} \tag{4.49}$$

Note that here we are summing only over the resonant excitations, as indicated by $\Lambda > 0$. Taking into account that the Φ_Λ amplitudes only require the excitation basis to be represented, the two integrals in Eq. (4.49) read

$$\begin{aligned}\int \mathrm{d}r_1'\left[\mathcal{A}^{l_w}_\Lambda\right]^{Ll_g}_{r_1r_1'} P_{n_gl_g}(r_1') &= 2\sum_{n_al_a,n_il_i}\left[\Phi^{l_w}_\Lambda\right]_{n_al_a,n_il_i} C^{x,l_w}_{Ll_g,l_il_a}\langle n_il_i|v_{l_w}(r_1)|n_al_a\rangle P_{n_gl_g}(r_1) \\ &\quad+\sum_{n_al_a,n_il_i}\left[\Phi^{l_w}_\Lambda\right]_{n_al_a,n_il_i}\sum_{l_c} C^{d,l_c}_{Ll_g,l_il_a}\langle n_il_i|v_{l_w}(r_1)|n_gl_g\rangle P_{n_al_a}(r_1) \\ &\quad+(a\leftrightarrow i\text{ terms}),\end{aligned} \tag{4.50}$$

$$\begin{aligned}\int \mathrm{d}r_1'\left[\mathcal{B}^{l_w}_\Lambda\right]^{l_gL}_{r_2r_2'} P_{n_gl_g}(r_2) &= \sum_{n_al_a,n_il_i}\left[\Phi^{l_w}_\Lambda\right]_{n_al_a,n_il_i} C^{x,l_w}_{l_al_i,l_gL}\langle n_al_a|v_{l_w}(r_2')|n_il_i\rangle P_{n_gl_g}(r_2') \\ &\quad+(a\leftrightarrow i\text{ term}).\end{aligned} \tag{4.51}$$

This form of the self-energy can be simply reduced to that of the 2B self-energy: in particular, the form given in Eqs. (3.18) and (3.19) is obtained by neglecting the second matrix in Eq. (4.42), which contains the kernel contributions from the BSE. This means diagonalizing

a trivial excitonic hamiltonian, which will yield $|\Omega_\Lambda| = \varepsilon_a - \varepsilon_i$ in Eq. (4.49), and the $|\Phi_\Lambda\rangle$ components appearing in the amplitudes defined in Eqs. (4.50) and (4.51) will belong to the canonical basis. There will no longer be mixing from different independent-particle transitions, giving back the simpler form of the 2B self-energy. Finally, it can be shown that the TDHF self-energy is self-screening free [73]; this is not true, however, of the Φ-derivable version devised by Shirley and Martin [34].

4.2 Numerical results

In this Section we will look at numerical results obtained from the implementation of the TDHF vertex for spherical atoms in AGWX. Only spin-saturated atoms will be considered in order to take advantage of the simplifications concerning the treatment of spin, as seen in Section 4.1.3. This means that the test set will be considerably reduced.

Intermediate diagrammatic inclusions will be considered between 2B/GW and the full TDHF vertex: these include the already seen GW+SOSEX, and also $\mathrm{GW}^{\mathrm{tc-tc}}$, which is obtained by replacing W^{RPA} with W^{TDHF} in GW; and $\mathrm{GW}^{\mathrm{tc-tc}}$+SOSEX, which is obtained by adding the SOSEX contribution to $\mathrm{GW}^{\mathrm{tc-tc}}$, with W consistently evaluated at the TDHF level in both terms. From a diagrammatic point of view, $\mathrm{GW}^{\mathrm{tc-tc}}$+SOSEX is obtained by truncating the summation of ladder diagrams in the TDHF self-energy while retaining all diagrams inside W; an analogous truncation has been done when considering the SO-TDGW self-energy [50, 83]. In other words, this means solving the BSE fully for W, but not for Σ. It is interesting to analyze this truncation for a number of reasons:

(i) It can give us an estimate of how well a finite-order expansion of the TDHF self-energy can approximate the whole TDHF self-energy.

(ii) If the approximation is good, we could use $\mathrm{GW}^{\mathrm{tc-tc}}$+SOSEX instead of the whole TDHF self-energy, the latter requiring the cumbersome implementation and numerical evaluation of Eq. (4.49); $\mathrm{GW}^{\mathrm{tc-tc}}$+SOSEX instead only requires the solution of the BSE, now a staple of many general-purpose codes, and the relatively cheap evaluation of the SOSEX term.

(iii) It is not known what diagrammatic inclusions should be made in W when building the GW+SOSEX self-energy. The first-order truncation of the vertex yielding the SOSEX term is risky to perform in the polarizability, due to the appearance of poles of higher order (see Section 3.1.2). In Section 3.6 we found that the RPA@PBE W works well with GW+SOSEX, but the explanation of this success relies on empirical arguments involving the screening given by the KS gap. The TDHF W is then the only formally justified, beyond-RPA, non-pathological form of W that one can try to plug in GW+SOSEX.

In Figure 4.3 a diagrammatic depiction is given of the self-energies considered for the assessment of the upcoming Sections. Here the irreducible vertex $\tilde{\Gamma}$ is emphasized instead of the reducible vertex Γ, in order to pack infinite summations of diagrams into the screened interaction W. The diagrams shown in Figure 4.3 are simply obtained by using the TDHF irreducible vertex (the first one in Figure 1.4) in Hedin's scheme, and then by performing truncations according to each approximation (including no truncation at all for the full

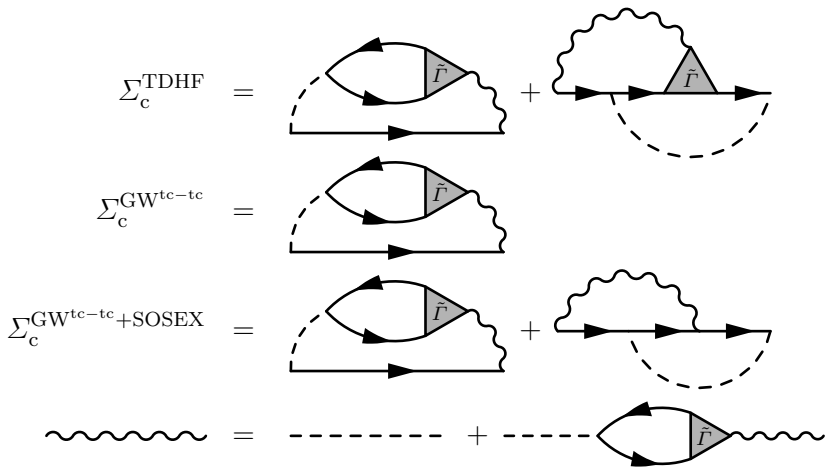

Figure 4.3. Diagrammatic representation of the correlation self-energies considered for the assessment of the upcoming Sections. The irreducible vertex $\tilde{\Gamma}$ is to be intended in the TDHF approximation, given in the first row of Figure 1.4.

TDHF self-energy). The diagrams thus found allow for a simpler diagrammatic comparison with the self-energy methods explored in Chapter 3 and summarized in Figure 3.1. We note that using the THDF $\tilde{\Gamma}$ within Hedin's scheme is completely equivalent to the iterative scheme devised in this Chapter in the TDHF approximation for Γ [74].

All self-energy calculations presented in the following are performed starting from HF orbitals and eigenvalues. This is compliant with the iterative scheme of Section 4.1.1: one obtains the initial G from the Σ^{HF} using the Dyson equation, Eq. (4.4); Σ^{HF} is then consistently used for the computation of Ξ, Eq. (2.96), so that the BSE of Eq. (4.5) can be solved; finally, Σ^{TDHF} is obtained from Eq. (4.6), and the final G with it by restarting from the Dyson equation, Eq. (4.4). This procedure allows for an unbiased assessment that is purely based on the inclusion of different classes of diagrams in the self-energy, and not on the tuning of a starting point.

In the following Sections I will present the results for the macroscopic polarizabilities (Section 4.2.1), the ionization energies (Section 4.2.2), the satellites and the upper valence (Section 4.2.3), and the xc potentials as obtained from the solution of the LSSE (Section 4.2.4).

4.2.1 TDHF polarizabilities

As a preliminary step of the accuracy assessment of the TDHF vertex, in this section we will look at the TDHF atomic polarizabilities, and compare them against the existing literature and the experimental results. In Figure 4.4 I report the computed TDHF dynamical dipole polarizability $\mathrm{Im}\{\alpha\}$, with α as defined in Section 3.3.3. We recall that $\mathrm{Im}\{\alpha\}$ has peaks in correspondence of the ^1P neutral excitation energies that can be measured in photoabsorption experiments. A comparison is made with the RPA@HF and RPA@LDA results, previously seen in Section 3.3.5. Figure 4.4 shows that a series of discrete levels

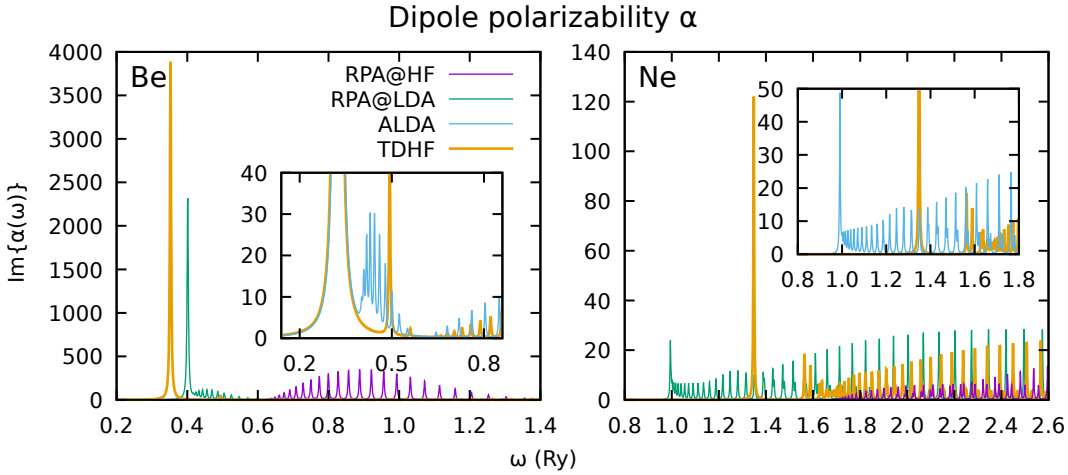

Figure 4.4. Imaginary part of the dynamical dipole polarizability α of Be and Ne as computed with RPA@HF, RPA@LDA and TDHF. The insets provide a zooming-in into the main TDHF peaks and a comparison with ALDA.

appear in the TDHF polarizability, whereas, as seen in Section 3.3.5, on one hand RPA@HF completely misses the bound excitation spectrum, and on the other hand RPA@LDA appears to have just one bound excitation with high oscillator strength, after which a ionization continuum onset quickly appears.

Upon close inspection, the RPA@LDA dipole polarizability qualitatively resembles the TDHF one in Be, but does not quantitatively match it in terms of peak positions and amplitudes. Using the ALDA response from TDDFT, which is obtained by including including the ALDA f_{xc} kernel in the Dyson equation for the response, brings the two descriptions much closer to each other: the first TDHF peak with most of the weight is faithfully reproduced by the ALDA; however, it is the only one produced by the ALDA, and the next TDHF peaks due to discrete bound excitations are replaced by an unbound continuum onset.

In Ne the differences are more relevant: RPA@LDA retains the strong peak with a continuum onset after it, while TDHF displays a series of peaks that decrease more slowly before reaching the continuum. This time the ALDA does not bring the description closer to that of TDHF, since it does not add further peaks with respect to RPA@LDA; furthermore, the ALDA does not even shift the first RPA@LDA peak as in Be, but simply renormalizes it.

As for RPA@HF, the only thing that it has in common with TDHF is the ionization continuum onset, by construction of the TDHF polarizability itself. In Be, the TDHF continuum loses most of the weight to the first bound excitation, whereas RPA@HF concentrates the weight of its continuum within a relatively narrow energy range from ~ 0.6 Ry to ~ 1.4 Ry. In Ne, much less weight of the continuum is transferred to the TDHF bound excitations. Furthermore, it is found that the continuum is peaked at a lower energy with TDHF (~ 3.0 Ry) than it is with RPA@HF (~ 4.2 Ry, both not visible in Figure 4.4).

In Table 4.1 I report the energies of the excited states of He as computed with the

Table 4.1. Neutral excitation energies (in Ry) of He as computed with the diagonalization of the TDHF excitonic hamiltonian, starting from the reference configuration He($1s^2[^1S]$). Comparison is made against TDHF results in the literature and experiment.

	Singlet				Triplet			
		This work	Lit.	Exp.[a]		This work	Lit.	Exp.
$1s2s$	^1S	1.5510	1.5518[b]	1.51523	^3S	1.4472	1.4474[b]	1.45671
$1s3s$	^1S	1.7149	1.7464	1.68461	^3S	1.6920	1.6998	1.66977
$1s4s$	^1S	1.7693		1.73997	^3S	1.7606		1.73412
$1s5s$	^1S	1.7938		1.76479	^3S	1.7896		1.76190
$1s6s$	^1S	1.8069		1.77801	^3S	1.8045		1.77639
$1s2p$	^1P	1.5939	1.59394[c]	1.55949	^3P	1.5592	1.5612[b]	1.54083
$1s3p$	^1P	1.7272	1.72722	1.69686	^3P	1.7170		1.69099
$1s4p$	^1P	1.7744	1.77444	1.74501	^3P	1.7701		1.74249
$1s5p$	^1P	1.7964	1.79644	1.76733	^3P	1.7942		1.76604
$1s6p$	^1P	1.8085	1.80844	1.77947	^3P	1.8071		1.77872
$1s3d$	^1D	1.7248		1.69591	^3D	1.7247		1.69588
$1s4d$	^1D	1.7734		1.74459	^3D	1.7733		1.74457
$1s5d$	^1D	1.7959		1.76711	^3D	1.7958		1.76710
$1s6d$	^1D	1.8081		1.77934	^3D	1.8081		1.77934
$1s4f$	^1F	1.7734		1.74463	^3F	1.7734		1.74463
$1s5f$	^1F	1.7959		1.76714	^3F	1.7959		1.76714
$1s6f$	^1F	1.8081		1.77936	^3F	1.8081		1.77936

[a] NIST [197, 214]
[b] Li et al. [150]
[c] Dalgarno and Victor [77]

diagonalization of the TDHF excitonic hamiltonian. The computations are performed with a 100-Bohr exponential grid and a basis set of 500 B-splines. Scaling the grid down to 65.0 Bohr was found to affect only the $1s6l$, $l = s, p, \ldots$ energies, and by a small difference amounting to less than 1 mRy; this guarantees that the energy values are converged. Considering that He is found to have an IE of 1.807 Ry with the TDHF vertex, the reported states are in the range from the lowest neutral state up to that corresponding to double ionization, at least limitedly to the considered angular momentum channels.

The results are overall in good agreement with the existing literature, and I had the chance to expand them over a broader set of final states thanks to the B-spline basis set being numerically well-behaved. It can be seen that the agreement with the results by Dalgarno and Victor [77], which are obtained with a numerical grid, is excellent for the first excited states and slightly degrades for the higher ones in energy. The agreement degrades more quickly in the comparison with the results by Li et al. [150], due to calculations with basis sets consisting of atom-centered wavefunctions being harder to converge. Results for triplet states are also provided in Table 4.1, which are often omitted.

Table 4.2. Neutral excitation energies (in Ry) of Be, Ne, Mg, Ar as computed with the diagonalization of the TDHF excitonic hamiltonian, starting from the neutral reference configurations. Comparison is made against TDHF results in the literature and experiment. Closed shells are omitted in the notation for electronic configurations.

		Singlet				Triplet		
			This work	Lit.	Exp.[a]		This work	Exp.
Be	$2s2p$	^1P	0.3527	0.35270[b]	0.38788	^3P		0.20028
	$2s3p$	^1P	0.4940	0.49414	0.54847	^3P		0.53680
	$2s4p$	^1P	0.5499	0.54992	0.61086	^3P		0.60883
	$2s5p$	^1P	0.5753	0.57550	0.63898	^3P		0.63848
	$2s6p$	^1P	0.5889		0.65380	^3P		0.65366
	$2s3d$	^1D	0.5086	0.50864	0.58711	^3D	0.5025	0.56547
	$2s4d$	^1D	0.5566	0.55658	0.62678	^3D	0.5536	0.61913
	$2s5d$	^1D	0.5788		0.64702	^3D	0.5772	0.64339
	$2s6d$	^1D	0.5909		0.65840	^3D	0.5900	0.65638
	$2s4f$	^1F	0.5561	0.55608	0.62186	^3F	0.5560	0.62186
	$2s5f$	^1F	0.5785	0.57856	0.64472	^3F	0.5785	0.64472
	$2s6f$	^1F	0.5908		0.65713	^3F	0.5907	0.65713
Ne	$2p^53s$	^1P	1.3482	1.3478[c]	1.23831	^3P	1.3210	1.22856
	$2p^54s$	^1P	1.5635	1.5636	1.44705	^3P	1.5578	1.45237
	$2p^53d$	^1P	1.5886	1.5888	1.47253	^3P	1.5877	1.47252
	$2p^55s$	^1P	1.6279	1.6278	1.51868	^3P	1.6258	1.51823
	$2p^54d$	^1P	1.6379		1.52182	^3P	1.6374	1.52181
	$2p^56s$	^1P	1.6557		1.54667	^3P	1.6546	1.54647
	$2p^55d$	^1P	1.6606		1.54462	^3P	1.6603	1.54461
Mg	$3s3p$	^1P	0.2960	0.2984[d]	0.31941	^3P	0.08098	0.19912
	$3s4p$	^1P	0.4028	0.4042	0.44968	^3P	0.38159	0.43596
	$3s5p$	^1P	0.4465		0.49852	^3P	0.43905	0.49435
	$3s6p$	^1P	0.4675		0.52138	^3P	0.46397	0.51958
Ar	$3p^54s$	^1P	0.8967	0.8950	0.86935	^3P	0.8713	0.86163
	$3p^55s$	^1P	1.0627		1.04773	^3P	1.0579	1.04669
	$3p^53d$	^1P	1.0678		1.02992	^3P	1.0284	1.02745
	$3p^56s$	^1P	1.1164		1.10410	^3P	1.1145	1.10351
	$3p^54d$	^1P	1.1182		1.08635	^3P	1.0982	1.08462

[a] NIST [197, 215–219]
[b] Stewart (1975a) [79]
[c] Stewart (1975b) [80]
[d] Stewart (1975c) [81]
see also Ref. 82

Table 4.3. Static dipole polarizabilities Re$\{\alpha(0)\}$ [in Bohr^3] computed using different theoretical methods and approaches. MBPT methods: IP = Independent Particle[LDA], RPA = RPA[LDA], LDA = RPA[LDA] + f_{xc}[LDA], TDHF = TDHF[HF]. Theoretical reference methods: CCSDT = coupled cluster with single, double and triple excitations, CICP = configuration interaction with semi-empirical core potential.

Atom	IP	RPA	LDA	TDHF	Theory	Method
He	1.810	1.465	1.660	1.322[a] 1.322[b]	1.384[d]	CCSDT
Be	80.39	32.47	43.75	45.617[a] 45.62[c]	37.69	CICP
Ne	3.487	2.767	3.055	2.377[a] 2.377[b]	2.69	CCSDT
Mg	121.9	52.95	71.28	81.599[a] 81.60[c]	71.35	CICP
Ar	17.98	10.63	12.01	10.757[a] 10.758[b]	11.08	CCSDT
Ca	276.2	106.4	148.3	185.468[a] 185.5[c]	159.4	CICP
Zn	68.392	30.602	38.523	54.084[a] 54.07[c]	38.12	CICP
Kr	27.79	15.83	18.05	16.475	16.80	CCSDT

[a]This work
[b]McEachran et al. [220]
[c]Markiewicz et al. [221]
[d]Mitroy et al. [196]

The comparison of TDHF results against the experiment is much more satisfactory than one has with RPA@LDA or RPA@HF, since in the RPA excitation energies are quite close to eigenvalue differences. However, many TDHF excitation energies are larger than the experimental ones by an amount of ~ 0.03 Ry. The best agreement is found for the $^3P[1s2p]$ triplet state. Screening v statically in the BSE kernel, i.e. considering a static TDGW (or equivalently time-dependent COHSEX [222]) vertex, was found to improve the situation by Li et al., but not by an amount sufficient to reach full agreement on the second decimal figure in Ry units. Therefore, it would be interesting to further explore the effect that screening v has in the BSE kernel, for example by removing the static approximation and using a scGW starting point; even if the static approximation were to be kept, the COHSEX starting point would be interesting to explore, since Li et al. used ev-scGW.

In Table 4.2 I report the TDHF neutral excitation energies of Be, Ne, Mg and Ar, which again agree well with the existing literature. The presence in real atoms of sizable multiplet splittings that go beyond total spin multiplets (i.e. singlet-triplet splitting) hinders the

comparison of results for Ne and Ar with experiment. The reported experimental energies are those of the spectral lines chosen by Stewart in Refs. 79, 80 and 81, updated to the most recent measurements [197]: in particular they correspond to the $^2[1/2]^o$ term for excitations to s levels, and to the $^2[7/2]^o$ term for excitations to d levels; of the two possible total angular momenta, the smaller one corresponds to the spin singlet (excited electron has the same spin orientation it had in the p shell), whereas the larger one to the spin triplet (excited electron has opposite spin orientation to that it had in the p shell).

The TDHF results are still way better than the RPA@HF and RPA@LDA ones, but the discrepancies with experiment are now becoming larger than they were in He. We note that, differently from the case of He, the reported energies are well below the HF HOMO-LUMO difference, so they are all bound states. In Be and Mg the discrepancy between the computed and the measured excitation energies is seen to increase as one goes higher in energy. In Ne the largest deviation is found, of ~ 0.1 Ry: the result is not as bad as the 2B one for the ionization energy, but these two results together suggest that Ne could benefit from some screening at the vertex level, pointing again at a TDGW approach. Although sharing the same valence shells with Ne, these having the most important role in the transitions determining the polarizability, Ar appears to be better suited for TDHF. Both Ne and Ar, however, present some wrong excitation ordering in TDHF: for example, the $2p^5 6s[^1P]$ excitation of Ne is energetically below the $2p^5 5d[^1P]$, while the opposite is true in the experiment.

Another indicator that the TDGW vertex should be considered is that the the triplet states of Be could not be computed in the TDHF approximation, due to the unsigned excitonic hamiltonian not being positive-definite: this implies negative excitation energies, i.e. a closing of the HOMO-LUMO gap, and is reminiscent of the problem found in the self-consistent calculation of the MP2 xc potential for Be using the LSSE. Although the issue has already been spotted in small molecules of the GW100 test set [41], it is striking that such issue is also found outside the KS-DFT framework (which suffers from the KS energy gap problem) in an atom having as few electrons as Be. Screening v in the vertex, as one would do in TDGW, could prevent the closing of the HOMO-LUMO gap. As in the LSSE-MP2 method, the same problem is found in Ca concerning triplet states.

In Table 4.3, we report the TDHF static dipole polarizabilities. A comparison is made with the results obtained within RPA@LDA and ALDA in the static limit, the latter simply called LDA; these were previously shown in Table 3.1 and discussed in Section 3.3.5. The improvement brought about by TDHF on previously seen methods is apparent for He and Kr, but not so large for other atoms. In group-2 atoms the LDA is still better, while in Ne RPA is. In Ar TDHF offers a slight improvement on RPA, while in Zn it performs poorly, possibly due to the excitations from the much populated d shell requiring some screening for an appropriate treatment.

4.2.2 TDHF ionization energies

To begin the assessment of the TDHF vertex and intermediate diagrammatic inclusions leading up to it, we consider the atomic IEs as computed from the negatives of the HOMO QP energies, similarly to what was done in Section 3.6.1. For a general assessment, we can consider Table 4.4 where the MAEs on the IEs are reported. The atomic test set was reduced for this benchmark, removing spin-polarized atoms, therefore the MAEs of methods

Table 4.4. Negative of HOMO energies (Ry) as computed with different self-energies and starting points: mean absolute error (MAE), maximum absolute error (Max AE) and minimum absolute error (Min AE). All calculations are one-shot on a HF reference, except where differently noted. Experimental IEs are from Ref. 139.

Method	MAE	Max AE	Min AE
HF	0.059	0.116	0.019
GW	0.021	0.048	0.003
2B	0.022	0.088	0.001
GW+SOSEX	0.031	0.054	0.006
GW^{tc-tc}	0.020	0.042	0.003
GW^{tc-tc}+SOSEX	0.018	0.030	0.002
TDHF	0.013	0.032	0.001
GW@PBE0	0.015	0.042	0.001
GW+SOSEX@PBE	0.009	0.018	0.001

seen previously differ from those reported in Figure 3.12 and Table 3.5. In particular, 2B@HF now has a performance comparable with that of GW@HF: in fact, all the atoms where 2B performs best are now absent; furthermore, the large error of 2B in Ne now has a larger weight in the average. We also compare with the best performing methods of the previous assessment, which enjoy an artificial improvement with the removal of spin-polarized atoms.

Looking at Table 4.4, the first remark that can be made is that all partial vertex corrections between GW and TDHF do not bring a substantial improvement to the IEs. Therefore, this general trend confirms that vertex corrections should be included consistently both in the self-energy and the polarizability. The previously unexplored GW^{tc-tc}+SOSEX self-energy does seek some consistency in this sense, but the contribution of higher-order ladder diagrams appears to be non-negligible a posteriori. The good news is that the performance of the TDHF vertex is in line with the best methods seen previously. This performance is expected to even improve should spin-polarized atoms be included, especially the ones from group 1. In fact, in the previous assessment we showed 2B to perform excellently in these atoms as compared to other methods, likely due the lone valence s electron being well described by a self-screening-free self-energy like 2B is. Since self-screening freedom is also a feature of TDHF, this self-energy should perform as satisfactorily.

For a more specific assessment, in Figure 4.5 I show the deviation from experiment of the IEs. In the few-body case, i.e. from Mg downwards, the TDHF self-energy is the superior approximation with respect to 2B and GW. While 2B and GW may each provide accurate IEs limitedly to given subsets of atoms, TDHF displays a consistency over all of them, equaling if not improving 2B and GW when they are at their best. In particular, GW appears to be the best choice for Be, Ne (where 2B encounters a striking failure) and Mg, whereas 2B is better for He; with the inclusion of relatively accurate screening and self-screening freedom, TDHF borrows the best from either method, bringing about a consistent improvement on all these light atoms. The trend is partially maintained even for heavier atoms, however here TDHF can be outperformed by either 2B (Ar, Ca, Kr)

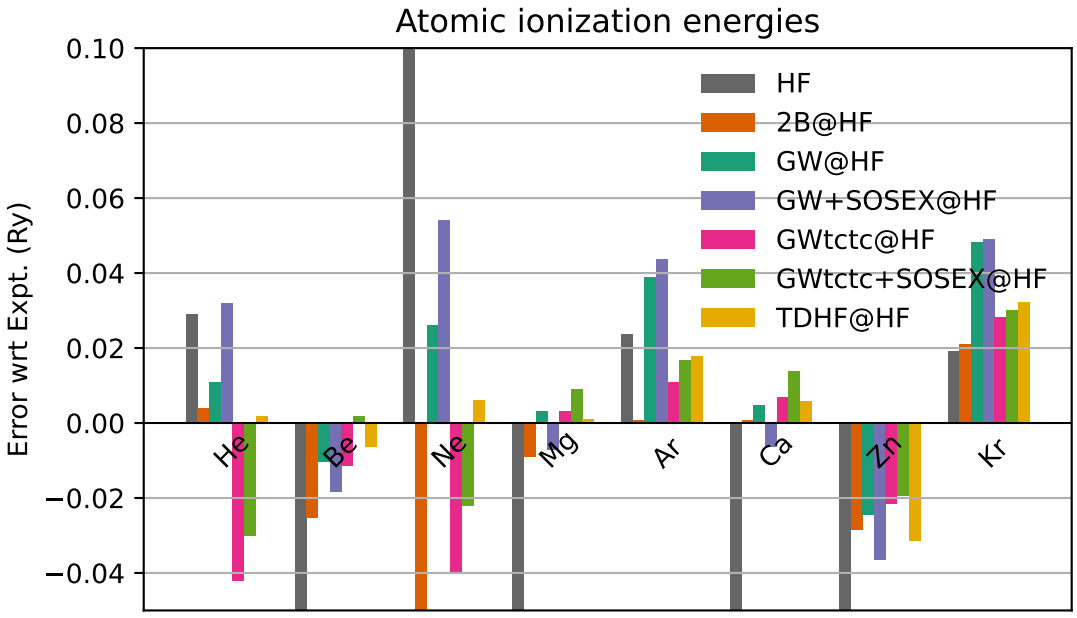

Figure 4.5. Deviation from experiment (Ry) of the atomic IEs as computed with selected diagrammatic inclusions between HF and TDHF. Experimental IEs are from Ref. 139.

or GW (Zn), and the errors generally increase, although remaining low in group 2 (Ca). Indeed, as also seen in Section 4.2.1, one expects that, as valence shells get more populated with electrons, the effect of screening becomes more important accordingly, requiring some accounting for it already at the level of the BSE.

As anticipated in the general MAE assessment following Table 4.4, the partial diagrammatic inclusions are not as satisfactory as the full TDHF vertex. GW^{tc-tc} presents large errors in He and Ne, suggesting that this is an imbalanced self-energy approximation in the few-body case: in fact, no exchange (or equivalently ladder) diagrams are being added to the self-energy with respect to GW; using the TDHF W in GW^{tc-tc} has instead the effect of increasing the number of direct (or bubble) diagrams, these now also having bare Coulomb insertions connecting the fermion and the hole propagators. As a consequence, there is an imbalance in the addition of diagrams that ends up exacerbating the self-screening error. It is however puzzling, following this interpretation, that GW^{tc-tc} is not as bad in Be. In heavier atoms GW^{tc-tc} does not behave as badly either: the performance is often on par (Mg, Ca, Zn) if not leagues better (Ar, Kr) than that of GW. This could shed light on the ambiguity about the inclusion of vertex corrections in the polarizability only, which has recently resurged within the context of small molecules [74, 100]: in particular, our results indicate that this is especially an issue in few-body systems, and improvement can be possible in systems with more electrons, although not always and systematically. Unfortunately, trying to correct for the imbalance of GW^{tc-tc} with the SOSEX diagram is quite unsuccessful: with the exception of Be, where a possibly fortuitous very good agreement with experiment is achieved, the results for lighter atoms show that the performance of

TDHF can hardly be attained by GW^{tc-tc}+SOSEX. In He, in particular, one can see that the improvement is quite modest, whereas in most atoms on the heavier end (Mg, Ar, Ca, Kr) GW^{tc-tc}+SOSEX does even worse than GW^{tc-tc}.

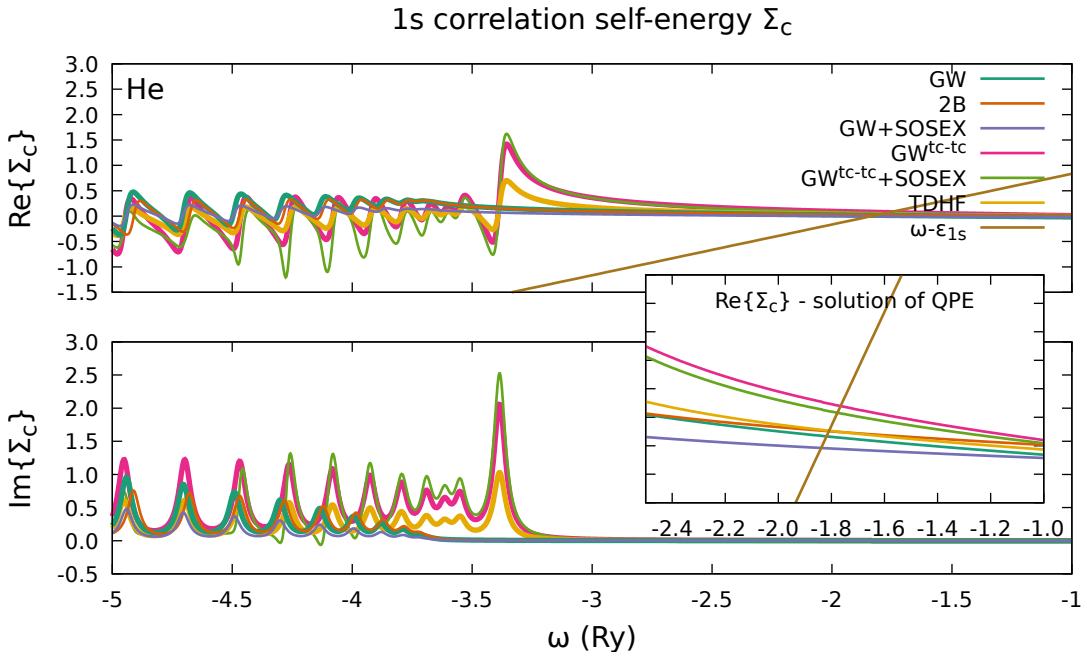

Figure 4.6. $\langle 1s|\Sigma_c|1s\rangle$ of He as computed with different diagrammatic inclusions between 2B and TDHF on a HF reference. The inset is a zooming-in on the frequency region where the QPE has a solution. Thick lines are used to emphasize the major qualitative differences.

More information on the behaviour of partial diagrammatic inclusions can be deduced from the orbital self-energies. These are indeed used to solve the QPE, Eq. (3.84), in order to obtain the HOMO QP energies from which the IEs are deduced. In Figures 4.6, 4.7 and 4.8, I show said orbital self-energies. The first general remark, looking at the energy regions where satellites are found, is that there is no smooth progression from GW to TDHF: the structures of each orbital self-energy are mainly influenced by the inclusion of the *whole* vertex, be it either in the self-energy, the polarizability, or both; truncations of it, which translate to 2-point self-energy diagrams such as SOSEX, have instead little effect. For instance, including the TDHF vertex in W only, as is done in GW^{tc-tc}, causes the first major change in the shape of the self-energy. A series of stronger, discrete, satellite peaks appears before the continuum onset: these are simply the excitations introduced by W beyond IP and RPA at the TDHF level, that have been mapped to the self-energy (with the zero centered at the HF energy according to Eq. (3.4)). Adding also all the ladder diagrams, i.e. building the full TDHF self-energy, causes another major change, consisting in a strong renormalization of the satellites. Low-order truncations of the vertex have rather a smaller and simply quantitative effect: this can be seen by looking at the little difference that it makes for the satellite spectrum when 2B, GW and GW+SOSEX are considered. When added to GW^{tc-tc}, the SOSEX diagram also completely fails at renormalizing the GW^{tc-tc}

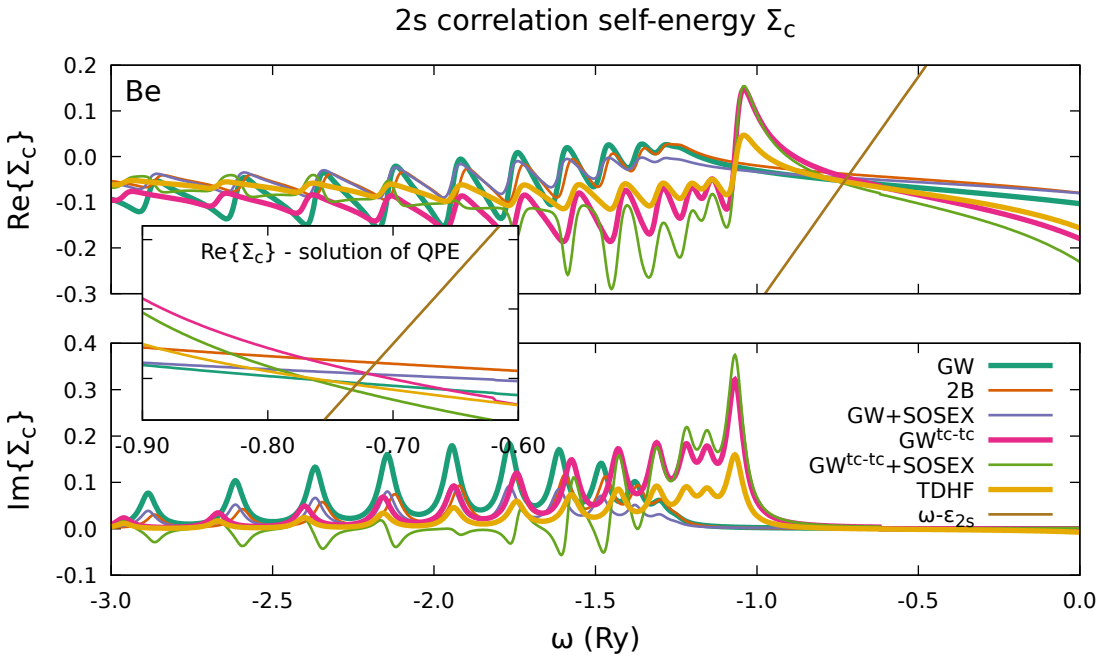

Figure 4.7. $\langle 2s|\Sigma_c|2s\rangle$ of Be as computed with different diagrammatic inclusions between 2B and TDHF on a HF reference.

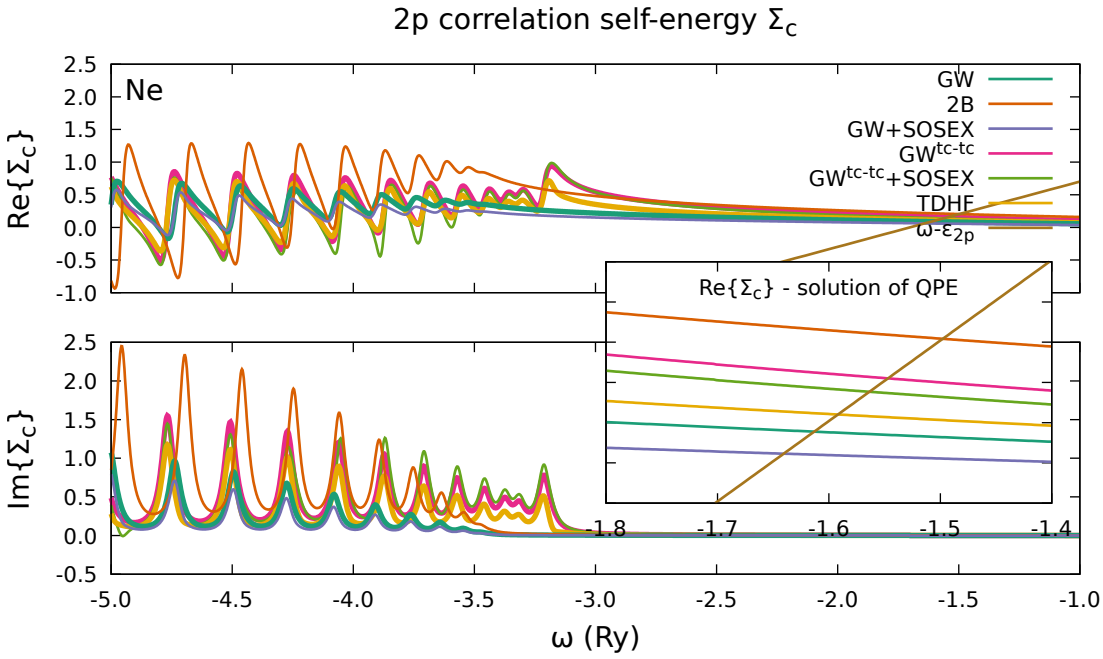

Figure 4.8. $\langle 2p|\Sigma_c|2p\rangle$ of Ne as computed with different diagrammatic inclusions between 2B and TDHF on a HF reference.

peaks, even increasing their height instead of reducing it toward the TDHF limit. However, in the region of the solution of the QPE the GW^{tc-tc}+SOSEX self-energy does get closer to the TDHF one, justifying the slight improvement of the IE in comparison to GW^{tc-tc}. In fact, a self-energy can actually give good predictions of QP properties while offering poor account for satellites, as 2B, GW and GW+SOSEX exemplify. In general, the success of these low-order expansions is due to higher-order diagrams canceling the effect of each other [34], at least in the energy region where the QPE is solved, which is usually smooth and sufficiently away from satellites. This is especially true of HOMO QP energies, while the computation of deeper QP energies can be hindered by a poor satellite description as we shall see in Section 4.2.3.

Looking at Be and Ne in Figures 4.7 and 4.8 respectively, the trends in going from one self-energy to the other are pretty much the same. We notice that in Be GW^{tc-tc}+SOSEX yields negative peaks in $\mathrm{Im}\{\Sigma_c\}$: these in turn map to negative peaks in the spectral function, violating the exact property of positive definiteness [88–90]. In principle, GW+SOSEX, GW^{tc-tc}+SOSEX, and TDHF are all self-energies that, by construction, should produce some violation of the spectral positive definiteness. In practice, I have found said violation to occur only in the instance just considered, and in TDHF, as we shall see Section 4.2.3; whereas, for GW+SOSEX I have found no such violation yet, which may require a careful analysis involving e.g. tuning of the numerical broadening of lorentzian peaks. It must be said that the violation of the spectral positive definiteness may hinder the prediction of satellites and the implementation of self-consistency, but in a one-shot scheme as the one presented here QP properties can still be accurate, as the TDHF results show.

Finally, by looking at Ne in Figure 4.8, we gain some insight on the failure of 2B in Ne that we also noticed in Section 3.6.1: the 2B satellite continuum shows a considerable weight at its onset, which pushes $\mathrm{Re}\{\Sigma_c\}$ way too high in the region of the QPE solution. The continuum at the onset gets substantially renormalized in all the self-energies including W, the latter at least at the RPA level. Therefore, in Ne the independent-particle polarizability appears to map to the self-energy satellite spectrum in a particularly inconvenient way for the prediction of the QP HOMO.

4.2.3 Satellites and deeper quasi-particles

As seen in Section 4.2.2, the TDHF polarizability introduces important changes in the satellite features of self-energies that adopt it to some level. It is then interesting to investigate how these map to the spectral function and compare with experimental data. We will consider He and Ne, of which experimental photoemission spectra are available [158, 159, 161] that can be directly compared against our calculations. In Figure 4.9 I show the spectral function of He as computed with GW, GW^{tc-tc} and TDHF, along with the photoemission spectrum. As polarizabilities, of which they are a product, satellites are more demanding to converge then QP energies with respect to numerical parameters, so for these calculations a basis set of 300 B-splines and a 100-Bohr cubic grid were used. In order to properly resolve the satellites, the broadenings of the lorentzian peaks were reduced with respect to those employed for computing the self-energies seen in Figures 4.6, 4.7, 4.8, them being as low as 0.001 Ry here. The Dyson equation is fully inverted on the frequency grid, bypassing the diagonal approximation for the spectral function, as in Eq. (2.116), and the solution of the QPE, Eq. (2.118).

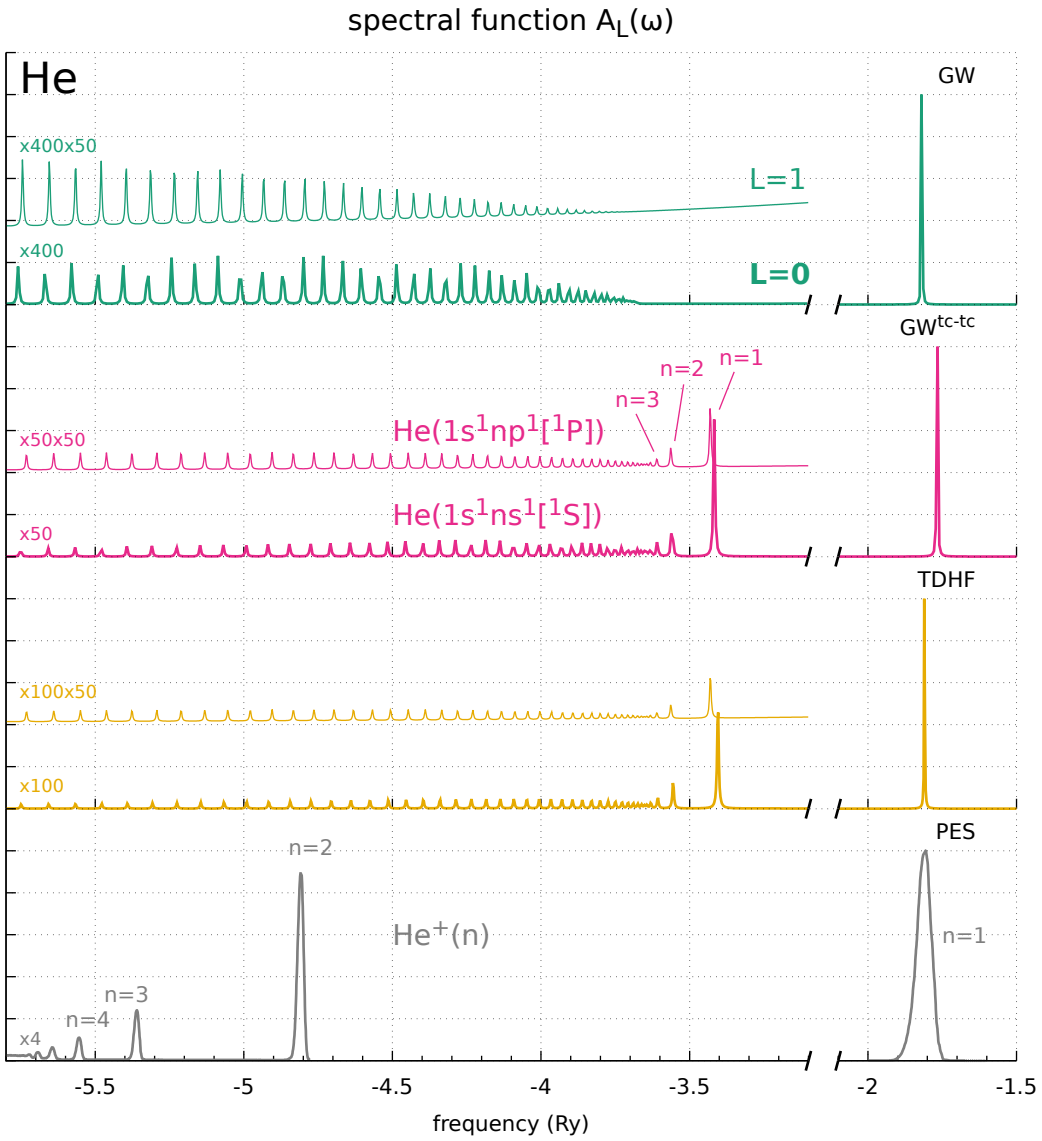

Figure 4.9. Spectral functions of He in the GW, GW$^{\mathrm{tc-tc}}$, and TDHF approximations to the self-energy. Thick lines refer to the $L = 0$ channel of the spectral function, thin lines to the $L = 1$ channel. The satellites of the $L = 0$ channel are due to monopole transitions ($[^1S]$ final state), whereas those of the $L = 1$ channel are due to dipole transitions ($[^1P]$ final state). In the bottom, a photoemission spectrum from Ref. 158 is plotted for reference. The spectra are normalized so that the QP peaks from different approximations/experiment all have the same height.

We can see that in GW the spectral function has a continuum onset at about twice the HF HOMO energy of He, i.e. ~ 3.670 Ry, in agreement with the pole structure of Σ_c seen in Eq. (3.4) (which is somewhat faithfully mapped by the Dyson equation to the spectral function, by comparison with Figure 4.6). A series of peaks due to the bound neutral excitations contained in the TDHF W appear in $\mathrm{GW}^{\mathrm{tc-tc}}$ before the continuum onset. As expected, GW and $\mathrm{GW}^{\mathrm{tc-tc}}$ mirror the results seen in Figure 4.4 for the RPA@HF and the TDHF polarizabilties respectively. Again, this is a reasonable result for the self-energies, given the pole structures in Eqs. (3.4) and (4.49): these pole structures then get mapped to the spectral function by the Dyson equation. Going beyond $\mathrm{GW}^{\mathrm{tc-tc}}$ by considering TDHF does not produce a different pole structure, but just a renormalization of the peaks, as also seen in Figure 4.6.

As for the characterization of the satellites, two angular momentum channels of the spectral function A_L are shown in Figure 4.9: the ones with $L = 0$ and $L = 1$. These correspond to the angular momentum channels of the self-energy $\Sigma_{c,L} \sim G_{l_g} W_{l_w}$. The angular momentum selection rules, which impose a non-vanishing angular delta

$$\{l_g, l_w, L\} \neq 0$$

as per Eq. (3.70), imply that for $L = 0$ we have that $l_g = 0$ and $l_w = 0$, therefore the satellites are given by *monopole* transitions ($[^1S]$ final state) in the atom; for $L = 1$ we must instead have $l_g = 0$ and $l_w = 1$, so the satellites are given by *dipole* ($[^1P]$ final state) transitions. We remark that $l_g = 0$ because we are looking at the satellites associated to the removal of an electron from the occupied $1s$ state. Furthermore, the requirement of non-vanishing angular delta of Eq. (3.70) is shared by the $\mathrm{GW}^{\mathrm{tc-tc}}$ and the TDHF self-energies: it follows that the excitations preserve their character in all the three theoretical spectra shown in Figure 4.9. In spectroscopic notation, the monopole transitions then read

$$1s^2[^1S] \to 1s^1 ns^1[^1S], \ n = 2,3,\dots, \tag{4.52}$$

while the dipole transitions read

$$1s^2[^1S] \to 1s^1 np^1[^1S], \ n = 2,3,\dots, \tag{4.53}$$

as also seen in Table 4.1. We recall from Section 1.6 that the satellites associated to bound transitions are called the shake-up satellites; whereas the continuum is called the shake-off continuum, in which double ionization occurs. We also recall that in photoemission experiments, the transitions with by far the largest cross sections are the dipole transitions, meaning that the photon transfers one unit of angular momentum to the system: here, in the case of He, it can be transferred either to the photoelectron, thus taking it to an unbound p state and inducing monopole transitions in He^+ ($L = 0$ channel of the spectral function); or to the electron remaining in the system, thus taking the photoelectron to an unbound s state ($L = 1$ channel of the spectral function, conjugate shake-up).

All three theoretical spectra share the same shake-off threshold for the double ionization continuum, amounting to about twice the HF HOMO energy, as mentioned earlier. This is the first symptom of a lacking description: the second ionization energy of an atom is usually quite higher than the first ionization energy [139]; therefore, it should take more than twice the first ionization energy to reach the shake-off threshold. Looking at the experimental spectrum in the bottom of Figure 4.9, we find that the shake-off threshold is

indeed at more than ~ 5.7 Ry, which is close to summing the first and the second ionization energy of He [139], giving ~ 5.8 Ry. More in general, the whole experimental satellite spectrum is found at lower energies than the theoretical ones obtained from $\mathrm{GW}^{\mathrm{tc-tc}}$ and TDHF, and with larger spacings between the peaks. As already explained in Section 1.6, the reason is that the shake-up satellites of He are given by the neutral transitions of the He^+ hydrogenic atom from the $\mathrm{He}^+(1)$ state to the $\mathrm{He}^+(n)$, $n = 2,3,\ldots$ excited states. This is not accounted for by $\mathrm{GW}^{\mathrm{tc-tc}}$ and TDHF, which, by Eq. (4.49), produce satellites due to transitions in the neutral atom. There is no account for relaxation in the He^+ atom, which can only be obtained with a dynamical vertex that can change the pole structure of Eq. (4.49). As a last remark on accuracy, we note that the intensity of the satellites is generally too weak: those of $\mathrm{GW}^{\mathrm{tc-tc}}$ are the closest to experiment, yet they are less intense by more than one order of magnitude.

Looking now at the results for Ne in Figure 4.10, we see that the the prediction of satellites suffers from the same problems that we saw in He, with the theoretical satellites being at too high energies, as is also the shake-off threshold of the $L = 1$ channel of the spectral function. Not only this, but the satellite onset of all theoretical methods is found at higher energies than the $2s$ energy, which is definitely not the case in the experimental spectrum! We will discuss later the implications of this discrepancy for the prediction of QP properties.

Connecting the theoretical and experimental results in Ne is more complicated than in He on a qualitative level. From Figure 4.9, we see that in He the energy at which the satellite is found is determined solely by the principal quantum number n of the final state: this is completely true for the experimental spectrum due to the eigenvalue degeneracy of hydrogenic atoms, and largely true for the theoretical spectra. In the latter case, the two angular momentum channels of the spectral function show substantially little difference in terms of peak positions; furthermore, the $L = 1$ channel is very much reduced in intensity as compared with the $L = 0$ channel.

In Ne, setting the quantitative differences aside and trying to trace qualitative connections is not as simple. On one hand, the excitations in the theoretical spectra have the $1s^2 2s^2 2p^6$ closed shell as a reference, and couple to the emission of a $2p$ electron. For this coupling to hold, one has to consider the $l_g = 1$ component of G_{l_g} and, following the usual rule of non-vanishing angular delta, for the $L = 0$ channel one needs to have $l_w = 1$ in W_{l_w}. Therefore, in the $L = 0$ channel, at variance with the case of He, the satellites are due to dipole transitions. Conversely, in the $L = 1$ channel we have that $l_w = 0,2$, so we are seeing monopole and quadrupole transitions ($[^1D]$ final state), the latter being very faint; dipole transitions with $l_w = 1$ are forbidden here by a further selection rule requiring that $l_g + l_w + L \mod 2 = 0$ (see bullet point (v) of Appendix A).

On the other hand, the experimental excitations producing the satellites have the $2s^2 2s^2 2p^5$ reference. Therefore, it is not guaranteed that, say, the $2p^6 \to 2p^5 3p$ transition we see in theoretical spectra should be mapped to the $2p^5 \to 2p^4 3p$ transition in the experimental spectrum. One could compare excitations having the same character in terms of final angular momentum, thus distinguishing them into monopole and dipole transitions, but the authors of Ref. 161 do not report this distinction; only the final single particle orbitals are specified as shown in Figure 4.10.

As mentioned earlier, the computed QP $2s$ peak of Ne in Figure 4.10 is found after the satellite onset. Not only is the energy ordering wrong, but the $2s$ peak appears noisy

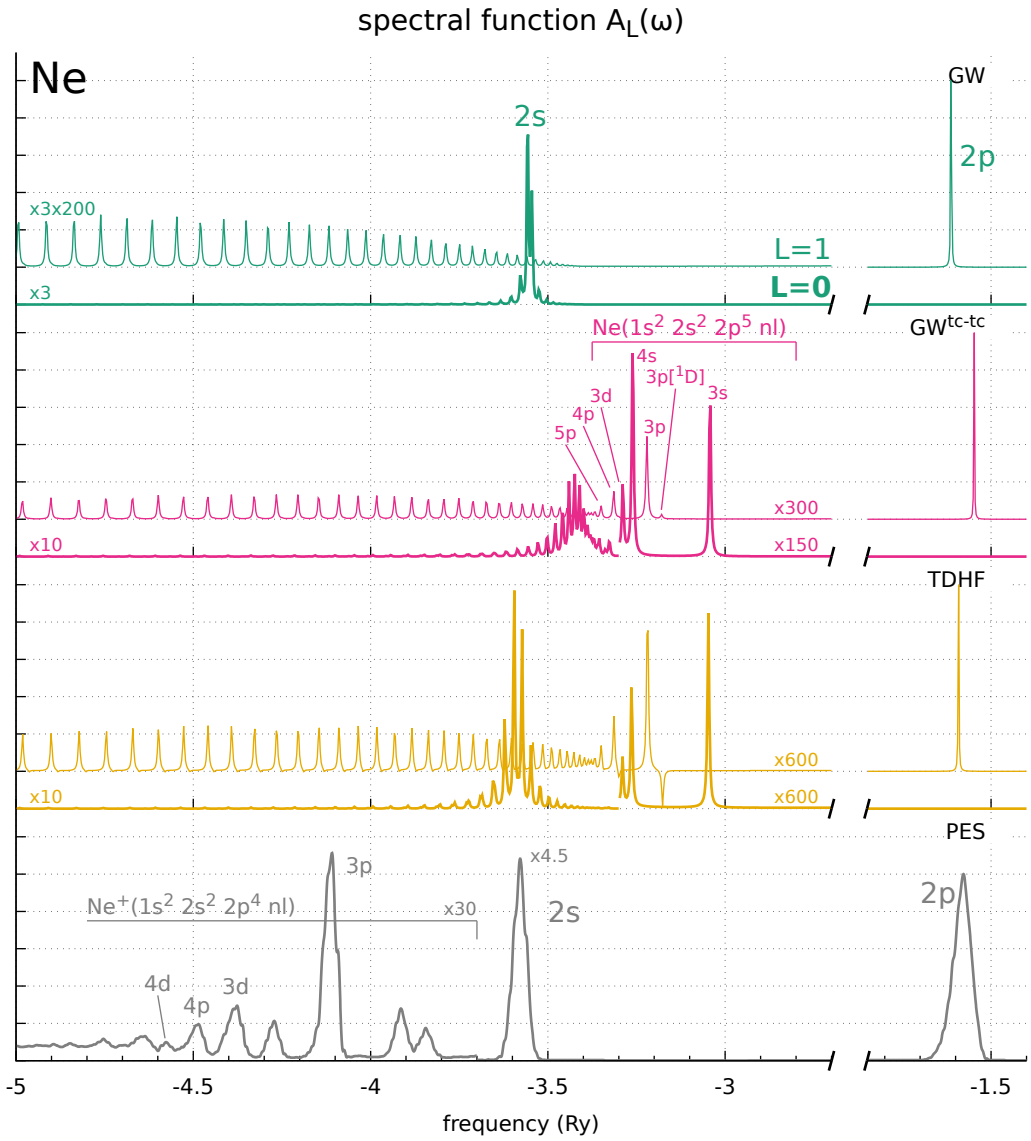

Figure 4.10. Spectral functions of Ne in the GW, GW^{tc-tc}, and TDHF approximations to the self-energy. Thick lines refer to the $L = 0$ channel of the spectral function, thin lines to the $L = 1$ channel. The satellites of the $L = 0$ channel are due to dipole transitions ($[^1P]$ final state), whereas those of the $L = 1$ channel are due to dipole transitions ($[^1S]$ final state), except where otherwise noted. In the bottom, a photoemission spectrum from Ref. 161 is plotted for reference. The spectra are normalized so that the QP peaks from different approximations/experiment all have the same height.

due to being spread over a number of lorentzians that concur to its formation. This is a direct consequence of the peak being found after the satellite onset. In the $\langle 2s|\Sigma_{c,L=0}|2s\rangle$ correlation self-energy, in fact, one finds satellites due to $2p^6[^1S] \to 2p^5ns[^1P]$ dipole transitions, since the condition $L = 0$ in Σ_c is obtained by coupling $G_{l_g=1}$ and $W_{l_w=1}$. As seen earlier, in GW the satellite onset, coinciding with the shake-off continuum, is found at twice the HF HOMO energy, which in Ne happens to lie higher in energy than the $2s$ level; in GW^{tc-tc} and TDHF the onset is even higher in energy due to the appearance of the bound excitations. Therefore, the solution of the QPE for the $2s$ level is found in a non-smooth region of the self-energy characterized by the presence of satellites, which has important qualitative repercussions on the related peak in the spectral function.

Similar issues have been found in the study of molecular core levels when employing GW@PBE [118]. In such a case, it was found that ev-scGW$_0$ pushes the satellite spectrum down below in energy, thus allowing the QPE to have a solution in a smoother region of the self-energy. However, in the present case no flavour of self-consistency appears to be a solution to the issue: in fact, GW self-consistency is known to often reduce the HF HOMO-LUMO gap, this being especially true for Ne [35, 146]. If self-consistency were pursued here, we would get an even shallower satellite onset.

Despite the noisy nature, the $2s$ peaks are still well defined if one works with full inversion of the Dyson equation as is done here. The GW and the TDHF $2s$ peaks are actually pretty accurate in their energy positioning, with the TDHF one being however too faint, and improvement is found in both cases with respect to the HF $2s$ level having an energy of -3.861 Ry. Solving the QPE and computing Z-factors is instead more problematic, due to the oscillating self-energy in the region of the solution. In this case, a smooth representation of the continuum should be sought: Shirley and Martin [34] adopted a pole-dependent broadening for smoothing the self-energy after the onset of satellites. Of course, such a procedure would also make the $2s$ peaks seen in Figure 4.10 smoother.

Numerical recipes aside, the energy ordering of the satellites and the $2s$ QP is still wrong, as a consequence of the satellite spectrum being wrongly positioned at large. Overall, despite the promising qualitative changes brought about by the TDHF polarizability, comparison with experiment is disappointing in both He and Ne. For the issue to be addressed, an account of the relaxation induced by the hole left by the photoelectron should be included in the theoretical description. This is the subject of the preliminary work presented in Chapter 5.

Before concluding, by looking at Figure 4.10 we note that a violation of the spectral positive definiteness occurs in TDHF for the $3p[^1D]$ satellite, and also for the following ones in the series of quadrupole transitions (less visible). Like GW^{tc-tc}+SOSEX, which produced a violation in Be as seen in Figure 4.7, the TDHF self-energy does not preserve the spectral positive-definiteness by construction. Nonetheless, accurate results for the QP properties are obtained from TDHF.

4.2.4 TDHF xc potentials

Although no presentation was given of the specialization of the LSSE for the TDHF vertex, the results of Section 3.5.5 can be easily adapted to the TDHF self-energy of Eq. (4.49). The expression as a sum over poles of the TDHF self-energy is in fact similar to that of GW, as can be seen by comparing Eqs. (4.49) and (3.4). Then one need only perform the last

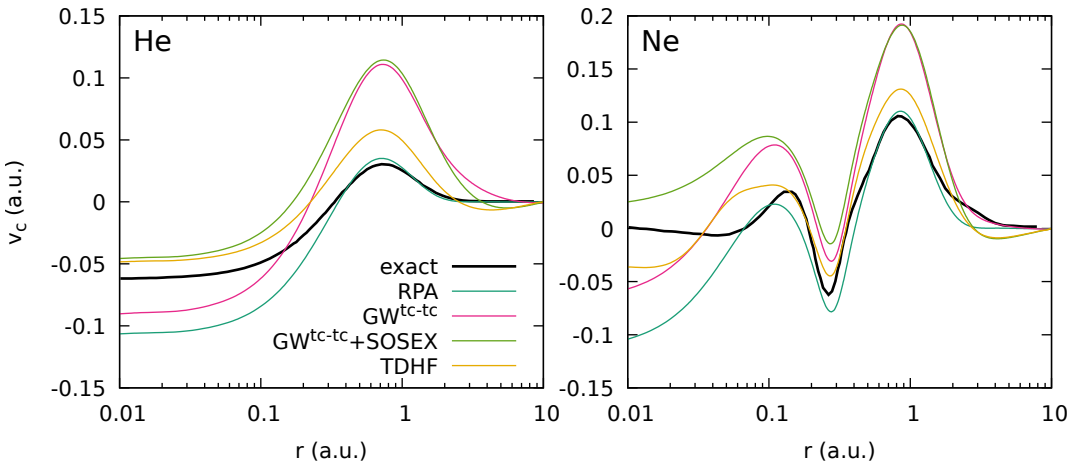

Figure 4.11. Correlation potentials as obtained from one iteration of the LSSE upon EXX orbitals and eigenvalues, in the GW (RPA), GW^{tc-tc}, GW^{tc-tc}+SOSEX, TDHF self-energy approximations. The exact potentials are from Ref. 112.

frequency integral in Section 3.5.5 by closing a contour instead of performing an analytical continuation to the imaginary axis. This is what was done in the LSSE implementation for the TDHF vertex in AGWX.

In this Section we briefly look at the results obtained from the LSSE-TDHF approach. A comprehensive study was not carried out since the TDHF vertex does not appear to be particularly accurate in the LSSE framework. In Figure 4.11 I show the correlation potentials obtained from the LSSE with self-energies incorporating the TDHF W, namely GW^{tc-tc}, GW^{tc-tc}+SOSEX, and TDHF; the RPA potentials, i.e. the most accurate ones found in Section 3.5.7, are also shown. The selected atoms are those for which an exact reference is available, i.e. He and Ne. The potentials are not obtained self-consistently, but just from the first iteration of the LSSE-TDHF on top of an EXX solution. Potentials for Be incorporating the TDHF W could not be obtained, since the unsigned excitonic hamiltonian was found not to be positive definite due to the small EXX KS gap (the same issue was found for the triplet states of Be, as seen in Section 4.2.1).

Indeed, the problem with using the TDHF vertex within the LSSE framework is that the whole scheme is devised with a HF starting point in mind, which considerably differs from an EXX starting point. The HF gap is large and the LUMO unbound in the neutral atom: TDHF increases the accuracy by reducing the gap and introducing bound excitations. Conversely, in EXX we have a bound LUMO and a smaller HOMO-LUMO gap from the very beginning, and a further reduction of the gap is likely to be inaccurate. As seen in Section 3.5.4, a $E_c^{\Delta\mathrm{HF}}$ contribution can be included the OEP method that accounts for using KS orbitals and eigenvalues instead of HF ones, but it is not clear how to do so with a non-variational self-energy like the THDF one [124]. Alternatively, one can rely on 2-point vertices which are properly framed within TDDFT: a 2-point vertex compliant with the KS-DFT and TDDFT formalisms, obtained with a SSE for the TDDFT kernel f_{xc}, was found to yield accurate potentials for atoms [208].

It is then not surprising, looking at Figure 4.11 that all the potentials relying on the TDHF W do not bring a consistent improvement on the RPA ones. Only in the short-range region some improvement is found, which was however already there in GW+SOSEX. In the long-range, the wrong asymptotic trend that we found for GW+SOSEX in Section 3.5.7 is present in the GW^{tc-tc} and GW^{tc-tc}+SOSEX correlation potentials. The peaks of the exact potentials are amplified by GW^{tc-tc}, and GW^{tc-tc}+SOSEX does not appear to solve the issue. The full TDHF vertex is instead closer to the exact potential. This finding substantiates the conclusion, expressed in Section 4.2.2, that the SOSEX contribution (with the TDHF W) is insufficient to bring the GW^{tc-tc} description close to the TDHF one.

Chapter 5

Towards the treatment of satellites in small systems

In Section 4.2.3 we found that the TDHF polarizability can introduce important qualitative features in the spectral function, that self-energies based on either the independent-particle or the RPA polarizability miss. However, the static TDHF vertex appears to be unfit for the account of hole relaxation when coupling G to W in the $GW\tilde{\Gamma}$ form of the self-energy, since the poles of Σ keep the positioning that they have in the $\mathrm{GW}^{\mathrm{tc-tc}}$ form of Σ. The results of Section 4.2.3 suggest that in small systems, e.g. atoms and molecules with few electrons, hole relaxation should be taken into account. Doing so should provide a better description of satellites, which are a signature of exictations of the photoionized system, while the static TDHF vertex causes them to be a product of the excitations of the neutral system.

In this Chapter I present an approximate theory that is aimed at accounting for hole relaxation. In Section 5.1 I introduce the theory and give a few preliminary steps for a formal justification of it; in Section 5.2 I present some promising preliminary results. The work of this Chapter is the product of a collaboration with Dr. Lucia Reining and Dr. Matteo Gatti from the Laboratoire des Solides Irradiés of the École Polytechnique (Palaiseau, France).

5.1 Approximate theory for hole relaxation

5.1.1 Tweaking GW: from self-screening to satellites

Following [62], let us introduce a modified Green's function G_β, in which its diagonal component g_β is removed,

$$G_\beta = G - g_\beta, \tag{5.1}$$

where we have defined

$$g_\beta(\mathbf{r},\mathbf{r}';\omega) = \varphi_\beta(\mathbf{r})\varphi^*_\beta(\mathbf{r}')\left(\frac{\theta_\beta}{\omega-\varepsilon_\beta+i\eta}+\frac{\bar{\theta}_\beta}{\omega-\varepsilon_\beta-i\eta}\right), \tag{5.2}$$

with $\theta_\beta = \theta(\mu - \varepsilon_\beta)$ being the Heaviside theta function (and μ the chemical potential) and $\bar{\theta}_\beta = 1 - \theta_\beta$. Obviously $G = \sum_\beta g_\beta$. From the standard result $\chi_0 = -iGG$, we obtain a Lehmann form of the independent-particle polarizability,

$$\chi_0(\mathbf{r}, \mathbf{r}', \omega) = \sum_{\mu\nu} \varphi_\mu(\mathbf{r})\varphi^*_\mu(\mathbf{r}')\varphi_\nu(\mathbf{r}')\varphi^*_\nu(\mathbf{r}) \times I_{\mu\nu}(\omega), \tag{5.3}$$

where we defined

$$I_{\mu\nu}(\omega) = \frac{\theta_\mu \bar{\theta}_\nu}{\omega - \varepsilon_\mu + \varepsilon_\nu + 2i\eta} - \frac{\bar{\theta}_\mu \theta_\nu}{\omega - \varepsilon_\mu + \varepsilon_\nu - 2i\eta}. \tag{5.4}$$

The same can be done by defining $\chi_{0\beta} = -iG_\beta G_\beta$, yielding the independent-particle polarizability where the state β does not participate in the transitions,

$$\begin{aligned}\chi_{0\beta}(\mathbf{r}, \mathbf{r}', \omega) = \chi_0(\mathbf{r}, \mathbf{r}', \omega) &- \sum_\mu \varphi_\mu(\mathbf{r})\varphi^*_\mu(\mathbf{r}')\varphi_\beta(\mathbf{r}')\varphi^*_\beta(\mathbf{r}) \times I_{\mu\beta}(\omega) \\ &- \sum_\nu \varphi_\beta(\mathbf{r})\varphi^*_\beta(\mathbf{r}')\varphi_\nu(\mathbf{r}')\varphi^*_\nu(\mathbf{r}) \times I_{\beta\nu}(\omega).\end{aligned} \tag{5.5}$$

In the RPA framework these correspond to irreducible polarizabilities. The reducible polarizabilities are obtained from the irreducible ones via

$$\chi_{(\beta)} = \chi_{0(\beta)} + \chi_{0(\beta)} v \chi_{(\beta)}, \tag{5.6}$$

and the screened interactions are

$$W_{(\beta)} = v + v\chi_{(\beta)}v. \tag{5.7}$$

In the following, we want to build a self-energy Σ using W_β instead of W. This choice is guided by intuition, since an electron being either added or removed from the system does not participate in its own screening. This self-screening effect is indeed present in the self-energy at low orders in W, and the inclusion of higher-order diagrams can eventually remove it (possibly combined with more refined choices of W beyond the RPA). One can hope to obtain the self-screening cancellation at lower orders by expanding Σ in powers of W_β, the latter being built from the definitions of Eqs. (5.5 – 5.7) in such a way that the contribution to screening from a particular state is manually removed. Following [62], one could therefore build e.g. a self-screening corrected GW (SSC-GW) self-energy using W_β in the following way,

$$\Sigma^{\text{SSC-GW}}(\mathbf{r}, \mathbf{r}'; t) = i \sum_\beta g_\beta(\mathbf{r}, \mathbf{r}'; t) W_\beta(\mathbf{r}', \mathbf{r}; -t). \tag{5.8}$$

It clearly follows from this definition that the GW self-energy is obtained by replacing W_β with W.

Another reason for using the self-energy introduced in Eq. (5.8) is for the description of satellites in finite systems. By inspection of the pole structure of the GW correlation self-energy seen in Section 3.1.1,

$$\Sigma_c^{\text{GW}}(\mathbf{r}, \mathbf{r}'; \omega) = \sum_{\beta s} \frac{\varphi_\beta(\mathbf{r})\varphi^*_\beta(\mathbf{r}')\, W^p_s(\mathbf{r}, \mathbf{r}')}{\omega + (\Omega_s - i\eta)\text{sgn}(\mu - \varepsilon_\beta) - \varepsilon_\beta^{\text{QP}}}, \tag{3.4}$$

(here and throughout computed in a one-shot fashion starting from single-particle orbitals and eigenvalues) one sees that its peaks are found at a quasi-particle (QP) energy $\varepsilon_\beta^{\mathrm{QP}}$ plus a neutral excitation energy Ω_s. This is a sensible result for the positioning of the photoemission satellites in the energy spectrum: Indeed, by indexing with β the QP excitations of the system and with s the neutral excitations of the singly ionized system, we have that the satellite peaks are found at the energies

$$\varepsilon_s = E^N - E_s^{N-1} = E^N - E_\beta^{N-1} + E_\beta^{N-1} - E_s^{N-1} = \varepsilon_\beta^{\mathrm{QP}} - \Omega_{s\beta}^{N-1}, \tag{5.9}$$

where we identified $\varepsilon_\beta^{\mathrm{QP}} = E_\beta^{N-1} - E^N$ and $\Omega_{s\beta}^{N-1} = E_s^{N-1} - E_\beta^{N-1}$, the latter being required to be positive . The similarity of this result to the poles of the GW self-energy is apparent. However, the two still differ in that (i) the polarizability employed in GW is the RPA polarizability, therefore Ω_s may not represent accurate neutral excitation energies, especially for finite systems; (ii) it is the polarizability of the system with N particles, whereas Eq. (5.9) requires the neutral transitions of the system with $N-1$ particles, these transitions having the QP state β as a reference. In light of these issues, Eq. (5.8) may offer a good compromise for the calculation of QP properties, but it is still unfit for satellite properties the way it is. In particular, not only should an accurate response function be sought, but this should also contain positive excitations starting from a reference QP state β of the "relaxed" system with $N-1$ particles. We emphasize that "relaxation" is not taken into account in Eq. (5.8), in which eigenvalues and orbitals are used of the system with N particles in the ground state. Therefore, for a more accurate positioning of satellites, Eq. (5.8) should be rewritten using a polarizability $\tilde{W}_\beta$ computed using excitations of the system "relaxed" on the β QP state, i.e.

$$\Sigma^{\mathrm{G\tilde{W}}}(\mathbf{r},\mathbf{r}';t) = i\sum_\beta g_\beta(\mathbf{r},\mathbf{r}';t)\tilde{W}_\beta(\mathbf{r}',\mathbf{r};-t); \tag{5.10}$$

in this way, Eq. (3.4) becomes

$$\Sigma_c^{\mathrm{G\tilde{W}}}(\mathbf{r},\mathbf{r}';\omega) = \sum_{\beta s}\frac{\varphi_\beta(\mathbf{r})\varphi_\beta^*(\mathbf{r}')\,\tilde{W}_{s\beta}^p(\mathbf{r},\mathbf{r}')}{\omega + (\tilde{\Omega}_{s\beta} - i\eta)\mathrm{sgn}(\mu - \varepsilon_\beta^{QP}) - \varepsilon_\beta^{\mathrm{QP}}}, \tag{5.11}$$

and the QP-dependence of the neutral excitations found in Eq. (5.9) is also recovered. This recipe, tailored around satellite prediction, rests upon the assumption that self-consistency is not an issue, and neither is the usage of the Dyson equation (see Appendix E for more): then it is safe to expect that the Green's function, and consequently the spectral function, have peaks in close correspondence of those of the self-energy used to compute it. It is also not clear how this self-energy impacts the prediction of QP properties: it may just be a single ingredient for an all-encompassing treatment of both QPs and satellites (separation in static – QP properties – and dynamical self-energy – satellites, also in Appendix E).

5.1.2 Cancellations in 2nd Born and in SSC-GW

What is suggested by intuition should be substantiated by analytical results. Here we verify that cancellations of analytical terms occur at given orders of v, both in the exact theory

and in SSC-GW. As seen in Section 3.1.3, at 2nd order in v we have the so-called 2nd Born (2B) self-energy, whose expression reads

$$\Sigma^{\mathrm{2B}} = \Sigma^{\mathrm{2Bd}} + \Sigma^{\mathrm{2Bx}}, \tag{5.12}$$

where the direct (2Bd) and exchange (2Bx) diagrams in frequency space are respectively expressed as

$$\begin{aligned}\Sigma^{\mathrm{2Bd}}(\mathbf{r},\mathbf{r}';\omega) = &-\int \frac{d\omega_1}{2\pi i}\frac{d\omega_2}{2\pi i}\int d\mathbf{r}_3 d\mathbf{r}_4\, G(\mathbf{r},\mathbf{r}',\omega+\omega_1)\\ &\times G(\mathbf{r}_3,\mathbf{r}_4,\omega_1+\omega_2)\, G(\mathbf{r}_4,\mathbf{r}_3,\omega_2) v(\mathbf{r},\mathbf{r}_4)\, v(\mathbf{r}_3,\mathbf{r}'),\\ = &-\int \frac{d\omega_1}{2\pi i}\int d\mathbf{r}_3 d\mathbf{r}_4\, G(\mathbf{r},\mathbf{r}',\omega+\omega_1)\, v(\mathbf{r},\mathbf{r}_4)\, \chi_0(\mathbf{r}_3,\mathbf{r}_4,\omega_1)\, v(\mathbf{r}_3,\mathbf{r}')\end{aligned} \tag{3.16}$$

and

$$\begin{aligned}\Sigma^{\mathrm{2Bx}}(\mathbf{r},\mathbf{r}';\omega) = &\int \frac{d\omega_1}{2\pi i}\frac{d\omega_2}{2\pi i}\int d\mathbf{r}_3 d\mathbf{r}_4\, G(\mathbf{r},\mathbf{r}_3,\omega+\omega_1)\\ &\times G(\mathbf{r}_3,\mathbf{r}_4,\omega_1+\omega_2)\, G(\mathbf{r}_4,\mathbf{r}',\omega_2) v(\mathbf{r},\mathbf{r}_4)\, v(\mathbf{r}_3,\mathbf{r}').\end{aligned} \tag{3.17}$$

One can solve the frequency integrals once the Lehmann representation is used for the Green's functions. These integrals are easily evaluated by closing the integration contour in the complex frequency plane and by applying the residue theorem. In particular, starting from the solution of an independent-particle problem, one gets

$$\Sigma_0^{\mathrm{2Bd}}(\mathbf{r},\mathbf{r}';\omega) = \sum_{\mu\nu\beta} \langle\mu|v(\mathbf{r})|\nu\rangle\langle\nu|v(\mathbf{r}')|\mu\rangle\, \varphi_\beta(\mathbf{r})\varphi_\beta^*(\mathbf{r}')\, \times I_{\mu\nu\beta}(\omega), \tag{3.18}$$

$$\Sigma_0^{\mathrm{2Bx}}(\mathbf{r},\mathbf{r}';\omega) = -\sum_{\mu\nu\beta} \langle\mu|v(\mathbf{r})|\nu\rangle\langle\beta|v(\mathbf{r}')|\mu\rangle\, \varphi_\beta(\mathbf{r})\varphi_\nu^*(\mathbf{r}')\, \times I_{\mu\nu\beta}(\omega), \tag{3.19}$$

with

$$I_{\mu\nu\beta}(\omega) = \frac{\theta_\mu\bar{\theta}_\nu\bar{\theta}_\beta}{\omega+\varepsilon_\mu-\varepsilon_\nu-\varepsilon_\beta-3i\eta} + \frac{\bar{\theta}_\mu\theta_\nu\theta_\beta}{\omega+\varepsilon_\mu-\varepsilon_\nu-\varepsilon_\beta+3i\eta}. \tag{3.20}$$

In order to make the formulas simpler, we have introduced here a compact notation for partially saturated Coulomb integrals, $\langle\mu|v(\mathbf{r})|\nu\rangle$. We refer the reader to Appendix C for their expression in the various representations. From these expressions one readily sees that the terms in the summations having $\nu=\beta$ cancel out, i.e. the summation

$$\sum_{\mu\beta} \langle\mu|v(\mathbf{r})|\beta\rangle\langle\beta|v(\mathbf{r}')|\mu\rangle\, \varphi_\beta(\mathbf{r})\varphi_\beta^*(\mathbf{r}')\, \times I_{\mu\beta\beta}(\omega), \tag{5.13}$$

is present in both the 2Bd and in the 2Bx with opposite signs.

In a one-electron system, the 2B self-energy produces no QP shift in the diagonal QP equation,

$$\varepsilon_\alpha^{\mathrm{QP}} = \varepsilon_\alpha^0 + \langle\alpha|\Sigma^{\mathrm{2B}}(\varepsilon_\alpha^{\mathrm{QP}})|\alpha\rangle = \varepsilon_\alpha^0, \tag{5.14}$$

for the occupied state $\alpha=1$. We will consider this as a definition of self-screening freedom from now on. Showing that $\langle 1|\Sigma^{\mathrm{2B}}(\omega)|1\rangle = 0$ in a one-electron system requires projecting

on the orbital basis the two self-energy diagrams of 2B, yielding

$$\langle\alpha|\Sigma^{\text{2Bd}}(\omega)|\alpha\rangle = \sum_{\beta\mu\nu}\langle\alpha\mu|v|\beta\nu\rangle\langle\beta\nu|v|\alpha\mu\rangle \times I_{\mu\nu\beta}(\omega), \qquad \text{and} \tag{5.15}$$

$$\langle\alpha|\Sigma^{\text{2Bx}}(\omega)|\alpha\rangle = -\sum_{\beta\mu\nu}\langle\alpha\mu|v|\beta\nu\rangle\langle\beta\nu|v|\mu\alpha\rangle \times I_{\mu\nu\beta}(\omega). \tag{5.16}$$

For the two self-energy diagrams to cancel out, the products of Coulomb integrals need to be the same. Considering now $\alpha = 1$, the constraints on the occupations of $I_{\mu\nu\beta}$ in Eq. (3.20) imply that, in a one-electron system, we either have $\mu = 1$, $\nu \neq 1$, $\beta \neq 1$, yielding the Coulomb integral product

$$\langle 11|v|\beta\nu\rangle\langle\beta\nu|v|11\rangle; \tag{5.17}$$

or $\mu \neq 1$, $\nu = \beta = 1$, yielding the Coulomb integral product

$$\langle 1\mu|v|11\rangle\langle 11|v|1\mu\rangle = \langle 1\mu|v|11\rangle\langle 11|v|\mu 1\rangle. \tag{5.18}$$

These Coulomb integrals appear with opposite signs in both the 2B self-energy diagrams, thus leading to them canceling out. The same does not happen for the projections of the self-energy on unoccupied states, i.e. for $\alpha \neq 1$. It is worth noting that the cancellation of the summation in Eq. (5.13) is the same that occurs here when $\beta = \nu$. The projection on the occupied state completes the cancellation for the "non-diagonal" terms having $\beta \neq \nu$. Furthermore, the projected self-energy cancels over the whole frequency range, with no need to evaluate it exactly at $\varepsilon_1^{\text{QP}}$ as prescribed by the QP equation, Eq. (5.14).

We now want to show that at 2nd order SSC-GW contains cancellations similar to those found in 2B. In particular, Eq. (3.16) highlights the presence of the independent-particle polarizability χ_0 in the 2Bd diagram. SSC-GW to second order corresponds to having the 2Bd diagram with χ_0 replaced by $\chi_{0\beta}$, and G by g_β, along with an additional summation over β,

$$\begin{aligned}\Sigma^{\text{SSC-GW(2)}}(\mathbf{r},\mathbf{r}';\omega) = -\sum_\beta \int \frac{d\omega_1}{2\pi i} \int d\mathbf{r}_3 d\mathbf{r}_4\, g_\beta(\mathbf{r},\mathbf{r}',\omega+\omega_1) \\ \times v(\mathbf{r},\mathbf{r}_4)\,\chi_{0\beta}(\mathbf{r}_3,\mathbf{r}_4,\omega_1)\,v(\mathbf{r}_3,\mathbf{r}').\end{aligned} \tag{5.19}$$

By replacing $\chi_{0\beta}$ using Eq. (5.5), we obtain

$$\Sigma^{\text{SSC-GW(2)}}(\mathbf{r},\mathbf{r}';\omega) = \Sigma^{\text{2Bd}}(\mathbf{r},\mathbf{r}';\omega) - \sum_{\mu\beta}\langle\mu|v(\mathbf{r})|\beta\rangle\langle\beta|v(\mathbf{r}')|\mu\rangle\,\varphi_\beta(\mathbf{r})\varphi^*_\beta(\mathbf{r}') \times I_{\mu\beta\beta}(\omega). \tag{5.20}$$

In performing the contour integrals, we notice that the poles in the second line of Eq. (5.5) do not contribute to the final result, since they are found on the same half of the complex plane where the poles of g_β are. The result of Eq. (5.20) is the 2Bd diagram minus the sum of Eq. (5.13), which proves that the same terms removed here are those that the 2Bx diagram would remove in the full Σ^{2B}. As mentioned earlier, this is *not* sufficient to make this self-energy self-screening free, since a whole summation over non-diagonal terms is missing when the diagonal QP equation, Eq. (5.14), is considered. In order to have full removal of the self-screening, one would have to consider a fully diagonal self-energy, i.e.

$$\Sigma_\alpha^{\text{SSC-GW}}(t) = i g_\alpha(t) W_\alpha(-t). \tag{5.21}$$

The cancellations found in this Section are just a a preliminary step in the justification of the schemes proposed in this Chapter. Future work will have to search for cancellations in higher-order self-energy terms generated by a dynamical vertex.

5.2 Preliminary results

In this Section I show how applying a $G\tilde{W}$-like self-energy, as presented in Section 5.1, can partially address the issues found in Section 4.2.3 when studying satellites as obtained from the TDHF vertex. To begin with, we consider an approximate version of the $G\tilde{W}$ self-energy of Eq. (5.10): since we are interested in the satellites that couple to the ionization of the outermost shell, we will choose $\beta = \text{HOMO}$ in W_β for all β's. We obtain

$$\Sigma^{\text{G}\tilde{\text{W}}}(\mathbf{r}, \mathbf{r}'; t) \simeq iG(\mathbf{r}, \mathbf{r}'; t)\tilde{W}_{\text{HOMO}}(\mathbf{r}, \mathbf{r}'; -t), \tag{5.22}$$

which requires only one evaluation of $\tilde{W}_\beta$, in particular the one with an electron missing in the outermost shell.

In He we have a notable case in which we know the exact polarizability of the ion, that being the independent-particle polarizability of the hydrogenic ion He^+. Therefore, I chose to compute the ingredients of Eq. (5.22) in the following way: the G is evaluated in the HF approximation, offering a decent estimate of the starting occupied orbital; while from $\chi_{0,1s}$ (Eq. (5.5)) as computed on top of the exact solution He^+, the polarization contribution $W^p_{\text{He}^+} = v\chi_{0,1s}v$ is obtained to be used as $\tilde{W}_{\text{HOMO}}$. With a decent guess for the energy $\varepsilon^{\text{HF}}_{1s}$ and exact neutral excitation energies $\Omega^{\text{He}^+}_s$, $\Sigma^{G\tilde{W}}_c$ is expected to have very accurate positioning of the satellites according to Eq. (5.11). This is indeed the case, as seen in Figure 5.1, which shows the results for spectral functions obtained from the full inversion of the Dyson equation on a frequency grid (in total analogy with what was done in Section 4.2.3). The improvement with respect to plain $\text{GW}^{\text{tc}-\text{tc}}$ is apparent: the satellites are shifted below in energy and the spacing is increased between them, all thanks to the correct account of the larger excitation gaps that He^+ has with respect to He.

One problem with the GW_{He^+} scheme is that the angular momentum degeneracy of the satellites is slightly broken in the spectral function: this is due to the QPE having a solution in correspondence of the first satellite in the $L = 0$ channel, while normally satellites are simply caused by peaks in $\text{Im}\{\Sigma\}$. If the peak is quite strong, as in this case, $\text{Re}\{\Sigma\}$ is also quite peaked, and yields a solution of the QPE other than the proper QP one (see also Section 2.1.6). This solution can actually be removed by decreasing the numerical broadening of the lorentzians, and therefore reducing the height of the peaks in $\text{Re}\{\Sigma\}$. Another problem with the GW_{He^+} scheme is that the intensity of the satellites with respect to the QP peak are underestimated by about one order of magnitude. This problem was also found with the self-energies explored in Section 4.2.3. Finally, the GW_{He^+} scheme guarantees nothing about the prediction of QP properties, since it is tailored around the prediction of satellites. The result in Figure 5.1 shows that the $1s$ QP energy is not catastrophically bad, but the HF result is nonetheless worsened and not improved upon.

Turning now our attention to Ne, a problem I faced is that AGWX can only treat spherical atoms: therefore, removing an electron is no trivial task here. He and the atoms of the first and the second group are all within the capabilities of the code when an electron is removed, but in noble gases one cannot rigorously perform the scf procedure and all

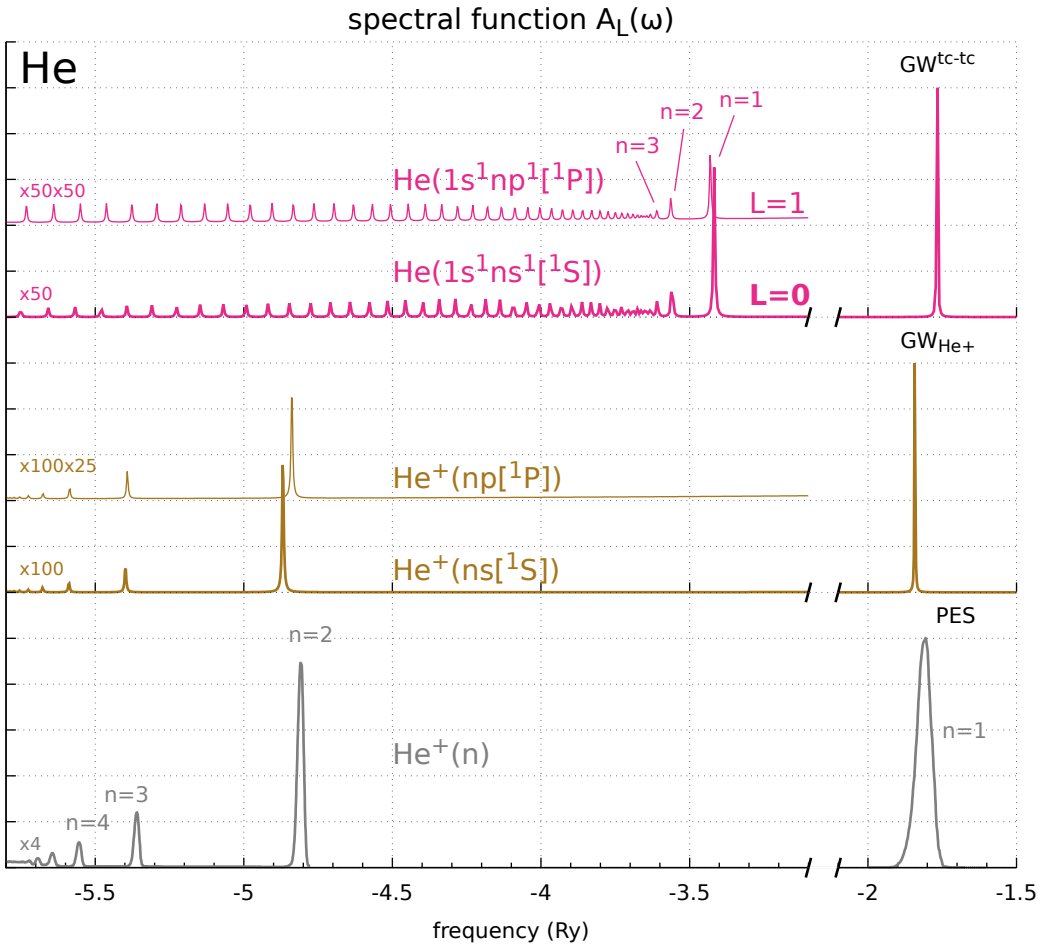

Figure 5.1. Spectral functions of He in the GW^{tc-tc}, and GW_{He^+} approximations to the self-energy. Thick lines refer to the $L = 0$ channel of the spectral function, thin lines to the $L = 1$ channel. The satellites of the $L = 0$ channel are due to monopole transitions ($[^1S]$ final state), whereas those of the $L = 1$ channel are due to dipole transitions ($[^1P]$ final state). In the bottom, a photoemission spectrum from Ref. 158 is plotted for reference. The spectra are normalized so that the QP peaks from different approximations/experiment all have the same height.

subsequent calculations with an electron missing from the valence p shell. Since Ne is a system of interest due to the availability of an experimental photoemission spectrum, I chose to treat its ion, Ne^+, as a spherical atom anyway. An electron was removed from the $2p$ shell and the calculation was kept at the spin-unpolarized level for simplicity. At the scf level, this meant occupying two p levels having opposite spin with half an electron each, while the remaining p levels were kept fully occupied. Doing so led to important changes with respect to the neutral atom in the density matrix (and therefore in the density as well) handled by the HF solver, which in turn made the HF orbitals more bound. Since the HF ionization energy of Ne^+ (2.931 Ry) was found to be in relatively good agreement with

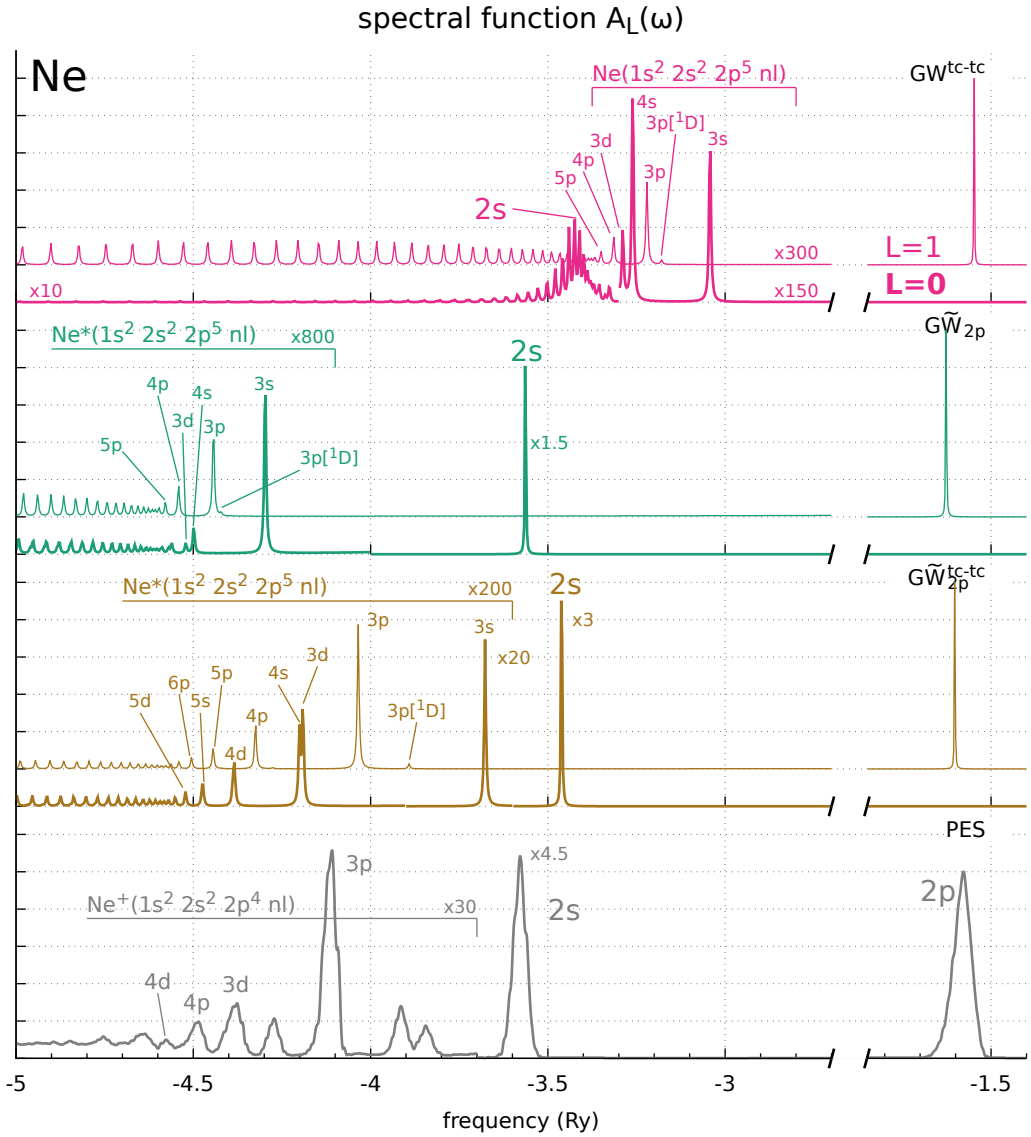

Figure 5.2. Spectral functions of Ne in the GW^{tc-tc}, $G\tilde{W}_{2p}$, and $G\tilde{W}^{tc-tc}_{2p}$ approximations to the self-energy. Thick lines refer to the $L = 0$ channel of the spectral function, thin lines to the $L = 1$ channel. The satellites of the $L = 0$ channel are due to dipole transitions ($[^1P]$ final state), whereas those of the $L = 1$ channel are due to dipole transitions ($[^1S]$ final state), except where otherwise noted. The Ne^* notation indicates that the underlying scf calculation, on top of which $\tilde{W}$ is obtained, has a $2p$ hole in the density. In the bottom, a photoemission spectrum from Ref. 161 is plotted for reference. The spectra are normalized so that the QP peaks from different approximations/experiment all have the same height.

the experimental result (3.011 Ry) [139], I deemed the spherical approximation successful and the HF result as a good starting point for the relaxed polarizability $\tilde{W}_{\text{HOMO}}$. In the calculation of the polarizability, which starts from the evaluation of $\chi_{0,2p}$ via the sum over poles of Eq. (5.5), the shells were considered as being fully occupied for simplicity, i.e. in the $1s^2 2s^2 2p^6$ configuration, so that the difference with respect to the neutral atom came solely from the relaxation of orbitals and eigenvalues due to the hole in the density. This means that there is quantitative change in the polarizability, but not a qualitative one, due to not considering the $1s^2 2s^2 2p^5$ shell as a reference for neutral excitations.

Given this premise, $\chi_{0,2\text{p}}$ was computed starting from a HF solution of Ne^+ according to Eq. (5.5), and $\tilde{W}_{2p}$ was obtained in the RPA from Eqs. (5.6) and (5.7). With a HF solution for G, the $G\tilde{W}_{2p}$ self-energy was then built. With the techniques of Section 4.1, the TDHF W was also built upon the HF solution of Ne^+, which was possible because the system was approximated as spin-unpolarized and in the $1s^2 2s^2 2p^6$ closed-shell configuration. With this, the $G\tilde{W}_{2p}^{\text{tc}-\text{tc}}$ self-energy could be evaluated, again using a G computed upon a HF solution for neutral Ne. The results for the spectral functions obtained with these self-energies are shown in Figure 5.2. As usual, the spectral function is obtained from full inversion of the Dyson equation.

As seen for He, the satellites are pushed to lower energies with respect to $\text{GW}^{\text{tc}-\text{tc}}$, and the spacing is increased. The shake-off threshold is captured with great accuracy. Interestingly, putting a hole in the valence density makes the RPA W qualitatively similar to the TDHF W: this is deduced from the satellites of $G\tilde{W}_{2p}$ and $G\tilde{W}_{2p}^{\text{tc}-\text{tc}}$ also sharing this similarity. The difference is rather quantitative, in that the $G\tilde{W}_{2p}$ shake-up satellites are closer to the shake-off continuum. The effect of the TDHF vertex is now not to create new bound neutral excitations, but to shift the existing ones in the RPA W to lower energies; this maps to the spectral function of $G\tilde{W}_{2p}^{\text{tc}-\text{tc}}$ as satellites being at higher energies than those of $G\tilde{W}_{2p}$. As to which approximation is better, the satellite onset of $G\tilde{W}_{2p}$ is too low in energy, whereas the opposite is true of $G\tilde{W}_{2p}^{\text{tc}-\text{tc}}$. As in Section 4.2.3, the comparison with experimental data is also hindered by the qualitative differences in the neutral transitions: in fact, here the reference shell for theoretical methods is still $1s^2 2s^2 2p^6$ instead of $1s^2 2s^2 2p^5$. All we can say is that both approximations succeed at moving the satellites to a more realistic energy range.

Perhaps the greatest success of the schemes shown here, and in particular of $G\tilde{W}_{2p}$, is the prediction of the $2s$ QP peak. Thanks to the shifting of the satellite onset to lower energies, the QPE now has a proper solution in a smooth region of $\text{Re}\{\Sigma_c\}$. The spreading of the weight among different lorentzian peaks is avoided, and the solution of the QPE does not have the prerequisite of a smooth description of the satellite continuum, as was found in Section 4.2.3. Of course, at the same time the correct energy ordering is recovered. This results suggest that an accurate description of satellites may be beneficial even for the prediction of QP properties.

Future work on the implementation of the schemes detailed here will have to involve an accurate description of open shells as a reference for the calculations of relaxed polarizabilities, i.e. of $\tilde{W}_\beta$.

Conclusions and perspectives

In this thesis, I have presented the accuracy assessment of a number of beyond-state-of-the-art approximations in MBPT schemes for the prediction of photoemission spectra. Such approximations are obtained by performing different truncations to self-energy expansions afforded by vertex corrections. The assessment was conducted using spherical atoms as a test set: these were chosen for the ease that they offer with respect to the numerical treatment, the availability of experimental data to compare against, and the interesting physics producing satellite features in the photoemission spectrum that are not commonly found in condensed matter. The work is aimed at going beyond the GW method by choosing approximations informed by physical arguments, like correcting for the GW self-screening error and fitting a more refined polarizability than the RPA one in the self-energy, such as the TDHF polarizability. These issues have in fact practical repercussions on delicate aspects of calculations, including the starting point ambiguity and a poor description of satellites. Furthermore, the work explores the LSSE as an alternative approach to the Dyson equation, and as a possible means to obtain consistent starting points for the Dyson equation itself.

A first benchmark involving the GW, GW+SOSEX and 2B self-energies was conducted. These self-energies are relatively lightweight to handle numerically, due to not requiring more than inverting Dyson equations on a frequency grid in order to obtain the spectral function. 2B and GW+SOSEX are meant to overcome some limitations of GW by design: 2B trades the RPA W for self-screening freedom, while GW+SOSEX is a compromise that attempts to incorporate both the RPA W and self-screening freedom up to some level. In this first benchmark, the self-energies were computed in a one-shot fashion with different starting points, including the LSSE ones, in order to determine how each was affected by the starting point ambiguity. The accuracy assessment focused on ionization energies as obtained from the negatives of QP HOMO energies given by the QPE. In this context, the QP shift was also considered as an indicator of charge density conservation in the process of solving the Dyson equation upon an LSSE solution [122].

It was found that the solutions of the LSSE indeed provide a consistent starting point for the QPE, yielding small to vanishing QP shifts in the HOMO, and therefore hinting at conservation of the starting electron density to a large degree. Comparison with the existing literature [35], however, suggests that this density does not approximate well the one of the self-consistent Dyson equation; therefore, further iterations of the Dyson equation starting from an LSSE solution are expected to eventually change the density more than the first one does. Spectral Sham-Schlüter equations, as detailed in Section 1.5, could provide better approximations to the density of the self-consistent Dyson equation.

From the accuracy standpoint the LSSE generally performs poorly as compared with the solution of the QPE upon commonly adopted starting points, like those given by either the HF method or semi-local/hybrid functionals in (generalized) KS-DFT. In this regard, the best performance was obtained from GW+SOSEX@PBE/PBE0, 2B@HF and GW@PBE0. This confirms the common knowledge that hybrid functionals provide good starting points for GW applied to finite systems [38], even in the atomic limit. The justification of the SOSEX diagram as a cure for the self-screening error of GW seems to be correct only with the PBE and PBE0 starting points. On the contrary, adding the SOSEX diagram to GW with the HF starting point appears to be inaccurate, likely due to the RPA@HF underscreening becoming inadequate at higher orders of the self-energy. These performances are in line with those found with larger test sets involving small molecules [87, 91]. Overall, the merit of GW+SOSEX is that it does not require a generalized formulation of KS-DFT in the starting point (justifying the usage of e.g. hybrid functionals like PBE0) for a good accuracy to be attained; and, along with the results of Ref. 87 for the SO-TDGW self-energy (named FSOS in said work), it suggests that expansions in the RPA@HF W should be avoided. Unfortunately, in the context of the LSSE the GW+SOSEX yielded no substantial improvement on the RPA xc potentials.

As for the 2B self-energy, its performance was found to be quite promising, save for some failures as in Ne. Furthermore, no starting point ambiguity was found with this self-energy, with HF being the clear winner. This motivated the exploration of an expansion in the bare v that could unambiguously rely on HF as a starting point. The TDHF vertex was then considered in order to go beyond the 2B level of theory, which required resorting to a numerical treatment more involved than that of simply inverting the Dyson equation on a frequency grid: in fact, I had to recast the problem of the vertex equation to that of the diagonalization of an excitonic hamiltonian in a 4-point formalism, as is usually done in BSE implementations; and then I had to contract back to 2-point quantities, such as polarizabilities and the self-energy. The resulting TDHF self-energy led to the second benchmark of this thesis. The TDHF self-energy was found to be accurate in yielding the ionization energies of light atoms, improving on both 2B and GW; notably, it fixed the striking failure that 2B experiences in Ne. The performance of TDHF consistently degraded for heavier atoms, in which one expects that screening becomes more relevant, and an expansion in v accordingly less justified. The physical picture is then clear and calls for the screening of v at the vertex level as the electron number increases, coherently with what is done in the many-electron regime of condensed matter. Intermediate truncations between GW and TDHF are not very successful, instead: $\mathrm{GW}^{\mathrm{tc-tc}}$ appears to be imbalanced in the few-body limit due to exacerbating the self-screening problem, although being almost as good as GW for the Be atom; it can offer some improvement on GW in heavier atoms, but not always. On the other hand, $\mathrm{GW}^{\mathrm{tc-tc}}$+SOSEX seems to correct the imbalance of $\mathrm{GW}^{\mathrm{tc-tc}}$ in lighter atoms, but not by a sufficient amount to match the accuracy of TDHF; furthermore, there is really little to no benefit in preferring it over $\mathrm{GW}^{\mathrm{tc-tc}}$ in heavier atoms, the whole TDHF self-energy not being particularly successful itself in this context.

Extending the assessment to the whole spectral function, the TDHF self-energy was also the first self-energy to qualitatively change the satellite spectrum. All the self-energies (and therefore spectral functions) relying on the IP or RPA polarizabilities, in fact, were found to be dominated by a double ionization continuum in the satellite region, with little (LDA starting point) to no account (HF starting point) for neutral excitations of the ionized atom

that appear in experimental spectra, i.e. the so-called shake-up processes. The GW^{tc-tc} and TDHF self-energies instead contain satellites corresponding to features of the TDHF polarizability, which is however that of the neutral atom. Due to having a static vertex, the TDHF self-energy lacks a description of hole relaxation, which I then tried to simulate by devising a $G\tilde{W}$ self-energy in which $\tilde{W}$ is computed on top of the solution given by an scf procedure lacking one electron; in the case of He, the exact W of the He^+ hydrogenic atom was directly considered. The preliminary results are promising, but the theory still lacks a complete formal justification, which is only sketched in this thesis, and is the subject of ongoing work.

In conclusion, the results reported in this thesis confirm that vertex corrections can indeed improve on GW. There are many flavours of GW that are most often up to the task. However, these are not always grounded in the systematic approach offered by vertex corrections, which gives precious insight on the physics. Here, joining the most recent efforts of practitioners in the field [50, 72, 74, 75, 86, 87, 90], I showed the improvements brought about by either truncating or fully considering vertex-corrected self-energies. The results point to future developments focusing on a dynamical vertex: this will yield an expansion in orders of the screened interaction W that will possibly offer a better description of quasi-particles in heavier atoms, as well as satellites in atoms at large. Last but not least, such an expansion could lead to a unified MBPT scheme for treating electronic excitations in finite systems and extended systems alike.

Appendix A

Spherical Harmonics

For internal reference, here we report some notable results concerning spherical harmonics (SH). More details can be found in Ref. [223].

A.1 Legendre polynomials

Associated Legendre polynomials $P_{lm}(x)$ are defined in the interval $[-1,1]$ as the solutions of the following equation:

$$(1-x^2)\frac{d^2P}{dx^2} - 2x\frac{dP}{dx} + \left[l(l+1) - \frac{m^2}{1-x^2}\right] P = 0. \tag{A.1}$$

Such equation reduces to the one for the regular Legendre polynomials $P_l(x)$ when $m = 0$. Also, for $0 \leq m \leq l$, one has:

$$P_l(x) = (2^l\, l!)^{-1} \frac{d^l}{dx^l}\left[(x^2-1)^l\right] \tag{A.2}$$

$$P_{lm}(x) = (-1)^m (1-x^2)^{m/2} \frac{d^m}{dx^m} P_l(x). \tag{A.3}$$

Concerning regular Legendre polynomials, one has:

$$P_0(x) = 1 \tag{A.4}$$

$$P_1(x) = x \tag{A.5}$$

$$P_2(x) = \frac{1}{2}(3x^2-1) \tag{A.6}$$

$$P_3(x) = \frac{1}{2}(5x^3-3x) \tag{A.7}$$

$$P_n(1) = 1 \qquad \forall n \geq 0 \tag{A.8}$$

The following identities are also valid:

$$(n+1)P_{n+1}(x) = (2n+1)xP_n(x) - nP_{n-1}(x), \tag{A.9}$$

(Bonnet's recursion formula),

$$P_n(x) = \frac{1}{2^n n!}\frac{d^2}{dx^2}\left[(x^2-1)^2\right], \tag{A.10}$$

(Rodriguez formula), and

$$\begin{aligned}(1-x^2)P_n'(x) &= -nxP_n(x) + nP_{n-1}(x) \\ &= (n+1)xP_n(x) - (n+1)P_{n+1}(x),\end{aligned} \tag{A.11}$$

the second expression being obtained by using Eq. (A.9).

Legendre polynomials are orthogonal over the interval [−1,1], subject to the following condition:

$$\int_{-1}^{1} P_m(x)P_n(x)\,dx = \frac{2}{2n+1}\delta_{mn}. \tag{A.12}$$

A.2 Definitions

Spherical harmonics (SH) are defined as:

$$Y_{lm}(\theta,\phi) = (-1)^m\sqrt{\frac{(2l+1)}{4\pi}\frac{(l-m)!}{(l+m)!}}\,P_{lm}(\cos\theta)e^{im\phi} \tag{A.13}$$

Notable cases include:

$$Y_{l0}(\theta,\phi) = \sqrt{\frac{(2l+1)}{4\pi}}\,P_l(\cos\theta), \tag{A.14}$$

$$Y_{lm}^*(\theta,\phi) = (-1)^m Y_{l-m}(\theta,\phi). \tag{A.15}$$

SH are an orthonormal and complete set of functions on a sphere and can be used to represent the angular dependency of a function, i.e.

$$f(\theta,\phi) = \sum_{l=0}^{\infty}\sum_{m=-l}^{l} f_{lm}Y_{lm}(\theta,\phi) \tag{A.16}$$

$$f_{lm} = \int d\Omega\, Y_{lm}^*(\theta,\phi)f(\theta,\phi), \tag{A.17}$$

or, in the form of a projector,

$$\sum_{lm} Y_{lm}(\hat{\mathbf{r}})Y_{lm}^*(\hat{\mathbf{r}}') = \delta(\hat{\mathbf{r}},\hat{\mathbf{r}}'). \tag{A.18}$$

A.3 Addition theorem

$$P_l(\cos(\omega)) = \frac{4\pi}{2l+1}\sum_{m=-l}^{l} Y_{lm}(\hat{\mathbf{r}})Y_{lm}^*(\hat{\mathbf{r}}'), \tag{A.19}$$

where $\cos(\omega) = \hat{\mathbf{r}}\cdot\hat{\mathbf{r}}'$, i.e. ω is the angle between $\hat{\mathbf{r}}$ and $\hat{\mathbf{r}}'$. Setting $\hat{\mathbf{r}} = \hat{\mathbf{r}}'$ one also obtains:

$$\sum_{m=-l}^{l} Y_{lm}^*(\hat{\mathbf{r}})Y_{lm}(\hat{\mathbf{r}}) = \frac{2l+1}{4\pi}. \tag{A.20}$$

A.4 Coupling of two spherical harmonics

Spherical harmonics are the projections in angular space of the abstract ket $|lm\rangle$, i.e.

$$Y_{lm}(\hat{\mathbf{r}}) = \langle \hat{\mathbf{r}}|lm\rangle. \tag{A.21}$$

These kets are eigenvectors of the angular momentum operator. One can form tensor products of two such kets,

$$|l_1 l_2 m_1 m_2\rangle = |l_1 m_1\rangle \otimes |l_2 m_2\rangle, \tag{A.22}$$

and a linear combination of these can give an eigenvector of the total angular momentum. The coefficients of the linear combination are the CG coefficients,

$$|l_1 l_2 LM\rangle = \sum_{m_1 m_2} \langle l_1 l_2 m_1 m_2|LM\rangle |l_1 l_2 m_1 m_2\rangle, \tag{A.23}$$

where we made use the convention $\langle l_1 l_2 m_1 m_2|LM\rangle = \langle l_1 l_2 m_1 m_2|l_1 l_2 LM\rangle$. This equation can be projected onto angular space to build an eigenfunction of total momentum:

$$Y^{LM}_{l_1 l_2}(\hat{\mathbf{r}}_1, \hat{\mathbf{r}}_2) = \sum_{m_1 m_2} \langle l_1 l_2 m_1 m_2|LM\rangle Y_{l_1 m_1}(\hat{\mathbf{r}}_1) Y_{l_2 m_2}(\hat{\mathbf{r}}_2). \tag{A.24}$$

These functions constitute a complete orthonormal set for the angular product space. They obey the following rules:

$$\int d\hat{\mathbf{r}}_1 d\hat{\mathbf{r}}_2 Y^{LM*}_{l_1 l_2}(\hat{\mathbf{r}}_1, \hat{\mathbf{r}}_2) Y^{L'M'}_{l'_1 l'_2}(\hat{\mathbf{r}}_1, \hat{\mathbf{r}}_2) = \delta_{LL'}\delta_{MM'}\delta_{l_1 l'_1}\delta_{l_2 l'_2}, \tag{A.25}$$

$$\sum_{m'} \int d\mathbf{r}_1 Y^{LM}_{l l_1}(\hat{\mathbf{r}}, \hat{\mathbf{r}_1}) Y^{*}_{l' m'}(\mathbf{r}_1) Y_{l' m'}(\mathbf{r}') = Y^{LM}_{l l'}(\hat{\mathbf{r}}, \hat{\mathbf{r}}')\delta_{l_1 l'}, \tag{A.26}$$

$$Y^{LM}_{l_1 l_2}(\hat{\mathbf{r}}, \hat{\mathbf{r}}) = (-1)^L \sqrt{\frac{(2l_1+1)(2l_2+1)}{4\pi}} \begin{pmatrix} l_1 & l_2 & L \\ 0 & 0 & 0 \end{pmatrix} Y_{LM}(\hat{\mathbf{r}}). \tag{A.27}$$

A.5 Clebsch-Gordan coefficients, 3j and 6j symbols

The Clebsch-Gordan coefficients obey an orthogonality relation,

$$\sum_{m_1, m_2} \langle LM|l_1 l_2 m_1 m_2\rangle \langle l_1 l_2 m_1 m_2|L'M'\rangle = \delta_{LL'}\delta_{MM'}. \tag{A.28}$$

They are related to the Wigner 3j symbols by

$$\begin{aligned} \langle l_1 l_2 m_1 m_2|LM\rangle &= (-1)^{M+l_1-l_2}\sqrt{2L+1} \\ &\times \begin{pmatrix} l_1 & l_2 & L \\ m_1 & m_2 & -M \end{pmatrix}. \end{aligned} \tag{A.29}$$

Concerning the 3j symbols, note that

$$\begin{pmatrix} l_1 & l_2 & l_3 \\ m_1 & m_2 & -m_3 \end{pmatrix} \neq 0 \tag{A.30}$$

if all the following conditions are satisfied:

(*i*) $m_i \in (-l_i, -l_i+1, \ldots, +l_i)$

(*ii*) $m_1 + m_2 = m_3$

(*iii*) $|l_1 - l_2| \leq l_3 \leq l_1 + l_2$

(*iv*) $l_1 + l_3 + l_3$ integer

(*v*) $l_1 + l_2 + l_3 \mod 2 = 0$ if $m_1 = m_2 = m_3 = 0$

Contracting four C coefficients yields

$$\begin{aligned}
&\delta_{l_3 l_3'} \delta_{m_3 m_3'} C^{l_1 l_2 l_3}_{L_1 L_2 L_3} \qquad (A.31)\\
&= \sum_{\substack{M_1 M_2 M_3 \\ m_1 m_2}} C^{l_2 m_2}_{L_3 M_3, L_1 M_1} C^{L_2 M_2}_{L_3 M_3 l_1 m_1} \times C^{l_3 m_3}_{L_1 M_1 L_2 M_2} C^{l_3' m_3'}_{l_1 m_1 l_2 m_2} \\
&= \delta_{l_3 l_3'} \delta_{m_3 m_3'} (-1)^{l_2 + L_2} \\
&\times \frac{(2l_1+1)(2l_2+1)(2L_1+1)(2L_2+1)(2L_3+1)}{(4\pi)^2} \\
&\times \begin{pmatrix} L_1 & l_2 & L_3 \\ 0 & 0 & 0 \end{pmatrix} \begin{pmatrix} l_1 & L_2 & L_3 \\ 0 & 0 & 0 \end{pmatrix} \begin{pmatrix} L_1 & L_2 & l_3 \\ 0 & 0 & 0 \end{pmatrix} \\
&\times \begin{pmatrix} l_1 & l_2 & l_3 \\ 0 & 0 & 0 \end{pmatrix} \begin{Bmatrix} l_1 & l_2 & l_3 \\ L_1 & L_2 & L_3 \end{Bmatrix}, \qquad (A.32)
\end{aligned}$$

where the Wigner 6j symbol can be defined by contracting four 3j symbols:

$$\begin{aligned}
&\sum_{\substack{M_1 M_2 M_3 \\ m_1 m_2}} (-1)^{L_1 + L_2 + L_3 + M_1 + M_2 + M_3} \\
&\times \begin{pmatrix} L_1 & L_2 & l_3 \\ M_1 & -M_2 & m_3 \end{pmatrix} \begin{pmatrix} L_2 & L_3 & l_1 \\ M_2 & -M_3 & m_1 \end{pmatrix} \\
&\times \begin{pmatrix} L_3 & L_1 & l_2 \\ M_3 & -M_1 & m_2 \end{pmatrix} \begin{pmatrix} l_1 & l_2 & l_3' \\ m_1 & m_2 & m_3' \end{pmatrix} \\
&= \delta_{j_3 j_3'} \delta_{m_3 m_3'} \frac{1}{2l_3 + 1} \begin{Bmatrix} l_1 & l_2 & l_3 \\ L_1 & L_2 & L_3 \end{Bmatrix}. \qquad (A.33)
\end{aligned}$$

A.6 Contraction rules

The following identities hold:

$$Y_{l_1 m_1}(\hat{\mathbf{r}}) Y_{l_2 m_2}(\hat{\mathbf{r}}) = \sum_{LM} C^{LM}_{l_1 m_1, l_2 m_2} Y_{LM}(\hat{\mathbf{r}}) \qquad (A.34)$$

where

$$C^{LM}_{l_1 m_1, l_2 m_2} = (-1)^M \sqrt{\frac{(2l_1+1)(2l_2+1)(2L+1)}{4\pi}} \times \begin{pmatrix} l_1 & l_2 & L \\ m_1 & m_2 & -M \end{pmatrix} \begin{pmatrix} l_1 & l_2 & L \\ 0 & 0 & 0 \end{pmatrix} \tag{A.35}$$

$$= \sqrt{\frac{(2l_1+1)(2l_2+1)}{4\pi(2L+1)}} \times \langle l_1 l_2 00 | L0 \rangle \langle l_1 l_2 m_1 m_2 | LM \rangle \tag{A.36}$$

According to Eqs. (A.16)-(A.17), equation (A.34) also implies:

$$\int d\Omega \, Y^*_{LM}(\hat{\mathbf{r}}) \, Y_{l_1 m_1}(\hat{\mathbf{r}}) Y_{l_2 m_2}(\hat{\mathbf{r}}) = C^{LM}_{l_1 m_1, l_2 m_2} \tag{A.37}$$

A.7 Coulomb potential

The Coulomb potential can be represented as follows:

$$\frac{1}{|\mathbf{r} - \mathbf{r}'|} = \sum_{l=0}^{\infty} \frac{r_<^l}{r_>^{l+1}} P_l(\cos(\omega)) \tag{A.38}$$

$$= \sum_{l=0}^{\infty} \sqrt{\frac{4\pi}{2l+1}} \frac{r_<^l}{r_>^{l+1}} Y_{l0}(\omega), \tag{A.39}$$

$$= \sum_{l=0}^{\infty} \sum_{m=-l}^{l} \frac{4\pi}{2l+1} \frac{r_<^l}{r_>^{l+1}} Y_{lm}(\hat{\mathbf{r}}) Y^*_{lm}(\hat{\mathbf{r}}') \tag{A.40}$$

$$= \frac{1}{r r'} \sum_{lm} Y_{lm}(\hat{\mathbf{r}}) Y^*_{lm}(\hat{\mathbf{r}}') v_l(r, r') \tag{A.41}$$

with $r_< = \min(r, r')$, $r_> = \max(r, r')$ and ω the angle between $\mathbf{r}$ and $\mathbf{r}'$. If we orient $\mathbf{r}$ along the z axis, the angle ω coincides with the integration variable θ in spherical polar coordinates.

Appendix B

The B-spline basis set

Here we introduce concepts and practicalities about the usage of B-spline basis sets as implemented in AGWX. Other attempts of using B-splines in atomic problems can be found in Refs. [203, 224] .

B.1 General properties of a basis

Given a basis set $\{|b_i\rangle\}$ on a vector space, every vector in the space can be represented as:

$$|v\rangle = \sum_i v^i |b_i\rangle, \tag{B.1}$$

$$v^i = \langle b^i|v\rangle, \tag{B.2}$$

$$\langle b^i| = \sum_j S^{-1}_{ij}\langle b_j| \qquad \text{(projectors)}, \tag{B.3}$$

$$S_{ij} = \langle b_i|b_j\rangle \qquad \text{(overlap matrix)}. \tag{B.4}$$

Note from Eq. (B.3) that the action of the inverse overlap matrix S^{-1}_{ij} is to *raise* indices of vector components (whereas the overlap matrix S_{ij} *lowers* them). Lower indices correspond to covariant representations, upper indices to contravariant representations. To simplify the notation we define:

$$S^{ij} := S^{-1}_{ij}, \tag{B.5}$$

so that raising and lowering indices will now read:

$$v_i = \sum_j S_{ij} v^j, \tag{B.6}$$

$$v^i = \sum_j S^{ij} v_j. \tag{B.7}$$

Linear operators acting on the elements of the vector space also have different representations:

$$O_{ij} = \langle b_i|\hat{O}|b_j\rangle \qquad \text{(cov.-cov.)}, \tag{B.8}$$
$$O^i{}_j = \langle b^i|\hat{O}|b_j\rangle \qquad \text{(contrav.-cov.)}, \tag{B.9}$$
$$O_i{}^j = \langle b_i|\hat{O}|b^j\rangle \qquad \text{(cov.-contrav.)}, \tag{B.10}$$
$$O^{ij} = \langle b^i|\hat{O}|b^j\rangle \qquad \text{(contrav.-contrav.)}; \tag{B.11}$$

and the overlap matrix and its inverse allow one to move from one to the other, e.g.:

$$O_i{}^j = \sum_k S_{ik} O^{kj}, \tag{B.12}$$
$$O^i{}_j = \sum_k S^{ik} O_{kj}. \tag{B.13}$$

Throughout this document we usually work in the covariant-covariant representation, taking projections on the B-spline basis in the following way:

$$\langle b_i|\hat{O}|b_j\rangle = \int dx_1 dx_2\, b_i^*(x_1) O(x_1, x_2) b_j(x_2). \tag{B.14}$$

Diagonalizing operators in this representation yields contravariant vector components v^i, which can be readily used to go back to real space using Eq. (B.1), i.e. $v(x) = \sum_i v^i b_i(x)$. Different representations may be needed when doing matrix multiplications, as we shall see right away.

The product $\hat{A}\hat{B}$ of two linear operators can be represented, like any other linear operator, on the basis of the vector space. Its representation on the basis itself can be obtained from the representations of the individual operators $\hat{A}$ and $\hat{B}$ on the same basis, provided that they have the correct index structure, e.g.:

$$(\hat{A}\hat{B})_{ij} = \sum_k A_i{}^k B_{kj}, \tag{B.15}$$
$$(\hat{A}\hat{B})_i{}^j = \sum_k A_{ik} B^{kj}. \tag{B.16}$$

This is also true on a continuous basis:

$$(\hat{A}\hat{B})(x, x') = \int dx_1 A(x, x_1) B(x_1, x'). \tag{B.17}$$

We conclude by stating that an operatorial product in a continuous basis, like the one displayed in Eq. (B.17), becomes a matrix multiplication in a discrete basis, like those in Eqs. (B.15) and (B.16).

B.2 Definition of B-splines

We now consider the case of functions belonging to the vector space $L^2[\mathbb{R}]$. If we consider localized basis functions with compact support (different from zero only over a compact

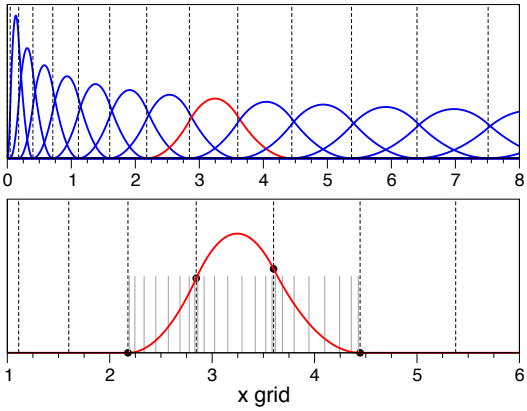

Figure B.1. B-spline basis set: (upper panel) cartoon showing the shape of the basis elements on a non-uniform grid (dashed vertical lines); (lower panel) a single B-spline function (cubit order) is shown, together with the generating grid knots (black bullets) and the Gauss-Legendre points used for grid integration (vertical grey lines).

interval), the overlap matrix can be rearranged to be banded, resulting in an overall numerical efficiency of the basis set. Among many possible localized basis set, here we consider the B-spline set. In the following we propose a summary of the main definitions and properties of B-splines. For a more detailed treatment, see Ref. [166167].

Given an increasing knot sequence $x_{i+1} > x_i$, the B-spline of order k corresponding to knot i, $B_{ik}(x)$, is a piece-wise polynomial of degree $< k$ which vanished identically outside the interval $[x_i, x_{i+k}]$ (B_{ik} spans k segments over $k+1$ knot points). Given the following partition of unity,

$$X_i(x) = \begin{cases} 1 & x \in [x_i, x_{i+1}[\\ 0 & \text{otherwise} \end{cases} \tag{B.18}$$

$$\sum_i X_i(x) = 1, \tag{B.19}$$

one has:

$$B_{ik}(x) = \sum_{j=i}^{i+k-1} b_{jk}(x) X_j(x), \tag{B.20}$$

$b_{jk}(x)$ being a polynomial of degree $k-1$. The $b_{jk}(x)$ polynomials are determined by imposing regularity conditions on the resulting B-spline. In particular, the parameters in the B-spline definition are completely determined by imposing $b_{jk}(x)$ to be C^{k-2} and fixing the overall normalization. By doing this, the definition of the B-spline set depends only on the knot sequence chosen. The following recurrence relation can be practically used to

determine the coefficients:

$$\begin{aligned} B_{i1}(x) &= X_i(x) && \text{(B.21)} \\ B_{ik}(x) &= \omega_{ik}(x)B_{i,k-1}(x) \\ &+ [1-\omega_{i+1,k}(x)]B_{i+1,k-1}(x) && \text{(B.22)} \\ \omega_{ik}(x) &= \begin{cases} \frac{x-x_i}{x_{i+k-1}-x_i} & \text{if } x_{i+k-1} \neq x_i \\ 0 & \text{otherwise} \end{cases} && \text{(B.23)} \end{aligned}$$

Once the coefficients of the polynomials for each segment ($k+1$ in total) have been determined, all derivatives can be performed analytically up to order $k-2$.

B.3 Integration

Being the B-spline piece-wise polynomial, it is very convenient to equip the basis set with Gauss-Legendre integration points for each segment, in order to integrate exactly all polynomials up to a chosen order. In this respect, the calculation of the overlap matrix of the B-spline basis set, Eq. (B.4), involving the integration of polynomials of order $2(k-1)$, can be computed exactly.

Within the Gaussian quadrature, the following estimate is made:

$$\int_{-1}^{1} f(x)\,dx \simeq \sum_{i}^{n} w_i^{(n)} f(x_i), \tag{B.24}$$

where n is the order of the quadrature, x_i are the zeros of the Legendre polynomial of order n in [-1,1], and $w_i^{(n)}$ the n-th order weights:

$$\begin{aligned} w_i^{(n)} &= \frac{2}{(1-x_i^2)\,|P_n'(x_i)|^2} && \text{(B.25)} \\ &= \frac{2((1-x_i^2)}{(n+1)^2\,|P_{n+1}(x_i)|^2}. && \text{(B.26)} \end{aligned}$$

where the second expression can be obtained by considering the identities in Eq. (A.11), together with the condition $P_n(x_i)=0$. Usually, weights and abscissas are either tabulated or recalculated on the fly. AGWX implements tabulated abscissas, while computes weights according to Eq. (B.26).

Within the above formulation, Eq. (B.24) becomes exact for polynomials of order $\leq 2n-1$. The approach can be generalized to the presence of a weight function $\omega(x)$ in the integral and to different integration extrema. The key aspect is to make reference to the suitable set of orthogonal polynomials, i.e. defined with the same weight function and integration interval.

Appendix C

Coulomb integrals

We introduce a notation to write down Coulomb integrals and partially saturated Coulomb integrals in a compact fashion. Integrals not relying on the SH/B-spline representation, having wavefunctions indexed with Greek letters, are to be intended in the usual Dirac way:

$$\langle \alpha\mu | v_c | \beta\nu \rangle = \int d\mathbf{r}_1 d\mathbf{r}_2 \varphi^*_\alpha(\mathbf{r}_1)\varphi^*_\mu(\mathbf{r}_2) v_c(\mathbf{r}_1,\mathbf{r}_2)\varphi_\beta(\mathbf{r}_1)\varphi_\nu(\mathbf{r}_2), \tag{C.1}$$

$$\begin{aligned}\langle \mu | v_c(\mathbf{r}) | \nu \rangle &= \int d\mathbf{r}_1 \varphi^*_\mu(\mathbf{r}_1) v_c(\mathbf{r},\mathbf{r}_1)\varphi^*_\nu(\mathbf{r}_1) \\ &= \int d\mathbf{r}_1 \varphi^*_\mu(\mathbf{r}_1) v_c(\mathbf{r}_1,\mathbf{r})\varphi^*_\nu(\mathbf{r}_1).\end{aligned} \tag{C.2}$$

Integrals written in the radial-axis/SH representation carry a $1/r$ factor:

$$\begin{aligned}\langle pl_p, ql_q | (v_c)_{l_c} | rl_r, sl_s \rangle = \int \frac{dr_1 dr_2}{r_1 r_2} P_{pl_p}(r_1) P_{ql_q}(r_2) \\ \times\, v_c(r_1,r_2)_{l_c} P_{rl_r}(r_1) P_{sl_s}(r_2),\end{aligned} \tag{C.3}$$

$$\langle ql_q\mu | v_c(r)_{l_c} | sl_s \rangle = \int \frac{dr_1}{r_1} P_{ql_q}(r_1) v_c(r,r_1)_{l_c} P_{sl_s}(r_1). \tag{C.4}$$

Taking these integrals to the B-spline/SH representation involves the projection of the product basis onto the basis itself, as seen in the calculation of the RPA irreducible polarizability in Section 3.3.4. This entails the usage of the B^3_{ijk} matrix:

$$\begin{aligned}\langle pl_p, ql_q | (v_c)_{l_c} | rl_r, sl_s \rangle = \sum_{ii'} \sum_{jk} B^3_{ijk} P^j_{pl_p} P^k_{rl_r} \\ \times\, (v_c)^{ii'}_{l_c} \sum_{j'k'} B^3_{i'j'k'} P^{j'}_{ql_q} P^{k'}_{sl_s},\end{aligned} \tag{C.5}$$

$$\langle ql_q | (v_c)_{l_c} | sl_s \rangle^i = (v_c)^{ii'}_{l_c} \sum_{j'k'} B^3_{i'j'k'} P^{j'}_{ql_q} P^{k'}_{sl_s}. \tag{C.6}$$

Appendix D

Semi-analytical integrals

We collect in this section the semi-analytical frequency integrals used throughout the text. These integrals are typically obtained by analytical continuation over the imaginary frequency axis and discretization of the domain, like in the contour deformation technique. They involve a product of a number of lorentzian functions and the screened interaction W, the poles and the residues of the latter being in general unknown. Thanks to the parity of W, the imaginary parts of the integrals vanish, and the real parts can be obtained by doubling the integral over the positive domain. The discretization over the positive domain is performed with a set of frequencies $\omega_1, \ldots, \omega_M$, defining $M-1$ intervals over which the integral of the function multiplying W is performed analytically; the value of W is kept fixed at $\Omega_m = \frac{\omega_{m+1}+\omega_m}{2}$ over the intervals. The integrals are reported in the following:

$$\begin{aligned}
&\int_{-\infty}^{+\infty} d\omega' \frac{1}{i\omega' - a} W(i\omega') \\
&\simeq -2 \sum_{m}^{M-1} \left[\arctan\left(\frac{\omega'}{a}\right) \right]_{\omega'_m}^{\omega'_{m+1}} \mathrm{Re}\left\{ W(i\Omega'_m) \right\}
\end{aligned} \tag{D.1}$$

$$\begin{aligned}
&\int_{-\infty}^{+\infty} d\omega' \frac{1}{(i\omega' - a)^2} W(i\omega') \\
&\simeq 2 \sum_{m}^{M-1} \left[\frac{\omega'}{(\omega')^2 + a^2} \right]_{\omega'_m}^{\omega'_{m+1}} \mathrm{Re}\left\{ W(i\Omega'_m) \right\},
\end{aligned} \tag{D.2}$$

$$\begin{aligned}
&\int_{-\infty}^{+\infty} d\omega' \frac{1}{(i\omega' - a)(i\omega' - b)} W(i\omega') \\
&\simeq 2 \sum_{m}^{M-1} \mathrm{Re}\left\{ W(i\Omega'_m) \right\} \frac{1}{(a-b)} \\
&\times \left[\arctan\left(\frac{\omega'}{b}\right) - \arctan\left(\frac{\omega'}{a}\right) \right]_{\omega'_m}^{\omega'_{m+1}};
\end{aligned} \tag{D.3}$$

$$\begin{aligned}
&\int_{-\infty}^{+\infty} d\omega' \frac{1}{(i\omega' - a)^2 (i\omega' - b)} W(i\omega') \\
&\simeq 2 \sum_{m}^{M-1} \mathrm{Re}\left\{W(i\Omega'_m)\right\} \frac{1}{(a-b)^2} \\
&\times \left[\frac{\omega'(a-b)}{a^2 + \omega'^2} + \arctan\left(\frac{\omega'}{a}\right) - \arctan\left(\frac{\omega'}{b}\right) \right]_{\omega'_m}^{\omega'_{m+1}}
\end{aligned} \tag{D.4}$$

$$\begin{aligned}
&\int_{-\infty}^{+\infty} d\omega' \frac{1}{(i\omega' - a)^3} W(i\omega') \\
&\simeq 2 \sum_{m}^{M-1} \mathrm{Re}\left\{W(i\Omega'_m)\right\} \left[-\frac{a\omega'}{(\omega'^2 + a^2)^2} \right]_{\omega'_m}^{\omega'_{m+1}}
\end{aligned} \tag{D.5}$$

Appendix E

Self-energy specifics for satellite treatment

E.1 Static component plus dynamical component

As mentioned in Section 5.1.1, treating both QP and satellite properties on the same footing with conventional diagrammatic expansions of the self-energy and subsequent application of the Dyson equation can become challenging. We can then consider a direct finite-order expansion of the Green's function in orders of G_0. With a GW-like self-energy, having the form

$$\Sigma(\omega) = \Sigma^s + \Sigma^d(\omega) = \Sigma^s + \frac{\alpha}{\omega - \varepsilon - \omega_p}, \tag{E.1}$$

this would mean having an exact alignment of the satellites in the self-energy with those in the spectral function, provided that the quasi-particle (QP) energy ε and the neutral excitations contained in ω_p are accurate. In fact, one could write

$$G(\omega) = \tilde{G}_0(\omega) + \tilde{G}_0(\omega)\Sigma^d(\omega)\tilde{G}_0(\omega), \tag{E.2}$$

where the accurate QPs would be given by $\tilde{G}_0(\omega) = G_0(\omega) + G_0(\omega)\Sigma^s\tilde{G}_0(\omega)$ and the accurate satellites by $\tilde{G}_0\Sigma^d\tilde{G}_0$. One could in principle count on the fact that the latter contribution does not shift the QP, while nevertheless introducing poles of order 2. Unfortunately, it turns out that within this scheme (see Sec. E.2.1), the QP and the satellite problem are intertwined if one wants to avoid the appearance of poles of higher order. The usual GW self-energy is a good choice for QP energies, but yields a poor description of e.g. shake-up satellites: for instance, GW@HF only produces a double ionization continuum in the spectral function.

One could then think of utilizing a more accurate W from the time-dependent Hartree-Fock (TDHF) scheme, but this is known to deteriorate the quasi-particle description. Furthermore, despite improving the qualitative description of the satellite region by introducing peaks associated to bound neutral excitations in the spectral function, the quantitative description is still off because the neutral excitations are those of the neutral atom; if one is to work with the GW-like self-energy of Eq. (E.1), they will need ω_p to contain the excitations of the singly ionized atom.

Finally, one could consider a W with one less electron: in the case of He one could even obtain exact neutral excitations of the ionized atom, if allowing for relaxation. However, it is unknown how a GW-like self-energy as such would perform for the QPs. If I were to guess, not so well because the wildly different HOMO-LUMO gaps that the neutral and ionized atoms have. In fact, the one time this recipe was applied by [62] for QP properties, relaxation was not allowed (which we would however need for a good satellite description).

E.2 Vertex corrections from a finite-order expansion of G

Let us suppose that we can perform a finite-order expansion of G without incurring in the problem of poles of higher order, i.e. we can safely write

$$G = \tilde{G}_0 + \tilde{G}_0 \Sigma^a \tilde{G}_0. \tag{E.3}$$

The Dyson equation still holds,

$$G = G_0 + G_0 \Sigma G, \tag{E.4}$$

and it can be inverted so as to give the self-energy:

$$\Sigma = G_0^{-1} - G^{-1} = G_0^{-1} - (\tilde{G}_0 + \tilde{G}_0 \Sigma^a \tilde{G}_0)^{-1} \tag{E.5}$$

where G^{-1} was substituted using Eq. (E.3). A self-energy is thus found that can be plugged into the Dyson equation and yield the same result given by the finite-order expansion of G. If the finite-order expansion is to yield a Green's function with beyond-GW accuracy, then Σ can be regarded as a vertex-corrected self-energy.

E.2.1 Expansion of G_0 to finite order

The usage of a finite-order expansion of G_0 instead of a full solution of the Dyson equation is supported by [67] and [68] (see also [213]): In fact, self-energy approximations to finite order are seen to cause the occurrence of spurious peaks in the spectral functions in a number of (model) systems (e.g. the so-called "plasmaron" peak in the homogeneous electron gas), upon using these approximations together with the Dyson equation. Truncating the Dyson equation to finite order prevents such occurrence, but causes the appearance of poles of higher order in the Green's functions. These can be removed with an energy shift in the starting point, following the prescription of [68], which we present in the following.

We write G as an expansion in orders of G^0:

$$G(\omega) = G^0(\omega) + \bar{G}^{(1)}(\omega) + \bar{G}^{(2)}(\omega) + \dots, \tag{E.6}$$

where $\bar{G}^{(n)} \sim (G^0)^{(n+1)}$. Assuming diagonality, i.e.

$$G^0(\omega) = \frac{1}{\omega - \varepsilon \pm i\delta}, \tag{E.7}$$

the first-order term in the GW approximation is

$$\begin{aligned} \bar{G}^{(1)}(\omega) &= (G^0(\omega))^2 \left[\Delta^x + \Sigma(\omega)\right] \\ &= (G^0(\omega))^2 \left[\Delta^x + i\lambda \int \frac{d\omega'}{2\pi} G(\omega + \omega') W(\omega')\right], \end{aligned} \tag{E.8}$$

where Δ^x is the quasi-particle (QP) energy shift due to the Fock self-energy, whereas the remainder in the square brackets is the GW correlation contribution. A coupling constant λ was also introduced, serving as a prefactor of the correlation contribution.

We also perform an expansion of the QP shift in orders of λ, simultaneously with the expansion of G:

$$G(\omega + \Delta^{(1)} + \Delta^{(2)} + \ldots) = G^0(\omega) + G^{(1)}(\omega) + G^{(2)}(\omega) + \ldots \tag{E.9}$$

We restrict ourselves to first order in λ and apply the Dyson equation to write

$$\begin{aligned} G(\omega + \Delta^{(1)}) &= G(\omega) - G(\omega)\Delta^{(1)}G(\omega + \Delta^{(1)}) \\ &= G(\omega) - G(\omega)\Delta^{(1)}G(\omega) + G(\omega)\Delta^{(1)}G(\omega)\Delta^{(1)}G(\omega) + \ldots; \end{aligned} \tag{E.10}$$

then we apply (E.6) and retain again only first-order terms in λ:

$$\begin{aligned} G(\omega + \Delta^{(1)}) &= \bar{G}^0(\omega) + \bar{G}^{(1)}(\omega) + \ldots \\ &\quad + (\bar{G}^0(\omega) + \bar{G}^{(1)}(\omega) + \ldots)\Delta^{(1)}(\bar{G}^0(\omega) + \bar{G}^{(1)}(\omega) + \ldots) + \ldots \\ &= G^0(\omega) + \bar{G}^{(1)}(\omega) - G^0(\omega)\Delta^{(1)}G^0(\omega) + \mathcal{O}(\lambda^2). \end{aligned} \tag{E.11}$$

By comparison with (E.9), we find

$$G^{(1)}(\omega) = \bar{G}^{(1)}(\omega) - G^0(\omega)\Delta^{(1)}G^0(\omega), \tag{E.12}$$

and, splitting $\Delta^{(1)}$ according to

$$\Delta^{(1)} = \Delta^x + \Delta^c, \tag{E.13}$$

we end up having

$$G^{(1)}(\omega) = (G^{(0)})^2 \left[\Sigma(\omega) - \Delta^c\right]. \tag{E.14}$$

We choose Δ^c such that the double pole occurring in the last equation due to $(G^0)^2$ gets canceled, namely

$$\Delta^c = \Sigma(\varepsilon); \tag{E.15}$$

in fact, with the GW self-energy this yields

$$\Sigma(\omega) - \Sigma(\varepsilon) \sim \frac{1}{\omega - \varepsilon + \omega_s} - \frac{1}{\omega_s} = -\frac{\omega - \varepsilon}{\omega_s(\omega - \varepsilon + \omega_s)}, \tag{E.16}$$

and the numerator of this expression exactly cancels the double pole of $(G^0)^2$.[1] We notice that this QP shift due to correlation is the same as the one normally found when solving the GW QP equation *without* renormalization factor.

The QP renormalization factor, representing the leftover weight of the QP peak, is defined in the vicinity of the QP peak as

$$Z\delta(\omega - \varepsilon - \Delta^{(1)}) = \frac{1}{2\pi}\rho(\omega), \tag{E.17}$$

with $\rho(\omega) = 2\mathrm{Im}|G(\omega)|$.

[1] Provided that the vanishing imaginary parts are somewhat treated consistently.

Acronyms

ALDA adiabatic local density approximation. 55

ARPES angle-resolved photoemission spectroscopy. 9

BSE Bethe-Salpeter equation. 43

CBM conduction band minimum. 11

COHSEX Coulomb hole-screened exchange. 123

DFT density functional theory. 12

DMFT dynamical mean-field theory. 16

EA electron affinity. 12

ev-scGW eigenvalue self-consistent GW. 21

EXX exact-exchange. 64

FEX Fock exchange. 21

GL Gauss-Legendre. 67

HEG homogeneous electron gas. 15

HF Hartree-Fock. 10

HOMO highest-occupied molecular orbital. 11

HPC high-perofrmance computing. 9

IE ionization energy. 12

IP independent particle. 10

KS Kohn-Sham. 12

LDA local density approximation. 15

LSSE linearized Sham-Schlüter equation. 22

LUMO lowest-unoccupied molecular orbital. 11, 12

MAE mean absolute error. 80

MBPT many-body perturbation theory. 9

ME mean error. 80

MP2 second-order Møller-Plesset theory. 64

OEP optimized effective potential. 21

PBE Perdew-Burke-Ernzherof. 25

QP quasi-particle. 12

QPE quasi-particle equation. 13

QSGW quasi-particle self-consistent GW. 21

RPA random-phase approximation. 15

scGW self-consistent GW. 20

SH spherical harmonic. 65

SO-TDGW second-order time-dependent GW. 19

SOSEX second-order screened exchange. 19

SPT spectral potential theory. 23

SSC-GW self-screening corrected GW. 138

SSE Sham-Schlüter equation. 22

TDDFT time-dependent density functional theory. 54

TDGW time-dependent GW. 17

TDHF time-dependent Hartree-Fock. 17

VBM valence band maximum. 11

Bibliography

[1] C. Mariani, G. Stefani in *Synchrotron Radiation: Basics, Methods and Applications*, (Eds.: S. Mobilio, F. Boscherini, C. Meneghini), Springer Berlin Heidelberg, Berlin, Heidelberg, **2015**, pp. 275–317.

[2] F. Reinert, S. Hüfner, *New J. Phys.* **2005**, *7*, 97–97.

[3] A. Damascelli, Z. Hussain, Z.-X. Shen, *Rev. Mod. Phys.* **2003**, *75*, 473–541.

[4] C. Chang, V. L. Deringer, K. S. Katti, V. Van Speybroeck, C. M. Wolverton, *Nat Rev Mater* **2023**, *8*, 309–313.

[5] S. Valeri, Spectroscopy lecture notes, **2015**.

[6] C. Froese Fischer, *The Hartree-Fock Method for Atoms: A Numerical Approach*, John Wiley & Sons Inc., New York, **1977**.

[7] C. Froese Fischer, T. Brage, P. Jönsson, *Computational Atomic Structure: an MCHF Approach*, IOP Publishing, Bristol, **1997**.

[8] A. Szabo, N. S. Ostlund, *Modern Quantum Chemistry*, McGraw-Hill, New York, **1989**.

[9] N. Ashcroft, N. D. Mermin, *Solid State Physics*, Saunders College Publishing, Philadelphia, **1976**.

[10] M. L. Cohen, V. Heine in (Eds.: H. Ehrenreich, F. Seitz, D. Turnbull), Solid State Physics, Academic Press, **1970**, pp. 37–248.

[11] P. Hohenberg, W. Kohn, *Phys. Rev.* **1964**, *136*, B864–B871.

[12] W. Kohn, L. J. Sham, *Phys. Rev.* **1965**, *140*, A1133–A1138.

[13] R. M. Martin, L. Reining, D. M. Ceperley, *Interacting Electrons*, Cambridge University Press, Cambridge, **2016**.

[14] D. Pines, P. Nozières, *The Theory of Quantum Liquids*, Addison-Wesley, New York, **1989**.

[15] R. D. Mattuck, *A guide to Feynman diagrams in the many-body problem*, McGraw-Hill, New York, **1976**.

[16] L. Hedin, *Phys. Rev.* **1965**, *139*, A796–A823.

[17] L. Hedin, *J. Phys.: Condens. Matter* **1999**, *11*, R489–R528.

[18] F. Aryasetiawan, O. Gunnarsson, *Rep. Prog. Phys.* **1998**, *61*, 237.

[19] G. Onida, L. Reining, A. Rubio, *Rev. Mod. Phys.* **2002**, *74*, 601–659.

[20] P. Nozières, D. Pines, *Phys. Rev.* **1958**, *111*, 442–454.

[21] G. D. Mahan, *Many-particle physics*, Springer, New York, **2000**.

[22] L. Hedin, *Int. J. Quantum Chem.* **1995**, *56*, 8.

[23] G. Strinati, *Phys. Rev. Lett.* **1982**, *49*, 1519–1522.

[24] N. Marzari, A. Ferretti, C. Wolverton, *Nat. Mater.* **2021**, *20*, 736–749.

[25] M. S. Hybertsen, S. G. Louie, *Phys. Rev. Lett.* **1985**, *55*, 1418–1421.

[26] M. S. Hybertsen, S. G. Louie, *Phys. Rev. B* **1986**, *34*, 5390–5413.

[27] R. W. Godby, M. Schlüter, L. J. Sham, *Phys. Rev. Lett.* **1986**, *56*, 2415–2418.

[28] R. W. Godby, M. Schlüter, L. J. Sham, *Phys. Rev. B* **1988**, *37*, 10159–10175.

[29] L. Reining, *Wiley Interdisciplinary Reviews: Computational Molecular Science* **2018**, *8*, e1344.

[30] D. Golze, M. Dvorak, P. Rinke, *Front. Chem.* **2019**, *7*, 377.

[31] J. P. Perdew, R. G. Parr, M. Levy, J. L. Balduz, *Phys. Rev. Lett.* **1982**, *49*, 1691–1694.

[32] J. P. Perdew, W. Yang, K. Burke, Z. Yang, E. K. U. Gross, M. Scheffler, G. E. Scuseria, T. M. Henderson, I. Y. Zhang, A. Ruzsinszky, H. Peng, J. Sun, E. Trushin, A. Görling, *PNAS* **2017**, *114*, 2801–2806.

[33] E. Kraisler, M. J. P. Hodgson, E. K. U. Gross, *J. Chem. Theory Comput.* **2021**, *17*, 1390–1407.

[34] E. L. Shirley, R. M. Martin, *Phys. Rev. B* **1993**, *47*, 15404–15412.

[35] A. Stan, N. E. Dahlen, R. van Leeuwen, *EPL* **2006**, *76*, 298.

[36] C. Rostgaard, K. W. Jacobsen, K. S. Thygesen, *Phys. Rev. B* **2010**, *81*, 085103.

[37] M. J. van Setten, F. Weigend, F. Evers, *J. Chem. Theory Comput.* **2013**, *9*, 232–246.

[38] F. Bruneval, M. A. L. Marques, *J. Chem. Theory Comput.* **2013**, *9*, 324–329.

[39] F. Kaplan, M. E. Harding, C. Seiler, F. Weigend, F. Evers, M. J. van Setten, *J. Chem. Theory Comput.* **2016**, *12*, 2528–2541.

[40] L. Hung, F. H. da Jornada, J. Souto-Casares, J. R. Chelikowsky, S. G. Louie, S. Öğüt, *Phys. Rev. B* **2016**, *94*, 085125.

[41] F. Bruneval, N. Dattani, M. J. van Setten, *Frontiers in Chemistry* **2021**, *9*, 811.

[42] K. W.-K. Shung, G. D. Mahan, *Phys. Rev. Lett.* **1986**, *57*, 1076–1079.

[43] K. W.-K. Shung, B. E. Sernelius, G. D. Mahan, *Phys. Rev. B* **1987**, *36*, 4499–4502.

[44] J. E. Northrup, M. S. Hybertsen, S. G. Louie, *Phys. Rev. Lett.* **1987**, *59*, 819–822.

[45] I.-W. Lyo, E. W. Plummer, *Phys. Rev. Lett.* **1988**, *60*, 1558–1561.

[46] H. Yasuhara, S. Yoshinaga, M. Higuchi, *Phys. Rev. Lett.* **1999**, *83*, 3250–3253.

[47] Y. Takada, *Phys. Rev. Lett.* **2001**, *87*, 226402.

[48] M. V. Schilfgaarde, T. Kotani, S. Faleev, *Phys. Rev. Lett.* **2006**, *96*, 226402.

[49] A. J. Morris, M. Stankovski, K. T. Delaney, P. Rinke, P. García-González, R. W. Godby, *Phys. Rev. B* **2007**, *76*, 155106.

[50] A. L. Kutepov, *Phys. Rev. B* **2016**, *94*, 155101.

[51] S. Choi, A. Kutepov, K. Haule, M. van Schilfgaarde, G. Kotliar, *npj Quantum Materials* **2016**, *1*, 16001.

[52] A. Liebsch, *Phys. Rev. B* **1981**, *23*, 5203–5212.

[53] D. Zhang, N. Q. Su, W. Yang, *J. Phys. Chem. Lett.* **2017**, *8*, 3223–3227.

[54] A. Georges, G. Kotliar, W. Krauth, M. J. Rozenberg, *Rev. Mod. Phys.* **1996**, *68*, 13–125.

[55] F. Fuchs, J. Furthmüller, F. Bechstedt, M. Shishkin, G. Kresse, *Phys. Rev. B* **2007**, *76*, 115109.

[56] N. Marom, F. Caruso, X. Ren, O. T. Hofmann, T. Körzdörfer, J. R. Chelikowsky, A. Rubio, M. Scheffler, P. Rinke, *Phys. Rev. B* **2012**, *86*, 245127.

[57] M. Guzzo, G. Lani, F. Sottile, P. Romaniello, M. Gatti, J. J. Kas, J. J. Rehr, M. G. Silly, F. Sirotti, L. Reining, *Phys. Rev. Lett.* **2011**, *107*, 166401.

[58] J. Lischner, D. Vigil-Fowler, S. G. Louie, *Phys. Rev. Lett.* **2013**, *110*, 146801.

[59] J. S. Zhou, M. Gatti, J. J. Kas, J. J. Rehr, L. Reining, *Phys. Rev. B* **2018**, *97*, 035137.

[60] G. Strinati, *Riv. Nuovo Cim.* **1988**, *11*, 1–86.

[61] P. Romaniello, S. Guyot, L. Reining, *J. Chem. Phys.* **2009**, *131*, 154111.

[62] F. Aryasetiawan, R. Sakuma, K. Karlsson, *Phys. Rev. B* **2012**, *85*, 035106.

[63] J. Wetherell, M. J. P. Hodgson, R. W. Godby, *Phys. Rev. B* **2018**, *97*, 121102.

[64] A. J. Cohen, P. Mori-Sánchez, W. Yang, *Science* **2008**, *321*, 792–794.

[65] L. Kronik, S. Kümmel, *Phys. Chem. Chem. Phys.* **2020**, 10.1039.D0CP02564J.

[66] L. Hedin, S. Lundqvist in (Eds.: F. Seitz, D. Turnbull, H. Ehrenreich), Solid State Physics, Academic Press, **1970**, pp. 1–181.

[67] C. Blomberg, B. Bergersen, *Can. J. Phys.* **1972**, *50*, 2286–2293.

[68] B. Bergersen, F. W. Kus, C. Blomberg, *Can. J. Phys.* **1973**, *51*, 102–110.

[69] D. C. Langreth, *Phys. Rev. B* **1970**, *1*, 471–477.

[70] L. Hedin, B. Lundqvist, S. Lundqvist, *J. RES. NATL. BUR. STAN. SECT. A.* **1970**, *74A*, 417.

[71] F. Krien, A. Kauch, K. Held, *Phys. Rev. Research* **2021**, *3*, 013149.

[72] C. Mejuto-Zaera, V. Vlček, *Phys. Rev. B* **2022**, *106*, 165129.

[73] Y.-W. Chang, B.-Y. Jin, *Phys. Scr.* **2012**, *86*, 065301.

[74] E. Maggio, G. Kresse, *J. Chem. Theory Comput.* **2017**, *13*, 4765–4778.

[75] C. Mejuto-Zaera, G. Weng, M. Romanova, S. J. Cotton, K. B. Whaley, N. M. Tubman, V. Vlček, *J. Chem. Phys.* **2021**, *154*, 121101.

[76] A. D. McLachlan, M. A. Ball, *Rev. Mod. Phys.* **1964**, *36*, 844–855.

[77] A. Dalgarno, G. A. Victor, *Proceedings of the Royal Society of London. Series A Mathematical and Physical Sciences* **1966**, *291*, 291–295.

[78] M. H. Alexander, R. G. Gordon, *J. Chem. Phys.* **1972**, *56*, 3823–3831.

[79] R. F. Stewart, *J. Phys. B: At. Mol. Phys.* **1975**, *8*, 1–10.

[80] R. F. Stewart, *Mol. Phys.* **1975**, *29*, 1577–1583.

[81] R. F. Stewart, *Mol. Phys.* **1975**, *30*, 745–754.

[82] B. C. Webster, M. J. Jamieson, R. F. Stewart in (Eds.: D. Bates, B. Bederson), Advances in Atomic and Molecular Physics, Academic Press, **1979**, pp. 87–125.

[83] A. Grüneis, G. Kresse, Y. Hinuma, F. Oba, *Phys. Rev. Lett.* **2014**, *112*, 096401.

[84] P. A. Bobbert, W. van Haeringen, *Phys. Rev. B* **1994**, *49*, 10326–10331.

[85] E. L. Shirley, *Phys. Rev. B* **1996**, *54*, 7758–7764.

[86] A. L. Kutepov, *Phys. Rev. B* **2017**, *95*, 195120.

[87] Y. Wang, P. Rinke, X. Ren, *J. Chem. Theory Comput.* **2021**, *17*, 5140–5154.

[88] G. Stefanucci, Y. Pavlyukh, A.-M. Uimonen, R. van Leeuwen, *Phys. Rev. B* **2014**, *90*, 115134.

[89] Y. Pavlyukh, A.-M. Uimonen, G. Stefanucci, R. van Leeuwen, *Phys. Rev. Lett.* **2016**, *117*, 206402.

[90] Y. Pavlyukh, G. Stefanucci, R. van Leeuwen, *Phys. Rev. B* **2020**, *102*, 045121.

[91] X. Ren, N. Marom, F. Caruso, M. Scheffler, P. Rinke, *Phys. Rev. B* **2015**, *92*, 081104.

[92] J. W. Knight, X. Wang, L. Gallandi, O. Dolgounitcheva, X. Ren, J. V. Ortiz, P. Rinke, T. Körzdörfer, N. Marom, *J. Chem. Theory Comput.* **2016**, *12*, 615–626.

[93] P.-F. Loos, P. Romaniello, J. A. Berger, *J. Chem. Theory Comput.* **2018**, *14*, 3071–3082.

[94] R. Del Sole, L. Reining, R. W. Godby, *Phys. Rev. B* **1994**, *49*, 8024–8028.

[95] F. Bruneval, F. Sottile, V. Olevano, R. Del Sole, L. Reining, *Phys. Rev. Lett.* **2005**, *94*, 186402.

[96] M. Shishkin, M. Marsman, G. Kresse, *Phys. Rev. Lett.* **2007**, *99*, 246403.

[97] W. Chen, A. Pasquarello, *Phys. Rev. B* **2015**, *92*, 041115.

[98] A. Tal, W. Chen, A. Pasquarello, *Phys. Rev. B* **2021**, *103*, L161104.

[99] D. Sangalli, A. Ferretti, H. Miranda, C. Attaccalite, I. Marri, E. Cannuccia, P. Melo, M. Marsili, F. Paleari, A. Marrazzo, G. Prandini, P. Bonfà, M. O. Atambo, F. Affinito, M. Palummo, A. Molina-Sánchez, C. Hogan, M. Grüning, D. Varsano, A. Marini, *J. Phys.: Condens. Matter* **2019**, *31*, 325902.

[100] A. M. Lewis, T. C. Berkelbach, *J. Chem. Theory Comput.* **2019**, *15*, 2925–2932.

[101] U. von Barth, B. Holm, *Phys. Rev. B* **1996**, *54*, 8411–8419.

[102] B. Holm, U. von Barth, *Phys. Rev. B* **1998**, *57*, 2108–2117.

[103] M. Shishkin, G. Kresse, *Phys. Rev. B* **2007**, *75*, 235102.

[104] A. Schindlmayr, P. García-González, R. W. Godby, *Phys. Rev. B* **2001**, *64*, 235106.

[105] A. Stan, N. E. Dahlen, R. van Leeuwen, *J. Chem. Phys.* **2009**, *130*, 114105.

[106] E. G. C. P. van Loon, M. Rösner, M. I. Katsnelson, T. O. Wehling, *Phys. Rev. B* **2021**, *104*, 045134.

[107] M. van Schilfgaarde, T. Kotani, S. Faleev, *Phys. Rev. Lett.* **2006**, *96*, 226402.

[108] T. Kotani, *J. Phys.: Condens. Matter* **1998**, *10*, 9241.

[109] P. Rinke, A. Qteish, J. Neugebauer, C. Freysoldt, M. Scheffler, *New J. Phys.* **2005**, *7*, 126–126.

[110] J. Klimeš, G. Kresse, *J. Chem. Phys.* **2014**, *140*, 054516.

[111] C.-O.Almbladth, U. von Barth, *Phys. Rev. B* **1985**, *31*, 3231–3244.

[112] C. J. Umrigar, X. Gonze, *Phys. Rev. A* **1994**, *50*, 3827–3837.

[113] T. Körzdörfer, N. Marom, *Phys. Rev. B* **2012**, *86*, 041110.

[114] V. Atalla, M. Yoon, F. Caruso, P. Rinke, M. Scheffler, *Phys. Rev. B* **2013**, *88*, 165122.

[115] V. Atalla, I. Y. Zhang, O. T. Hofmann, X. Ren, P. Rinke, M. Scheffler, *Phys. Rev. B* **2016**, *94*, 035140.

[116] M. Dauth, F. Caruso, S. Kümmel, P. Rinke, *Phys. Rev. B* **2016**, *93*, 121115.

[117] J. P. Perdew, A. Zunger, *Phys. Rev. B* **1981**, *23*, 5048–5079.

[118] D. Golze, L. Keller, P. Rinke, *J. Phys. Chem. Lett.* **2020**, *11*, 1840–1847.

[119] L. J. Sham, M. Schlüter, *Phys. Rev. Lett.* **1983**, *51*, 1888–1891.

[120] R. T. Sharp, G. K. Horton, *Phys. Rev.* **1953**, *90*, 317–317.

[121] J. D. Talman, W. F. Shadwick, *Phys. Rev. A* **1976**, *14*, 36–40.

[122] M. E. Casida, *Phys. Rev. A* **1995**, *51*, 2005–2013.

[123] E. Engel, R. M. Dreizler, *Journal of Computational Chemistry* **1998**, *20*, 20.

[124] E. Engel in *A Primer in Density Functional Theory*, (Eds.: C. Fiolhais, F. Nogueira, M. A. L. Marques), Springer Berlin Heidelberg, Berlin, Heidelberg, **2003**, pp. 56–122.

[125] S. Kümmel, L. Kronik, *Rev. Mod. Phys.* **2008**, *80*, 3–60.

[126] Y. M. Niquet, M. Fuchs, X. Gonze, *J. Chem. Phys.* **2003**, *118*, 9504–9518.

[127] Y. M. Niquet, X. Gonze, *Phys. Rev. B* **2004**, *70*, 245115.

[128] E. Engel, S. H. Vosko, *Phys. Rev. A* **1993**, *47*, 2800–2811.

[129] J. P. Perdew, M. Levy, *Phys. Rev. Lett.* **1983**, *51*, 1884–1887.

[130] M. Hellgren, L. Baguet, M. Calandra, F. Mauri, L. Wirtz, *Phys. Rev. B* **2021**, *103*, 075101.

[131] M. Gatti, V. Olevano, L. Reining, I. V. Tokatly, *Phys. Rev. Lett.* **2007**, *99*, 057401.

[132] M. Vanzini, L. Reining, M. Gatti, *Eur. Phys. J. B* **2018**, *91*, 1–22.

[133] A. Aouina, M. Gatti, L. Reining, *Faraday Discuss.* **2020**, *224*, 27–55.

[134] D. A. León, C. Cardoso, T. Chiarotti, D. Varsano, E. Molinari, A. Ferretti, *Phys. Rev. B* **2021**, *104*, 115157.

[135] T. Chiarotti, N. Marzari, A. Ferretti, *Phys. Rev. Research* **2022**, *4*, 013242.

[136] T. Chiarotti, A. Ferretti, N. Marzari, Energies and Spectra of Solids from the Algorithmic Inversion of Localized GW, **2023**, http://arxiv.org/abs/2302.12193 (visited on 08/31/2023), preprint.

[137] A. Ferretti, I. Dabo, M. Cococcioni, N. Marzari, *Phys. Rev. B* **2014**, *89*, 195134.

[138] C. E. Moore, *Atomic Energy Levels As Derived From the Analisys of Optical Spectra, Vol. 1*, Circular of the National Bureau of Standards, Washington DC, **1949**.

[139] *CRC Handbook of Chemistry and Physics*, (Ed.: J. R. Rumble), CRC Press, **2010**.

[140] D. Varsano, M. Barborini, L. Guidoni, *J. Chem. Phys.* **2014**, *140*, 054102.

[141] K. Krause, M. E. Harding, W. Klopper, *Molecular Physics* **2015**, *113*, 1952–1960.

[142] M. J. van Setten, F. Caruso, S. Sharifzadeh, X. Ren, M. Scheffler, F. Liu, J. Lischner, L. Lin, J. R. Deslippe, S. G. Louie, C. Yang, F. Weigend, J. B. Neaton, F. Evers, P. Rinke, *J. Chem. Theory Comput.* **2015**, *11*, 5665–5687.

[143] F. Caruso, M. Dauth, M. J. van Setten, P. Rinke, *J. Chem. Theory Comput.* **2016**, *12*, 5076–5087.

[144] E. Maggio, P. Liu, M. J. van Setten, G. Kresse, GW100: A Plane Wave Perspective for Small Molecules, arXiv, **2016**.

[145] M. Govoni, G. Galli, *J. Chem. Theory Comput.* **2018**, *14*, 1895–1909.

[146] F. Bruneval, *J. Chem. Phys.* **2012**, *136*, 194107.

[147] P. Koval, D. Foerster, D. Sánchez-Portal, *Phys. Rev. B* **2014**, *89*, 155417.

[148] W. Nelson, P. Bokes, P. Rinke, R. W. Godby, *Phys. Rev. A* **2007**, *75*, 032505.

[149] R. Sakuma, F. Aryasetiawan, *Physical Review A* **2012**, 6.

[150] J. Li, M. Holzmann, I. Duchemin, X. Blase, V. Olevano, *Phys. Rev. Lett.* **2017**, *118*, 163001.

[151] X. Blase, C. Attaccalite, V. Olevano, *Phys. Rev. B* **2011**, *83*, 115103.

[152] C. Faber, C. Attaccalite, V. Olevano, E. Runge, X. Blase, *Phys. Rev. B* **2011**, *83*, 115123.

[153] X. Blase, P. Boulanger, F. Bruneval, M. Fernandez-Serra, I. Duchemin, *J. Chem. Phys.* **2016**, *144*, 034109.

[154] M. J. van Setten, R. Costa, F. Viñes, F. Illas, *J. Chem. Theory Comput.* **2018**, *14*, 877–883.

[155] M. Tzavala, J. J. Kas, L. Reining, J. J. Rehr, *Phys. Rev. Research* **2020**, *2*, 033147.

[156] F. D. Vila, J. J. Rehr, J. J. Kas, K. Kowalski, B. Peng, *J. Chem. Theory Comput.* **2020**, *16*, 6983–6992.

[157] F. D. Vila, K. Kowalski, B. Peng, J. J. Kas, J. J. Rehr, *J. Chem. Theory Comput.* **2022**, *18*, 1799–1807.

[158] R. Wehlitz, B. Langer, N. Berrah, S. B. Whitfield, J. Viefhaus, U. Becker, *J. Phys. B: At. Mol. Opt. Phys.* **1993**, *26*, L783–L788.

[159] U. Becker, *Journal of Electron Spectroscopy and Related Phenomena*, Future Perspectives for Electron Spectroscopy with Synchrotron Radiation **1995**, *75*, 23–34.

[160] U. Becker, D. A. Shirley, *VUV and Soft X-Ray Photoionization*, Springer US, Boston, MA, **1996**.

[161] U. Becker, D. A. Shirley in *VUV and Soft X-Ray Photoionization*, (Eds.: U. Becker, D. A. Shirley), Springer US, Boston, MA, **1996**, pp. 135–180.

[162] B. Langer, J. Viefhaus, O. Hemmers, A. Menzel, R. Wehlitz, U. Becker, *Phys. Rev. A* **1991**, *43*, 1652–1655.

[163] T. J. Pollehn, A. Schindlmayr, R. W. Godby, *J. Phys.: Condens. Matter* **1998**, *10*, 1273–1283.

[164] H. Ness, L. K. Dash, M. Stankovski, R. W. Godby, *Phys. Rev. B* **2011**, *84*, 195114.

[165] J. S. Zhou, PhD thesis, École Polytechnique, **2016**.

[166] C. de Boor, *preprint* **1998**.

[167] C. de Boor, *A practical guide to splines (Revised edition)*, Springer-Verlag, New York, **2001**.

[168] B. W. Shore, *J. Chem. Phys.* **1973**, *58*, 3855–3866.

[169] M. Hellgren, U. von Barth, *Phys. Rev. B* **2007**, *76*, 075107.

[170] M. Labeye, F. Zapata, E. Coccia, V. Véniard, J. Toulouse, J. Caillat, R. Taïeb, E. Luppi, *J. Chem. Theory Comput.* **2018**, *14*, 5846–5858.

[171] E. K. Gross, E. Runge, H. Heinonen, *Many-particle theory*, Hilger, **1991**.

[172] P. C. Martin, J. Schwinger, *Phys. Rev.* **1959**, *115*, 1342–1372.

[173] J. Schwinger, *Proceedings of the National Academy of Sciences* **1951**, *37*, 452–455.

[174] G. Baym, L. P. Kadanoff, *Phys. Rev.* **1961**, *124*, 287–299.

[175] B. H. Bransden, C. J. Joachain, *Physics of atoms and molecules*, Longman Scientific & Technical, **1983**.

[176] J. F. Janak, *Phys. Rev. B* **1978**, *18*, 7165–7168.

[177] D. P. Chong, O. V. Gritsenko, E. J. Baerends, *J. Chem. Phys.* **2002**, *116*, 1760–1772.

[178] O. V. Gritsenko, B. Braïda, E. J. Baerends, *J. Chem. Phys.* **2003**, *119*, 1937–1950.

[179] D. M. Ceperley, B. J. Alder, *Phys. Rev. Lett.* **1980**, *45*, 566–569.

[180] J. P. Perdew, K. Burke, M. Ernzerhof, *Phys. Rev. Lett.* **1996**, *77*, 3865–3868.

[181] J. P. Perdew, M. Ernzerhof, K. Burke, *The Journal of Chemical Physics* **1996**, *105*, 9982–9985.

[182] C. Adamo, V. Barone, *The Journal of Chemical Physics* **1999**, *110*, 6158–6170.

[183] M. Ernzerhof, G. E. Scuseria, *The Journal of Chemical Physics* **1999**, *110*, 5029–5036.

[184] C. Adamo, V. Barone, *The Journal of Chemical Physics* **1999**, *110*, 6158–6170.

[185] E. Runge, E. K. U. Gross, *Phys. Rev. Lett.* **1984**, *52*, 997–1000.

[186] J. M. Luttinger, J. C. Ward, *Phys. Rev.* **1960**, *118*, 1417–1427.

[187] A. Klein, *Phys. Rev.* **1961**, *121*, 950–956.

[188] N. E. Dahlen, R. van Leeuwen, U. von Barth, *Phys. Rev. A* **2006**, *73*, 012511.

[189] U. von Barth, N. E. Dahlen, R. van Leeuwen, G. Stefanucci, *Phys. Rev. B* **2005**, *72*, 235109.

[190] S. Ismail-Beigi, *Phys. Rev. B* **2010**, *81*, 195126.

[191] G. Stefanucci, R. van Leeuwen, *Nonequilibrium Many-Body Theory of Quantum Systems: A Modern Introduction*, Cambridge University Press, **2013**.

[192] A. Grüneis, M. Marsman, J. Harl, L. Schimka, G. Kresse, *J. Chem. Phys.* **2009**, *131*, 154115.

[193] X. Ren, P. Rinke, G. E. Scuseria, M. Scheffler, *Phys. Rev. B* **2013**, *88*, 035120.

[194] S. Vacondio, MA thesis, Università degli Studi di Modena e Reggio Emilia, **2018**.

[195] R. W. Godby, R. J. Needs, *Phys. Rev. Lett.* **1989**, *62*, 1169–1172.

[196] J. Mitroy, M. S Safronova, C. Clark, *Journal of Physics B: Atomic Molecular and Optical Physics* **2010**, *43*, 202001.

[197] A. Kramida, Yu. Ralchenko, J. Reader, and NIST ASD Team, NIST Atomic Spectra Database (ver. 5.10), [Online]. Available: `https://physics.nist.gov/asd` [2023, August 8]. National Institute of Standards and Technology, Gaithersburg, MD. **2022**.

[198] H. Jiang, E. Engel, *J. Chem. Phys.* **2005**, *123*, 224102.

[199] F. M. Larkin, *Comput J* **1967**, *10*, 178–187.

[200] L. Wuytack, *Rocky Mountain J. Math.* **1974**, *4*, 395–398.

[201] H. J. Vidberg, J. W. Serene, *J Low Temp Phys* **1977**, *29*, 179–192.

[202] K.-H. Lee, K. J. Chang, *Phys. Rev. B* **1996**, *54*, R8285–R8288.

[203] M. Hellgren, U. von Barth, *Phys. Rev. B* **2007**, *76*, 075107.

[204] Y. Wang, J. P. Perdew, J. A. Chevary, L. D. Macdonald, S. H. Vosko, *Phys. Rev. A* **1990**, *41*, 78–86.

[205] J. B. Krieger, Y. Li, G. J. Iafrate, *Physics Letters A* **1990**, *146*, 256–260.

[206] J. B. Krieger, Y. Li, G. J. Iafrate, *Phys. Rev. A* **1992**, *45*, 101–126.

[207] A. Facco Bonetti, E. Engel, R. N. Schmid, R. M. Dreizler, *Phys. Rev. Lett.* **2001**, *86*, 2241–2244.

[208] M. Hellgren, U. von Barth, *J. Chem. Phys.* **2010**, *132*, 044101.

[209] R. van Leeuwen, O. Gritsenko, E. J. Baerends, *Z Phys D - Atoms Molecules and Clusters* **1995**, *33*, 229–238.

[210] C.-O. Almbladh, U. V. Barth, R. V. Leeuwen, *Int. J. Mod. Phys. B* **1999**, *13*, 535–541.

[211] N. E. Dahlen, R. van Leeuwen, *J. Chem. Phys.* **2005**, *122*, 164102.

[212] X. Ren, P. Rinke, V. Blum, J. Wieferink, A. Tkatchenko, A. Sanfilippo, K. Reuter, M. Scheffler, *New J. Phys.* **2012**, *14*, 053020.

[213] F. Bechstedt, *Many-Body Approach to Electronic Excitations*, Springer-Verlag, Berlin, Heidelberg, **2015**.

[214] D. C. Morton, Q. Wu, G. W. Drake, *Canadian Journal of Physics* **2006**, *84*, 83–105.

[215] A. Kramida, W. C. Martin, *Journal of Physical and Chemical Reference Data* **1997**, *26*, 1185–1194.

[216] E. C. Cook, A. D. Vira, C. Patterson, E. Livernois, W. D. Williams, *Phys. Rev. Lett.* **2018**, *121*, 053001.

[217] E. B. Saloman, C. J. Sansonetti, *Journal of Physical and Chemical Reference Data* **2005**, *33*, 1113–1158.

[218] W. C. Martin, R. Zalubas, *Journal of Physical and Chemical Reference Data* **1980**, *9*, 1–58.

[219] L. Minnhagen, *J. Opt. Soc. Am.* **1973**, *63*, 1185–1198.

[220] R. P. McEachran, A. G. Ryman, A. D. Stauffer, *J. Phys. B: At. Mol. Phys.* **1977**, *10*, L681–L684.

[221] E. Markiewicz, R. P. McEachran, A. D. Stauffer, *J. Phys. B: At. Mol. Phys.* **1981**, *14*, 949–953.

[222] S. Albrecht, L. Reining, R. Del Sole, G. Onida, *Phys. Rev. Lett.* **1998**, *80*, 4510–4513.

[223] P. Dennery, A. Krzywicki, *Mathematics for physicists*, Dover Publications, Inc., Mineola, New York, **1996**.

[224] J. Xi, X. He, B. Li, *Phys. Rev. A* **1992**, *46*, 5806–5811.

Acknowledgements

I wish to thank my PhD advisor Alice Ruini, my PI Andrea Ferretti, and my co-advisor Daniele Varsano, for their constant support during my PhD program, and for the freedom I was granted in developing my work. I am also grateful to Lucia Reining and Matteo Gatti for having me at the Laboratoire des Solides Irradiés of the École Polytechnique in Palaiseau, and for the fruitful discussions we had there together.

I thank all the friends and colleagues in Modena and Palaiseau for all the shared moments and the moral support during and outside working hours.

Most of all, I am deeply indebted to my parents.

Or poserai per sempre,
Stanco mio *core*.
G. Leopardi (attributed)